

UNIVERSITY OF LEEDS

Spatial Structure and Scale Interactions of Tropical Atmospheric Convection

James Bassford

Submitted in accordance with the requirements for the degree of PhD in Climate and Atmospheric Science

The University of Leeds

Faculty of Environment

School of Earth and Environment

June 2026

Abstract

In the tropical atmosphere, convection drives motion from the turbulent cloud–scale to the global overturning circulations. None of these scales of motion occur in isolation, instead their coexistence results in complex scale–interactions from which additional emergent dynamics and phenomena arise. Due to spatial resolution constraints, weather and climate models have historically struggled to represent convection and the associated scale–interactions, leading to errors in tropical forecasting and uncertainty in climate projections. This thesis aims to diagnose scale–interactions in modern, high–resolution models, and to assess the impact of the representation of convection in each case, over a range of scales and modelling domains.

Spatio-temporal relationships are identified between convection and later convection at sub-daily scales, supporting a growing body of evidence that scale–interactions provide predictability on short timescales. The aggregated effect of some of the same mesoscale dynamics, convective cold–pools, then alter regional scale circulation. Model representations of convection, and domain size, also affect measures of rainfall and moisture variability. The observed correlation between convective clustering and net radiation is examined at the regional scale over Africa, and the mechanism for the correlation is shown to be more realistic in a km–scale model. Finally, using concepts from statistical mechanics, model errors in distributions of water vapour are explained in terms of statistical contributions to moisture tendency. This final analysis sheds light on the processes leading to the observed bimodal distribution of column vapour over the tropical oceans, and offers an explanation for why it is often poorly represented in models. All these results contribute novel understanding to the field of tropical scale–interactions, provide new diagnostics for future model evaluation, and support investment in both km–scale simulation capacity and continued parameterization development.

Intellectual Property

The candidate confirms that the work submitted is his own and that appropriate credit has been given where reference has been made to the work of others. This copy has been supplied on the understanding that it is copyright material and that no quotation from the thesis may be published without proper acknowledgement.

Material in Chapter 4 (and some of the content of the literature review in Chapter 2) is based on the following article: Bassford, J., Parker, D.J., Marsham, J., Warner, J. (2026) Scale interactions of deep convection in the Sahel: Exploring ring patterns in lagged cross-correlations of rainfall. Quarterly Journal of the Royal Meteorological Society, https://doi.org/10.1002/qj.70041.

Material in Chapter 7 (and some of the content of the literature review in Chapter 2) is based on the following article: Bassford, J., Marsham, J., Maybee, B., Parker, D. J. (2026). Tropical TCV as a process diagnostic: Connecting probability to processes in km–scale models via moisture budget statistics. Geophysical Research Letters, https://doi.org/10.1029/2025GL120807.

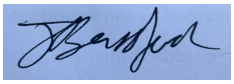
For both of the above publications, the candidate is the lead author of the article. He performed the scientific analysis, wrote the manuscript, and generated the figures. Co-authors provided suggestions for the methods to be used, as well as editorial corrections to the manuscript.

Material in Sections 5.1.1 and 5.1.2, including Figures 5.1 and 5.2, are based on the candidates contributions to the following article: Maybee, B., Bassford, J., Marsham, J.H., Lewis, H., Field, P., Klein, C., et al. (2025) How sensitive are Sahelian mesoscale convective systems to cold-pool suppression?. Quarterly Journal of the Royal Meteorological Society, https://doi.org/10.1002/qj.5032.

The candidate is the second author of this third publication, but for the portion used in this thesis he performed the analysis, generated the figures, and wrote the corresponding text. The first author Dr. Ben Maybee performed and produced the remainder of the publication's

analysis, figures, and text. Other co-authors ran simulations and provided data, gave suggestions for the methodology, and offered editorial corrections to the manuscript.

© 2026 The University of Leeds, James Bassford

Signed 

Acknowledgements

Firstly, thank you to my supervisors at Leeds, Doug Parker and John Marsham, for being as enthusiastic and supportive as possible throughout this project, and for all the opportunities they have given me to develop as a scientist and researcher along the way. Secondly, thanks to all of the people who co–authored or otherwise contributed to my first papers, for making the process more enjoyable and giving me confidence when I needed it. I would especially like to thank Ben Maybee, for being an invaluable mentor, as well as a consistent collaborator and friend, and for doing most of the work organising group meetings. I am also grateful to everybody at the Met Office who engaged with or contributed to this work. Particular thanks to my CASE supervisor Huw Lewis, along with James, Richard, and the rest of the RMED team for their consistent support both moral and technical.

To all the friends I have made in the office and beyond, cheers for being cool people, and for putting up with my chat. Being part of a community in Leeds and across the world has been the best thing about the past four years. This includes everyone in SEE, in ICAS, in Dynamics, those frequenting the Africa MAC and K-Scale gatherings, and of course the testbed troops. Last but not least, thank you to my friends and family. To my friends for their genuine interest, and for listening patiently to me ramble on over a pint or a coffee. To Mabel dog, for sitting with me while I write, and for making me stop writing to go outside and throw sticks. To Leah, for always keeping me grounded, for always being there for me, and for giving meaning to basically everything. To my family, for never questioning or doubting, and for all the years of support that led me to this point. To Mum, I know you would be proud of me.

Thank you all.

Contents

1 Introduction **1**

2 Multi–Scale Structures in Tropical Convection: Present Understanding and Challenges **7**

2.1 Convection and Tropical Dynamics 8

2.2 Global and Regional Scale Structures of Convection 10

2.2.1 Convergence Zones and Overturning Circulations 10

2.2.2 Monsoons and Monsoon Scale–Interaction 13

2.3 Synoptic Scale Convectively Coupled Features 15

2.3.1 Convectively Coupled Equatorial Waves 15

2.3.2 African Easterly Waves 16

2.4 Mesoscale Structures in Convection 18

2.4.1 Convective Self-Aggregation 18

2.4.2 Mesoscale Convective Systems 22

2.5 Convection and Moisture Dynamics 25

2.6 Convection and Climate Uncertainty 29

2.7 Summary and Thesis Outlook 32

3 Data and Methodology **34**

3.1 Data 34

3.1.1 The Met Office Unified Model 34

3.1.2 Satellite Retrievals 37

3.1.3 ERA5 Reanalysis 39

3.2 Methods 40

3.2.1 Lagged Cross–Correlation 40
3.2.2 Autocorrelation of Rainfall 41
3.2.3 Decorrelation of Total Column Vapour 42
3.2.4 Organisation Indices 43
3.2.5 Stochasticity and Fokker–Planck Equations 46

4 Scale Interaction and Patterns of Deep Convection in the West African Sahel 48
4.1 Data and Methods 49
4.1.1 Models and Rainfall Retrievals 49
4.1.2 Lagged cross–correlations 50
4.2 Lagged Rainfall to Rainfall cross-correlation 52
4.3 Investigating physical mechanisms 55
4.4 Summary of results 59
4.5 Start time sensitivity and storm lifecyles 60
4.6 Adaptability of the method 63
4.7 Conclusions and Discussion 65

5 Upscale Impacts of Convective Processes on the Regional Scale 67
5.1 Part 1: Cold Pools and the West African Monsoon Structure 68
5.1.1 Identifying cold pools and their gust fronts 69
5.1.2 Mean States and the Monsoon 70
5.1.3 Thermal Wind Balance 73
5.1.4 Heat Low Ventilation 74
5.1.5 Vertical Momentum Fluxes 77
5.1.6 Summary of Part 1 77
5.2 Part 2: Model hierarchy and distributions of precipitation and moisture 80
5.2.1 Lag–1 Autocorrelation of Rainfall in the DYAMOND Summer Period . . 81
5.2.2 Decorrelation of Total Column Vapour 86
5.2.3 Summary of Part 2 90
5.3 Conclusions and Discussion 91

6 Convective Clustering and Radiation Budgets in Regional Climate Simulations for Africa 94

6.1 Data and Methods 96
6.2 Measuring organisation of convection in regional climate models 97
6.2.1 Means, variability, and scales in the clustering index 97
6.2.2 Diurnal cycles in the clustering index and clustering scales 99
6.2.3 Response of model clustering to warming as a function of scale 101
6.3 Clustering–radiation relationships 103
6.3.1 Net radiation and clustering over Africa 104
6.3.2 Relationships with moisture and cloud 105
6.3.3 Diurnal phasing in radiation budget relationships 106
6.4 Conclusions and Discussion 110

7 Moisture Budgets, Convective Processes, and the Bimodal Distribution of Water Vapour over the Tropical Oceans 113

7.1 Data 115
7.2 TCV frequency distributions 115
7.3 Relating the TCV distribution to the Moisture Budget 117
7.3.1 The moisture budget equation 117
7.3.2 Average and stochastic tendencies and their relationship to the frequency distribution 117
7.3.3 Relating average tendency to physical processes using the moisture budget equation 119
7.3.4 Exploring expected tendencies in moisture budget analysis of low-rainfall environments 120
7.4 Conclusions and Discussion 123

8 Multi–Scale Structures in Tropical Convection: New Understanding and Future Directions 126

8.1 Overall Summary and Evaluation of Outcomes: Answering and Connecting the Research Questions 126
8.2 Current Limitations and Future Outlook 134
8.2.1 Limitations 134
8.2.2 Future Tropical Scale–Interactions Research 136

References **140**

List of Figures

3.1 A conceptual example of how cross–correlation can be used to reveal spatiotemporal patterns in noisy data. 41

3.2 Conceptual examples of calculations of I_{org} and L_{org} from binary arrays, where white dots are the object locations. The top row shows the distribution of objects for two cases with (a) regularly spaced clusters and (b) a cluster of clusters. The bottom row shows respective plots of the measured CDF values against the values expected from theory were the objects randomly distributed. The indices are the integrated difference between the blue and dotted black line for I_{org}, and between the orange and dotted black line for L_{org}, and are shown on the figure. (Adapted from a similar demonstration in Biagioli and Tompkins (2023b)) 46

4.1 Mean diurnal cycles of the thresholds used to define t_0 rain event and t_1 convective rain locations. (a) The sub-domain 99th percentile rainfall values at all possible t0 for CP4, P25, and IMERG. (b) The percentile corresponding to 2mm/hr at all possible t1 for CP4, P25, and IMERG. 51

4.2 An example of a probability map derived from cross-correlation (c) for a single day with $t_0 = 6Z$ and $t_1 = 15Z$. Location with rainfall over the thresholds are shaded blue in (a) and (b). The sub-domain (a) is shown in (b) by the red rectangle. 52

4.3 Probability of rain >2mm at t_1, surrounding the mean 99th percentile $6Z$ rain location, with $t_1 = 9Z, 12Z, 15Z, 18Z$ for CP4, P25, and IMERG. See section 2.2 for the calculation method. 53

4.4 Maximum, mean, and standard deviations of the probabilities (P) in Figure 4.3. 54

4.5 Results of radially normalizing the probability maps in figure 4.3. For a given direction the highest and lowest probabilities are represented in pale blue and brown respectively. See section 2.3 for calculation details. 55

4.6 Mean CP4 cross-correlation of 6Z rainfall locations over the threshold with $t_1 = 12Z$ 925hPa temperature anomalies in K (black contours) and 925hPa horizontal wind anomalies (arrows). Blue shading shows the top 20% of the radially normalized rainfall probabilities at $t_1 = 15Z$. 56

4.7 A north-south cross section through x=0 of figure 4.6, and the same for the 15Z CP4 radially normalized rainfall probabilities. Note that only the meridional component of the wind anomalies are shown. 57

4.8 A latitude-height cross-section through x=0 of the mean CP4 rainfall and omega anomaly cross-correlation with $t_0 = 6Z$ and $t_1 = 9Z$ and $21Z$. On both panels are the $\pm 0.1 Pas^{-1}$ contours for t1=9Z. 58

4.9 A north-south cross-section through x=0 of the CP4 rainfall and omega anom. cross-correlation (red) with $t_0, t_1 = 6Z, 12Z$. In blue is the cross-section of the CP4 radially normalized probabilities for $t_1 = 15Z$. 59

4.10 Sections of probability maps at $t_0 + 9hrs$ for t_0 in 0,14Z. Only the northward direction from the mean t_0 rainfall location is shown for simplicity. Meridional distance northward from the origin is shown by the y-axis. The lower x-axis shows t_0, and the upper x-axis is the corresponding $t1 = t_0 + 9$ hours. 61

4.11 Meridional mean of CP4 probability maps in figure 4.3, but for hourly t_1 up to 23Z. $t_0 = 6Z$. 62

5.1 The difference in the magnitude of 925hPa virtual potential temperature gradients at 18Z on the first day of simulations. Difference is defined as EVAPOFF minus control, such that negative values show where gradients are much larger in the control run and positive value for vice versa. 70

5.2 Differences in time means, EVAPOFF minus Control. Panel (a) shows differences in time–mean 850hPa winds (vectors), and surface temperature (colors). Panels (b) and (c) show time–mean temperature and moist static energy profile differences, averaged over 5° latitudinal sections. Panel (d) is like (a), but with 650hPa winds and total column water vapour. Finally, (e) and (f) show differences in time–zonal–mean 650hPa winds and precipitation respectively. 71

5.3 Latitude-height cross-sections of EVAPOFF minus Control zonal mean temperature (colors) and zonal wind (contours) differences. The mean differences are calculated over the first 1, 5, 10, 15, 20, and 30 days of the simulations respectively. 75

5.4 Changes to the Saharan Heat Low region and associated eddy temperature fluxes in the first 7 days of simulation. (a) is mean Low-level Atmospheric Thickness in the northwestern Sahara over time. (b) is a latitude-height cross section of model differences in zonal mean eddy temperature flux divergence, where the zonal means are calculated between the longitudinal boundaries of the LLAT calculation zone. (c) is the EVAPOFF mean low-level layer mean temperature over the first 7 days of simulation, with the box used to calculate (a) shown in red. Dotted black lines show the edges of the region used to calculate the zonal means in (b). (d) is as for (c) but for the Control run. 76

5.5 79

5.6 Lag–1 autocorrelation of daily rainfall over the DYAMOND Summer period, using Pearson correlation coefficients. Correlations are calculated on a common 0.1° grid, and only shown for where daily mean rainfall is greater than 1mm/day. The black box indicates the Africa LAM domain. 82

5.7 As for Figure 5.6, but instead using Spearman's rank correlation coefficients. . . 83

5.8 Mean lag–1 autocorrelations of daily rainfall over the Africa LAM domain for each model configuration in the K-Scale Hierarchy run over the DYAMOND Summer period. Again, areas where daily mean rainfall is less than 1mm/day are masked and so do not contribute to the mean. Green (GAL9) or red (RAL3) bar colours indicate the configurations internal physics settings, and hatching (RAL3 global driver) or no hatching (GAL9 global driver) indicates the driving model configuration for nested runs. The equivalent mean autocorrelation for GPM IMERG version 7 is also shown in grey. 85

5.9 As for Figure 5.8, but expanded to show the zonal mean lag–1 autocorrelation of daily rainfall over the Africa LAM domain. Again colour indicates the model physics settings, while solid (or dashed) lines indicate if run has GAL9 (or RAL3) boundary conditions. Individual configurations are not labelled here. The zonal mean lag–1 autocorrelation for IMERG retrievals is shown now by the black line. 86

5.10 3–hourly correlations between models' total column vapour (TCV) fields in LAM domains, on a common 0.1° grid. Correlations are calculated using Pearson correlation coefficients. The acronyms DS and DW refer to the DYAMOND Summer and Winter periods respectively. The labels 'glob10', 'CTC4p4', and '*_LAM4p4' refer to the GAL9 global, 4.4km CTC, and the 4.4km LAM configurations respectively. 88

5.11 As for Figure 5.10, but now showing correlations between model and ERA5 reanalysis TCV for the same domain and period. 90

6.1 Estimated L–functions (left) used for calculating the mean L_{org} (centre). Estimated PDFs of monthly anomalies in L_{org} (right); anomalies are calculated after deseasonalizing each monthly time series and removing linear trends. 98

6.2 Mean diurnal cycles of L_{org}. Present climates model runs are in blue, future climates are in red. Solid lines are CP4 and dashed are P25. The black line is observations. 100

6.3 Mean diurnal cycles of $(\hat{L} - L)/R_{max}$ for each model run and for observations. Shaded contours shows values as a function of both normalized scale R/R_{max} and time of day. The white dotted line in each panel indicates the scale where $(\hat{L} - L)$ is maximised throughout the diurnal cycle. 101

6.4 Climate change (future minus present) in mean diurnal cycles of $(\hat{L} - L)/R_{max}$. This is shown for all scales (left), and with the R-axis limited to mesoscales (right). Δ is shorthand for change. Note that here the time axis is repeated for clarity of interpreting values near 0UTC, and that different colour–scales are used for each model. 102

6.5 Relationships between detrended and deseasonalized monthly anomalies in African domain average net top–of–atmosphere radiation and clustering index L_{org}, for both CP4 and P25 models and for observations. Scatters are fitted with linear regressions with 95% confidence internals, and corresponding Pearson correlation R– and p–values are shown in the top left. 104

6.6 As in Figure 6.5, but for clear–sky net radiation and L_{org}. 105

6.7 Grid of correlations between monthly anomalies (deseasonalized and detrended) in the CP4 present climate. Variables correlated are L_{org}, domain mean net (N) and clear–sky net (CSN) TOA radiation, domain mean mid–level relative humidity (RH500), deep convective fraction (frac), and domain mean cloud–radiative effects (CRE). Numbers and colours in each box indicate the Pearson R–value for the correlation, and the adjacent stars indicate statistical significance based on p–values. More stars means a more significant correlation. 107

6.8 As for Figure 6.7, but for P25 in the present climate. 108

6.9 Grid of correlations between monthly anomalies (deseasonalized and detrended) in the model present climates, calculated separately for time of day at 3–hourly intervals. For each sub–figure, the hour is on the x–axis, and correlation R–value on the y–axis. The variables being correlated are labelled at the left of each row and the bottom of each column. Markers indicate the correlation for each hour, with standard error bars shown. Where correlations are statistically insignificant, they are plotted more faintly using a cross. On the rightmost plot in each row, the mean diurnal cycles of the row–variable are also plotted as solid lines (e.g. Mean N is plotted with the correlation of N and L_{org}). Lastly, vertical red dashed lines indicate where mean N changes sign in the diurnal cycle. 109

7.1 Frequency distributions of TCV for (a) ERA5 & IMERG (b) the explicit model, and (c) the parameterized model. Unconditional frequency distributions are shown in dark blue. Other distributions shown are when grid cells with rainfall below a threshold are excluded. Thresholds increase by factors of ten from $10^{-3}\,\mathrm{mm\,hr^{-1}}$ (cyan) to $1\,\mathrm{mm\,hr^{-1}}$ (orange). 116

7.2 A conceptual example of how sign changes in $\mu(Q)$ can lead to a bimodal steady state PDF. The PDF shown is the steady state solution in equation (7.3) when $\mu(Q) = rQ_* - Q_*^3$ and constant $\sigma^2 = k > 0$. Blue regions are where μ is positive (moistening on average), and red where μ is negative (drying on average). Labelled on the x-axis are the three solutions to $\mu(Q) = 0$, which correspond to turning points in the PDF. Arrows on the $\mu(q)$ line indicate the direction of the mean flow in $(Q, dQ/dt)$ phase space. 119

7.3 Distributions of MFD in TCV, $\log_{10}$(P) space. Shading shows bin-mean MFD for TCV, for (a)-(c) as in 7.1. Panel (d) shows the bin differences between explicit and parameterized models. Text on each subfigure indicates the proportion of the data where $P < 10^{-3}\,\mathrm{mm\,hr^{-1}}$. Contours show bin-density, other than (d) where they show the difference in bin-density between (b) and (c). Also overlaid in grey in (d) are TCV frequency distributions from Fig.7.1. The dark green line indicates the explicit model's frequency minimum, and the light green line highlights the change in the difference pattern above and below $P = 10^{-1}\,\mathrm{mm\,hr^{-1}}$. 121

7.4 TCV bin-anomalies $\overline{X|Q}' = \overline{X|Q} - \overline{X}$ of mean moisture budget terms only where precipitation is less than $0.1\,\mathrm{mm\,hr^{-1}}$. Bin-anomalies are defined for each term X as the mean of X where TCV $= Q$ in 1 mm bins minus the mean of X over the range of TCV from 30 to 60 mm. 122

8.1 TCV PDFs over the South-East Asia LAM domain in DYAMOND Winter model runs Jan-Feb 2020. Dry mode values are independent of domain size, but moist modes in smaller domains are more shifted towards the global driver. Moist extremes appear consistent between the CTC and LAM with the same physics and resolution. 130

8.2 Monthly Mean ERA5 Tropical Ocean TCV PDFs from 2001-2017, grouped by terciles of convective clustering (I_{org}), mean TCV, net TOA radiation (N), and monthly mean precipitation (GPM IMERG). The first column shows the PDFs for each tercile, and the second column the anomalies associated with each tercile relative to the mean TCV PDF. 132

8.3 Decadal Mean ERA5 Total Column Vapour PDFs for 1990-1999 and 2014-2023, and the decadal trend in density for each 1kgm^{-2} wide bin. For example, the frequency of columns in just the 60-61kgm^{-2} bin has increased by around 0.2% per decade. 133

List of Tables

3.1 Summary of model configurations, domains, resolutions, and physics options. . . 37

Chapter 1

Introduction

The atmosphere of the Earth is a chaotic fluid system. At any given moment, dynamical processes are moving and transforming energy on a continuum from the microscopic to planetary scale. Perhaps the most obvious forms of this energy are the heat in the air around us and the winds that move the clouds through the sky. The clouds themselves result from transformations of energy within a parcel of the atmosphere, when moisture carried in the air condenses and releases heat. Phenomena resulting from the interactions between heat, moisture, and motion are the primary concern of atmospheric dynamics, and over decades of research and observation the study of scale in the atmosphere has shown distinct phenomena occur at different scales in both space and time. An example of a relatively fast and small-scale process is moist convection, the vertical motion within an atmospheric column. In aggregate, latent heating from condensation in moist convection is the primary source of energy for disturbances in the tropical troposphere (Holton, 2004). The subsequent production of precipitation and clouds means moist convection is of leading order importance to both tropical weather in the short term, and to tropical and global climate more generally.

Tropical convection has been observed to organise into recognisable structures across a range of scales. Each scale of convective phenomena displays coupling to other aspects of circulation in a mutually inclusive fashion. That is to say that many forms of circulation cannot occur without convection, and also that convection itself can only be intensified and sustained when organised by those coupled circulations. For the initiation of a single convective updraft a trigger or driving mechanism for instability is simple to diagnose; the heating of the surface and condensation of moisture provide energy for continued ascent. However once many updrafts,

downdrafts, clouds, and phase changes of water begin to interact with each other and the environment, the outcome quickly becomes an inherently unpredictable and complex multi-vortex, multi-process problem. Discussions of causation between processes and across scales can also be unavailing, for example arguing whether moist convergence sustains convection or that convection promotes moist convergence. These kind of chicken-and-egg relationships make it difficult to always derive causal arguments in analysis of interactions between convection and the surrounding flow. Despite this, it remains possible and very useful to identify distinct phenomena in space and time using conventional labels for discrete ranges of scales (such as mesoscale or synoptic), whilst keeping in mind the continuous nature of the physics. Delineating distinct scales of phenomena is integral for the development of impactful weather forecasting at a range of lead times, and for building statistical descriptions of the climate and climate change.

The largest structures of convection on the planet are the convergence zones of the atmosphere's overturning general circulation, within which are embedded synoptic scale convectively coupled waves, organised convective storms, and convective features down to individual cloud scale. Diagnosing any upscale and downscale interactions between these is crucial to understanding and usefully predicting long–term and transient characteristics of both tropical and global weather and climate. This is especially important with regard to extremes of precipitation and humid heat, both of which are strongly correlated with the presence and circulation of moisture (Neelin et al., 2022; Jackson et al., 2025) and dangerous to exposed communities. For example, much of the diabatic heating and associated precipitation during monsoons is produced in organized convective storms, collections of spatially structured convective elements which can reach hundreds of kilometres across. These largest storms are known as mesoscale convective systems (MCS), and are associated with a significant proportion of tropical rainfall (Feng et al., 2021) including very intense and impactful weather events (Houze, 2018). The study of convective organisation is already broad (Holloway et al., 2017; Wing, 2019; Muller et al., 2022) and salient because of the known impacts of the events themselves, but the upscale effects of organisation on regional circulation and on climate more generally are still poorly understood.

Whilst extratropical dynamics can be usefully simplified using quasi-geostrophic theory, there is no analogous theoretical framework for how tropical convective heating impacts larger-scale circulation. Furthermore, historical and contemporary observations of the tropical atmosphere are more sparse than in the global north due to long-term socio-economic challenges (Parker

et al., 2008). The parallel development of weather forecasting alongside expansion of meteorological knowledge has been slowed by this lack of observation (Bechtold, 2019), and by the inherently different nature of the atmospheres in different latitudes. Huge progress has been made in forecasting globally since the introduction of Earth observation satellites, but daily scale forecasting of tropical rainfall location remains a challenge. The difficulty is due to the inherently stochastic nature of convective initiation during the strong tropical diurnal cycle. A lack of advance warnings for intense convective events leaves many communities vulnerable to impactful weather like flash flooding. Additional approaches from conventional forecasting have been developed to aid in managing risks from tropical storms, such as combining statistical data–driven models with real-time satellite data. These emerging approaches, as with traditional forecasting, benefit from better understanding of the underlying physical system, such as how existing convection in a given environment relates to near-term predictability of further convection nearby.

For many forecast users in tropical regions, a priority concern is economic and food security; information on seasonal rainfall in both the present and future climate is critical for agriculture and other industries. In these contexts, better understanding of how convective-scale processes relate locally and remotely to large-scale patterns can aid predictability at longer sub-seasonal and seasonal timescales. An important example is how the variability of rainfall within a given wet season is influenced strongly by the movements of moist and dry air masses (Parker et al., 2016; Aslam et al., 2024). The shifting spatial arrangements of moisture and interaction with convection and associated upscale processes is an active area of research (Mapes et al., 2018; Mayta and Corraliza, 2024; Robinson et al., 2025). Patterns of moisture and convective rainfall are also very much connected to overturning circulations and their variability at seasonal and interannual timescales.

The effects of scale interactions are also not confined to the tropical troposphere but have been shown to affect the middle atmosphere and the extra-tropics by influencing global-scale circulations (Holt et al., 2016; Schwendike et al., 2021; Tomassini and Yang, 2022). Convective cloud also plays a large role in the energy balance of the tropical region, and poor representation of convection in models leads to large uncertainty in the response of cloud characteristics and spatial organisation to climate change (Bony et al., 2015). Quantifying interactions between convection and climate that may be missing from existing projections can further constrain

uncertainty, particularly in future energy budget changes including temperature and rainfall. Narrowing the range of possible future changes is essential to provide actionable information for adaptation, especially in low-resource communities disproportionately exposed to climate impacts (Harrington et al., 2018; Hosseinzadehtalaei et al., 2025).

Because the Earth system is so complex, prediction and projection of weather and climate on all timescales relies on numerical simulation. These numerical models come in many forms including both regional and global numerical weather prediction (NWP), and both regional and global climate models (RCM or GCM). However, numerical simulations require the discretizations of space and time at a finite resolution. There is therefore always some cutoff scale where anything smaller isn't represented explicitly in the model fluid dynamics. Historically, these cutoff scales have been forced by practical considerations to be far larger than the scale of convection itself, and so convection must be approximated in the model by a separate set of equations called parameterizations. Discretizations and parameterizations are fundamentally at odds with the continuous nature of the interaction of scales within fluid flow.

Modern state-of-the-art models now use higher resolution that allows for convection to be more explicitly resolved alongside horizontal flows. Models run without parametrization are referred to as having 'explicit convection'. This is of course only ever a partly true description again due to discretization, and so terms like 'storm-resolving' or 'convection-permitting' are often used instead. Recent advances in technology, computation, and modeling science have allowed more and longer of these high-resolution runs to be performed than ever before (Stevens et al., 2019). However, parameterization is still required in many contexts such as multidecadal GCM runs or ensemble simulations. The ongoing need for parameterization motivates continued examination and quantification of the associated model errors and uncertainties. Since weather and climate systems are chaotic, errors on the smallest scales can grow to significantly affect the large scales (Lorenz, 1969; Sánchez et al., 2020; Craig et al., 2021). Understanding the mechanisms of this error growth is a key motivator for studying scale interactions, since many models perform poorly in the tropics due to a failure to capture the upscale impacts of unresolved physical processes such as convection (Stephens et al., 2010; Steiner et al., 2018).

In this thesis, we present evidence of tropical convective scale-interaction from convective to global scales, and over sub–daily to interannual timescales. We explore each set of scales and processes in observations and/or reanalyses, and analyse how they are captured by both global and

regional models with varying representations for the physics of convection, including kilometre-scale and convection-permitting climate simulations. In showing a full spectrum of interactions across a hierarchy of models, the aim is to show in one place a wide breadth of convection's role in the real and simulated tropical atmosphere. We hope to convince readers that silos of research focused on a given scale of phenomena are insufficient to fully understand those phenomena, let alone the whole system. Understanding scale–interaction remains key to progressing the science needed to protect more people from the impacts of the present and changing tropical climate.

We firstly present an overview (chapter 2) of contemporary research on tropical convection including that on precipitation and storms, the organisation of convection in idealized and realistic contexts, the roles of and interactions with moisture, waves and large-scale circulation, and the importance of convective cloud in the climate system. The review also discusses existing research on the roles of convective processes in climate feedbacks and the future characteristics and changing impact of convection in a warmer future climate. Chapter 3 describes the observations, reanalyses, and model data used throughout the thesis, and explains in detail the more complex of the statistical methods and metrics used in later analyses. Chapters 4 to 7 show results aiming to answer specific research questions which are outlined below.

- Chapter 4: Are there spatial correlations between intense precipitation locations on the same day, and what are the physical mechanisms responsible for these correlations?
- Chapter 5: How can convection and its representation in models affect regional scale circulation, and the spatiotemporal distributions of moisture and precipitation?
- Chapter 6: How does the spatial pattern of convection relate to the net top of atmosphere radiation budget in regional climate simulations of a tropical continent?
- Chapter 7: How do the mean relationships between convective dynamics and moisture relate to the bimodal distribution of column moisture over the tropical oceans?

In chapter 4 and part of chapter 5, we focus on the West African region during the monsoon. Due to vast but relatively flat continental orography, the presence of high wind shear, and a strong diurnal cycle, West Africa is a good 'natural laboratory' for studying deep convection and it's organisation into MCSs. West Africa also contains a full gradient of subtropical and tropical climates from the Sahara desert in the north to savannah and rainforest regions in the south. Monsoon rains and storms are particularly impactful in the semi-arid Sahel region,

between the tropical forests and savannahs to the south and the desert to the north. This gradient of thermodynamic conditions across West Africa is associated with prominent regional scale circulations which interact with convection and convective storms. Chapter 4 quantifies spatiotemporal patterns of rainfall during the monsoon, and links these patterns to low-level outflows (cold pools) and gravity waves produced by intense convection such as that in MCSs. Chapter 5 is in two parts, with the first showing upscale effects of not representing cold pools in a model on large–scale monsoon characteristics. This is followed by a more general exploration of how the choice of model domain, boundary conditions, and sub-grid physics can affect the distributions of moisture and precipitation.

Chapter 6 moves to a regional climate scale, building on existing observational work showing that convective clustering impacts tropical radiation budgets (Bony et al., 2020). Our work focuses on whether these effects are present in RCMs of the African continent, and how the representation of convection affects mechanistic pathways connecting spatial structure to net radiation. Chapter 7 similarly looks at how observed distributions of tropical moisture (Mapes et al., 2018; Robinson et al., 2024) are represented in km-scale models with different representations of convection, in this context over the whole of the tropical oceans. Using moisture budgets and concepts from statistical mechanics, we identify key relationships between moisture and processes associated with convection that are important for models to capture. Finally, chapter 8 is a discussion bridging each set of results and motivating suggestions for future research avenues.

Chapter 2

Multi–Scale Structures in Tropical Convection: Present Understanding and Challenges

This chapter will introduce some broad concepts in tropical meteorology and climate, and highlight the relevant and important supporting literature for the results later in the thesis. It begins with an introduction of the dynamics of atmospheric moist convection and its role in distinguishing tropical weather and climate dynamics from those in the higher latitudes. This is followed by an outline of how convection is currently and diversely represented in models at various scales. Content thereafter consists of a parallel discussion of physical science and associated modelling and predictability challenges.

Due to the pre–eminent role of latent heating in tropical disturbances, many spatiotemporal patterns in tropical thermodynamic fields are signals of scale–interactions involving convection. Current understanding of coherent structures in tropical dynamics is therefore presented here, starting with the largest scales of motion before moving on to embedded synoptic and mesoscale features. Circulation structures are then connected to existing research on convective coupling and convective organisation, the latter of which includes the dynamics of tropical mesoscale convective systems (MCS). There is then a discussion on the contemporary literature of tropical moisture dynamics, including both physical and statistical understanding of moisture–convection coupling in tropical precipitation and regional and global circulation. The

final part of the chapter returns to tropical climate, and the uncertain role of interactions between convective cloud, organisation, and circulation in both present and future climate.

2.1 Convection and Tropical Dynamics

Convection is a dynamic process common to all fluid systems that acts to equilibrate unevenly distributed energy; the atmosphere of Earth is one such system. Whether convective flows are turbulent and three-dimensional depends on the relative scales of the driving thermal gradients. For example, the atmosphere has a much larger horizontal extent than vertical height, and average thermal gradients in the vertical are far larger than horizontal gradients. As such, convection in the atmospheric sciences refers to the vertical motion of warm air rising in a column, and moist convection refers to convection where water vapour condensation counteracts adiabatic cooling and provides further heating for continued vertical motion. Deep convection, with vertical motion through the whole tropospheric column, would not be possible without the presence of water in the system. Diabatic latent heating is the primary source of heating in the tropical troposphere (Holton, 2004), and so moist convection is part of tropical circulations across all scales.

The astronomical definition bounds the tropics to approximately 23° either side of the equator. In this region, the Coriolis effect is weak and so the atmosphere's Rossby radius is large. Gravity waves generated by any local diabatic heating can therefore rapidly smooth out the temperature perturbation over large distances, by inducing vertical motion that adiabatically cools the heated column while warming the surroundings. Low Coriolis therefore leads to a free troposphere with relatively weak temperature and pressure gradients, compared to the higher latitudes, and much weaker mean winds, with the important exception of monsoon flows. Without strong horizontal gradients, the dominant balance for local heating or cooling is vertical fluxes (e.g. Sobel et al. (2001)). Weak rotation also means that the assumptions of the quasi-geostrophic approximation do not hold in the tropics (Charney, 1963). Without an equivalent simplification for the equations of motion there is no equivalently successful theory for tropical synoptic dynamics, aside from perhaps the theory of equatorial waves (Matsuno, 1966; Gill, 1982).

For large-scale vertical structure, the general framework of radiative-convective-equilibrium (RCE) (Manabe and Wetherald, 1967) posits that heating from convection and surface fluxes is balanced by radiative cooling to space to maintain a steady-state temperature profile. On

Earth, RCE is an effective approximation for large-scale temperature profiles over warm tropical oceans (Popke et al., 2013), and RCE idealization is used widely to study scale-interactions in tropical climate dynamics (Silvers et al., 2016; Jakob et al., 2019; Wing et al., 2020). However, RCE is very much an idealization with respect to regional and transient profiles. Near-RCE is observed if considering the whole tropics over timescales of days or longer, but at smaller spatial scales the RCE assumption breaks down (Jakob et al., 2019). The development of stable layers at low levels can inhibit convection, decoupling the surface from the free-troposphere (Jeevanjee et al., 2022). In these cases, the profile cannot adjust to RCE in the same manner, and to assume so in a modeling context would be inappropriate.

The defining weak horizontal gradients of the tropics recover from perturbations via redistributions of energy, including by gravity waves and divergent upper-level circulations associated with convection. The weak temperature gradient (WTG) approximation (Sobel et al., 2001) is a simplification of the equations for tropical dynamics by assuming horizontal temperature gradients are always small. Where this assumption holds, vertical dynamics can be reduced to a balance between diabatic heating and vertical advection of static energy. This relationship explicitly couples convection and circulation. A lack of pressure and temperature gradients means the primary modes of variability are in the moisture field, and indeed the simplified WTG equations permit wave solutions in the moisture field (Sobel et al., 2001; Adames, 2022). The WTG approximation has been been used for studying problems over a wide range of scales (e.g. Bretherton and Sobel (2002); Wolding et al. (2017); Ruppert and Hohenegger (2018); Stephens and Jackson (2020)). In idealized modeling, WTG is often used in conjunction with RCE (Wong and Kuang, 2023) with varying results depending on the chosen implementation.

Scale separation between small regions of latent heating with rapid ascent and larger areas of slow descent with radiative cooling also underlies the concept of convective-quasi-equilibrium (CQE) (Arakawa and Schubert, 1974; Emanuel et al., 1994; Yano and Plant, 2012). Under CQE assumptions, the relatively fast process of convection rapidly responds to larger scale perturbations, maintaining a steady state thermodynamic profile. This gives an approximation of the convection in a column given the boundary fluxes, and has been the basis for a closure of parameterizations of convection in models (e.g. (Bechtold et al., 2014)), but with some major criticisms (e.g. Yano and Plant (2020)). While the assumption that convective adjustment timescales are negligible is sound over climate timescales, it gets increasingly more inaccurate

with smaller timesteps, and so CQE is a much poorer representation of tropical convection for NWP scales (e.g. less than daily, (Zhang, 2003)) . Another major issue is that CQE is often at odds with the pre-existing idea of conditional instability, which allows for convective inhibition to prevent deep convection until some trigger event occurs. Convective inhibition forms part of the CISK mechanism of convective interaction (Charney and Eliassen, 1964; Smith, 1997), where large scale convective disturbances result from the release of build ups of large amounts of when inhibition is overcome. In contrast, the assumption in CQE that convection responds rapidly doesn't account for this build up of energy over intermediate periods between single updraft and sub-daily timescales. A full review of these contrasting theories is found in Tomassini (2020).

The assumptions that go into the above frameworks are scale-dependent, and their application to parameterization closure in GCMs or NWP models is difficult due to heterogeneity in the variables most associated with convective intensity (Yano et al., 2013). Another major criticism of such simplified frameworks is that they can neglect embedded processes and structure at intermediate scales between convection and the RCE or CQE-valid scale. Intermediate scale processes might contribute to large-scale thermodynamic tendencies beyond simple convective adjustments or responses to large scale forcing or trigger events, and such processes shouldn't be neglected in modelling (Colin et al., 2019). The problematic "diagnostic assumption" for sub-grid processes such as convection continues to motivate both process-based understanding of scale interaction, higher-resolution modelling, and non-deterministic forms of parameterization (Arakawa, 2004; Berner et al., 2017; Colin et al., 2019; Stevens et al., 2019).

2.2 Global and Regional Scale Structures of Convection

2.2.1 Convergence Zones and Overturning Circulations

The largest form of convective structure is the inter-tropical convergence zone (ITCZ), a region of time-mean convergence and ascent in the deep tropics. The north-south migration of the ITCZ or 'rain-belt' throughout the annual cycle has been long understood as a leading order control on wet/dry periods throughout the tropics on multiple timescales, although over Africa this view is challenged by contemporary observation and modeling (Nicholson, 2018). The zonal extent of the ITCZ and the variability in its intensity and position is strongly a function of longitude and whether the surface is land or ocean. Theory suggests the mean position of the ITCZ north of the equator results from hemispheric ocean energy imbalance, due to ocean

heat transport across the equator (Schneider et al., 2014). There are some additional zones of distinct and persistent convergence in the southern hemisphere, particularly active in the Austral Summer. The most active of these is in the South Pacific (SPCZ, Vincent (1994); Brown et al. (2020)), but others are documented in the South Atlantic (SAPZ, Carvalho et al. (2004)) and Indian Oceans (SICZ, Cook (2000)). The characteristic north-west to south-east orientation of these southern convergence zones is thought to originate from the interaction of deep convection with subtropical wave-trains (van der Wiel et al., 2015). Extratropical interaction is also a frequently observed source of tropical moisture exports (Knippertz et al., 2013), in which airmasses with high column moisture are filamented by cyclonic flow and carried eastward, sometimes associated with downstream development of subtropical trough features (Todd and Washington, 1999; Hart et al., 2013).

The ITCZ is associated with the ascending branch of the Hadley Circulation (Schneider, 2006), the mean meridional overturning of the tropical-subtropical atmosphere driven by differential solar heating of the surface. The original conception of the Hadley Circulation as thermally direct is inconsistent with observed profiles of atmospheric stability, and instead a 'hot towers' picture of ascent within the ITCZ is required (Holton, 2004). This is to say that all vertical heat transport in the ITCZ happens within horizontally narrow convective plumes. Large scale zonal heterogeneity in convection also largely follows global patterns of tropical sea-surface temperature (SST), associated with zonally overturning Walker Circulations (Bjerknes, 1969). Ascent contributing to the Walker Circulations is, like in their Hadley counterparts, in deep convective plumes. Convection and convective scales therefore have crucial roles in large-scale energy balance in the tropics, and globally via exports to the extratropics.

A consequence of the overturning circulations is that subtropical regions, and some equatorial regions, experience seasonal or persistent subsidence drying of the atmosphere, creating both terrestrial aridity and 'marine deserts' where relatively little rain or cloud can form. For example, zonal overturning in the Indian Ocean rises in the warmer seas to the east and descends in the Western Indian Ocean. This, combined with orographic effects, leads to a climate in Eastern Africa that is relatively dry despite its equatorial location (Nicholson, 2017; Munday et al., 2021). The region's people rely heavily on seasonal enhancements of convective rainfall, the mechanisms for which are debated (Nicholson, 2018). A lack of understanding of interactions between overturning circulations and convection or convectively coupled phenomena risks

unexpected impacts in the drier tropical and subtropical regions, both presently and in a changing climate. For example, Hart et al. (2018) found that model representations of convection change the seasonal strength of the overturning circulation. In this case a model with explicit convection has a stronger overturning, reducing a wet bias in southern subtropical Africa during Austral Summer. However, Hart et al. (2018) do not explain how the large–scale differences in vertical motion emerge, only that they are consistent with stability changes as one might expect. Jackson et al. (2020) explore statistics of the rain belts in the same models in more detail, and find a reduced frequency of rain–belt rainfall when using explicit convection. A reduced rain frequency, with the same mean rainfall and ascent, may be consistent with a narrower and stronger ascending branch of the Hadley Circulation and compensating stronger and/or broader descent. However, the relationship of a regional mean rain–belt's size and strength to its internal heterogeneity and intensity of convection is still not well understood, nor is the impact of parameterization on these relationships. It is non–trivial to relate changing properties of transient convection to some characteristic ratio in the 'widths' of ascent and descent, since those widths are only ever well defined in the means of shifting heterogeneous patterns over long periods.

Whilst mean descriptions for the dynamics of the overturning circulation and the ITCZ are well established (Held and Hou, 1980; Lindzen and Hou, 1988), the understanding of their variability regionally is an active field of research. The modern availability of many years of reliable atmospheric reanalyses have allowed for more detailed statistical and dynamical descriptions of regional differences in circulation (Schwendike et al., 2014; Hoskins et al., 2020; Hoskins and Yang, 2021). Aiding this effort are the development of mathematical techniques for two-dimensional partitioning three-dimensional flows for application to tropical overturning (Schwendike et al., 2014). The findings of reanalysis studies point to clear regional differences and low-frequency variability in local contributions to the global mean circulations. More overturning occurs in zones with a convectively active tropics, and mean tropical-extratropical motion is largely composed of transient and non-uniform flow structures (Hoskins et al., 2020). Idealized simulations of the Hadley and Walker Circulations have also been used to study transient behaviour (Slawinska et al., 2016; Gonzalez et al., 2017), and multi–scale interactions involving convection are abundant. Idealized transients correspond to subseasonal variability of the real overturning circulations, consistent with a local form of the hot towers view of ITCZ convection, where variability in the quantity and intensity of convective plumes is coupled to

mean overturning strength. Mean–transient interaction is explored explicitly by Tomassini and Yang (2022), who quantify Atlantic Hadley circulation variability down to daily timescales and show mechanistic links to convectively coupled waves. Similarly, Schwendike et al. (2021) show that local overturning varies with respect to convective enhancement and suppression by the Madden–Julian Oscillation.

2.2.2 Monsoons and Monsoon Scale–Interaction

Monsoons are defined by large seasonal reversals in regional circulation, and occur across multiple tropical continents. During the months of a seasonal monsoon, regional scale winds bring large quantities of oceanic moisture inland to regions that can be arid much of the rest of the year, such as the West African Sahel. This moisture, and a strong diurnal cycle of land-surface heating, provides fuel for large amounts of convection. Monsoon circulations promote intense convective rainfall much further poleward over land than the northernmost position of the oceanic ITCZ, and so are fundamental to life and livelihoods in semi-arid regions. It has also been argued that diabatic heating from Monsoon rainfall plays a key role in maintaining subtropical dryness during the Summer months (Rodwell and Hoskins, 1996).

Monsoons have been classically understood as large scale sea–breezes defined by regional geography (Webster, 2020b; Gadgil, 2018). More contemporary theories describe monsoons as parts of a global mode of variability in the overturning circulation, as reviewed by Geen et al. (2020). These more modern theories account for the observed criticality in monsoon onset despite the slower growth of land-sea temperature contrasts (Schneider and Bordoni, 2008; Bordoni and Schneider, 2008). Integrating monsoons into theories for the overturning circulation rather than viewing them as separate circulations is an important development for studying multiscale variability. However, each regional monsoon still has some distinct dynamics and characteristic phenomena due to factors like the underlying surface and position relative to other monsoons.

The West African Monsoon (WAM) is the seasonal reversal of the low-level winds between the Gulf of Guinea and the continent, alternating from north-easterly in winter to south-westerly in Summer (Fink et al., 2017b). The summer south westerlies bring moisture far inland; the northern boundary of this moist air mass is relatively sharp and referred to as the inter-tropical discontinuity (ITD). The ITD position oscillates, including with the diurnal cycle due to boundary layer stabilization (Parker et al., 2005a; Pospichal et al., 2010). Other key features of the

WAM are the mid-level African Easterly Jet (AEJ), Tropical Easterly Jet (TEJ), and the Saharan Heat Low (SHL). The SHL is located to the north of the monsoon region, where strong surface heating creates a low throughout the lower-troposphere. This sets up a large enough meridional gradient in geopotential to drive an easterly thermal wind jet (the AEJ), despite relatively weak Coriolis forces at these latitudes (around 10 to 20°N). The upper-level TEJ is not confined to Africa, and in fact its eastern–most extent is in the southern flank of the Summer anticyclonic circulation centered on the upper-level heating in the Himalaya. This relationship with the upper levels of the WAM downstream of the South–Asian Monsoon (SAM) has led to some exploration of remote impacts of SAM onset and variability on the WAM (e.g. Flaounas et al. (2012); Strnad et al. (2025)). Wave-activity has been documented on both the TEJ and AEJ (Nicholson et al., 2007; Cornforth et al., 2017), and the AEJ is a source of strong wind shear for the organisation of monsoon convection into intense mesoscale storms (Rotunno et al., 1988; Taylor et al., 2017; Fitzpatrick et al., 2020). Both the AEJ and TEJ interact with mesoscale dynamics and the associated storms (Besson and Lemaître, 2014).

Moisture and its transport clearly have a leading order role in the dynamics of monsoon rainfall. However the moisture dynamics defining onset and maintaining the supply of available energy for intense convection are more nuanced than simple advection. Interaction between air masses, particularly via vertical moisture advection and mixing by convection, has been shown to explain better the geographical progression of monsoon onset than simple horizontal advection by low-level flow (Parker et al., 2016; Turner et al., 2020). Similar interactions between airmasses during the monsoon, with moist monsoon flow at low level and dry subtropical air in the mid-levels leads to conditional instability and associated convective inhibition.

The large-scale nature of monsoon dynamics doesn't mean monsoon rainfall is at all homogeneous. Predicting seasonal totals or defining the seasonal onset of the monsoon locally is extremely challenging. Traditional methods for measuring onset for agricultural decision making use rainfall thresholds, both daily and accumulating, to determine if the monsoons have started and when crops should be planted. However, precipitation is an inherently heterogeneous field compared to more smoothly varying thermodynamic variables like temperature or humidity. This means that rainfall thresholds being met at a point observation is not necessarily a good indicator for onset in the surrounding region. Satellite retrievals allow for a wider view, but still the scale over which rainfall rates are averaged has an impact on whether thresholds

are met. Conventional regional scale onset prediction provides little benefit over climatology (Fitzpatrick et al., 2015), and onset metrics calculated at regional and local scales correlate poorly with each other (Moron and Robertson, 2014; Fitzpatrick et al., 2015). It has been shown that some smaller but coherent local onset regions exists in both the WAM and SAM Fitzpatrick et al. (2016a,b). Areas of onset coherence can be explained by more predictable synoptic scale mechanisms, but elsewhere in the region stochasticity associated with convection still dominates onset variability and the local scale.

Modeling studies have shown that the representation of convection, whether explicit or parameterized, has a significant impact on the large-scale monsoon structure (Marsham et al., 2013; Birch et al., 2014). The model treatment of initiation in regions with high inhibition changes the diurnal cycle of convection, with a significant upscale impact on meridional gradients in latent and cloud-radiative heating. Birch et al. (2014) showed that fast-growing errors in the monsoon flow due to the first incorrect diurnal cycle are maintained by feedbacks in the water budget, meaning that NWP during the monsoon rapidly loses large-scale skill without a better representation of convection. In the Indian monsoon region, systematic forecast biases also grow quickly (Keane et al., 2019), and similar mechanisms involving large-scale gradient changes are shown to improve monsoon representation in models with explicit convection (Willetts et al., 2017). Modes of sub–seasonal variability, combined with the inherent heterogeneity of convection, can also lead to local extremes during the wet season, with impactful flooding or crop-killing dry-spells. A realistic representation of convection in models is therefore essential for forecasting in monsoon regions, both for onset and for subseasonal variability.

2.3 Synoptic Scale Convectively Coupled Features

2.3.1 Convectively Coupled Equatorial Waves

Arguably the most successful theory for tropical disturbances is Equatorial Wave Theory (Matsuno, 1966; Lindzen, 1967; Gill, 1982). The theory derives a variety of modes of variability as normal mode solutions to a set of idealized equatorial shallow water equations. The common feature to all these modes is that they decay away from the equator due to the increase in the Coriolis effect, meaning that they predominantly propagate zonally and vertically. Transforming satellite retrievals of outgoing longwave radiation (OLR) into frequency-wavenumber space has shown that real equatorial waves are convectively coupled (Wheeler and Kiladis, 1999).

The formation and evolution of equatorial waves is therefore strongly associated with diabatic heating from convection. A first consequence of this coupling is that waves coupled to moist convection propagate more slowly than predicted by dry theory (Gill, 1982; Kiladis et al., 2009).

The scales of equatorial waves vary significantly. Individual wave events can have large impacts on convective rainfall on the synoptic scale (Horinouchi, 2013; Serra et al., 2020; Ferrett et al., 2020), through both dynamic and thermodynamic mechanisms. In aggregate, equatorial waves can alter the strengths of local and regional portions of the general circulation (Wang and Fu, 2007; Schwendike et al., 2021; Tomassini and Yang, 2022). Wave wind components alter horizontal circulation, while through convective coupling waves also have a role in triggering or suppressing the moist convective activity in regions with mean large-scale ascent. This is a good example of a downscale interaction mediating an upscale interaction, both of which involve moist convection.

2.3.2 African Easterly Waves

In the West African monsoon, a significant synoptic-scale mode of variability is African Easterly Waves (AEW). These are not a solution to the shallow equations, but do appear in the observed spectra (Kiladis et al., 2009). A popular theory is that AEWs form due to mixed barotropic–baroclinic instability in the zonal shear flow (AEJ) in the lower troposphere over West Africa (Burpee, 1972; Thorncroft and Hoskins, 1994; Hsieh and Cook, 2008). Thorncroft et al. (2008) later showed that finite–amplitude latent heating perturbations on a linearly stable background state also resemble AEW–like waves. In both cases, wave–generation and development are strongly coupled to convection.

In the mixed barotropic–baroclinic theory, destabilization occurs when diabatic heating from convection reverses the meridional potential vorticity gradient across the AEJ region. Associated barotropic and baroclinic processes involve both upscale and downscale interaction, including energy conversions between the AEJ and convectively generated eddies. The region to the west of high orography east of the AEJ has been suggested as a key source for initial perturbations for wave activity, with convection favoured by elevated heating and orographic uplift (Mekonnen et al., 2006; White et al., 2021). It has also been shown that existing AEWs can affect upstream development of new AEWs to their east (Diaz and Aiyyer, 2013).

The wavelengths of AEWs range from 2000-5000km, and their periods from 2-6 days (Cornforth

et al., 2017). They are most prominent in the lower troposphere with the peak trough amplitude at the height of the AEJ. A displacement of the ITD is associated with the AEW trough, and patterns of anomalous column water and low-level vorticity largely follow the wave structure. These anomalies create patterns of favorable conditions for the development of organised deep convection, which reinforce and sustain the wave anomalies via further diabatic heating heterogeneity and PV generation (Tomassini et al., 2017; Tomassini, 2018; Russell et al., 2020). This is a very clear example where scale-interactions between the large-scale zonal flow, AEWs, and organized convection are fundamental to synoptic variability in the West African Monsoon, and provide a source of predictability.

Because of the major role of diabatic heating in upscale pertubation growth, the representation of convection in models will impact skill in wave-related weather prediction (Elless and Torn, 2019; Sánchez et al., 2020; Craig et al., 2021). For example, an incorrect diurnal cycle of convection places local convection in a different place or time than reality given the same initial conditions, leading to incorrect diabatic heating patterns and therefore incorrect evolution of the wave in which that convection is embedded. Errors then grow rapidly in a feedback loop, since the incorrectly evolved wave-state alters the pattern of conditions favourable for later convection. Studies comparing models with parameterized and explicit convection have shown significant differences in AEW characteristics (Birch et al., 2014; Morris et al., 2024), and some suggest resolving more convection improves equatorial wave realism more generally (Judt and Rios-Berrios, 2021).

There are further impacts of misrepresenting convection in AEWs beyond West Africa, since many AEWs propagate westward over warm Atlantic surface waters and become precursor disturbances for Tropical Cyclones (TCs) (Russell et al., 2017; Ocasio et al., 2020; Duvel, 2021). Atlantic TC track prediction is improved by 'optimizing small-scale convective activity' (Gao et al., 2023) to better represent the upscale impacts of that convective activity on the larger-scale flows, in which the TC is embedded. The track of a TC changing due to its own impact on circulation is an example of a high-impact scale-interaction between convection and circulation. Cyclogenesis has also been linked to equatorial waves in other basins (Schreck et al., 2012; Schreck, 2015; Feng et al., 2023a). Other westward propagating waves, tropical depressions (TD) and equatorial Rossby (ER) waves, are also seen as precursors to TCs, while enhancement of TC circulation has been associated with the convectively active phase of the eastward propagating

Kelvin waves. The representation of convection in models will therefore affect TC genesis prediction and statistics, via the simulated evolution of precursor disturbances. Modelling choices also impact the convective processes in mature TCs, with implications for track and intensity prediction skill (Taraphdar et al., 2014; Lim et al., 2015; Judt, 2020; Baker et al., 2024).

2.4 Mesoscale Structures in Convection

As well as structure emerging from couplings with larger circulatory features, multiple individual convective elements will also interact with each other and the environment at smaller scales. This can give rise to mesoscale substructure within a given envelope of enhanced convection. Here the label of 'organisation' is often used, but definitions vary with context; some use organisation as shorthand for the dynamics of spatial structure in general, and others specifically to describe mesoscale storms. Discussion of these two concepts are separated here for clarity, starting with the more general use of organisation for spatial patterns such as clustering of cloud or updrafts.

Convective organization in its many forms has been the subject of extensive research and review (Mapes, 1993; Stevens, 2005; Moncrieff, 2010; Muller et al., 2022). Understanding how two patterns of convection are connected in time through self–interaction mechanisms offers a potential measure of predictability as well as a means of evaluating the physical realism of model processes. However, the mechanisms for mesoscale organisation are fundamentally unresolved in coarse global NWP and GCM simulations, and so the potential interaction of mesoscale organisation with large-scale coupled circulations is not well-understood. This has been one of the key motivators for performing km-scale, non-idealized, tropical or global simulations (Bony et al., 2015; Stevens et al., 2019; Stephan et al., 2021), in order to determine the dynamics of mesoscale organisation in a realistic context, and to quantify any apparent systematic differences from coarser models when organising dynamics are resolved.

2.4.1 Convective Self-Aggregation

The phenomenon of convection determining its own spatial patterns is commonly referred to as self-organization or self–aggregation. The study of self–aggregation makes extensive use of small-domain, high-resolution cloud-resolving model (CRMs) simulations. These models

are run in idealized non-rotating ocean domains, and designed to evolve towards RCE. Under certain conditions, convection spontaneously clusters into sub-regions of the total domain. Self–aggregation occurs even in simulations with uniform boundary conditions and a fixed domain total mass-flux. This kind of idealized organisation is dynamically distinct from wind-shear driven organisation in squall-lines, since there is no required background flow to produce the spatial structure.

Determining whether convection will self-aggregate for a given domain and boundary conditions is complex. In the single column model of Sobel et al. (2007), the number of possible stable states changes from one to two when SSTs are raised above a critical value. These two supercritical stable states are a dry free-troposphere with no deep convection, and a convective state with a deep moist column. Whether the model evolves into one state or the other here depends on the initial moisture profile. This sensitivity to surface fluxes has since been referred to as radiative-convective instability (RCI) (Emanuel et al., 2014; Wing and Emanuel, 2014). This theory describes the existence of multiple equilibria as the result of instability in the normal RCE state to large-scale overturning circulation above some critical surface heat flux, controlled by SSTs. Above the critical SST therefore, a small positive perturbation in vertical velocity away from zero leads to the strong convective balanced state where average vertical velocity is positive and the free-troposphere is moist. Conversely, a small negative perturbation leads to a balanced state with mean descent and a dry free-troposphere. The mechanism proposed for this bi-stability involves feedbacks between longwave-cooling and moisture. In simple terms, stable columns are either moist-convective or dry and subsiding. These arguments have been used to explain the two-dimensional pattern of aggregation in CRMs, as well as the seemingly non-deterministic and heterogeneous nature of real tropical precipitation in otherwise smoothly varying environments.

The dynamical mechanisms of aggregation, those that take a set of columns from RCI to some combination of statistically steady states, are what is largely investigated using CRMs. These mechanisms include radiative feedbacks (Bretherton et al., 2005; Wing and Emanuel, 2014) as well as independent moisture feedbacks (Tompkins, 2001a; Muller and Bony, 2015; Holloway and Woolnough, 2016). The main radiative feedbacks are the direct feedback between column drying and longwave cooling, and a second indirect feedback where shallow circulation develops as a response to horizontal gradients in longwave cooling. These radiatively driven shallow

circulations sustain existing patterns of convection by advection of moist static energy (MSE) up the MSE gradient (Muller and Held, 2012; Muller and Bony, 2015). Potential moisture feedbacks driving self-aggregation are related to how convection strengthens with column moisture (Neelin et al., 2009; Wolding et al., 2020), while the associated diabatic heating drives horizontal convergence and vertical motion that moistens columns and sustains that high moisture content (Tompkins, 2001a; Craig and Mack, 2013; Windmiller and Craig, 2019; Biagioli and Tompkins, 2023a). The strength of this moisture feedback is potentially limited by the evaporation of precipitation generating cold-pools which cool and dry the boundary layer, inhibiting further convection (Tompkins, 2001b). However, lifting at the turbulent edges of cold pools has been linked to initiation of new convection (Torri et al., 2015; Drager and van den Heever, 2017; Meyer and Haerter, 2020), and so the overall effect of cold-pools on aggregation is not straightforwardly enhancing or inhibiting (Jeevanjee and Romps, 2013; Haerter, 2019; Haerter and Muller, 2023; Cerlini et al., 2023).

Beyond the effect of SST criticality, simulated self-aggregation has been shown to be dependent on the size of the domain (Jeevanjee and Romps, 2013), the horizontal resolution (Muller and Held, 2012; Wing et al., 2017), and sub–grid physics parameterizations (Wing et al., 2020). Unintentionally running CRMs with SSTs close to the critical value for RCI might explain sensitivities to parameterization (Emanuel et al., 2014), since different physics might shift this critical value slightly giving aggregation in some simulations but not others. The treatment of moisture in CRMs also impacts the relative contributions of each feedback to the aggregation process (Cerlini et al., 2023), giving different impacts of aggregation on the mean state.

Important features of the real large-scale atmosphere, such as diurnal cycles and the presence of rotation, are neglected in many of the theory-supporting idealized simulations. However, Haerter et al. (2020) introduce a diurnal cycle in a CRM experiment, and find it strongly impacts the timescale and persistence of aggregation. If the cycle amplitude is large enough, convection aggregates spontaneously during the second day and then oscillates between more aggregated and disaggregated states every other day. In another step towards realism, Wing and Cronin (2016) perform RCE experiments in a 10^4km long channel as a proxy for the real geometry of the tropics. They found aggregation occurred periodically in the long axis of the domain, with separation between aggregated regions shrinking with increasing SSTs. Finally, Davison and Haynes (2024) investigate the effect of rotation on coarsening of the moisture field,

by coupling a reaction-diffusion type model for moisture to a simple dynamical model on a rotating f-plane. They find the impact of rotation, when combined with thermal and frictional damping, is to limit the scale of coarsening, analogous to limiting the growth of concurrent convecting and non–convecting regions.

In order to quantitatively compare and contrast organisation in idealized models with that in real atmospheric observations, some measure of organisation is needed. A variety of metrics are used in the literature, as reviewed by Biagioli and Tompkins (2023b). Issues with more simple metrics, such a simple spatial variances of column moisture, are that there is no monotonic relationship between them and the aggregation observed in models. Statistical measures of clustering, which measure the distance of a given spatial pattern from a theoretically derived randomness, have been developed as alternatives and used on both CRM output and satellite retrievals (Tompkins and Semie, 2017; Semie and Bony, 2020; Bony et al., 2020; Biagioli and Tompkins, 2023b; Mandorli and Stubenrauch, 2024). However, these methods require a binary definition of convecting locations in order to measure distances between those locations. The choice of high enough resolution fields from which to define these locations in observations is limited; gridded patterns of real vertical velocities at updraft scale are unavailable. The sensitivity of the indices themselves to the data used also makes measuring organisation in observations nuanced and challenging (Mandorli and Stubenrauch, 2024).

There is some doubt about whether phenomena that occur in idealized RCE in smaller domains are relevant to the real earth system. While the tropics as a whole is in near-RCE at daily timescales and longer, less is certain about smaller scales. Jakob et al. (2019) found that satellite–derived tropical energy balance stays near RCE 80% of the time only when considering domains with scales of 5000km^2 or larger. Near-RCE is not even a long–term mean for smaller domains, meaning that the larger–scale RCE is achieved only by balancing net heating in the moist tropics with net cooling in the dry subtropics and other subsidence regions. This suggests that any self–structuring within the ITCZ, for example, is not sufficient to achieve equilibrium.

Despite the challenges of quantitative descriptions of aggregation, and the absence of RCE in small domains of the real atmosphere, qualitative clustering remains an obvious feature of tropical convection. Holloway et al. (2017) discuss determining if real clustering is at all self–structuring, by considering how to observe aggregating mechanisms seen in idealization. A lack of smaller scale RCE doesn't necessarily preclude the existence of those same mechanisms in

non-equilibria, or imply they do not act in the direction towards equilibria as they do in the absence of larger scale dynamics. Whatever the mechanisms for the spatial structure are, there are still important measurable impacts of instantaneous clustering of convection on interannual energy balance variability (Mauritsen and Stevens, 2015; Bony et al., 2020). This fact continues to deserve attention; if a tropics with more clustering of deep convection radiatively cools to space more for a given fractional coverage of deep cold cloud, then this more clustered tropics has the potential for higher ratios of arid and semi-arid subtropical to climatologically moist area. The implications of this effect for climate sensitivity to greenhouse gas (GHG) forcing are discussed later, along with the implications for rainfall impacts, in the section on convection and climate uncertainty. It remains pertinent to understand how the key mechanisms for structure in idealizations relates to existing theory for the organisation of real convection, such as into mesoscale convective systems.

2.4.2 Mesoscale Convective Systems

Both over tropical land and ocean, convection frequently "organises" into mesoscale convective systems (MCS). These are very large collections of thunderstorms on the scale of hundreds of kilometres across. MCS produce 50–70% of the total rainfall over the tropical oceans (Webster, 2020a), and even larger proportions over some tropical landmasses (Mathon et al., 2002; Schumacher and Rasmussen, 2020; Feng et al., 2021). The global MCS population consists of many diverse morphologies, yet they share some common characteristic scales and structural features. Ascent within a canonical MCS consists of many closely clustered moist–convective updrafts in a core or leading edge like structure, and corresponding downdrafts generated by evaporation and mass–loading of rainfall. Where the updrafts meet the level of neutral buoyancy or tropopause, air is forced to diverge outwards by continued vertical convergence. Upper–level divergence and gravity–waves generated by strong latent heating in the MCS core or leading edge (e.g. (Pandya and Durran, 1996)) support the production and spreading of thin, horizontally expansive high cloud structures known as anvils. The scale and coldness of those anvil clouds allows MCS to be easily identified in satellite imagery. While precipitation rates are most intense in the convective core region, significant amounts of a storm's total precipitation are stratiform, with exact proportions depending on the environment (Schumacher and Houze, 2003; Schumacher and Houze JR., 2006a).

While dominant conceptual descriptions of MCSs are mostly derived from observations of specif-

ically land–based storms in high–shear environments like the US Great Plains or West Africa, globally MCS structures vary dramatically both within and between regions (Houze, 2018; Schumacher and Rasmussen, 2020; Feng et al., 2021). The presence of a distinct core and anvil, the relative size and orientation of convective and stratiform components, and the direction and speed of propagation, all depends on the environment in which an MCS is organised. Theories for the organisation and maintenance of MCS involve varying degrees of interaction between environmental wind–shear, stability, and the cold pools generated by cool dry downdraft air spreading out near the surface (Rotunno et al., 1988; Parker, 1996; Lin, 2007; Alfaro, 2017). All agree however that the organization process is fundamentally some scale–interaction between the microphysics of precipitation, convective heating, the resulting mesoscale circulation, and the synoptic scale shear flow. In the West African Sahel, the strong low– to mid–level zonal shear between the moist monsoon flow and the AEJ acts to organise MCSs into westward propagating systems such as squall lines, and higher shear is associated with larger systems with more extreme precipitation (Taylor et al., 2017; Abramian et al., 2023; Maybee et al., 2024).

Interaction with the environment persists during the mature stages of an MCS lifecycle. Environmental moisture is very influential, since the entrainment of environmental air into updrafts can suppress them when that air is significantly drier. In this way, moisture mediates the shear–response of MCSs, since highly–sheared MCSs have larger updraft cores, making them less susceptible to dry–entrainment dilution (Mulholland et al., 2021). It has been observed over land that the depths of wider cores are less sensitive to moisture, and are better predicted by conditional instability (i.e. CAPE) (Varble et al., 2024). Narrower cores however are more sensitive to mid–level moisture and not to CAPE. The size distribution of convective cores, and the relative importance of conditional instability, is therefore strongly coupled to the joint PDF of shear and moisture. Environment–MCS interactions are also upscale, such as when temperature and momentum fluxes in MCS circulations alter the synoptic flow (Lafore and Moncrieff, 1989; Moncrieff, 1992; Morris et al., 2024). Cold pool outflows can also carry air long distances, with the aggregate effect of mixing the thermodynamics properties of the boundary layer across synoptic scales. For example, cold pools in the Sahel transport cooler and moist air northward, ventilating the Saharan heat low (Garcia-Carreras et al., 2013; Marsham et al., 2013; Trzeciak et al., 2017). This redistribution changes large–scale thermodynamics gradients, which feeds back on the circulation in which the MCS are embedded, giving cold pools a non–negligible role in the West African climate (Marsham et al., 2013; Birch et al., 2014).

Beyond just the atmospheric environment, interactions with surface heterogeneity constrain spatial distributions of the initiation, tracks, and intensity of MCS. In particular for the Sahel, soil moisture is negatively correlated with subsequent MCS track and initiation (Taylor et al., 2011a,b; Klein and Taylor, 2020), and more homogeneous soil moisture distributions reduce the frequency of storms (Maybee et al., 2025b). Gradients of soil moisture can generate density-driven flows which enhance convection at the edges between wetter and dryer regions (Taylor et al., 2010; Garcia-Carreras et al., 2011). When the enhanced low-level flow aligns with the mean–flow the local wind–shear increases, enhancing the MCS organisation process and increasing its size and capacity for precipitation (Taylor et al., 2017; Barton et al., 2025). At synoptic timescales, because MCS precipitation substantially wets the ground and suppresses both new convection and the passage of upstream storms, soil–moisture effects lead to negatively correlated rainfall locations from one day to the next. Land surface effects can also be remote from existing systems, for example Birch et al. (2013) present a case study where a gravity wave generated by an MCS initiated further convection upon propagating over favorable soil moisture conditions. In this case, convergence was present at the synoptic scale, but the trigger was a combination of mesoscale features.

Circulations at scales below the effective resolution of a given model are fundamentally unresolved, and so coarse–resolution global NWP and GCMs struggle to accurately represent MCSs and their upscale impacts (Moncrieff et al., 2017; Slingo et al., 2022). Approaches to correct these issues either require the development of parameterization of organisation itself (e.g. Mapes and Neale (2011); Moncrieff (2019)), or by increasing the resolution of models to resolve more convection explicitly. Using km–scale grids resolves more of the MCS circulation explicitly, and as such MCS representations and scale–interaction are improved (Crook et al., 2019; Feng et al., 2023b; Morris et al., 2024; Maybee et al., 2024). However, errors still remain if convection is completely explicit at km–scales. These errors include a common tendency among km–scale models to overestimate convective rainfall rates and cloud-top heights; possibly related to still poorly represented sub-km mixing processes. The area of stratiform rainfall is also underestimated (Feng et al., 2023b), which is a crucial control on the shape of the tropical mean precipitation–moisture relationship (Ahmed and Schumacher, 2015). The assessment of MCS characteristics also depends on the method of identifying MCSs in model data and observations (Feng et al., 2025). Feature–tracking has limited utility in the search for common governing dynamics, due to the diversity of mesoscale structures, but has very high utility in forecasting

and impact–assessment and reduction.

The initiation location of an impactful MCS is fundamentally difficult to predict, but such systems are quasi–stable once formed and propagating. An alternative approach to conventional forecasting is therefore to monitor and project the track of existing storms in satellite imagery, rather than simulate the following day's convection using NWP. This approach, focusing on lead times of up to 6 hours, is known as Nowcasting, and has seen successful development and application in an African setting (Parker et al., 2022; Roberts et al., 2022; Ageet et al., 2024). As opposed to purely physics–based synoptic NWP, tools for Nowcasting are generally statistical or data–driven. For example, as part of the NFLICS project (Cole et al., 2022; Anderson et al., 2023), past observations of MCS convection were used to build a nowcasting tool that uses a database of location-conditioned probabilities to calculate likelihood maps of near-term future convective activity, based on the current pattern. Methods using proxy observations of soil moisture also show skill in nowcasting the tracks of MCS (Taylor et al., 2022). Beyond Nowcasting, other statistical methods have used previous days' rain to predict a day ahead, and this has been shown to outperform a global ensemble in West Africa (Vogel et al., 2021). The skill of such an approach is mainly still in predicting propagating features, such as MCS and Easterly Waves (Vogel et al., 2021; Rasheeda Satheesh et al., 2023).

2.5 Convection and Moisture Dynamics

Across all scales previously discussed in this chapter, it is apparent that moisture is a crucial variable in the dynamics of convection. The influence of moisture spans from the basic thermodynamic role of phase changes in the buoyancy of a single parcel, to global scale feedbacks on the Earth's energy budget. The most abundant state of moisture in the atmosphere is water vapour; a fundamental component of the climate system, nowhere more so than in the tropics.

The distribution of water vapour is reliably estimated over tropical oceans using satellite remote sensing. Bimodal water vapour distributions have been observed, first in the upper–troposphere (Zhang et al., 2003), and then later in the full column (Mapes et al., 2018). A bimodal frequency distribution, with dry and moist peaks and a local minimum in between, is well defined in the climatological frequency distribution and is the dominant daily pattern. Mapes et al. (2018) describes the narrow boundary between the moist and dry regions of the tropics as a 'moist margin', the location of which shifts significantly on synoptic timescales independently of SST

variability (Mapes et al., 2018; Robinson et al., 2024). Deep convection occurs almost exclusively on the moist side of the margin, and so the feature represents a strong but mobile spatial constraint on tropical rainfall location. Importantly, Mapes et al. (2018) also shows that some climate models completely fail to reproduce the bimodal nature of the observed distribution, the implications of which are not well–understood.

The spatial distribution of water vapour is coupled to atmospheric dynamics via the production of precipitation and cloud, which are in turn major components of the energy budget. Water vapour directly interacts with radiation, as do the clouds produced by its condensation. There is also a growing body of ideas and evidence for how coupling between local convective processes and circulation leads to a measurable amount of self–sensitivity in the atmospheric moisture field and its structure. Realistic vapour–circulation coupling, or 'moisture dynamics', is therefore essential for accurate modelling of the system on a range of timescales from hours to decades (Bony et al., 2015; Slingo et al., 2022).

One definition of moisture dynamics is the characteristic behaviour of the moisture budget in space and time. A simplified version of this budget considering just total column vapour (TCV) is

$$\frac{dM}{dt} = E - P - \mathrm{MFD}\,, \tag{2.1}$$

where M is total column vapour, E is evaporation, P is precipitation, and MFD is vertically integrated moisture flux divergence. In words, any change of vapour content in a column is a balance between phase changes and horizontal transports into and out of the column.

While not independent of other aspects of atmospheric dynamics, it has been observed that terms on the right of the moisture budget are themselves non-linearly related to TCV, making the budget non-linear also. For example, precipitation P has been observed to be non-linearly related to column moisture in both the absolute and relative sense. Bretherton et al. (2004) found non-linear relationships between satellite vapour path and precipitation retrievals at monthly to daily timescales over tropical oceans. Peters and Neelin (2006) and Neelin et al. (2009) also found a power–law scaling for P with TCV, along with other statistical relationships that suggest P-TCV dynamics are an instance of self-organising criticality. This criticality means that rainfall, and therefore inferred convection, transitions sharply to high intensity above some

critical value of TCV.

Neelin et al. (2009) also showed that the role of SST in precipitation intensity is not direct, and instead is mediated by the moisture PDF, since higher SSTs imply more frequent instances of column vapour near the critical value for convection. Since condensation into rain removes vapour from the column, where there is deep convection in the tropics the TCV distribution is constrained by criticality. The PDF of TCV in those higher SST environments therefore sharply drops off near and around the critical value found by Neelin et al. (2009), giving an approximately Gaussian distribution near a subcritical TCV value, but with an exponential tail of drier columns.

In terms of column relative humidity (CRH), rather than TCV, a non-linear relationship with precipitation is also well-documented (Bretherton et al., 2004; Holloway and Neelin, 2009, 2010; Rushley et al., 2018). In this case an exponential dependence on CRH is observed when averaging over large samples or over time. These simple statistical relationships allow for the evaluation and improvement of NWP or GCM moisture–precipitation. For example, Rushley et al. (2018) found that precipitation increases at systematically lower CRH in CMIP5 models than obsevations, and relates this to how parameterized convection produces too much rain in drier columns (Derbyshire et al., 2004). The implication is that the entrainment rate of dry air into convection is potentially too weak in the parameterization schemes of these models.

The mean precipitation-moisture relationships described above are a collapsed representation of a more nuanced co-evolution of the two variables in time. Holloway and Neelin (2010) used ground–observations to determine that convective precipitation events are preceded by slowly increasing TCV on a synoptic timescale (1-2 days), until hours before the event a certain value of TCV is reached and the moistening rapidly accelerates. This mesoscale acceleration of moistening continues until the peak in precipitation and then reverses, with TCV returning to the pre-mesoscale enhanced levels within 12 hours. Wolding et al. (2020) explore this co-evolution in a 2D phase space of precipitation and column saturation fraction (CSF), the latter being analogous to CRH. By averaging tendencies over 12 hour periods centred on a precipitation event, they find that columns orbit an attractor in the phase space. The position of the attractor aligns with the critical transition point described in previous work using time means. Correlations between the mesoscale tendencies of precipitation and moisture therefore depend on the position in this phase space relative to the attractor. Wolding et al. (2020) then go on to

demonstrate that models with a variety of mass-flux type parameterizations of convection have orbits in the opposite direction around the attractor, indicating the corresponding tendencies aren't correctly correlated. The only model in the study able to produce the correct orbits instead uses a super–parametrization for convection (Li et al., 2012); a 2D CRM is coupled to each grid-box allowing simplified but explicit sub-grid structure to contribute to grid-scale tendencies.

Multiple studies therefore show that traditional parametrizations for convection struggle to reproduce observed joint PDFs of precipitation and column moisture. However, the high variance in the precipitation–moisture relationships (a lack of a one–to–one relation) limits its direct integration into deterministic parametrizations. The observation that precipitation is stochastic in nature at the column and model grid scales has instead motivated alternative probabilistic approaches (O'Gorman and Schneider, 2006; Neelin et al., 2008; Berner et al., 2017). These models represent the mean relationships and the variance by parametrizing the observed increase in the *probability* of more intense precipitation with increases in column moisture (Holloway and Neelin, 2010).

Simple models for column moisture budgets that incorporate stochasticity are also quite powerful for explaining moisture dynamics in more complex systems. In O'Gorman and Schneider (2006) for example, stochasticity is introduced for Langrangian parcel motion to represent turbulent flow. This parcel motion then provides stochastic advection of moisture in a simple advection-condensation model for the moisture budget. Simulations with this type of model can produce realistic moisture PDFs (Sukhatme and Young, 2011; Beucler, 2016). Furthermore, two-dimensional stochastic reaction-diffusion models for column moisture are sufficient to reproduce the moisture feedbacks analogous to the self–aggregation phenomenon introduced in the previous section; a tendency towards spatial clustering of high moisture columns and persistent dryness elsewhere. By choosing appropriate scales for the relevant processes in a simple stochastic model, Biagioli and Tompkins (2023a) argue it is possible to estimate if convection in a more complex system, like the CRM simulations, is likely to aggregate or not. A universal moisture coarsening theory for CRM aggregation behaviour has also been proposed by Craig and Mack (2013), and later applied to other models for aggregation by Windmiller and Craig (2019). The coarsening theory considers the clustering of convection as fundamentally an evolution towards a two-phase moist or dry system driven by the bi-stability of column

moisture.

What is missing in some simple models is explicit vertical structure. Since moisture profiles tend to be bottom heavy, and deep moist convection is initiated from low levels, lower free tropospheric moisture is most closely correlated with TCV (Holloway and Neelin, 2009). Muller et al. (2009) split the column into a two–layer model, and redefine the criticality of precipitation based only on the lower tropospheric moisture. This is consistent with RCI arguments, where the deep convective state is an equilibrium response to an optically thick lower troposphere. The critical dependence of convection on moisture profiles will lead to different vertical structures of horizontal advection, which will then contribute differently to total column moisture tendencies. Ahmed and Schumacher (2015) found that the shape of the mean precipitation–moisture relationship very much depends on the vertical structure producing the precipitation. They found that deep convective rainfall rates themselves are only linearly related to CRH, and that the non-linearity is predominantly in the growth of the area fraction of mostly stratiform rainfall. Ahmed and Schumacher (2015) suggest the limiting of convective rain scaling to linearity is due to entrainment dilution, which further highlights the importance of MCS formation in the net scaling since observed tropical stratiform rain is almost all produced in MCS outflows.

2.6 Convection and Climate Uncertainty

Because the earth system is extremely complex, and because models which explicitly resolve this complexity are practically impossible, climate projection is inherently uncertain. Uncertainty here refers to the fact that any projection of change, for example in mean surface temperatures or in rainfall patterns, is only ever accurate to within some range. One goal of climate modeling is to reduce the uncertainty range in a given projection as much as possible, closer to the inherent limits of predictability of such a system. Uncertainty has many sources, but both a lack of understanding of the physical processes of change and the representation of those processes in models limit progress towards uncertainty reduction.

Processes involving convection contribute to both global and regional climate uncertainty. At the global scale, clouds produced by tropical convection both warm and cool the planet radiatively. Confidence is now high that net cloud–feedbacks are positive, meaning they amplify warming, but uncertainty around the magnitude of clouds–feedbacks remains high due to large inter–model spread, which has been related to the parameterization of unresolved processes

including convection (Ceppi et al., 2017; Webb et al., 2017; Forster et al., 2021). In addition to the role of convection in producing cloud in a given column, the coupling between convection and multi-scale circulations implies that future change is likely also a coupled process. This means that changes to circulation are uncertain in a similar way to changes to cloud, including because of parameterization. This is further compounded by the interaction of cloud–radiative effects with convection and circulation (Bony et al., 2015).

One of the major impacts of any coupled convection–circulation change is in changes to precipitation. Because a warmer atmosphere can hold more water vapour without saturating, mean column moisture increases follow the Clausius–Clapeyron (CC) relationship of ∼7% per degree of warming (Trenberth, 1999, 2011). GCM simulations show a robust response to increased moisture, particularly lower tropospheric moisture, with a decrease in total convective mass–flux and increased variance in precipitation (Held and Soden, 2006). Increases in column moisture are therefore associated with more frequent intense rainfall rates, particularly in the tropics where moisture is already high. Total rainfall must continue to balance the energy budget, meaning that any change must accompany a compensating change in adiabatic (upward mass flux) or diabatic (radiative) cooling. More efficient production of rainfall, that is more latent heating per unit mass flux, allows for the same or increased mean rainfall in a weaker circulation (Clement and Soden, 2005; Mauritsen and Stevens, 2015). Energy balance requires then that the reduced adiabatic cooling in upward mass–flux be offset by increased radiative cooling rates.

Changes to mean convective mass–flux manifest in space to changes to the area and intensity of convection in the ITCZ or the tropical rain–bands. The ITCZ narrows in many simulated future climates, but the width response is non-monotonic in general (Byrne and Schneider, 2016a,b; Byrne et al., 2018). Byrne and Schneider (2016b) propose that an enhanced meridional gradient in MSE leads to higher MSE advection by the mean circulation which, combined with increased divergence of MSE by transient eddies, tends to narrow the ITCZ. Higher upper–level MSE divergence is consistent with the 'stability–iris mechanism', where reduced convergence in the upper troposphere leads to reduced coverage of high cloud associated with deep convection (Mauritsen and Stevens, 2015; Bony et al., 2016). An increase in the degree of convective clustering within the ITCZ, and the associated modulation of the net radiation budget (Wing, 2019; Bony et al., 2020), has been suggested as a potential mechanism for an iris–effect. In-

creased clustering is also consistent with bulk arguments for reduced total convectively active area (Zhang and Fueglistaler, 2019), and for increased frequency of rainfall extremes (Bao et al., 2024), if precipitation is more efficient in a more clustered state.

Using coarse-resolution GCMs to understand how ITCZ or rain–band structures change in a warming climate is limited however, primarily by their poor representation of convection and the associated coupling to mesoscale and synoptic circulations such as storm organisation or wave–modes (Maloney et al., 2019; Bartana et al., 2023; Spät et al., 2024). Rios-Berrios et al. (2025) find that an idealized aqua–planet simulation run at convection–permitting resolutions does have ITCZ narrowing and Hadley cell weakening with warming, the same as coarser models. They show the ITCZ narrowing is related to a narrowing of the region where precipitation efficiency is maximized. There are also non-linear changes at the fine scales that aren't represented in coarser models, including super–CC scaling rainfall extremes. These runs are uncoupled to the ocean, however, with the atmosphere subject to uniform surface warming rather than realistic patterns of warming that result from ocean–atmosphere interaction (Xie et al., 2010; Andrews and Webb, 2018; Trenberth et al., 2025). Furthermore, even when it becomes feasible for coupled models that can resolve internal ITCZ structure to be used for century–scale simulation, large ensembles would still be needed to mitigate model uncertainties, particularly those around the subgrid representation of clouds.

Model representation of internal structure changes are also important in their own right, beyond resolving their interaction with the mean. This is because "nobody lives in the mean" applies to the annual or seasonal mean ITCZ or rain–bands. The real impacts of any change in any mean structure depends on the underlying change to the statistics of spatiotemporal variability. While GCMs robustly show clear changes in the global mean circulation, regional changes over tropical land are distinct if convection is explicitly resolved or parametrized. For example, Jackson et al. (2020) show that a future African climate modelled with explicit convection has significantly higher reduction in mean rain-belt vertical motion versus a parametrized counterpart. Underlying this result are differences in future changes to precipitation PDFs, which are coupled to changes in TCV PDFs via the moisture budget. In the same future climate, Kendon et al. (2019) found enhanced wet and dry extremes across the continent. At smaller but still regional scales, Finney et al. (2020) showed explicit convection is associated with a larger increase in rainfall heterogeneity in East Africa in response to moistening of the atmosphere by

climate change, meaning more rainfall extremes in the future. In the West African Sahel, where rainfall predominantly occurs in MCSs, the driver of change is still primarily increased moisture, but the scaling of this moisture increase with warming is again quite heterogeneous when using explicit convection (Fitzpatrick et al., 2020). In West Africa, the monsoon circulation and the associated local overturning are stronger when using explicit convection, allowing the monsoon to penetrate further north (Jackson et al., 2022). The monsoon circulation ascent in Jackson et al. (2022), like the Africa–wide ascent in Jackson et al. (2020), weakens more with explicit convection despite larger increases in mean rainfall rates. Increases in moisture allow for more rainfall events to occur outside of the currently defined rainfall seasons, and so the parameterization of convection is also a source of uncertainty with respect to changes in seasonality (Wainwright et al., 2021). There is a theme throughout the literature of explicit convection leading to a more intense but more heterogeneous response of moist processes to warming. Confidence in model representation of the joint moisture–rainfall–dynamics PDF constitutes a more impactful reduction of uncertainty than mean or PDF changes in any variable in isolation.

2.7 Summary and Thesis Outlook

This chapter has gone through a full spectrum of scales of tropical phenomena, explored current understanding of the role of convection in those phenomena, and highlighted related improvements both already achieved and still needed in weather and climate models. The review also identified key themes in the literature relating to scale–interactions of tropical convection and their representation in models. These are;

1. The emergence of spatiotemporal structure and its representation in models as a function of resolution and model sub-grid physics.
2. The upscale impact of model convection on weather–defining circulations, including monsoons and modes of variability.
3. The aggregate impacts of the first two themes on climate via mean circulation and the energy budget.
4. The key role of atmospheric moisture as a mediator of all the above.

A large literature now supports the claim of improved scale–interactions when modelling with a more realistic representation of convection. This often means higher resolution, and the reduced

use or complete forgoing of parameterization for convection.

Use of convection–permitting resolutions in NWP operations motivates continued evaluation of the model performance, and better understanding of the underlying processes. Even at convection–permitting resolution, NWP still has predictability limitations related to scale. Patterns of the initiation of convection are poorly understood and unpredictable unless constrained by some scale–interaction process. Reliable prediction also requires good representations of circulations connecting regions to each other; these being tropical circulations which are coupled locally to convection in both the upstream and downstream region. Poor representation of convective coupling in circulations may therefore drive error propagation across the domain in global models, or introduce errors via boundary conditions in regional models even if those regional models have improved local coupling. Process–orientated understanding of model errors is integral to any development of physics–based models, especially if those models are ever intended to meet growing demand for training data for cheaper but non–physical machine–learning forecasting models (Bouallègue et al., 2024; Bonavita, 2024).

The same principle of process understanding applies to climate modelling also. Results of past and contemporary research show clearly that convective–scale processes can not be neglected in regional and global climate projection. The continued investment of large resources into developing km-scale climate modelling capacity needs to be justified by evidence–based reasoning and physical understanding of the apparent benefits of those higher costs.

This thesis aims to contribute to process-understanding of tropical scale–interaction across the connected themes in the literature, and to demonstrate the added value of convection–permitting modelling in each set of processes. We evaluate models against contemporary ideas and observational work, and use novel concepts and diagnostics for process identification to extend and connect existing hypotheses. Our results make use of large datasets from a hierarchy of full complexity atmospheric model configurations, with the intention of motivating and informing future model development efforts.

Chapter 3

Data and Methodology

The following chapter outlines the key sources of data used in the results of this thesis. These data include output from km–scale weather and climate simulations, data from Earth observation satellites, and from global reanalysis. Particular detail is needed for describing the configurations of all the simulations use, since any differences can lead to different behaviour in the model atmosphere. Model data and reanalysis are used for all dynamical results, since three-dimensional kinematics are not directly observable at the scales we wish to study. Satellite observation is used for fields derived from radiative fluxes, including properties of clouds and crucial estimates of rainfall rate. All the data used are analysed on various latitude–longitude grids, both two and three dimensional. Regridding of the data is required to fairly compare sources of data, including comparing models run at different resolution. It is therefore common to analyse model data at a resolution lower than that at which the model is run.

We also include in this chapter the basic description of some of the mathematical tools used in the results chapters, for the sake of later clarity. These explanations will introduce the concepts needed in a simple form, but their exact application and any extensions in complexity will be introduced in context in the relevant chapters.

3.1 Data

3.1.1 The Met Office Unified Model

The UK Met Office and its partners develop the Unified Model (UM) for both operational forecasting and for weather and climate research. The model is purposefully developed such

that the same core dynamics can be used for simulations over all scales, from idealized 100m resolutions for a few simulation days to decade long climate simulations. The UM can be run in global and limited domains on different types and resolutions of grid. Crucially for our investigations, the model can also be run with a large range of sub–grid physics parameterizations. We will refer to the set of physics schemes used by a given simulation as its 'settings', and to the combination of domain, resolution, and settings as a 'configuration'. For a given modelling context, common settings for the UM are developed and named according to their intended use. We use these names where appropriate in describing results but also endeavour to highlight the most relevant differences in settings in parallel, to limit the need to continually cross–reference acronyms.

CP4-Africa

As part of the IMPALA project (Senior et al., 2021), two regional atmosphere–land configurations of the UM were run over the African continent for two 10–year simulation periods. These were a present climate period, using Reynolds daily SST observations from 1997-2006 (Reynolds et al., 2007), and a future climate period with warmer SSTs informed by a coupled HadGEM2-ES run under the RCP8.5 climate change scenario (van Vuuren et al., 2011; Jones et al., 2011). More specifically, the future SSTs are the sum of the present-day observations and the average change in climatological SSTs from 1975–2005 to 2085–2115 in the coupled run. Future SST change is therefore not spatially homogeneous, but the interannual SST variability of the present run is preserved. Further details can be found in the methods section of Kendon et al. (2019).

The two configurations are a 4.4km resolution run with explicit convection, called CP4, and a coarser 25km resolution run with parametrized convection, which we refer to as P25. Both CP4 and P25 are nested in a global model with the same 25km resolution and similar settings to P25. This provides the lateral boundary conditions for the African domain, but there is no feedback on the evolution of the global driving model by any change inside the nested domain. The P25 atmosphere settings are similar to Walters et al. (2019) (GA7), using the 6A convection scheme and the PC2 large-scale cloud scheme, whereas CP4 has no convection scheme and uses the Smith (1990) cloud scheme. Both simulations use the same microphysics schemes, the same land surface settings, but different boundary layer schemes. Full details and references for schemes for each model can be found in Stratton et al. (2018).

The simulations have a 'free-running' atmosphere and land–surface state, meaning that they are not adjusted towards any real observation of the atmosphere at any point. As such, the exact state in the present climate run quickly moves away from the observational record, and only large–scales and statistics related to the prescribed SST forcing will follow similar patterns of variability between model and observation. The free–running in the present climate makes that run more fairly comparable to the future climate run, for which there is no option to adjust towards observation.

DYAMOND Summer/Winter and The K-Scale Hierarchy

The K-Scale hierarchy is a set of 40–day free–running UM simulations with a variety of configurations, performed to investigate the impact of resolving smaller processes like convection on large–scale circulation and weather patterns. The hierarchy consists of several domain scales, including a global domain, a cyclic tropical channel (CTC) domain, and multiple limited area models (LAM) of tropical land regions. The global models provide the boundary conditions for the one–way nested CTC and LAM runs. Each configuration is run for two 40–day periods, called DYAMOND Summer and Winter respectively. The Summer runs were initialized on 01 August 2016, and the Winter runs on 01 January 2020. We include here details only for members of the hierarchy used in this thesis, and the models providing boundary conditions.

The global driving model uses the N1280 grid, a spectral rectilinear method with tropical resolutions of approximately 15x10km, on 70 model levels with a model top at 80km. The CTCs are double the resolution of the global driving model, on the N2560 grid, and the LAMs use a 0.02° resolution equivalent to approximately 2.2km.

Two versions of the hierarchy exist, each beginning with the global driving model. The majority of the work in this thesis uses the set of runs where the driving model uses the GAL9 settings for model physics. This includes an updated set of atmospheric schemes to those used in GA7. In particular, the distinct convection schemes for mid–level and deep convection have been combined into one scheme in GAL9. There are therefore just two distinct convection schemes in GAL9, one for shallow and one for mid-to-deep convection. The GAL9 setting use single-moment microphysics (Wilson and Ballard, 1999), and a prognostic cloud scheme (Wilson et al., 2008). A second driving model uses RAL3.2 physics (Bush et al., 2024), which includes explicit convection, CASIM two-moment microphysics (Field et al., 2023), and a bi-modal cloud scheme

(Weverberg et al., 2021). Each of the two driving models provide boundary conditions for respective runs in the LAM domains, which all use RAL3.2 model physics. Finally, for each driving model, two CTCs were run, one with GAL9 physics and one with RAL3.2.

The EVAPOFF Experiment

Using the same base configuration as the DYAMOND Summer Africa LAM, an additional experiment was run where the evaporation of rainfall was switched off in the microphysics scheme. This run is referred to as the EVAPOFF configuration, and it was produced with the intention of directly suppressing cold pools and their upscale effects. This turns out to be the case, and in chapter 5 we will compare EVAPOFF to its corresponding LAM run to explore the impact of cold pools on model mean states and large–scale structures.

Configuration	**Domain**	**Horizontal Resolution**	**Physics Settings**	**Parametrized Convection**
CP4	Africa	4.4 km	RAL2T	No
P25	Africa	25 km	GA7 (+ land surface scheme?)	Yes
DYAMOND Driving Model	Global	N1280 (10 km at equator)	RAL3.2 + GAL9	Both
DYAMOND CTC	25°N–39°S	N2560 (5 km at equator)	RAL3.2 + GAL9	Both
DYAMOND LAMs	Africa, South America, Southeast Asia	2.2 km	RAL3.2	No

Table 3.1: Summary of model configurations, domains, resolutions, and physics options.

3.1.2 Satellite Retrievals

Instruments on satellites measure the electromagnetic radiation emitted by the Earth in the view from their orbits, and careful analysis of these measurements allows for the construction of gridded estimates of many two–dimensional fields. These gridded products are not direct observation, since they require significant post–processing of multiple channels of data from

multiple satellite instrument platforms. Despite this, satellite estimates are extremely valuable tools and are the best approximation available for both mean and spatial characteristics of the atmosphere.

CERES EBAF TOA Energy Balance

The net energy flux at the top of the atmosphere (TOA) is a very important quantity for climate variability; a hypothetical steady state atmosphere should have global mean net zero energy flux at it's top boundary, meaning all the energy imported by solar radiation is emitted back through or by the atmosphere. The real atmosphere exhibits multiple timescales of variability, and the global mean net flux is small but non-zero (e.g. Johnson et al. (2016)).

Incoming solar radiation has predominantly short wavelengths (shortwave radiation). The Earth and atmosphere absorb some of the incoming shortwave, generating heat. The return flux at TOA therefore consists of both reflected shortwave and thermal radiation with much longer wavelengths (longwave). Separate measurements of the outgoing shortwave (OSR) and longwave (OLR) flux patterns are vital for determining mean and spatial distribution of clouds.

The international Earth Observing System (EOS) mission includes satellite observations of the TOA energy budget. This includes the post-processed and gridded Clouds and the Earth's Radiant Energy System (CERES) Energy Balance and filled (EBAF) product (Wielicki et al., 1996). CERES EBAF includes monthly mean all–sky, clear–sky, and cloud–radiative effect measurements on a 1° grid.

Geostationary IR Channel Brightness Temperature - GridSat B1

Because thermal radiation is largely in the infrared (IR) part of the spectrum, brightness in the IR is used to derive temperature estimates for clouds. This IR brightness temperatures (BT) is a good proxy for locating and quantifying the strength of deep convection in the atmosphere, since stronger updrafts are associated with higher and therefore colder cumulus and anvils. While BT is empirically related to OLR, BT gives a better height reference relative to the temperature profile of the atmosphere.

In chapter 6, we will compare with models diagnostics derived using the GridSat B1 product (Knapp et al., 2011). GridSat is constructed from previously archived International Satellite Cloud Climatology Project (ISCCP) B1 data, and includes a high–resolution gridded BT

dataset. GridSat BT data is 3-hourly with a 0.07° resolution and goes back to 1980.

GPM IMERG Rainfall Rate Retrievals

Throughout this thesis, we use the Global Precipitation Measurement (GPM) missions's Integrated Multi-satellitE Retrievals for GPM (IMERG) product as an estimate for ground truth rainfall rates (Huffman et al., 2020). This product is derived from a combination of active radar and passive microwave satellite measurements, and is provided at a at 0.1° × 30 minute resolution. We use the most recent version of the IMERG product, version 7 (Huffman et al., 2023).

3.1.3 ERA5 Reanalysis

Reanalysis products are a blend of forecast model simulation and observation, with the aim of providing data about the complete, and physically consistent, dynamics and thermodynamics of an atmosphere as close as possible to the real atmospheric state. This is done by continuously assimilating data from multiple sources including ground observations and satellite retrievals. The assimilation of data moves the evolution of the forecast model towards the observed state at every available observation point and timestep. While reanalysis is the best available 'ground–truth' for global circulation patterns, the lack of smaller–scale observation means that fine–scale structure and dynamics are still the product of parameterizations within the forecast model. This means that reanalysis is a good model evaluation tool for the larger scales, but not for processes such as individual convective updraft strength and rainfall. The amount of data available for assimilation has also increased over time, with a step change upon the introduction of Earth observing satellites; more recent decades of reanalysis are likely more realistic than historical ones.

The European Centre for Medium-range Weather Forecasting (ECMWF) produces a reanalysis dataset called ERA5 (Hersbach et al., 2020). In this thesis, we use 3D and 2D hourly ERA5 data openly available via the Copernicus Climate Data Store (CDS) (Hersbach et al., 2023b,a). The dataset begins in 1940, and is updated to the near–present day. It is available on a standard 0.25° grid, with 25hPa pressure–level spacing in the lower and upper troposphere, and 50hPa spacing in the mid–troposphere. More levels in the stratosphere are available but not used in this thesis.

3.2 Methods

3.2.1 Lagged Cross–Correlation

In chapter 4, we use spatial cross–correlation to explore the relationship between spatial patterns in various fields at different times. Below is the formula for the cross–correlation of two–dimensional arrays S and P, at times t_0 and t_1 respectively. S has shape $A \times B$ and P has shape $M \times N$. The full lagged cross correlation z of size $(M + A - 1) \times (N + B - 1)$ is,

$$z(k,l)[t_0,t_1] = \sum_{m=0}^{M-1} \sum_{n=0}^{N-1} P_{t_1}(m,n) S_{t_0}(m-k, n-l), \tag{3.1}$$

where $-(A-1) \leq k \leq M-1$ and $-(B-1) \leq l \leq N-1$. Because we will choose S and P such that $A \leq M$ and $B \leq N$, the full cross-correlation can be reduced from z to z_r with size $A \times B$ to match the size of P. If S and P are simply binary arrays of locations, z is then the result of adding one to each point (k, l) for each pair of coincident ones in the overlap of S and P centred on (k, l). If S is binary and P is continuously valued, then z is similar to a summed composite of the values of P around each location where $S = 1$, and this result can be divided by the sum of S to retrieve the mean pattern.

The effect of lagged cross–correlation is to highlight spatial relationships between two timesteps, including those that are repeated across across the domain. Below in Figure 3.1 is a conceptual example using binary arrays. Figure 3.1(a) shows a set of locations in (x,y) at t_0, and (b) shows a P that includes many squares centred on the points in S. In (c), random binary noise is added to (b), breaking up the obvious pattern. The cross–correlation of (a) and (c) is largest in a centred square; the centre of (d) represents locations where $S = 1$, around which a square pattern is common in P. The cross–correlation reveals patterns such as these, even with a noisy signal.

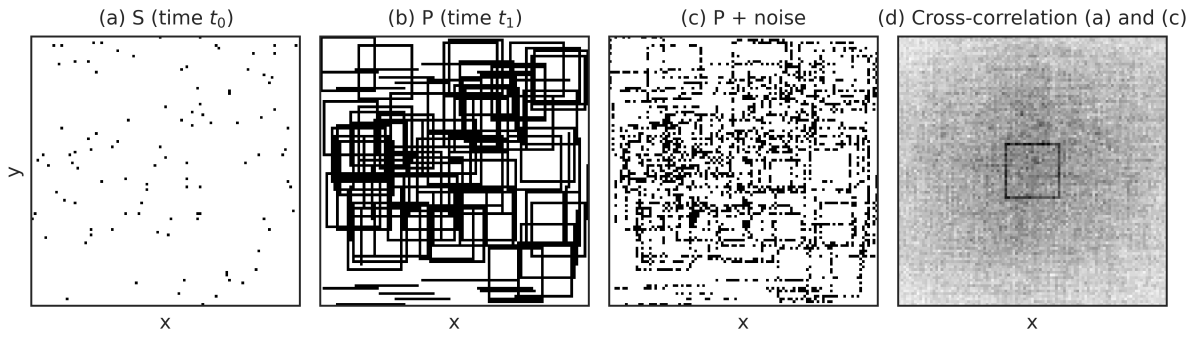


Figure 3.1: A conceptual example of how cross–correlation can be used to reveal spatiotemporal patterns in noisy data.

3.2.2 Autocorrelation of Rainfall

Autocorrelation is a measure of the statistical relationship between a time series' present and past values. For a given time series of daily rainfall values, a 1–day lagged autocorrelation indicates to what extent rain on a given day is correlated to it raining the day before. This measure ranges from -1 to 1, and we shall refer to it from now on as just the lag–1 autocorrelation. A positive value for the lag–1 autocorrelation would suggest that rain days are often preceded by a rainy day of similar magnitude. A negative value however, indicates that a rainy day is more often preceded by a day with significantly less rain or no rain at all. Large positive and negative autocorrelations are therefore representative of rainfall persistence and 'every–other–day' type variability, respectively. An autocorrelation of zero indicates daily rainfall is not at all predictable from knowing the previous day's rain. Calculating lag–1 autocorrelation for each gridpoint in a daily rainfall dataset indicates which kind of variability is apparent in each location.

Past studies have found that, even where non-zero daily mean rainfall values are the same, lag–1 autocorrelation of observed tropical rainfall is highly location dependent (Roehrig et al., 2013; Spät et al., 2024). While lag–1 autocorrelation is most commonly positive, significant areas of near-zero or negative autocorrelation exist in parts of the two large tropical landmasses of Africa and South America. Africa during the boreal Summer in particular, during the West African Monsoon period, is particularly exceptional for the broadness of its region of negative auto-correlations.

3.2.3 Decorrelation of Total Column Vapour

In the paper outlining the DYAMOND protocol, on which the K-Scale Hierarchy model runs are based, Stevens et al. (2019) include analysis of correlations between the column moisture (TCV) in different models and different configurations of the same model. The aim in doing so is to identify any timescales of coherence in the evolution of the model moisture field. For their set of models, Stevens et al. (2019) find results that agree with previous work cited therein; several studies therefore show that correlation between model moisture fields decreases and then plateaus after 2–3 weeks. The term decorrelation can be used to describe this phenomena, how the correlation between two model runs, or between model runs and reanalysis, may generally decrease with time. This is analogous to the commonly used difference energy diagnostics for error growth, which increase over time as model errors grow. As for difference energy growth, decorrelation slowing and remaining roughly constant indicates that the fields being compared are as different as they can get. This plateauing or 'saturation' indicates that a certain level of inherent similarity is present because of common large–scale features or forcing (e.g SST patterns).

While Stevens et al. (2019) analyse globally averaged and normalized decorrelation, here we are interested in diagnosing decorrelation over regional domains as a function of domain size and resolution. We are also interested in absolute decorrelation, meaning that we care about the differences in the stable correlation values for each pair of models analysed. This simplifies the diagnostic to just the mean spatial correlation of two column water fields over a given rectangular domain, plotted over time.

Decorrelation refers to the rolling mean behaviour of correlations of this kind. This is not to say that transient modes of variability can not temporarily increase correlation if those modes are collocated in both fields being correlated. This is important when comparing correlations of global drivers with different nested setups, since the propagation of wave modes, and any more general inter-regional stirring of the moisture field, are by design not independent between a LAM its driving model. A disturbance propagating across a boundary location in the driver will do so at the same time in the LAM. Similarly, one–way nesting prevents the internal dynamics of the LAM feeding back on any larger moisture circulations. The above considerations support a hypothesis that TCV decorrelation of a nested run from its driving model will be a function of the size of the nested domain. We explicitly test this hypothesis as part of Chapter 5.

3.2.4 Organisation Indices

As discussed in chapter 2.4, there are multiple definitions for the organisation of convection from which diagnostic measures can be derived. One definition of organisation is the spatial clustering of objects in a domain, where the objects correspond to the location of convective elements such as updrafts or cold cloud tops. Measuring the extent of clustering in a given spatial arrangement of those objects can be done statistically as long as there are enough objects in the domain. This is the approach used to construct the $Iorg$ (Tompkins and Semie, 2017) and L_{org} (Biagioli and Tompkins, 2023b) indices for convective clustering. The following explanation for these indices is largely an adaptation and simplification of that published in Biagioli and Tompkins (2023b).

Assuming it is already decided how to define a convective object, we start with a binary array of object locations. From here we can quantify a spatial pattern by taking measurements of the distances between objects. This can be done in multiple ways, including by measuring the distance from each object to it's nearest–neighbor, or by counting the number of other objects within a given distance from each object. The central idea is to compare statistics of such measurements to those expected for an analytically defined random spatial pattern. For the I_{org} index only the nearest–neighbour is considered, whereas L_{org} uses the area–count approach. This gives each index some advantages over the other, but in Chapter 6 we choose to use the L_{org} index because it is better suited to our research questions. Reasons for suitability will be explained in more detail after the following simplified derivation of the L_{org} index, based on Biagioli and Tompkins (2023b).

For a given arrangement of objects in a domain, Ripley's K-function defines the expected number of objects within a distance r of a given object. This can be written $\lambda K(r) = \mathbb{E}[\text{number of objects within distance } r]$, where λ is the mean density of objects in the domain (objects per unit area). A homogeneous Poisson process is a model for a random spatial distribution of objects, where $K(r) = \pi r^2$. In the random pattern then, the expected number of objects within distance r of any object is simply proportional to the area being searched for objects. As r increases, the search area increases, and so the likelihood of finding new objects increases. However, in the random process $K(r)$ increase like r^2, which is difficult to interpret for a large range of scales. The area–normalized version of the K–function is Besag's L–function, written as $L(r) = \sqrt{K/\pi}$. The L–function for the homogeneous Poisson process is therefore simply

$L(r) = r$.

The actual spatial distribution of convective cloud objects in observations or in models won't be a homogeneous Poisson process. Instead the K–function and associated L–function will have their own forms as a function of r. This can be estimated for each r using the average density of objects in the domain and counting the number of distances less than r between objects. Repeating the count for all r gives the estimated K-function $\hat{K}(r)$, which can then be area–normalized as before to get the estimated L–function $\hat{L}(r)$. We can then compare for each r the difference in $\hat{L}(r)$ from $L(r)$ to understand if the pattern is random at the r–scale. Where $\hat{L}(r) > L(r)$, there are more objects than expected from randomness, and so the pattern is clustered at that scale. In contrast, if $\hat{L}(r) < L(r)$ then there are less objects than expected within a distance r, implying regularity in the spatial pattern at that scale.

To condense information from all scales into a single–valued index, the distance from randomness at each scale is summed and normalized by the largest possible search radius r_{max}. The final formula for calculating L_{org} is therefore,

$$L_{org} = \frac{1}{r_{\max}} \int_0^{r_{\max}} \frac{(\hat{L} - L)}{r_{max}} \, dr, \tag{3.2}$$

where $\hat{L}$ is the estimated Besag's L–function from the data, and L is just the L–function of the random spatial distribution. For discrete sets of scales, the integration is performed numerically using the trapezoidal rule. Note that for a given set of scales, the defining contributions to the index and any differences between indexes from different datasets result from differences in $\hat{L} - L$ across scales and across datasets. In practise, we use the numerical L–function estimator method in the Astropy Python Package to calculate $\hat{L}$ (Astropy Collaboration et al., 2022).

The I_{org} index is constructed in a similiar fashion, but with the nearest–neighbour cumulative distribution function (NNCDF) in place of the L–function. The NNCDF also has an analytical solution for a homogeneous poisson process as a function of r, and so I_{org} is the integrated difference of the observed and random NNCDFs. For details, see Tompkins and Semie (2017) or Biagioli and Tompkins (2023b).

The single–valued I_{org} and L_{org} indices are integrated differences across scales. Scales with clustering contribute positively to this integral, and scales with regularity contribute negatively. The primary difference between the two indices is that I_{org} uses nearest–neighbours and L_{org}

uses area–counts. The benefit of I_{org} is that it is conceptually more simple, in that changes in the position of more distant objects don't change the nearest neighbour distance, making strong signals of smaller scale clustering robust to weaker variability at the larger scale. However, for the same reasons, I_{org} is incapable of measuring multi–scale structure such as clusters of clusters. This means I_{org} cannot distinguish an arrangement with clustering at scale l_1 and randomness at scale l_2 from one with clustering at both l_1 and l_2, when $l_1 < l_2$ (see Figure 3.2). Because the area–counting for L_{org} is equivalent to knowing all the distances between all the objects in the domain, it retains sensitivity to structure at all scales being considered.

If one knew that clustering likely first occurs at a given scale in the chosen data, and if measuring that kind of clustering was the only goal, then I_{org} would be the more appropriate tool. For example, if we assume that the mesoscale is the smallest dominant scale of clustering in the tropics, then I_{org} and the NNCDF CDFs can more reliably measure the amount of specifically mesoscale clustering in a given snapshot of the tropics. However if we wish to include contributions from both mesoscale and synoptic structure simultaneously, or how mesoscale clusters are spaced relative to each other, then I_{org} is insufficient and L_{org} and the L–function are the better tools.

Both the single valued indices are limited in that by themselves they don't communicate any scale information. They simply provide a quantity for comparing one arrangement to another or from which to calculate anomalies from the mean. Retaining the full NNCDF or L–function gives a clearer and more nuanced view.

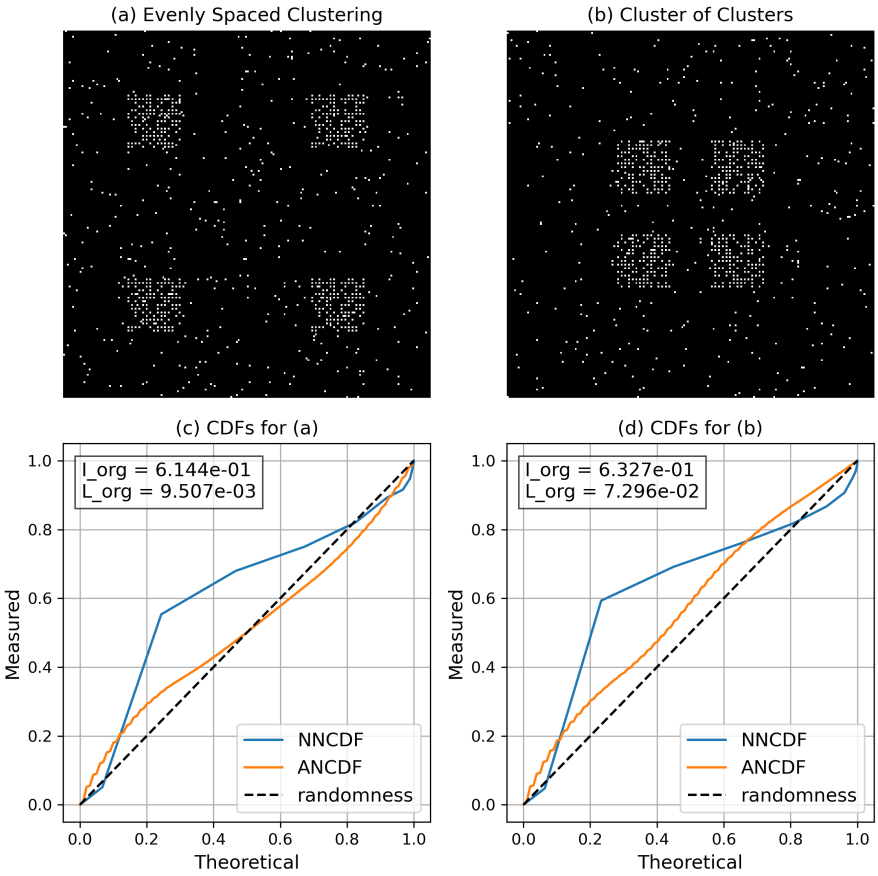


Figure 3.2: Conceptual examples of calculations of I_{org} and L_{org} from binary arrays, where white dots are the object locations. The top row shows the distribution of objects for two cases with (a) regularly spaced clusters and (b) a cluster of clusters. The bottom row shows respective plots of the measured CDF values against the values expected from theory were the objects randomly distributed. The indices are the integrated difference between the blue and dotted black line for I_{org}, and between the orange and dotted black line for L_{org}, and are shown on the figure. (Adapted from a similar demonstration in Biagioli and Tompkins (2023b))

3.2.5 Stochasticity and Fokker–Planck Equations

A powerful and convenient way to model some of the turbulent nature of the atmosphere is stochasticity. Stochastic processes are those with an evolution indistinct from that drawn from some random probability distribution. Importantly, the apparent instantaneous randomness of such a process does not prevent the characterization and prediction of it's long term or average behaviour. Stochastic models can therefore represent both the scales of behaviour resolved deterministically in other models, and also implicit contributions from smaller scales modelled as added randomness.

A simple example of stochasticity is the Wiener process, where increments in a variable are randomly drawn from a Gaussian distribution with a mean of zero. The Wiener process is

the integral of the White Noise process, and is equivalent to Brownian motion in the context of random motion in space. A simple model with both a deterministic and stochastic part is therefore,

$$d\xi(t) = \mu(\xi, t)dt + \sigma(\xi, t)dW_t, \tag{3.3}$$

where $d\xi$ is the increment in the variable ξ being modelled in time t. On the right–hand side, μdt is a deterministic contribution to the increment defined by the function μ, and dW_t is the Wiener process which is scaled by σ. Note that the limit of equation 3.2 divided by dt, as $dt \to 0$, gives the time tendency of ξ as deterministic μ plus White Noise. Also, because the expected value of the Wiener process is zero, the expected value of the whole increment, or tendency in the limit case, is given by the function μ.

With equation 3.2 as a model for the evolution of each instance of ξ, it is possible to derive an equation for the evolution of a whole collection of instances of ξ, via the probability density function (PDF) $p(\xi, t)$. This equation is the Fokker–Planck equation,

$$\frac{\delta}{\delta t}p(\xi, t) = -\frac{\delta}{\delta \xi}[\mu(\xi)p] + \frac{1}{2}\frac{\delta^2}{\delta \xi^2}[\sigma^2(\xi)p]\,. \tag{3.4}$$

The Fokker–Planck equation can be used to determine the shape of the PDF for a given system defined by the functions μ and σ, and also to understand the dynamics leading to an observed PDF assuming similarity to the stochastic model holds. We will make use of the Stochastic model and the Fokker–Planck equation in chapter 7, where the collection of instances will be a gridded dataset of column moisture values. For further reference, see Kwok (2018).

Chapter 4

Scale Interaction and Patterns of Deep Convection in the West African Sahel

This chapter is based on the following published article: Bassford, J., Parker, D.J., Marsham, J., Warner, J. (2026) Scale interactions of deep convection in the Sahel: Exploring ring patterns in lagged cross-correlations of rainfall. Quarterly Journal of the Royal Meteorological Society, https://doi.org/10.1002/qj.70041.

This chapter is concerned with interactions between convection and the mesoscale and synoptic environments at sub-daily scales. In these analyses, we examine the sub–daily spatiotemporal patterns in convective rainfall in the West African Monsoon region. Specifically, we show how patterns of convection at one time relate to the patterns of convection at a later time on the same day. The inherent motivations are two–fold: understanding how two patterns of rainfall are connected in time offers a potential measure of predictability, and a means of evaluating the physical realism of model processes.

West Africa is chosen for its reputation as a 'natural laboratory' for organized tropical deep convection, and also because it is representative of tropical regions where near-term information about rainfall is critical to local livelihoods and flood vulnerability. Because rainfall in West Africa, and across the tropics more broadly, is inherently unpredictable at a 1 to 7-day lead time (Keane et al., 2025), there is a need to better quantify spatiotemporal patterns in rainfall

at shorter, sub-daily timescales. These sub-daily patterns can then be used to evaluate models, assess their value for short-range prediction, and better understand the associated physical processes and how model errors may relate to these. This chapter identifies novel spatio-temporal patterns of rainfall that provide predictability on the sub-daily timescale. We show these patterns exist in both observations and in a climate model, and link them to well-studied dynamical processes. We present examples of using the patterns for model evaluation, comparing the results from observations to those from a regional climate model with both explicit convection and parameterized convection. In the next section, we discuss the data used and the methods of pattern construction. Then we present results relating rainfall to rainfall at a later time, and then those relating rainfall with other model fields at a later time. The latter relationships are chosen to explore associations between time-lagged patterns in rainfall and known mechanisms of convective initiation, gravity waves and cold pools. We then discuss some sensitivities of the method in the context of storm lifecycles, suggest potential applications such as the development or improvement of nowcasting tools, and place the results in the broader context of convective scale interactions.

4.1 Data and Methods

4.1.1 Models and Rainfall Retrievals

This chapter uses data from two regional climate model configurations CP4 and P25, with explicit and parameterized convection respectively (see chapter 3.1.1), and also uses GPM IMERG satellite rainfall retrievals (see chapter 3.1.2). In JJA in West Africa, P25 has a seasonal dry bias relative to satellite retrievals of rainfall. CP4 has a smaller but still negative seasonal bias and a higher frequency of higher rain rates, but produces too much rain over steep terrain (Stratton et al., 2018). CP4 also has a better representation of land-based MCS over the region, particularly of the long-lived and fast moving storms (Crook et al., 2019). See Stratton et al. (2018) for more detail on general rainfall biases, and Crook et al. (2019) for details of MCS representation. The analyses are performed on data from 1998-2006 June to September inclusive. This gives 9 years of 120-day seasons, giving a total of 1080 days of data for both CP4 and P25. The model fields used are hourly rainfall rates and three-hourly winds, temperature, and pressure tendency (omega). All variables are instantaneous. We compare the models to satellite-based retrievals of rainfall rate from GPM-IMERG version 6 (Hou et al., 2014), which

are on a 0.1° grid which approximates a 10km resolution in the analysis domain.

The analysis domain is in two parts, a parent and a sub-domain. The parent domain is from 16°W to 16°E and from 2°N to 26°N, which encompasses the majority of the land surface of tropical West Africa and some adjacent ocean. It is worth remembering throughout that UTC is approximately LST in this domain, given the importance of diurnal cycles for convective rainfall. The sub-domain is the Western Sahel from 8°W to 8°E and 10°N to 18°N. The sub-domain was chosen to be entirely continental, to minimize coastal effects, and to minimize the presence of significant orography. A higher proportion of the largest and longest-lived systems also develop in the chosen sub-domain (Lafore et al., 2017b). These large systems produce the most intense updrafts and rainfall, and are often active through the night. The parent domain is 8° larger in all directions than the sub-domain, with a common center at (0°,14°N). The parent domain includes both the south and west coasts of tropical West Africa as well as both inland and coastal areas of significant orography, the implications of which are discussed later.

4.1.2 Lagged cross–correlations

To quantify the relationship between spatial patterns of convection at different times of day, we calculate cross-correlations (see chapter 3.2.1) between the sub-domain high rainfall locations at time t_0, and the parent domain convective rainfall locations at t_1. 'High' here refers to rainfall above the t_0 99th percentile for the sub-domain, relative to the respective climatology of the data source. At t_1, a threshold of 2mm/hour is chosen simply as a representative rain rate for convection. Using percentiles at t_0 samples similar numbers of t_0 events in each data source. At t_1 the primary concern is the differences between the models and between models and observations. Figure 4.1 shows (a) how the t_0 thresholds change through the diurnal cycle in the sub-domain, and (b) how much rain >2mm/hr one might expect in the parent domain for each model throughout the day. By using a fixed t_1 threshold we clearly keep the diurnal cycle biases of the models in the results, highlighting their leading-order impact on the timing of the development of spatial structure.

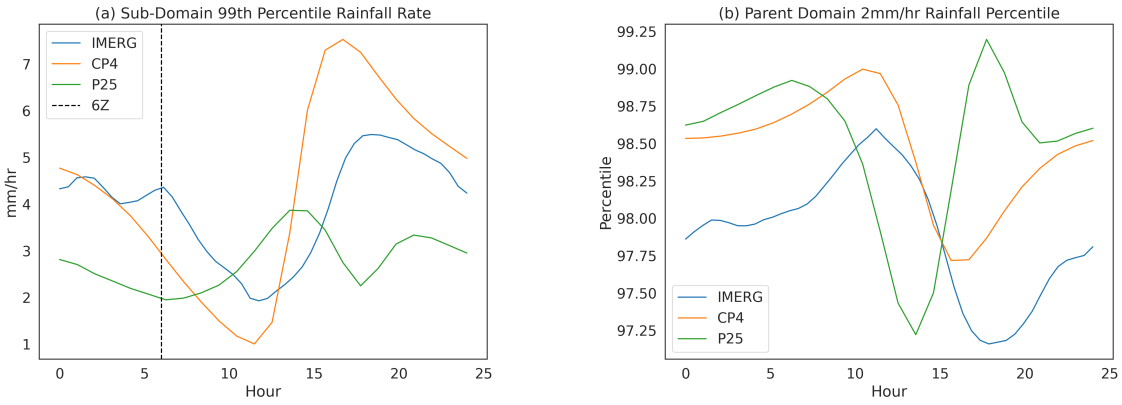


Figure 4.1: Mean diurnal cycles of the thresholds used to define t_0 rain event and t_1 convective rain locations. (a) The sub-domain 99th percentile rainfall values at all possible t0 for CP4, P25, and IMERG. (b) The percentile corresponding to 2mm/hr at all possible t1 for CP4, P25, and IMERG.

The cross-correlations are also calculated between high rainfall at t_0 and anomalies at t_1 of temperature at 925hPa, horizontal winds at 925hPa and pressure tendency (omega) at 500hPa. The anomalies are defined as deviations from the 10-year grid cell mean for a given time of day and pentad. All cross-correlations are calculated for a range of t_0 and t_1 values, but we restrict the majority of the discussion to the results of cross-correlations with a fixed t_0 of 6Z for which signals were strongest. The evolution of the patterns with increasing lag time (i.e. by advancing t_1) then gives patterns in rainfall throughout the day relative to rainfall locations at 6Z. The highest rainfall at 6Z is often found in long-lived nocturnal MCS.

To create the maps of rainfall locations, the rainfall field (in mm/hr) is passed through a Heaviside function to create a binary array which is one where rainfall is above the threshold, and zero elsewhere. This is done separately for the parent and sub-domain with their respective thresholds. For t_1 temperature and wind anomalies, the Heaviside is not applied. The cross-correlation is then calculated using the standard 'signal.correlate' method in the signal processing library from the open-source SciPy Python package. We make use of the built in FFT option to speed up the calculation. We also use the built in option to trim the edges of the full cross-correlation to the size of the parent domain, keeping the center the same. Because the sub-domain and parent domain have a common center, the center of the resulting cross-correlation represents the location of a t_0 rainfall event, which will be labeled as the origin. An example is illustrated in Figure 4.2 for a single day of data with $(t_0, t_1) = (6Z, 15Z)$.

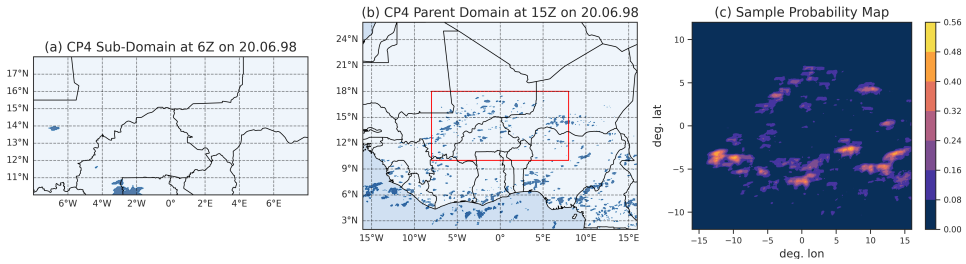


Figure 4.2: An example of a probability map derived from cross-correlation (c) for a single day with $t_0 = 6Z$ and $t_1 = 15Z$. Location with rainfall over the thresholds are shaded blue in (a) and (b). The sub-domain (a) is shown in (b) by the red rectangle.

For a start time t_0, a set of cross-correlations are calculated for each lag time $t_1 - t_0$. Dividing each by the total number of rain events in the t_0 domain gives a conditional probability map. This map shows the probability of rain at $(x, y, t1)$, given high rainfall at (0,0,t_0). This calculation is repeated for each day in the JJAS period of each year from 1998 to 2006, giving a total of 1080 cross-correlations for each lag time. Taking point means over all 1080 cases gives one final set of probabilities for each lag time. In the following results, $t_0 = 6Z$ in all cases.

The distance of maximum probability from the average t_0 rain location for a given radial direction can be found by transforming into polar coordinates (r, θ), and normalizing the correlation values in each of $2\pi/\alpha$ sectors of a domain-wide circle around the origin, for a small angle α. This shows, for each θ independently, where on the radius the highest probabilities are located. This approach highlights radial structures when changes in the intensity of the signal with angle make the patterns otherwise harder to perceive. In this case, $\alpha = 0.5°$ is used, and the values are normalized in $[0, 1]$. We are then able to identify if coherent radial structure exists in which the higher values of probability in a given direction are found at similar distances from the t_0 rain location.

4.2 Lagged Rainfall to Rainfall cross-correlation

Figure 4.3 shows the mean conditional probability maps between sub-domain rainfall at 6Z and the parent domain at 3-hourly intervals. All three datasets show an area of high probability propagating in a WSW direction. This direction is known to be the dominant climatological propagation direction for Sahelian squall lines (Mathon et al., 2002; Tulich and Kiladis, 2012; Crook et al., 2019). By visual inspection, the shape and propagation of these areas in the CP4 map are more similar than P25 to those in observations. The P25 map also shows an additional

ENE moving feature which is not consistent with known climatologies. These model differences are consistent with previous work comparing organized convective rainfall in CP4 and P25 (Crook et al., 2019). In both CP4 and IMERG probability maps, there are stationary features associated with orography to the SE for +6 to +12 hours. The feature is likely associated with climatological orographic rainfall in the Jos Plateau, approximately (10N,8E), and the mountains of northwestern Cameroon and southwestern Nigeria.

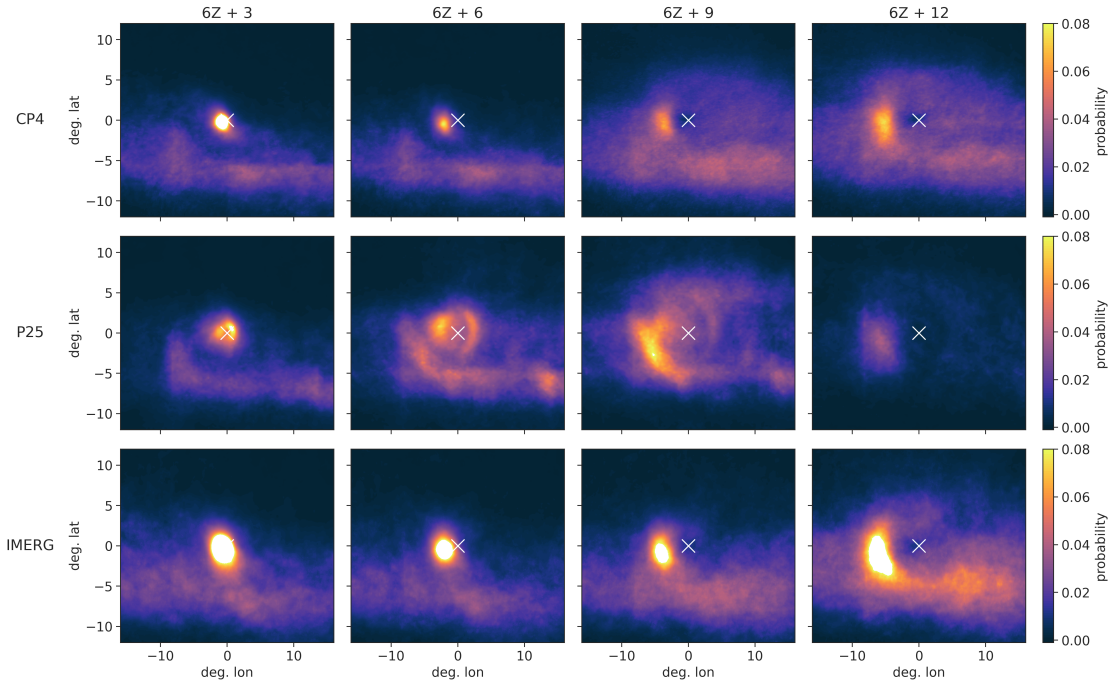


Figure 4.3: Probability of rain >2mm at t_1, surrounding the mean 99th percentile $6Z$ rain location, with $t_1 = 9Z, 12Z, 15Z, 18Z$ for CP4, P25, and IMERG. See section 2.2 for the calculation method.

In Figure 4.4, differences in spatial maximum probability are due to combination of model rainfall biases and resolution. Probabilities are generally higher in the IMERG map at all lag times than for both models. By using a fixed threshold at t_1 the time evolution of the mean probability closely follows the diurnal cycle of the 2mm/hr percentile shown in Figure 4.1. However, the evolution of the spatial variability in CP4 probabilities is also closer to observations. The improved mean diurnal cycle is a known advantage of convection permitting simulations more generally (Birch et al., 2014; Stratton et al., 2018).

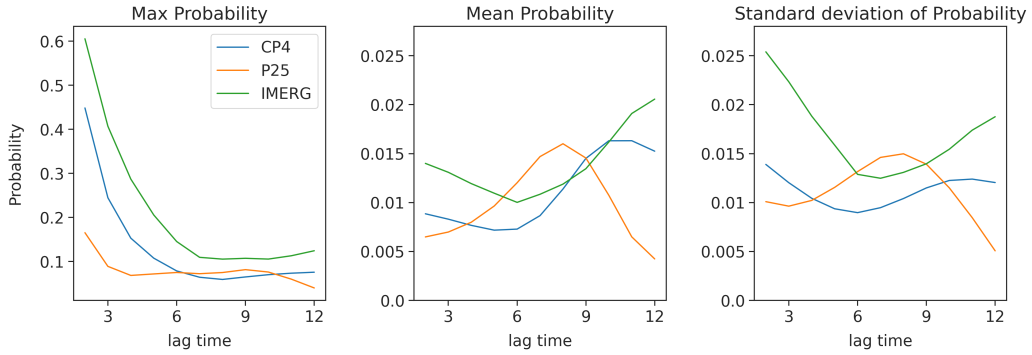


Figure 4.4: Maximum, mean, and standard deviations of the probabilities (P) in Figure 4.3.

Figure 4.5 shows the same data as Figure 4.3, but each probability map has been normalized radially using the method described previously. The result is a coherent ring-like structure of higher values around the t_0 location of convection. The rings are of similar size for all data sources, with the average radius of 600km at a lag of +12 hours. Considering the ring as growing with time, the average propagation speed is approximately 14ms^{-1}. This is faster than the modal range of MCS propagation in both models and in observations, which ranges from 4-12ms^{-1} depending on the model or observations (see Crook et al. (2019) Figure 6a). However, 14ms^{-1} is well inside the observed spread. Patterns in Figure 4.5 for CP4 and IMERG are more similar, particularly up until +9 hours. A tight range of radii for the highest values of the radially normalized probabilities are common to all at lag +12. For CP4 and IMERG, there are clear local minima close to and west of the origin, and the pattern becomes much noisier to the east. The pattern in P25 at +12 is generally more zonally symmetric, including in the central minimal.

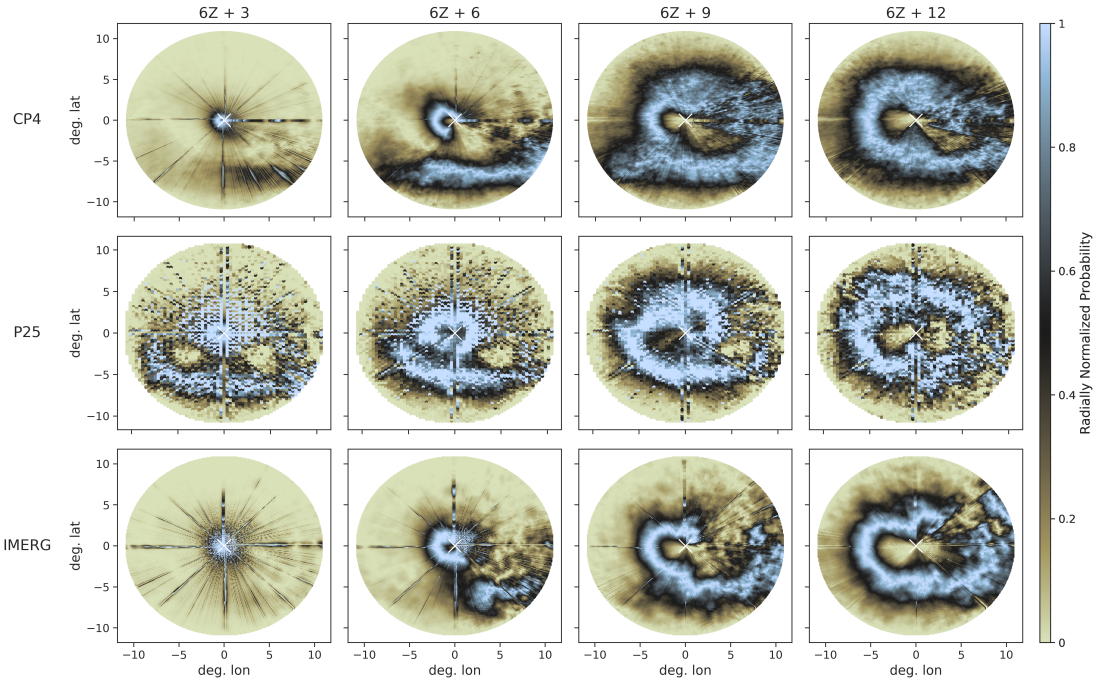


Figure 4.5: Results of radially normalizing the probability maps in figure 4.3. For a given direction the highest and lowest probabilities are represented in pale blue and brown respectively. See section 2.3 for calculation details.

4.3 Investigating physical mechanisms

In testing for organizing mechanisms we will therefore continue to use data from the CP4 model, based on its better agreement with IMERG in Figures 4.3 and 4.5, whilst remaining aware of the temporal differences seen in Figure 4.4. Since the rings in 4.5 have some radial thickness, we assume a range of propagation speeds exist in the associated mechanisms. The speed of ring 'growth' can be used to begin to determine which parts of the pattern are potentially associated with cold pools and which with waves. We can first use a cross-correlation of $6Z$ rainfall with t_1 temperature and wind anomalies to determine the likely location of cold pool gust fronts.

Figure 4.6 shows the 9-season mean cross correlation of $6Z$ high rainfall locations with $t_1 = 12Z$ temperature (contours) and meridional wind anomalies (arrows) at 925hPa. Overlaid in blue are the values of the highest 20% of the radially normalized probabilities for three lag hours later at $t1 = 15Z$. This is done to make $t_1 = 12Z$ the pre-rain environment. Again the origin represents the location of the $6Z$ high rainfall. The temperature and wind cross correlation

values have been divided by the number of high rain points at t_0: this gives an estimate for the mean magnitudes of the anomalies. At 12Z, there is an elliptically shaped mesoscale cold anomaly centred just westward of the intense rainfall location six hours prior. The majority of high values in the $15Z$ radially normalized probabilities are found at the edge of the cold anomaly between the -0.5K and 0K contours. The wind anomalies near the origin show a component of divergent flow outward from the earlier rain location, except to the east. In many places there is convergence of the wind anomalies where we find high values of the radially normalized probabilities three hours later. The western part of the pattern is reminiscent of cold outflow-driven lifting ahead of a propagating MCS. To the north, however, a propagating storm doesn't explain the ring location, so we will next examine just a cross-section of the pattern.

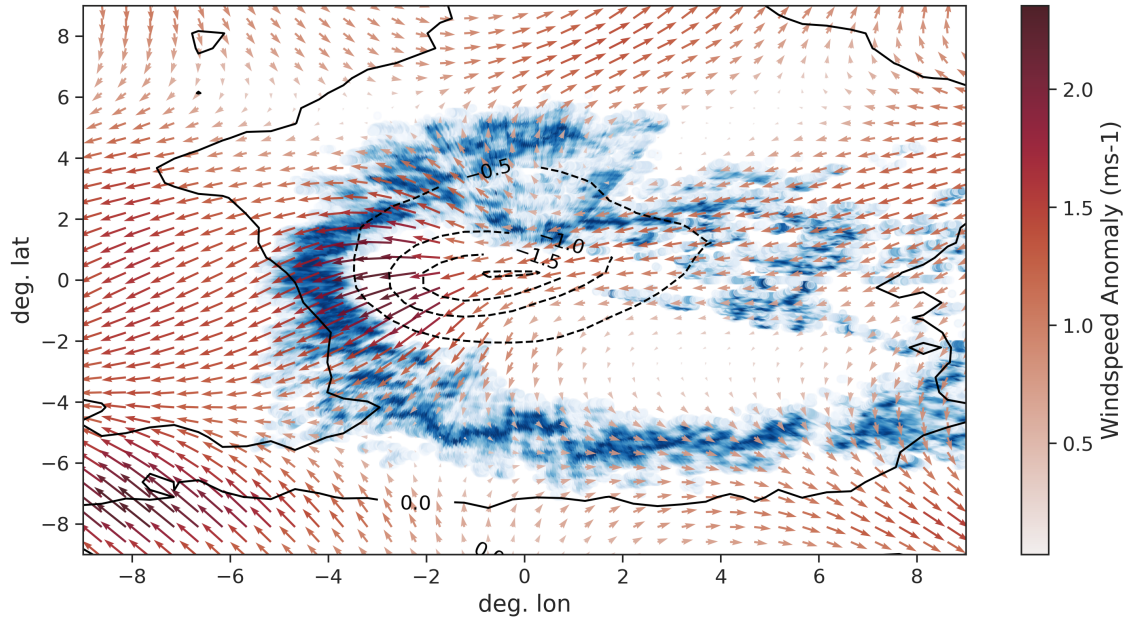


Figure 4.6: Mean CP4 cross-correlation of 6Z rainfall locations over the threshold with $t_1 = 12Z$ 925hPa temperature anomalies in K (black contours) and 925hPa horizontal wind anomalies (arrows). Blue shading shows the top 20% of the radially normalized rainfall probabilities at $t_1 = 15Z$.

Figure 4.7 shows a north-south cross-section of Figure 4.6. Overlaid now are all the values of the radially normalized probabilities on that cross-section for $t_1 = 15Z$. The cross-section is chosen to mostly exclude the propagating 'MCS' itself and focus instead on the surrounding environment. The maximum magnitude of the wind anomalies coincident with negative temperature

anomalies in this cross-section is $< 1ms^{-1}$. If this speed were maintained it would give a radius of $<$ 100km (or 1°) in 12 hours. This is a conservative estimate since not every event used to construct the average will have a strong cold pool, bringing down the average magnitude of the anomalies. Using instead the JJAS composite cold pool front speed of $6.5ms^{-1}$ in Provod et al. (2016) gives an estimated radius of $<$ 300km (or 3°) in 12 hours. The sections of the rings to the north and south extend as far as 600km from the average 6Z rain point. These more distant correlations are more likely the result of faster cold-pool gusts or gravity waves as seen in Birch et al. (2013). Meridional asymmetry is present in both the temperature and wind anomalies. The mean cold anomaly extends further north than it does south, potentially because a given expanding pool of cold air at a given temperature will be more negatively anomalous in the warmer north. These asymmetries could also be due to contrasting boundary layer characteristics that favour more or less cold pool propagation.

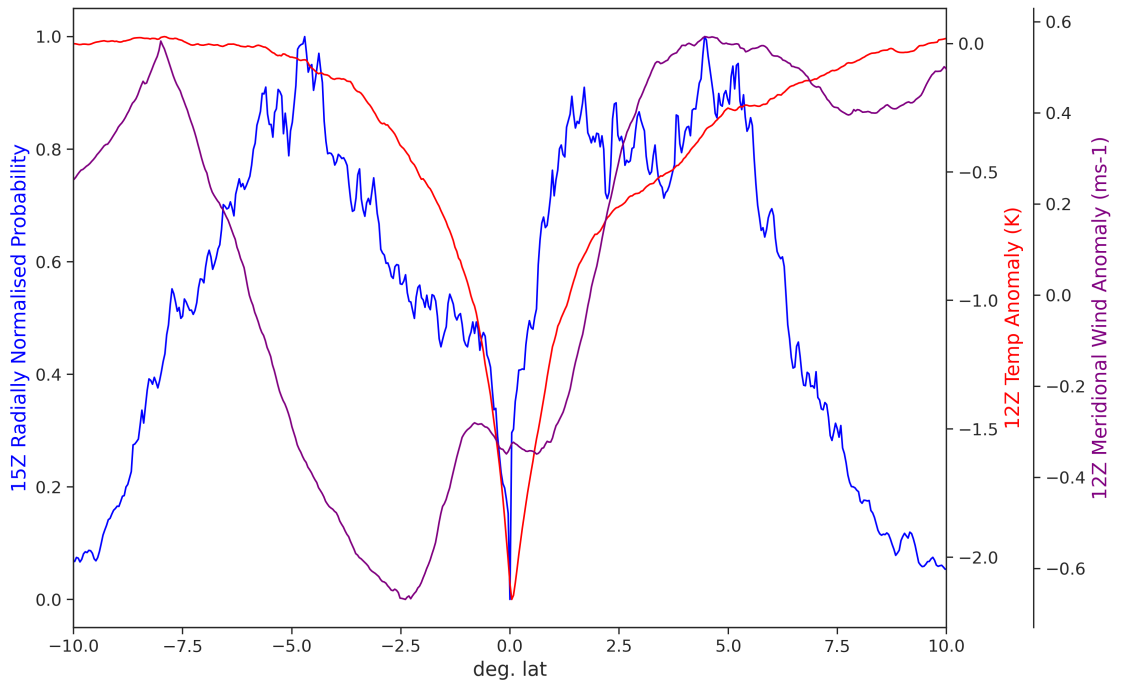


Figure 4.7: A north-south cross section through x=0 of figure 4.6, and the same for the 15Z CP4 radially normalized rainfall probabilities. Note that only the meridional component of the wind anomalies are shown.

Next, we search the same cross-sections for the presence of wave-like signals in anomalies of vertical motion. Figure 4.8 shows two latitude-height sections of the mean cross-correlation of 6Z

rainfall with omega and meridional wind anomalies between 925hPa and 100hPa where $t_1 = 9Z$ (left) and $t1 = 21Z$ (right). At 9Z, positive/negative omega anomalies (descending/ascending air) dominate the lower/upper column in the area surrounding the 6Z rain event. Twelve hours later, at 21Z, a region of weak descent extends northward from the 6Z rain location approximately 6°, and up to ∼600hPa with ascent above. The vertical structure to the north is similar to that associated with stratiform heating (Houze Jr., 2004; Schumacher et al., 2004; Schumacher and Houze JR., 2006b), with upper level ascent and lower level descent. Combined with the deep ascent seen to the south this would be the expected contribution to the signal from a southwesterly propagating MCS with a trailing stratiform region. Figure 4.9 is another cross section, this time of the 12Z 500hPa omega anomaly cross correlations alongside the subsequent 15Z radially normalized probabilities. The amplitudes of the two are clearly out of phase to distances of 6-7°.

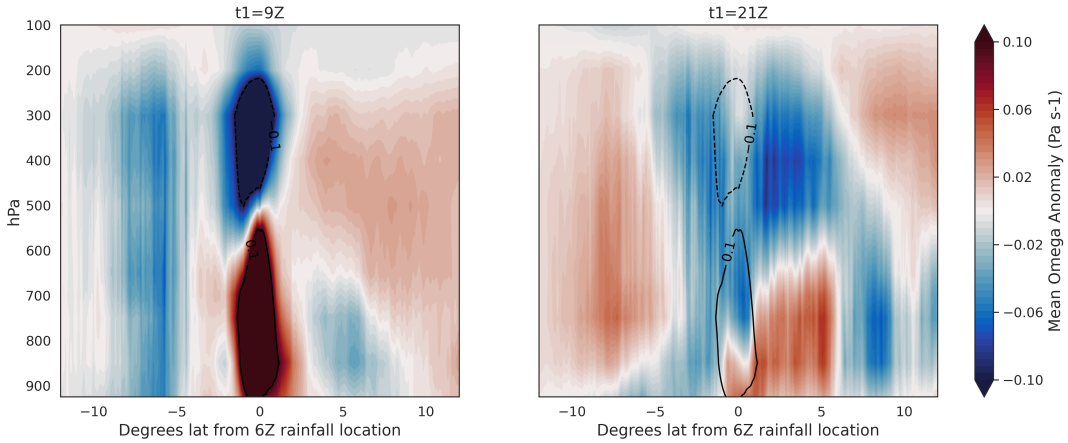


Figure 4.8: A latitude-height cross-section through x=0 of the mean CP4 rainfall and omega anomaly cross-correlation with $t_0 = 6Z$ and $t_1 = 9Z$ and $21Z$. On both panels are the $\pm 0.1 Pas^{-1}$ contours for t1=9Z.

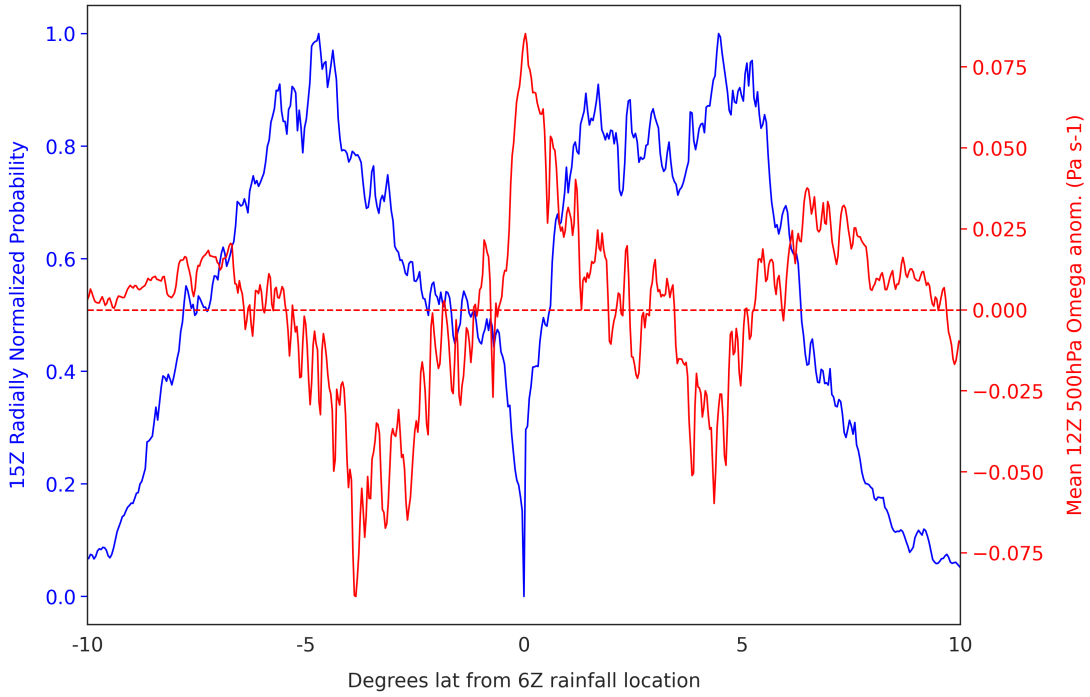


Figure 4.9: A north-south cross-section through x=0 of the CP4 rainfall and omega anom. cross-correlation (red) with $t_0, t_1 = 6Z, 12Z$. In blue is the cross-section of the CP4 radially normalized probabilities for $t_1 = 15Z$.

4.4 Summary of results

A coherent ring-like pattern of higher conditional probabilities of rainfall around earlier rainfall is accentuated by radially normalizing. The rings have a scale of $\sim$ 1000km at a lag time of t_0+ 9-12 hours and include a region of high-probability to the west of the earlier rainfall, indicative of MCS propagation. The patterns calculated from a model with explicit convection show spatial and diurnal cycle characteristics more similar to those in observations, compared to a model with parameterized convection. We present statistical indications that convective memory may contribute to improved diurnal cycles—an improvement noted in previous studies of convection-permitting models.

The mechanisms for coherent patterns are explored in the convection-permitting model, and we find patterns in the dynamics with features common to cold pools and gravity waves. Cold pools are identified by anomalously cold and divergent regions at time t_1, around where convective rainfall occurred at time t_0. At the edge of thse regions, anomalous convergence leads to

an enhancement of the radially normalized probabilities, particularly in the western half of the coherent pattern. Cross-sections through composite cross-correlations of rainfall with vertical motion show 12Z anomalies in 500hPa ascent are anti-correlated to 6Z rain locations but correlated in a region 2-6° away. This ascent is colocated with the peaks in a similar cross-section of the radially normalized probabilities.

4.5 Start time sensitivity and storm lifecyles

As mentioned in Section 2, the choice of start time used in the cross-correlations (CC) was dictated by which produced the strongest correlations that were not attributable to stationary features such as coasts and orography. However, this is not to say that starting at other times does not produce coherent patterns. To quantify the sensitivity of the method to start time, we can calculate mean CC for the full range of t_0 all with a fixed lag time. Taking one-dimensional cross-sections of the resulting arrays and stacking them along a common axis shows us the distribution of conditional probabilities in (t_0, D) space, where D is the distance from the mean t_0 rain point as in figures in section 3.

The (t_0, D) space plot gives us information about both the amount and speeds at which t_0 rain enhances t_1 rain in the surrounding area. Figure 4.10 shows such a plot for northward cross-sections of CC with t_0 from 0-14Z, all with a fixed lag of 9 hours. As such the corresponding t_1 are from 9Z on the same day to 23Z. We can interpret this under the assumption that higher probability results from some propagating response of the atmosphere to t_0 rainfall after 9 hours. For example, a significant correlation at 5 degrees north corresponds to some propagating feature that travels at $\sim$17ms^{-1}. We see the strongest correlation at distances requiring speeds between $\sim$5-20ms^{-1} when t_0 is 5-8Z, and only up to $\sim$10ms^{-1} for t_0 of 12-14Z. All these speeds can be achieved by cold pool gust fronts (Provod et al., 2016) or gravity waves, other than the first baroclinic mode which is much faster.

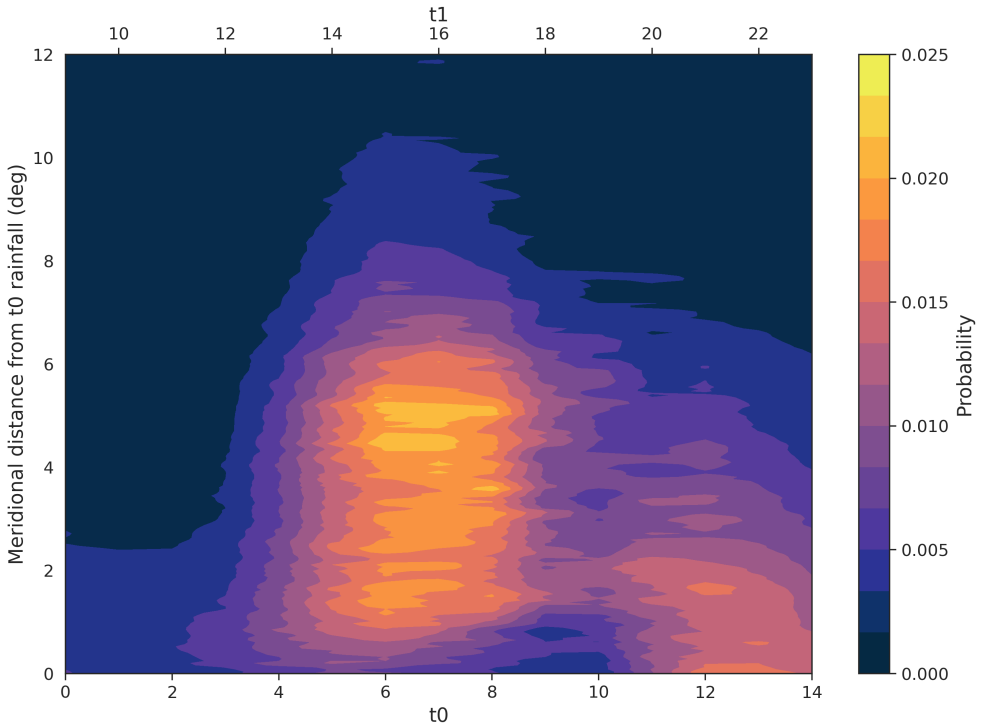


Figure 4.10: Sections of probability maps at $t_0 + 9hrs$ for t_0 in 0,14Z. Only the northward direction from the mean t_0 rainfall location is shown for simplicity. Meridional distance northward from the origin is shown by the y-axis. The lower x-axis shows t_0, and the upper x-axis is the corresponding $t1 = t_0 + 9$ hours.

Fast moving gust-fronts and large amplitude gravity waves are generated by large buoyancy perturbations in MCSs. The slower speeds for afternoon t_0 could be the result of local clustering of new afternoon initiations around surface features (Garcia-Carreras et al., 2011), or enhancement by slower gust fronts generated in smaller storms (Meyer and Haerter, 2020). The afternoon boundary layer is less stable, and so doesn't allow for as fast of a propagation of waves along its top as could be possible at night or in the early morning. At 5-8Z, the likelihood of initiation of new isolated convection and subsequent generation of CCGW is low (Fink et al., 2017a). We assume that any intense rainfall at these times is from existing MCS that have been maintained through the night. The impact of the collapse of MCSs in the morning on the subsequent afternoon initiations could be a potential explanation for the significance of the 5-8Z choice of t_0. Similarly to how initiation is associated with CCGW, collapse should also generate similar waves but with the opposite phase. Storm collapse will also be associated with mesoscale subsidence, low-level evaporative cooling, and soil moisture feedbacks. All these arguments support suppression of convection in storm collapse regions, with enhanced convection

at the interface with the surrounding environment. These long-lived nocturnal storms are more common in the chosen sub-domain than further to the south (Lafore et al., 2017b).

If a very intense MCS can maintain itself until diurnal heating peaks again, then the storm can survive multiple days (Lafore et al., 2017a). If not then the storm weakens and decays. Figure 4.11 shows the time evolution of a meridional mean of CP4 rainfall probability maps in Figure 4.3. We see that the rainfall probability decays through the morning, but then reappears later in the afternoon. The system appears to have continued to 'propagate' westward, despite producing little to no rainfall for a period of time. This is suggestive of MCS decay and regeneration along the same track (Laing et al., 2008, 2011; Lafore et al., 2017a).

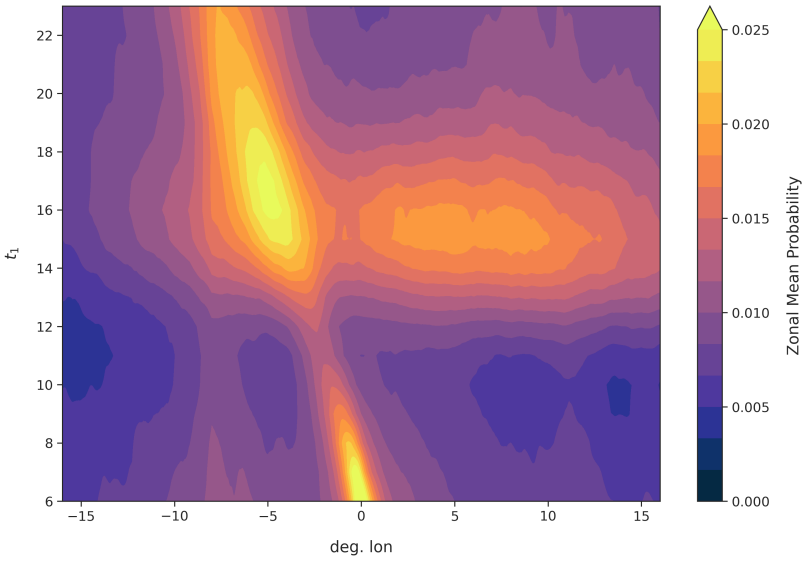


Figure 4.11: Meridional mean of CP4 probability maps in figure 4.3, but for hourly t_1 up to 23Z. $t_0 = 6Z$.

Another interesting and relevant conceptual discussion is the existence of a relationship between storm lifetimes, diurnal cycles, and the growth of the ring pattern. The role of rotation in dampening tropospheric perturbations is determined by the Rossby radius (Ro), which is on the order of ∼10,000km at 13°N. When considering the depth of the entire troposphere, rotational effects are insignificant on the scale of the patterns in our results, which are ∼1000km at most. However, consider an external Rossby radius λ_R, defined as

$$\lambda_R = \frac{\sqrt{gH\Delta\theta/\theta_0}}{f}, \tag{4.1}$$

where g is gravitational acceleration, H is the initial depth of the cold pool, $\Delta\theta/\theta_0$ is the temperature perturbation, and f the Coriolis parameter. This defines a limit on the scale of the cold pool over timescales of $\sim 1/f$. With tropical scale $f \sim 10^{-5}s^{-1}$, and cold pool characteristic scales of $H \sim 10^3m$, $\Delta\theta \sim 3K$, and $\theta_0 \sim 300K$, the value of $\lambda_R \sim 10^6m$. At latitudes 10-18N the $1/f$ timescale ranges between approximately 11 and 6 hours respectively. Temperatures recover in the interiors on average in a few hours but large cold-pools from MCSs, and the gust fronts in particular, may survive longer (Tompkins, 2001a; Provod et al., 2016), up to and beyond the $1/f$ timescale. The time elapsed between 6Z and peak diurnal heating is close to $1/f$ for those latitudes where nocturnal MCS are common, and the size order of the ringlike pattern in rainfall enhancement at 9-12 hours is similar to the above calculation of λ_R. The variation of this inertial scale with f over the domain could also explain the 'thickness' of the contributions to the composite ring pattern that result from boundary layer interactions such as cold pool driven moisture convergence and lifting.

4.6 Adaptability of the method

There is nuance to the potential conversion of these results to a statistical forecasting tool, since the probabilities shown are conditional on the chosen times, locations, thresholds and domain used to calculate them. The current method also only uses 99th percentile t_0 rainfall locations and says nothing about the relationship between location and intensity for t_0 and/or t_1. Surpassing a given threshold of rainfall might result from different mechanisms over higher terrain, for example. We should also remember that the threshold for t_0 is not fixed here and instead changes with time of day. The rainfall probability maps in these results are analogous to a composite of binary arrays around the most intense rainfall locations in the sub-domain at t_0. This could easily be adapted to include magnitudes in both t_0 and t_1 rainfall intensity above a given threshold, but would likely require some normalization relative to the time of day to remove the dominant diurnal signal. Including magnitude gives greater weight to the most intense rainfall events, but also adds another condition to the probability map.

The interaction of local rainfall responses and seasonal climatology is one of the main themes of investigation in tropical scale interactions. In the current method, areas of high climatological mean rainfall appear as "smudged" stationary features at t_1. This is because we chose to retain information about the climatological rainfall patterns as well as local links to previous rainfall.

An event doesn't need to be anomalous to be impactful and vice versa. Given the stochastic nature of convection and the inherent difficulties in modeling its intensity on a local scale, probability of any amount of convective rain is arguably more interpretable and more useful for users of this kind of information. Also, from a scientific perspective, we are interested in any rainfall with a meaningful physical connection to convection. For this, the actual instantaneous rate and not the anomalous rate is required. For example, a negative anomaly could still be strongly convective but just less so than the mean and vice versa. A focus only on large local positive anomalies therefore restricts the sample of convective events.

A simple prediction tool conceivable with this method is one where a forecaster inputs the location of a storm at t_0 within a given sub-domain S, retrieves a t_1 cross correlation between S and its wider environment from a large store of observational data and model rainfall analysis, and maps likelihoods of rainfall over a chosen threshold at t_1 given the storms current location. Methods of this kind offer advantages over simply tracking or propagating existing features in the domain, as they incorporate information about potential interaction at distance. Crucially, this includes the relationship between existing and new convection which tracking alone cannot capture. Of course, the robustness of such a tool requires great care and is beyond the scope of this study. A similar tool has already been developed by the NFLICS project (Anderson et al.), but here we show the potential to enhance the physical understanding of patterns using high-resolution model data alongside satellite rainfall retrievals.

While the computational simplicity of the method in this chapter has its merits, it is conceivable that patterns such as these could be learned with more complex machine learning techniques with higher dimensional inputs. For example, using convolutional methods for spatial rainfall pattern learning (e.g. Badrinath et al. (2023)) could yield similar results to ours, since convolutions are mathematically similar to cross-correlation. Deep learning is increasingly used for nowcasting, with models trained using satellite data (e.g. MetNet in Andrychowicz et al. (2023)). However, training these models with the existing observational record alone is not ideal due to the non-stationary nature of the climate system both within that period and more generally (Palmer, 1999). A potential solution is to use km-scale model data to better fill the sample space. However, this requires continued evaluation of the realism of model patterns and processes; our results are an example of a pattern-based evaluation. There are also developments in hybrid approaches that combine machine learning with physical models (Kashinath

et al., 2021; Das et al., 2024). Future analysis could also use methods for explicitly diagnosing cold pools from km-scale model data (e.g. Drager and van den Heever (2017)) and, supported with datasets of rainfall and identified cold-pools in observations (Provod et al., 2016; Hoeller et al., 2024; Kirsch et al., 2024), use these to again predict patterns of rainfall enhancement by previous rain.

Waves and cold pools are ubiquitous and universal features of atmospheric convection, and as such the relationships shown in our results should be relevant across other tropical domains where convection dominates climatological rainfall. Similar methods could be used to explore patterns in other domains or examine the behaviour of other models and their processes. For example, Mapes (2024) shows frequency composites of observed cold cloud objects in a South American domain, and the inferred spatial pattern of self enhancement/suppression is both elliptical and dependent on the diurnal cycle. The application of the method to model fields of quantities not observable by remote sensing also presents interesting possibilities. However, the patterns produced are sensitive to model process representations, such as the parametrization of convection, and the question of whether pattern mechanisms are common between observations and models remains an important consideration.

4.7 Conclusions and Discussion

Our results demonstrate that lagged cross-correlations can uncover coherent structures of enhanced convective rainfall probability around early morning rainfall events in the West African Sahel. These patterns appear in both observations and regional climate model simulations. Notably, the convection-permitting model reproduces these patterns with greater fidelity in terms of magnitude and timing, aligning more closely with satellite observations than its parametrized counterpart. The closer similarity of the observed and explicit model's pattern likely stems from an improved representation of the diurnal cycle, better representation of MCS and their lifecycles, and increased sensitivity of convection to previous convection via spatially resolved non-linear interactions such as with cold-pool gust fronts and convectively generated gravity waves. The analysis therefore links several perspectives on scale–interaction at meso–synoptic scales.

Given the inherent unpredictability of rainfall at daily timescales in tropical regions such as the Sahel (Keane et al., 2025), there is a clear need to exploit sub-daily patterns and mechanisms

to develop and evaluate models and tools that provide early warnings to vulnerable populations. This approach will become increasingly critical as both daily and sub-daily extremes are projected to intensify in the future (Taylor et al., 2017; Biasutti, 2019; Kendon et al., 2019; Fitzpatrick et al., 2020). We expect that these efforts could be enhanced by the use of more sophisticated statistical methods than used in this chapter, or with machine learning. We highlight that km-scale models produce spatiotemporal patterns similar to observations, which lends credence to using the existing large volumes of model data to supplement and enhance statistical forecasts or machine learning training datasets. Additionally, improved spatiotemporal characteristics of model rainfall at km-scale resolutions increase confidence that model processes can be evaluated with respect to observed rainfall patterns. For coarser resolutions, parameterizations need either to represent the spatial statistics, or the underlying drivers. Process evaluation remains fundamental for improving forecast accuracy and constraining uncertainty in modelling of future changes.

In a broader context, the patterns we visualize here should be somewhat universal across convectively active regions; for example Mapes (2025) finds radial patterns in South American convection using a similar method. If sub–daily structures such as we and others have shown are misrepresented in models, then the level of heterogeneity in a given domain risks being unrealistic. Heterogeneity in cloud cover and rainfall latent heating is a primary mechanism for the coupling of convection to larger–scale circulations. Misrepresented probability patterns are therefore important beyond near–term forecasting or nowcasting applications, and should be thought of as an emergent property of sub-optimal model physics at the sub–grid scale. One–dimensional column models or analyses obviously lack the dimensions in which this structure emerges, and any parameterization derived from column arguments may not be representative of the real range of possible feedbacks. As we move through this thesis, we will continue to examine statistical patterns at larger scales, including spatial ones. The next chapter includes analysis of how the same processes that drive sub–daily patterns can impact the mean–state and variability of synoptic circulatory features.

Chapter 5

Upscale Impacts of Convective Processes on the Regional Scale

In the previous chapter, we quantified a way in which spatial patterns of convection are correlated over time for sub–daily timescales. In the real atmosphere and in non–idealized simulations, the mechanisms of convection–convection interaction are embedded in a responsive large–scale dynamic and thermodynamic environment. This chapter now explores some aggregate dynamic and thermodynamic effects of sets of smaller interaction processes on more regional scale features. Impacts of convection on the mean and variability of this larger scale are a second level of 'upscale' effects, beyond the mesoscale structuring into MCS or statistical patterns as in the previous chapter.

The motivations for the following analyses are like those for the previous chapter, but now with the upscale effects measured over longer and larger scales. Documenting and understanding the upscale effects of model convection beyond mesoscale and synoptic patterns, on seasonal mean circulation and weather statistics, is important for understanding uncertainties in predictions at sub-seasonal timescales and beyond. Many operational models for these timescales, especially ensembles on global domains, do not currently resolve the intermediary–scale mechanisms responsible for upscale interactions. After demonstrating that physics and resolution choices have upscaling effects, it is then important to quantify the relative importance of model physics relative to impacts of other modelling choices such as domain size. Results here may therefore further justify the adoption of higher–resolution modelling over larger domains, variable reso-

lution model hierarchies, or new parameterizations for intermediary–scale processes to improve predictions beyond the medium range.

In part 1, we stay focussed on the West African monsoon region, and on quantifying regional impacts of one of the proposed mechanisms for the patterns of convection described in Chapter 4 – cold pools. Then in part 2, we move on to a more general consideration of the spatiotemporal variability of both rainfall and moisture across multiple tropical regions as a function of model physics and domain size. The latter remains a study of the upscale impacts of convection, but in the context of evaluating different modelling approaches rather than highlighting specific mechanisms.

5.1 Part 1: Cold Pools and the West African Monsoon Structure

Sections 5.1.1 and 5.1.2, including Figures 5.1 and 5.2, are adapted from the candidate's contributions to the following published article: Maybee, B., Bassford, J., Marsham, J.H., Lewis, H., Field, P., Klein, C., et al. (2025) How sensitive are Sahelian mesoscale convective systems to cold-pool suppression?. Quarterly Journal of the Royal Meteorological Society, https://doi.org/10.1002/qj.5032.

In this first set of analyses, the focus is on the upscale impact of better represented cold–pools generated by organised deep convective systems. We are motivated to highlight cold–pools here specifically, because they arise from subgrid microphysical processes but make their accumulated impacts on the large scale via the resolved flow on the mesoscale. This is precisely the type of upscale cascade that coarser sub–seasonal models can not represent explicitly, which leaves a potential source of uncertainty in their predictions. Improved representations of cold–pools include higher grid resolution, resolving the flow in and around the mesoscale storms, coupled to sophisticated microphysics parameterizations. The following results make use of a storm–resolving modelling experiment where cold–pools are suppressed by altering just the microphysics. This is arguably more powerful than simply comparing a higher resolution model to a coarser one, since differences can be more easily attributed to missing cold–pools without conflation with problems of unresolved scales of flow.

5.1.1 Identifying cold pools and their gust fronts

Cold pools generated by rainfall evaporation in the column are distinct from a surface temperature anomaly due to evaporative cooling of the wet land surface after rainfall. This is because elevated evaporative cooling and mass–loading of rainfall generates strong downdrafts which diverge at the surface, spreading the cool anomaly more broadly than the footprint of the rainfall itself. The edge of this divergent flow is known as the gust–front. In addition, strong downdrafts entrain dry environmental air from above and bring it down to the surface (Tompkins, 2001a). The result is the relative divergence of low–level moisture underneath the downdraft into a thin moist filament along the gust front. The gust–front can carry this moisture great distances, long after the interior of the cold pool has returned to the environmental temperature (Garcia-Carreras et al., 2013; Trzeciak et al., 2017).

Because gust fronts are essentially density currents, they can be identified by the combined effect of moisture and temperature anomalies on the buoyancy gradient. Gradients in buoyancy can be represented by gradients in virtual potential temperature θ_v (sometimes called density temperature e.g. Drager and van den Heever (2017)). Ignoring condensate and considering just vapour, this θ_v is calculated as $\theta_v = \theta(1 + 0.61r)$, where θ is potential temperature and r is the water vapour mixing ratio. The magnitude of the horizontal gradient in θ_v is large at the gust front, because the air just behind it is much more dense than the environment.

Using the diagnostic $|\nabla\theta_v|$, we can show that turning off the model's evaporation of rainfall in the EVAPOFF experiment (see Chapter 3.1.1) has suppressed cold pools and gust fronts. Specifically, we can take the difference in $|\nabla\theta_v|$ between the EVAPOFF and control runs during the first evening in the simulation, when due to common initialization and strong diurnal cycle most of the rain producing systems are approximately co-located in each run respectively. We take this difference at 925hPa, away from the surface but still in the boundary layer, to reduce noise from surface features and highlight only density currents deep enough to be characteristic of cold pools. Figure 5.1 shows the difference in 925hPa $|\nabla\theta_v|$ in the evening on the first day of the simulation. The first day's storms are well developed by this point in the diurnal cycle, and their respective cold pools should also be mature. Thin blue filaments in Figure 5.1 show the gust front locations that are absent in the EVAPOFF run. While there are some locations where $|\nabla\theta_v|$ is larger in the EVAPOFF run, these structures are mostly not filamentary so do not resemble gust fronts. From Figure 5.1 therefore, it appears that gust fronts are successfully

suppressed by switching off rainfall evaporation. Using the same model runs Maybee et al. (2025a) also compare composites of low–level temperatures around tracked MCSs, providing further evidence that cold pools are suppressed in EVAPOFF case.

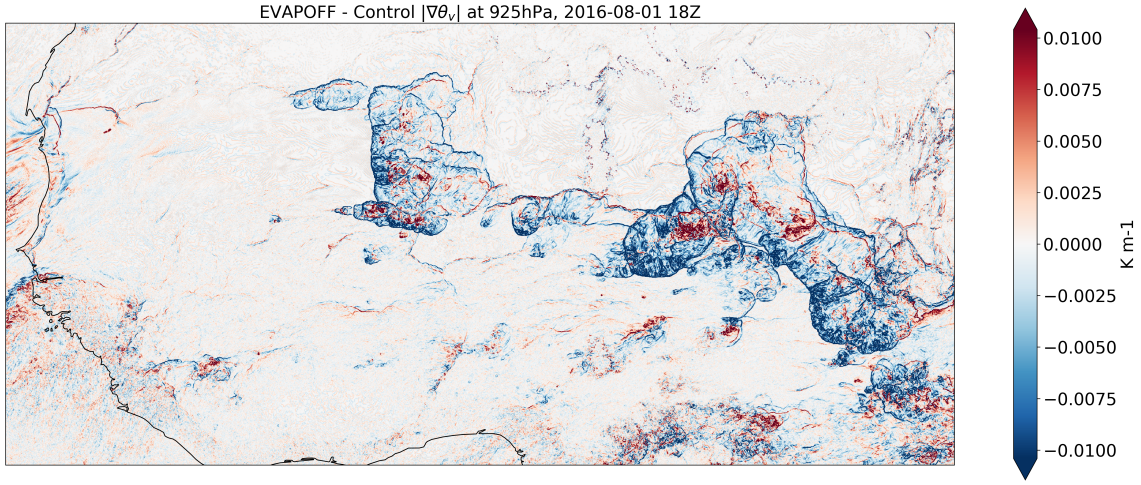


Figure 5.1: The difference in the magnitude of 925hPa virtual potential temperature gradients at 18Z on the first day of simulations. Difference is defined as EVAPOFF minus control, such that negative values show where gradients are much larger in the control run and positive value for vice versa.

5.1.2 Mean States and the Monsoon

We can now move on to the impact of the suppression of the gust fronts on the mean–state structure of the monsoon. In what follows, where we refer to change in some variable, we mean the difference made by switching off evaporation of rainfall.

Figure 5.2(b) shows that across the domain, time–zonal mean temperatures are higher below the mid–levels without evaporating rainfall. This makes sense if deep convective rainfall heating is largely in the mid–levels and the evaporation takes place mostly as rain falls through subcloud air that is warmer and much less saturated. The depth and level of maximum temperature difference depends on latitude. The strongest signals of warming are between 10°N and 20°N, which includes the Sahel. The surface temperatures in the same region are also up to 2K warmer. This is consistent with a lack of cooling by evaporation, and a lack of the downward flux of entrained cool air in downdrafts. In the Saharan latitudes, the near surface is slightly cooler, but away from the surface is warmer up to around 400hPa. In all latitudes south of the Sahara, there is a slight cooling of the upper troposphere in EVAPOFF. Reducing evaporation at a given height can only have a warming effect locally at that level, so the upper level cooling

effect is likely an indirect effect of changes to evaporation lower in the column.

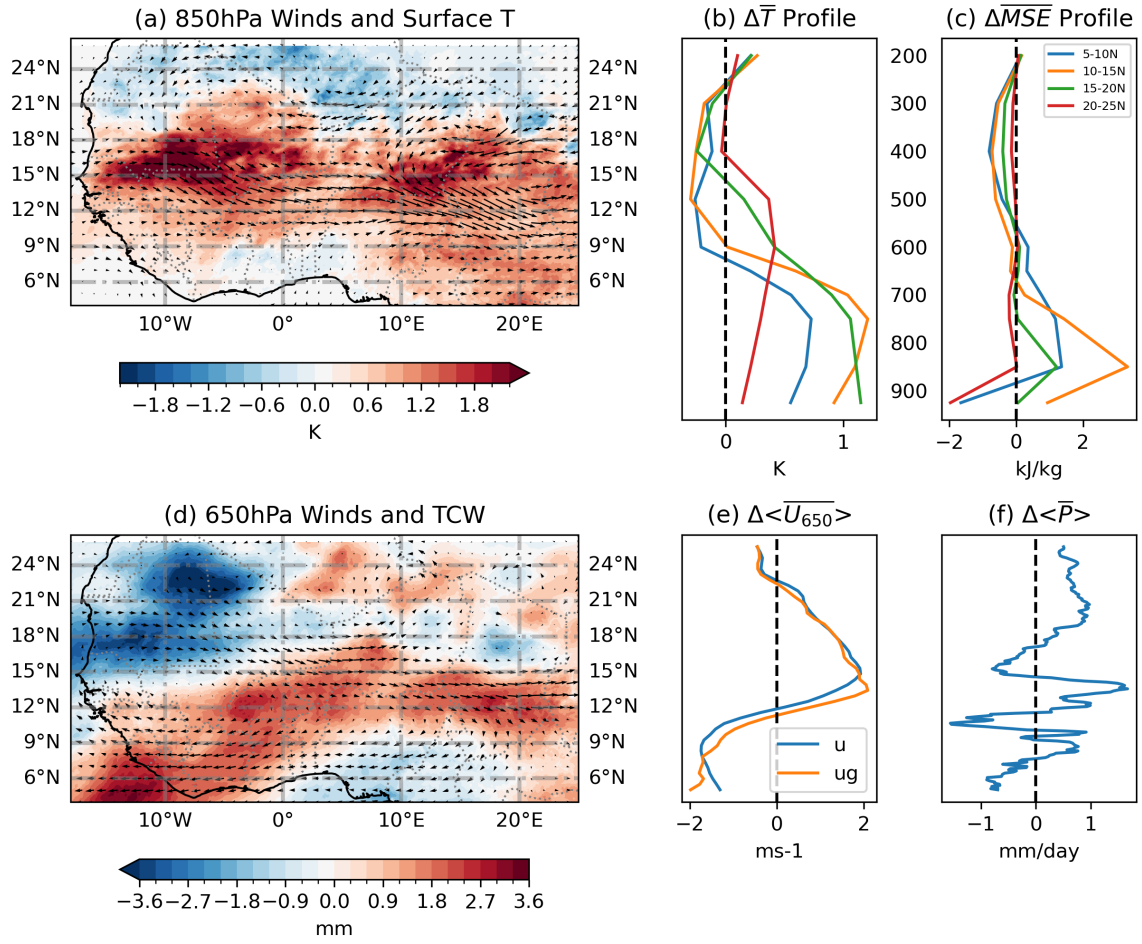


Figure 5.2: Differences in time means, EVAPOFF minus Control. Panel (a) shows differences in time–mean 850hPa winds (vectors), and surface temperature (colors). Panels (b) and (c) show time–mean temperature and moist static energy profile differences, averaged over 5° latitudinal sections. Panel (d) is like (a), but with 650hPa winds and total column water vapour. Finally, (e) and (f) show differences in time–zonal–mean 650hPa winds and precipitation respectively.

To examine the impact of temperature differences on average stability, we can compare mean static energy profiles. Moist–static energy (MSE) is defined here as the sum $c_pT + L_vq + gz$, where T is temperature, q is specific humidity, and z is height, and c_p, L_v, and g are the specific heat of dry air, the latent heat of vaporization and the gravitational constant, respectively. The difference in MSE profiles therefore contain contributions from the differences in temperature, but in Figure 5.2(c) temperature does not explain the overall difference in MSE. Increases in MSE are maximized around 850hPa, especially in the Sahel. The temperature difference of approximately 1K only explains about half the difference in MSE on average over the low levels, meaning that differences in moisture contributions are also significant. The MSE differences

imply that rainfall evaporation has a role in the average profile of stability.

When evaporation of rainfall is switched off, less precipitation is converted to vapour on descent. One might then expect lower column vapour content and higher precipitation flux at the surface everywhere where rain is common. However this is not true; Figure 5.2(d) shows how column vapour increases in the Sahel and western Guinea Coastal regions, which are associated with strongly organized convection and high precipitation rates. In contrast, there is a distinct drying in the western Sahara around the location of the Saharan heat low. Zonal mean precipitation changes themselves are also not homogeneous in Figure 5.2(f). This last statement is salient because it means that there is a connection between rainfall evaporation and the mean spatial distribution of that rainfall. Equally salient is that this connection is now apparent at scales larger than the statistical patterns associated with individual cold–pool effects shown in Chapter 4.

Alongside these changes to precipitation and to the mean thermodynamic state, there are significant differences in the climatological circulations. Two key circulation features of the monsoon are the low–level moist south–westerly flow, and the mid–level African Easterly Jet (AEJ). When evaporation is switched off, the 850hPa flow in Figure 5.2(a) becomes more westerly in the Sahel, where surface temperatures are increased. There is also a northerly component to the wind changes where surface temperatures are most strongly affected. This change constitutes a strengthening of the monsoon flow from the west, but a reduction in southerly flow in those latitudes with the largest differences in surface temperature, in the Northern Sahel and the edge of the Sahara.

As for the AEJ, Figure 5.2(d) and (e) show that the zonal flow in EVAPOFF at 650hPa is less easterly in EVAPOFF between 12-22N, with a maximum weakening of 2ms^{-1} at around 15N, and is similarly more easterly in the south. The mean AEJ in reanalysis and the control run has mean speeds of around 10-15ms^{-1} (e.g. Nicholson (2009), also see Figure 5b in Maybee et al. (2025a)), so the difference due to rainfall evaporation is potentially 13-20%. Given the importance of the AEJ and the associated wind–shear in the development of MCSs, we focus next on exploring possible mechanisms for these circulation changes.

5.1.3 Thermal Wind Balance

The mean state changes described above include direct thermodynamics effects and changes to circulation. Large–scale circulation is the tendency of atmospheric flow towards equilibrating thermodynamic gradients, and so we shall examine now the ways in which the removal of rainfall evaporation has changed the large scale thermodynamic gradient, and how this leads to circulation change and over what timescales. We also consider how the mean flow is impacted explicitly by cold pools, by analyzing the change in the eddy fluxes of temperature and momentum when the cold pools are suppressed.

Figure 5.3 shows latitude–height cross sections of the time and zonal mean temperature and zonal wind for EVAPOFF minus Control, between 15°W and 20°E. Each section is the mean over the first n days of simulation, for a range of n. Low–levels are already warmer and upper levels cooler on average after the first day, with the difference centred around 15°N. The respective change in winds is small after day 1, but the mean difference over the first 5 days is already very significant and highly structured. The pattern is tilted, with winds more easterly in EVAPOFF extending from the lower levels in the south to upper levels in the Northern Sahel, and more westerly in the lower–level Sahel and mid–level Sahara. As the simulations progress, the additional heat at low levels in EVAPOFF increases and becomes more tilted, with additionally warmer mid levels in the far north of the domain. The wind differences also become more tilted, and two easterly maxima and one westerly emerge in the difference pattern. The cross-sectional difference patterns appears mostly stable after the first 10 days, suggesting that the upscale effects of rain evaporation and cold pools are communicated to the monsoon structure over a period 10 days or less.

The difference patterns in zonal mean temperature and geostrophic circulation are connected by thermal wind balance. Zonal thermal wind balance is described by,

$$p\frac{\delta u_g}{\delta p} = \frac{R}{f}(\frac{\delta T}{\delta y})_p, \tag{5.1}$$

where u_g is geostrophic zonal wind, f is the Coriolis parameter, R is the ideal gas constant, T is temperature, and p is pressure. Subscript p denotes that the meridional temperature gradient here is on pressure surfaces. Equation 5.1 tells us that geostrophic zonal wind shear between two pressure levels balances the meridional temperature gradient across the layer between those

two levels. The AEJ can be thought of as a thermal wind that balances how temperatures in the lower troposphere increase from the humid south across the Sahel and into the Sahara (Cook, 1999; Parker et al., 2005b; Taylor et al., 2017).

The local temperature increases in the Sahel caused by turning off rainfall evaporation therefore shift the regional low–level temperature gradient further south, and with it the mid–level thermal wind. The southward shift is as seen in Figure 5.2(e), where the total 650hPa zonal mean wind differences can be almost entirely explained by differences in zonal mean u_g. From similar arguments the pattern in the zonal wind differences in Figure 5.3 is tilted because the temperature structure difference is also titled.

Many other questions still remain regarding this upscale effect, however. For example, why is the altered temperature structure tilted with deeper warming in the Sahara, and is this related to the additional SHL dryness in Figure 5.2(d). Is there a role for transient cold pool dynamics in the mean changes just described, beyond the impact of local temperatures change on large–scale gradients?

5.1.4 Heat Low Ventilation

As mentioned in Chapter 2.4.2, several studies have suggested that cold pools act to ventilate the SHL (Garcia-Carreras et al., 2013; Trzeciak et al., 2017). Ventilation here is a northward flux of moisture and relatively cool air into the low levels in the northwestern Sahara. This reduces the average layer temperature of the low–levels, bringing down the depth of the low, altering the north–south baroclinicity in the region. To diagnose this from the models, we use two measures: low–level atmospheric thickness (LLAT), and low-level mean temperatures (LLMT). The first is the difference in geopotential height between the 925hPa and 700hPa pressure surfaces, related to the temperature driven dilation of the layer (Lavaysse et al., 2009). The second is the mean layer temperature between these two levels, taken over the available pressure levels and including the top and bottom levels. To measure change in thickness over time, a box is defined in the northwestern Sahara for LLAT calculation which contains all the locations of maximum LLAT over the first 7 days.

Figure 5.4(a) shows how the mean low–level atmospheric thickness (LLAT) in the northwestern Sahara evolves over the first week of the two simulations, and Figure 5.4(b) shows the difference in time–zonal mean of the meridional eddy temperature flux divergence over that first week.

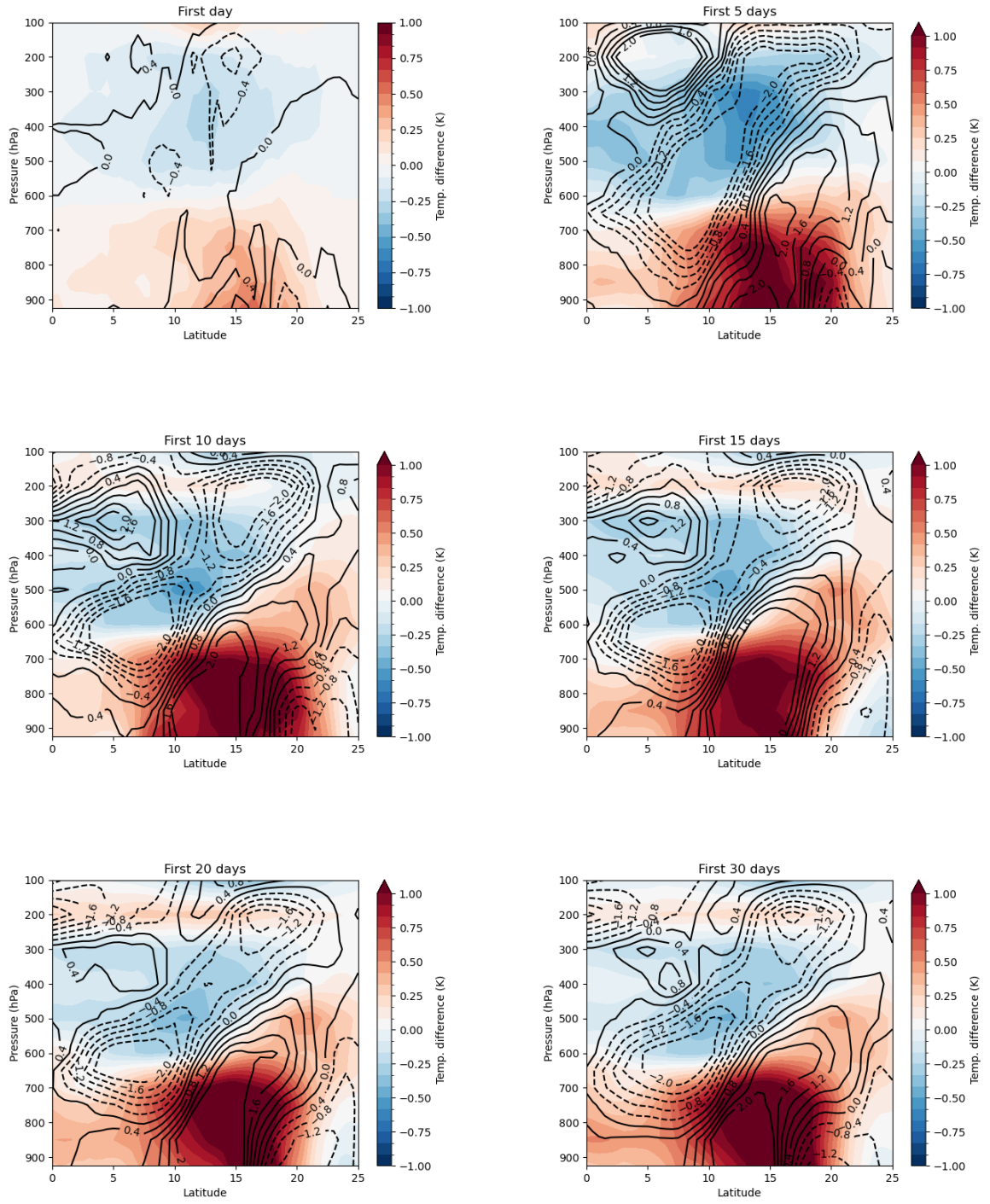


Figure 5.3: Latitude-height cross-sections of EVAPOFF minus Control zonal mean temperature (colors) and zonal wind (contours) differences. The mean differences are calculated over the first 1, 5, 10, 15, 20, and 30 days of the simulations respectively.

The mean LLAT systematically decreases in the control run over this period, and the mean eddy fluxes of temperature are more divergent in the far north. A more divergent eddy temperature flux is equivalent to a convergence of negative temperature anomalies, which would lower the layer temperature and therefore the LLAT. Figure 5.4(c) and (d) then shows respective mean low-level mean temperatures (LLMT) on a map, and we can see that the control run is in fact cooler. This apparent cooling and shrinking of the SHL when cold pools are active is consistent with previous work on ventilation and its role in regional forecast errors (Marsham et al., 2013; Garcia-Carreras et al., 2013).

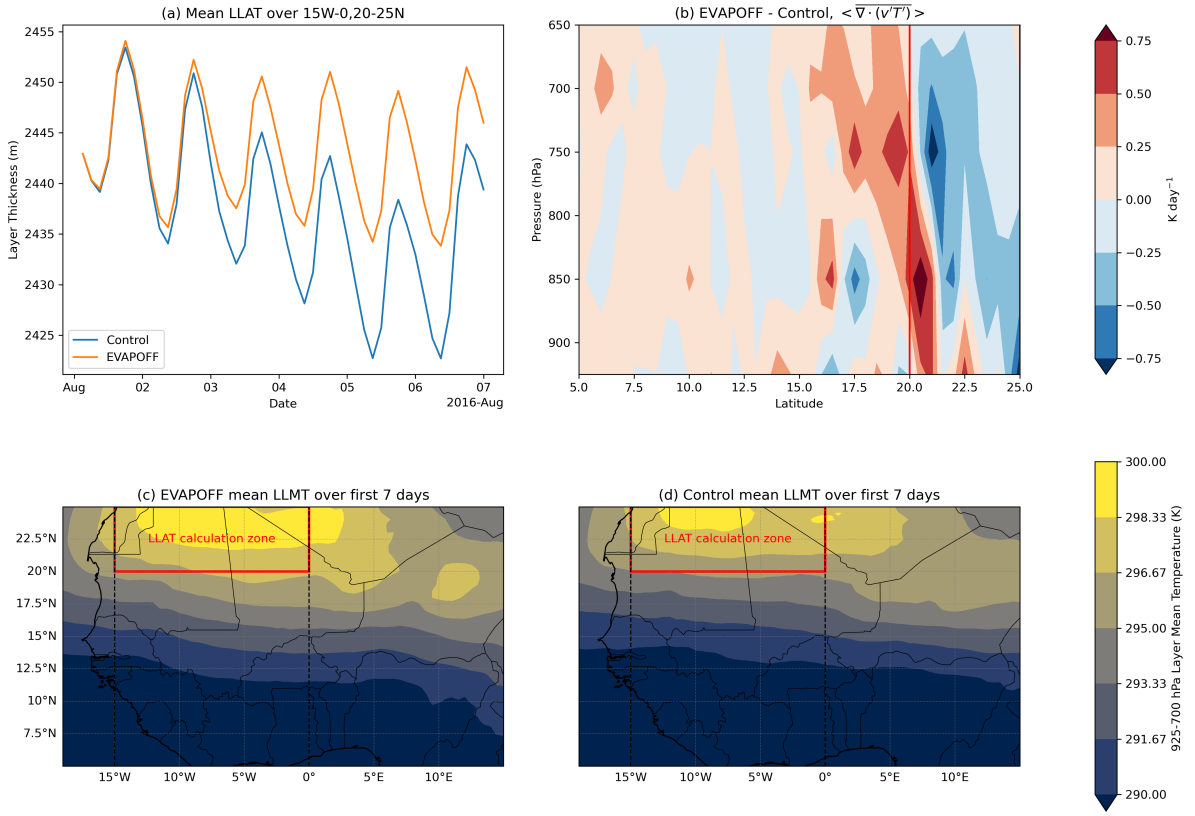


Figure 5.4: Changes to the Saharan Heat Low region and associated eddy temperature fluxes in the first 7 days of simulation. (a) is mean Low-level Atmospheric Thickness in the northwestern Sahara over time. (b) is a latitude-height cross section of model differences in zonal mean eddy temperature flux divergence, where the zonal means are calculated between the longitudinal boundaries of the LLAT calculation zone. (c) is the EVAPOFF mean low-level layer mean temperature over the first 7 days of simulation, with the box used to calculate (a) shown in red. Dotted black lines show the edges of the region used to calculate the zonal means in (b). (d) is as for (c) but for the Control run.

5.1.5 Vertical Momentum Fluxes

According to the RKW theory of MCS organisation (Rotunno et al., 1988), cold pools play a major role in maintaining tilt in storm updrafts. One of the findings of Maybee et al. (2025a), for which the focus is comparing MCSs in the same two model runs as here, is that storm updrafts are more tilted backward (eastward) with height in the run with cold pools, consistent with RKW theory. Here we quantify the impact of this tilt on vertical momentum fluxes, by simplifying conceptually the vertical structure of a storm to an overturning eddy. Eastward storm tilt is then associated with a net upward eddy flux of westerly eddy momentum, or equivalently a downward eddy flux of easterly eddy momentum. Figure 5.5 shows that EVAPOFF has weaker zonal mean vertical eddy momentum fluxes across the Sahel latitutes, with the largest differences in the mid–upper troposphere. Less redistribution of momentum throughout the column in EVAPOFF is also consistent with the pattern of stronger low–level westerlies and easterlies aloft in Figure 5.3.

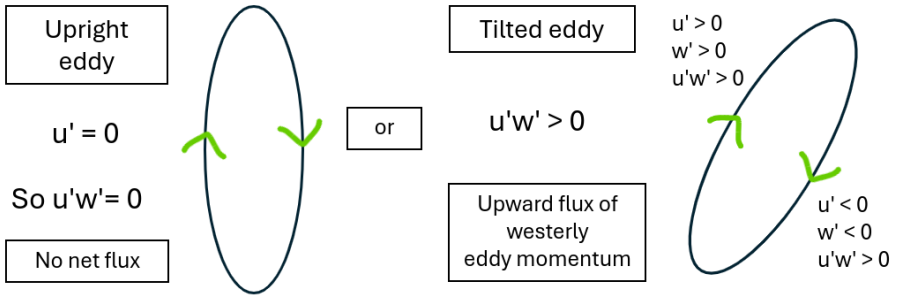
5.1.6 Summary of Part 1

We have shown here that a single change to model microphysics has a profound impact on the synoptic scale structure of the atmosphere, which can be explained mechanistically. The simple design of the experiment, with just this one process removed, allows for the express identification of the upscale impacts of that process. This experiment has provided further evidence that the smallest scale processes included in a model are the beginning of a upscale cascade of interactions. This conceptual cascade begins with microphysics, and moves up through the scale of clouds and updrafts to the storm scale and beyond to alter the synoptic circulation.

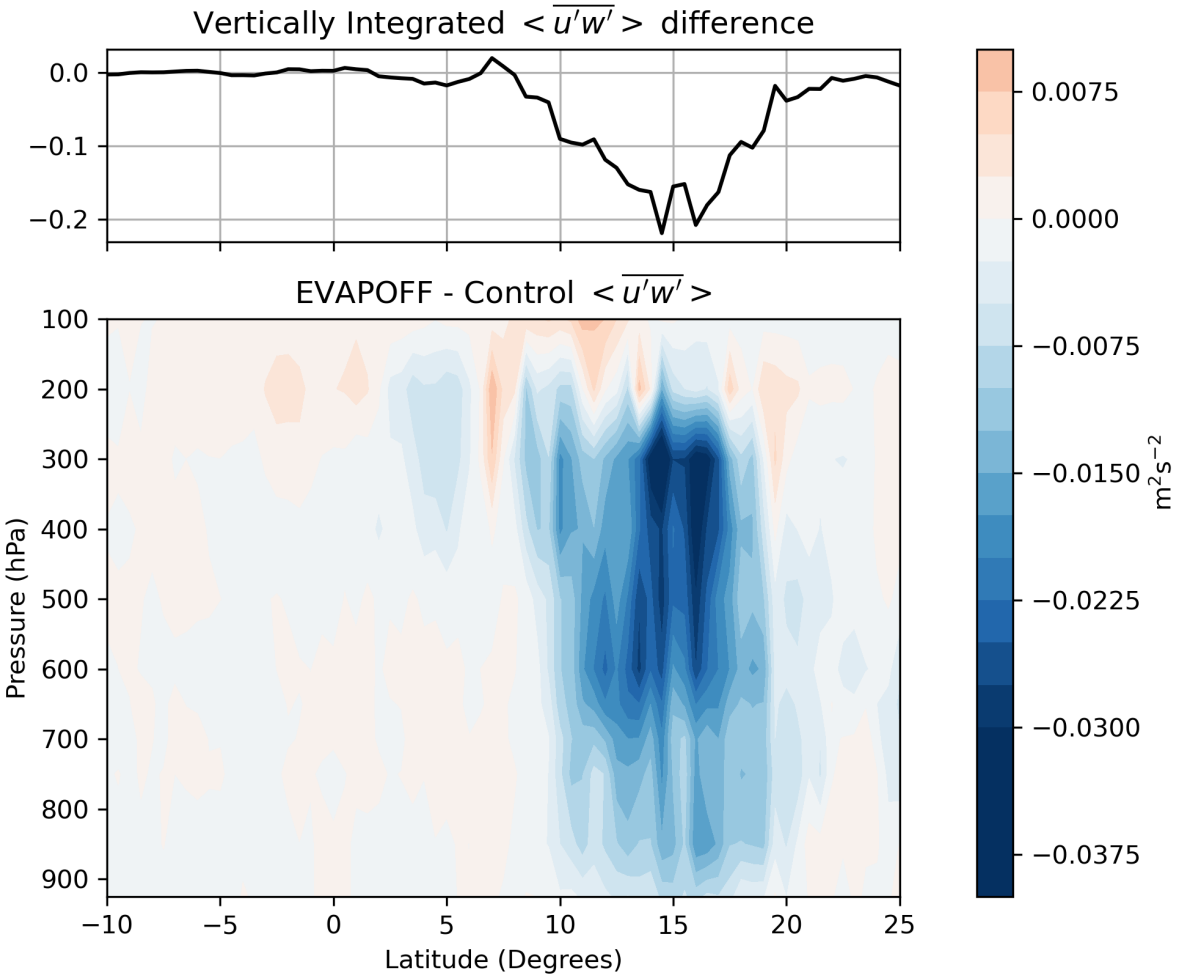
We have shown that aggregate rainfall evaporation significantly cools the Sahel at low levels, and we provide further evidence that outflows from evaporation driven gust fronts transport cool moist air northward into the Sahara, ventilating the heat low. These aggregate thermodynamic effects are at scales large enough to then change the mean synoptic scale flow in crucial components of the monsoon system such as the mid–level easterly flow, and the low–level westerlies. Precipitation itself is non-uniformly redistributed in the absence of its own evaporation; a more complex, coupled response than might be expected in a system without an existing background state. We also show that transient fluxes are systematically shifted or modulated by the evaporation of rainfall, specifically the northward eddy temperature flux and the upward

eddy momentum flux.

Relatively easy interpretation of the results here is possible because the experiment is designed with the exact same domain and boundary conditions as the original Africa LAM configuration (the control run). However this leaves some questions unanswerable, since the boundary conditions obviously do not respond to changes in the internal domain. In reality, the change in circulation within the LAM domain may feedback on the global circulation in some important way that is not possible to replicate with the LAM approach. Questions concerning the impact of boundary conditions, and of nesting generally, in masking potential feedbacks between regionally defined model physics and larger–scale circulations is the subject of the next part of this chapter.



(a) A schematic illustration of the idealized role of tilt in the production of upward westerly eddy momentum flux. The notation u' and w' refers to eddy velocities in the zonal and vertical direction respectively. Net flux here refers to eddy fluxes only.



(b) Difference (EVAPOFF minus control) in zonal and time–mean upward eddy flux of zonal eddy momentum. Zonal means are calculated over 15°E to 20°W.

Figure 5.5

5.2 Part 2: Model hierarchy and distributions of precipitation and moisture

We now shift focus to the second set of overall motivations for this chapter. Part 1 showed an example of resolved mesoscale structure mediating how local model physical processes alter the large scale mean state. The next set of results are concerned with the relative importance of representing such interactions, via resolution and sub–grid physics choices, with respect to other fundamental model design features such as boundary conditions and domain size. The term model hierarchy is used here to describe a tree diagram of connected model configurations, with various combinations of domain, physics, and boundary conditions. Specifically, the following analyses take advantage of the Unified Model K–Scale Hierarchy described in Chapter 3.

A particularly impact–relevant result of part 1 was a model physics dependent structure in two highly coupled fields, precipitation and column moisture. However, part 1 concerns itself only with the mean state, whereas the real impacts of precipitation are highly dependent on variability in time. In addition, because of the chaotic nature of the system and a lack of perfect initial conditions, a free–running model's thermodynamics will always drift from reality over some timescale. There is some limit to predictability therefore in every approach, but better understanding of how model states diverge over given timescales can clarify if additional information is provided by a given modelling approach relative to another. Evaluating the relative roles of model physics and boundary conditions is pertinent in this context.

In the second part of this chapter, we apply simple diagnostics to explore the impacts of model hierarchy on first the characteristic variability of daily precipitation, and second the impact of boundary conditions on the uniqueness and predictability of the moisture field. In the former case the impacts are relatively straightforward; if a model has a poorer representation of variability at some scale, it will provide poorer information for decision making at that scale. The latter analysis is concerned with column moisture distributions; a smoother field than precipitation, permitting a less sensitive quantitative comparison of spatial patterns. In terms of understanding the quality of model information for impact prediction, column moisture is a important proxy because of its inherent coupling to impactful rainfall and humidity extremes.

5.2.1 Lag–1 Autocorrelation of Rainfall in the DYAMOND Summer Period

Autocorrelation across the tropics

In this part of the chapter we show how well the autocorrelation of daily rainfall, and the variability it represents, is captured by models across the K-Scale hierarchy described in chapter 3.1.1. We are specifically interested in the impact on autocorrelation of model resolution, domain size (i.e. boundary conditions), and model physics, and their combination in a given configuration.

We will start by calculating lag–1 autocorrelations across the whole tropical channel (CTC) domain in the DYAMOND Summer period, comparing the results for IMERG rainfall retrievals to the GAL9 global driving model with parametrized convection, and to the RAL3.2 CTC with explicit convection. We calculate two sets of autocorrelations, using both Pearson correlation and Spearman correlation coefficients, which are shown in Figures 5.6 and 5.7 respectively. We calculate all autocorrelations on a common 1° grid, and only where mean daily rainfall is greater than 1mm/hr, as in Spät et al. (2024).

When using a Pearson coefficient, we are assuming a linear relationship between day–0 and day–+1 rainfall and that the daily rainfall rates are normally distributed. In this case, we find as in previous work the same signal of negative IMERG autocorrelation across tropical West and Central Africa, and to a lesser extent in northern South America. The two models, however, show very different areal extents of negative correlation, particularly over Africa. The GAL9 global run clearly has a far smaller fractional coverage of negatively autocorrelated gridpoints in Africa than IMERG. On the other hand, the RAL3.2 CTC more accurately matches the area of negative autocorrelation from IMERG, albeit with lower magnitudes.

The Spearman coefficient assumes only a monotonic relationship and doesn't assume any distribution. Given that daily rainfall distributions can be highly skewed, and knowing that daily extremes are likely in our regions of interest, a Spearman correlation is arguably more appropriate. Comparing Figures 5.6 and 5.7, autocorrelation is generally more positive everywhere when using Spearman coefficients. Therefore using Spearman rather than Pearson shrinks but doesn't remove the regions with negative autocorrelation. Likewise, the higher similarity between IMERG and the CTC over Africa remains when using Spearman, but is perhaps less obvious than in the Pearson case from visual inspection alone.

The above comparison motivates two hypotheses. The first is that increased resolution, and explicit representation of convection, has allowed the RAL3.2 CTC to better represent rainfall variability in Africa over this period. The second is that representing the proper magnitude of variability, as measured by autocorrelation, is impacted by the physics of the global driving model providing boundary conditions. Both these hypotheses can be tested neatly by leveraging the design of the K-Scale model hierarchy and comparing autocorrelation across many configurations.

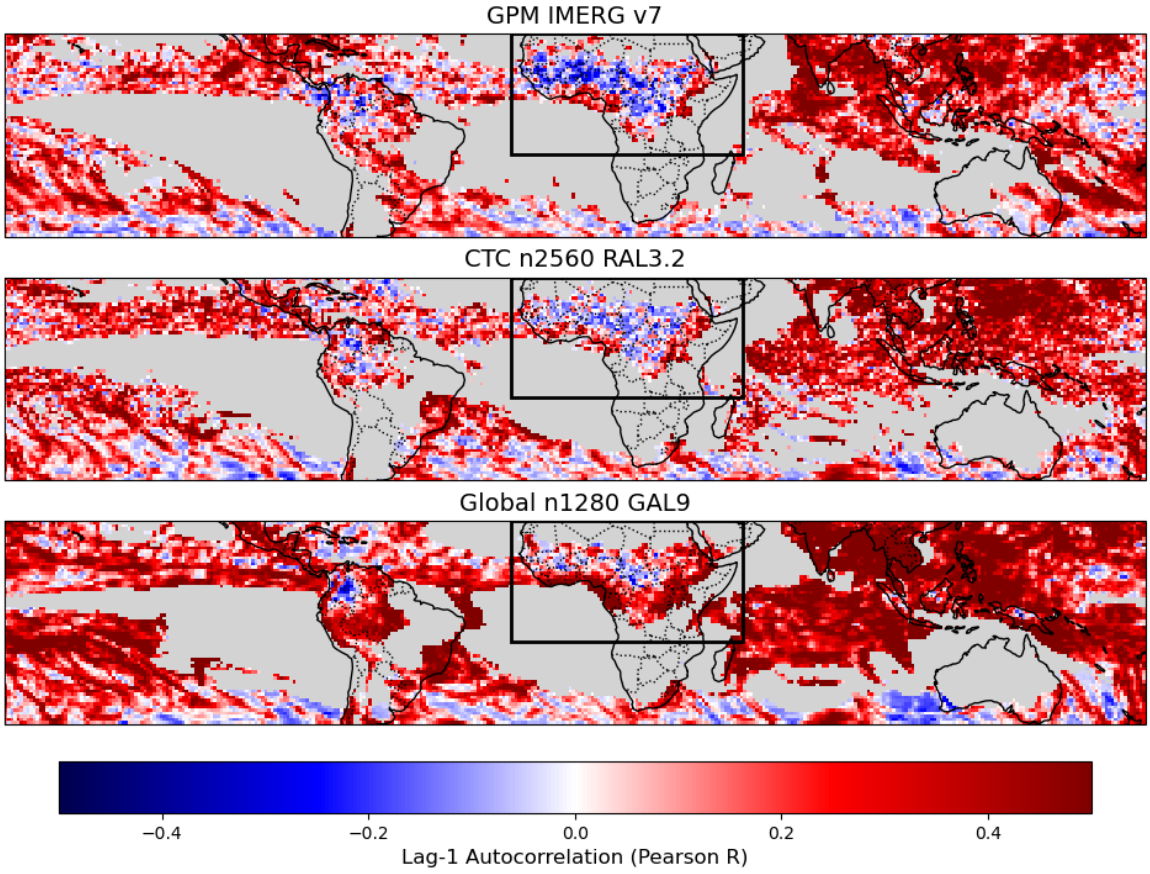


Figure 5.6: Lag–1 autocorrelation of daily rainfall over the DYAMOND Summer period, using Pearson correlation coefficients. Correlations are calculated on a common 0.1° grid, and only shown for where daily mean rainfall is greater than 1mm/day. The black box indicates the Africa LAM domain.

Autocorrelation in Africa across the model hierarchy

The design of the K-Scale hierarchy means that a total of 11 DYAMOND Summer runs include the region of interest in Africa in Section 5.2.2. The smallest of these is the Africa LAM itself, and so we will next compare the characteristics of lag–1 autocorrelation in Africa for each of the 11 setups. These setups are two global runs, six tropical channels, and three LAMs. The

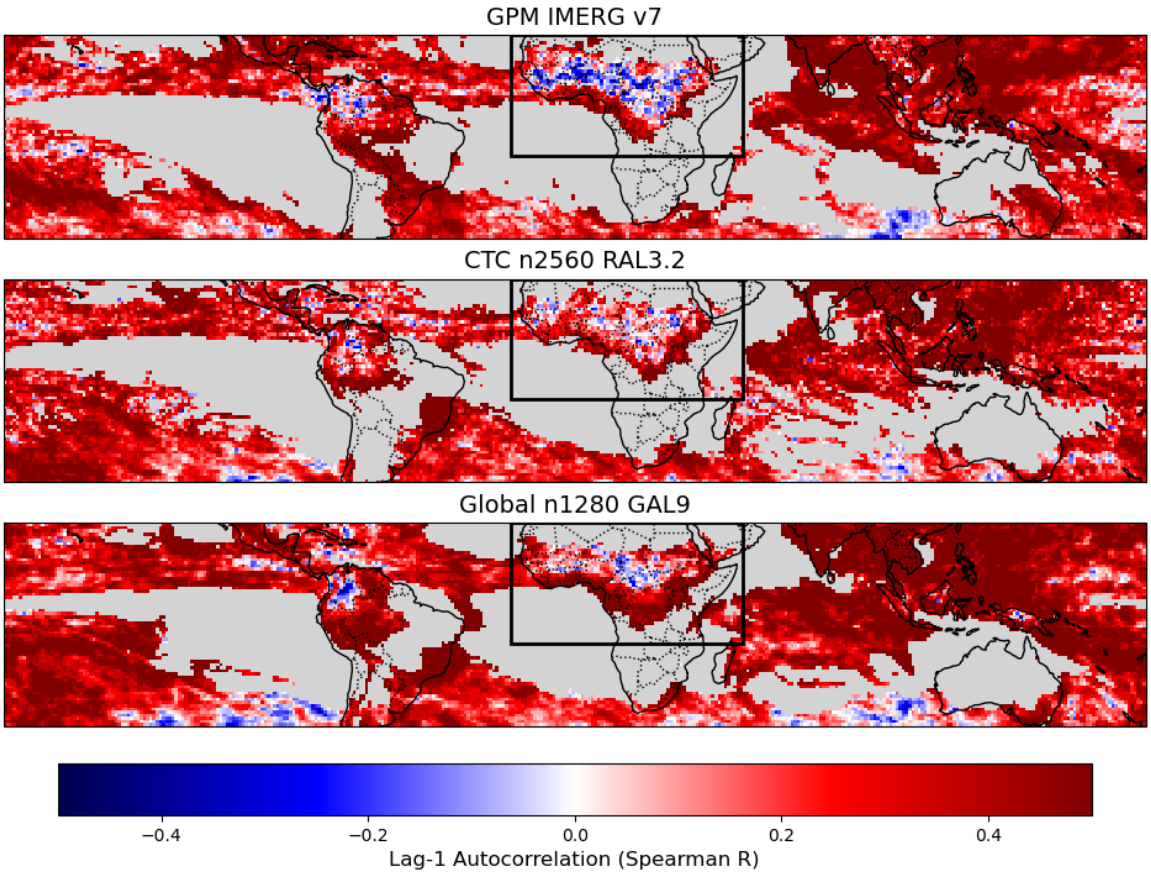


Figure 5.7: As for Figure 5.6, but instead using Spearman's rank correlation coefficients.

four important identifiers for each run are the boundary conditions, the domain, the resolution, and the physics settings. We therefore refer to a given run using short names that reflect these identifiers. For example, gLAM 2.2km RAL3 refers to the LAM domain run at 2.2km using RAL3 physics locally, but with boundary conditions provided by the GAL9 driving model as indicated by the lower case 'g' before LAM or CTC. Similarly, rLAM or rCTC are driven by the global model with RAL3 physics. For grouping runs by driving model, we use the labels 'DMRAL3' or 'DMGAL9' to indicate the driving model of that group.

Figure 5.8 shows the area–mean lag–1 Spearman autocorrelation of rainfall over the Africa LAM domain, as indicated by the black box in 5.7, for all 11 model runs and for IMERG. While all area–means are positive, we assume models with smaller means have proportionally more grid boxes with near–zero or negative autocorrelation. Green bars indicate runs using GAL9 physics, and red bars those using RAL3 physics. Hatching on the bars indicates if the runs are in the DMGAL9 or DMRAL3 group. Firstly, autocorrelation in GAL9 runs (green bars) is larger than in the respective RAL3 equivalent setups. In addition, there is a step change decrease in autocorrelation when moving from the DMGAL9 runs on the left to the DMRAL3

runs on the right. The runs with mean autocorrelation most similar to that for IMERG are those using RAL3 physics for both boundary conditions and internal model physics. Finally, by comparing global runs to CTCs but holding physics constant, we see that a decrease in mean autocorrelation when going from ∼10km to ∼5km resolution only occurs when using GAL9 physics. Besides this, resolution appears to have a much smaller effect than physics or boundary conditions.

For slightly more information, Figure 5.9 shows the zonal mean lag–1 Spearman autocorrelation in the same LAM domain, for each of the models and IMERG. Here, blue lines show the GAL9 runs, and orange lines the RAL3 runs. The driving model is indicated here by solid or dashed lines. Again there is a clear systematic difference between groups of runs, with RAL3 runs more closely following the zonal mean autocorrelation pattern for IMERG (black line). The effect of boundary conditions is less clear, except for in the Sahel latitudes around 10-15°N, where the zonal mean autocorrelation is minimized. Here the DMRAL3 group has systematically lower zonal mean autocorrelation, more in line with IMERG.

The above results indicate that models using physics settings intended to improve the representation of convection can also have a better representation of day–to–day rainfall variability, somewhat regardless of domain size or resolution. In addition, this variability is clearly subject to some control by boundary conditions provided to nested domains. Specifically, this control may primarily come from the meridional boundaries with the extratropics, since the zonal extent of the nested model has little impact on the mean autocorrelation.

The result that explicit convection reduces the mean autocorrelation is consistent with previous work by Spät et al. (2024). In their paper, Spät et al. (2024) go on to connect negative autocorrelation with so–called 'high–frequency' wave modes with periods of around two days. This fits with characteristics of some AEWs, and so the result could be connected to a more realistic simulation of wave–precipitation coupling characteristics with explicit convection. Other work indicates that soil–moisture feedbacks are a mechanism for alternating wet–dry days in the Sahel (Taylor et al., 2013; Moon et al., 2019), feedbacks which are more realistically represented by models with explicit convection. If waves were the mechanism, then our results suggest that wave mode statistics are impacted not only by local model physics, but also by the physics of the driving model providing boundary conditions. To begin a more thorough exploration of this line of reasoning, one might wish to identify which tropical–extratropical interactions

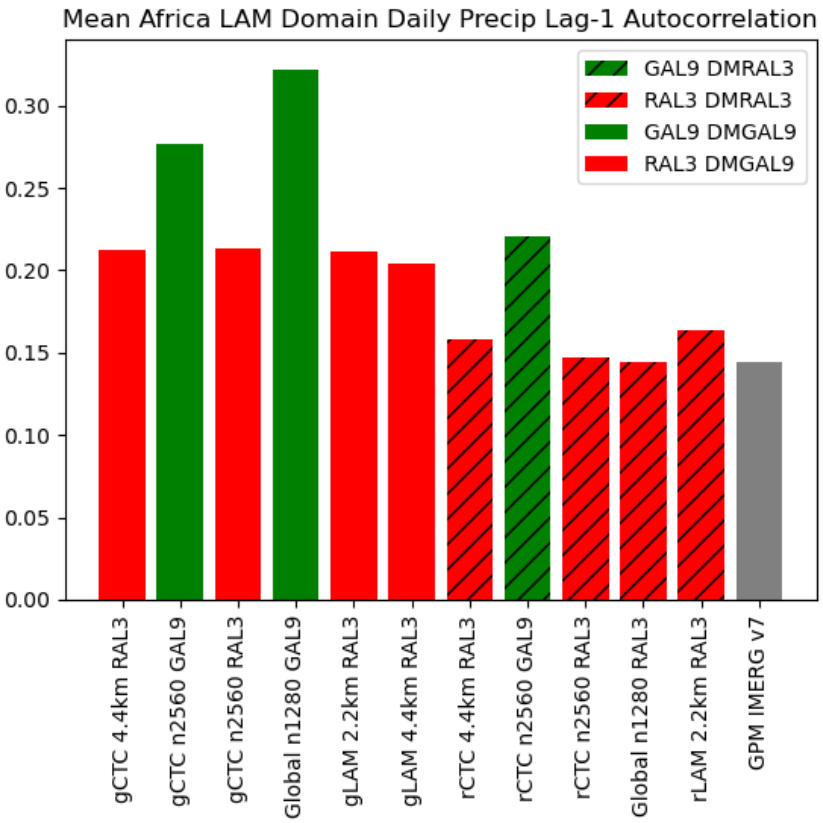


Figure 5.8: Mean lag–1 autocorrelations of daily rainfall over the Africa LAM domain for each model configuration in the K-Scale Hierarchy run over the DYAMOND Summer period. Again, areas where daily mean rainfall is less than 1mm/day are masked and so do not contribute to the mean. Green (GAL9) or red (RAL3) bar colours indicate the configurations internal physics settings, and hatching (RAL3 global driver) or no hatching (GAL9 global driver) indicates the driving model configuration for nested runs. The equivalent mean autocorrelation for GPM IMERG version 7 is also shown in grey.

relate to the relevant instability growth, and show for which model configurations this growth is then suppressed by boundary conditions. Negative daily Autocorrelation could also be a daily extension of mechanisms in Chapter 4, where likelihood of rainfall is lower where it recently rained, to daily timescales.

In the context of forecasting, autocorrelation is not a replacement for forecast skill. However, the results here do indicate that for this kind of daily variability, at least in Africa and over this period, the larger domain higher resolution runs provide little benefit over the more conventionally sized LAMs when they are both driven by the same global model. Resolution increases here also do not necessarily constitute a good return on resources with respect to this metric, or even a monotonic improvement. Those looking to improve forecasting in the African region, with respect to daily scale variability, should remain focused on model physics realism and possibly on mitigating the inherently limited representation of extratropical interactions in one–way nested

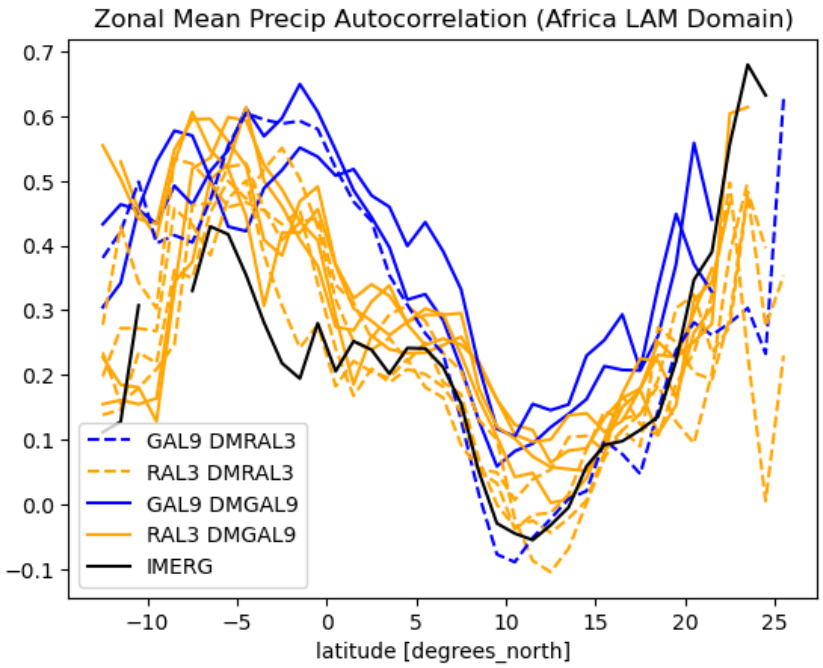


Figure 5.9: As for Figure 5.8, but expanded to show the zonal mean lag–1 autocorrelation of daily rainfall over the Africa LAM domain. Again colour indicates the model physics settings, while solid (or dashed) lines indicate if run has GAL9 (or RAL3) boundary conditions. Individual configurations are not labelled here. The zonal mean lag–1 autocorrelation for IMERG retrievals is shown now by the black line.

models.

5.2.2 Decorrelation of Total Column Vapour

Decorrelation from the driving model

A reasonable hypothesis is that TCV in smaller LAM configurations remains more closely correlated to driving model TCV than for larger pan–tropical runs which allow for independent zonal mode propagation and zonal circulatory feedbacks. Here we test this expectation by calculating decorrelation between nested runs and their drivers. We then further quantify some predictability implications by calculating decorrelation of nested and global setups from reanalysis.

Figure 5.10 shows time series of spatial correlation between model TCV fields at 3–hourly timesteps. Correlations are shown between each pair from the 4.4km CTC and LAM configurations and the ∼10km global driving model, using data only from the LAM domain regridded to a common 0.1° grid. In this context, we use only the GAL9 global model, and a subset of the nested models driven by it. This decorrelation analysis is performed over three LAM

domains, in DYAMOND Summer and Winter for Africa and South America respectively, and both seasons in the South–East Asia (SEA) domain.

Blue lines in each panel of Figure 5.10 show correlations of the LAMs with the driving model in their respective regional domains. In all panels, there is an initial decorrelation period, ranging from a few days to around two weeks depending on domain and season. Over the 40 day simulation period however, the correlations between LAM and driver never fall below 0.9 in any domains. In both the continental LAM domains, Africa and South America, the initial decorrelation period is 7-10 days in length before correlation levels off between 0.9 and 0.95. In the SEA domain in DYAMOND Summer, the decorrelation period is longer at around 15 days, and there is some slow fluctuation through the simulation again ranging between 0.9 and 0.95. In DYAMOND Winter, the SEA domain decorrelates more quickly, levels off earlier, before again exhibiting slow fluctuation. Note that all the correlations between LAM and driver show clear diurnal variation.

Orange lines in Figure 5.10 show time series of correlation between the global driver and the CTC, but still for just within the LAM boundaries. This allows us to show how the 'local' regional TCV field can evolve more independently when the nested domain is pan–tropical. In this case, the period of initial decorrelation varies greatly between regions. In SEA, this period is again 15 days or more, with correlation decreasing and fluctuating around 0.8 to 0.85. In South America, the initial decorrelation period is relatively rapid, taking around 3 days to drop to 0.8, followed by slow fluctuations between 0.75 and 0.9 and a large diurnal amplitude. For Africa, 7-10 days of initial decorrelation to almost 0.85 is followed by fluctuations between 0.8 and 0.9 with periods also 7-10 days.

Finally, green lines in Figure 5.10 show the correlation between the CTC and the LAM. These largely follow the orange lines, indicating the CTC evolves almost as distinctly from the LAM as it does the global driver, despite the common resolution and physics between the two nested models. More closely comparing green to orange however, there is slightly slower initial decorrelation then some independent variability later in the simulations in the Summer SEA and South America domains.

Overall, it is clear that the TCV field in the LAMs remains very close to the driving model's TCV structure. There is a second but much smaller signal of the shared local physics between the nested configurations, where they are initially slightly more correlated to each other than



Figure 5.10: 3–hourly correlations between models' total column vapour (TCV) fields in LAM domains, on a common 0.1° grid. Correlations are calculated using Pearson correlation coefficients. The acronyms DS and DW refer to the DYAMOND Summer and Winter periods respectively. The labels 'glob10', 'CTC4p4', and '*_LAM4p4' refer to the GAL9 global, 4.4km CTC, and the 4.4km LAM configurations respectively.

the CTC to the global driver. On the whole however, the dominant difference in decorrelation is domain size i.e. boundary conditions. This implies that changing local physics in a regional domain has very limited power to change the moisture structure inherited from the global models circulation.

While the representation of some given convection in a given regional structure may be improved by model physics alone, predicting long term evolution in that structure relies on convective couplings beyond the boundaries; couplings which we know are weaker for models with parametrized convection. To quantify this, we next examine the extent to which dependence on physics and boundary conditions limits predictability of the TCV field. We do this by correlating each of the three configurations with ERA5 reanalysis, now regridded to the 0.25° ERA5 grid.

Decorrelation from reanalysis

In all configurations in the K-Scale Hierarchy, the model is initialised from a global reanalysis dataset that assimilates observations similarly to ERA5. As such, the TCV spatial pattern in the models and ERA5 is approximately the same at the initialisation time. We proceed on the basis that models start very close to ERA5, and over some period of time drift away from the approximate reality of reanalysis, as indicated by decorrelation of the TCV field. The first timestep of available output is at +3hr, so the first correlation shown will be close to but not exactly one. Taking reanalysis as an approximate ground truth, a slower decorrelation here therefore represents a simple diagnostic proxy for better predictions of the evolution of the column moisture field.

In Figure 5.11, TCV in all configurations decorrelates approximately equally from ERA5 TCV for an initial period. The length of this initial decorrelation period is approximately the same for each region as in Figure 5.10. After this however, there is a second period where the CTC model is more correlated to ERA5 than either of the other configurations. This higher correlation with the CTC is sustained for varying amounts of time in each region, including for the remainder of the simulation in SEA DYAMOND Winter.

Also apparent after the initial decorrelation period are a series of oscillations in the correlation strength, with varying periods depending on the domain size. For example, in the SEA domain in DYAMOND winter all models have a long decorrelation period followed by similarly paced increases and decreases in correlation around a value of approximately 0.7. The variability in all correlations in February in SEA resemble a relatively slow mode of atmospheric variability with a period of around 20 days. Oscillations where the LAM domain TCV becomes more and less correlated with ERA5 suggest there are large–scale forcings in both models and reanalysis that temporarily move the moisture field closer to reanalysis. One candidate for this is SST variability, given that the SSTs are prescribed from an ocean analysis/observation dataset in both reanalysis and the models and so will be very similar.

The extent to which the LAM follows the global driver, now in the context of their respective similarities to ERA5, also varies by domain. In South America and in SEA in February, the correlations of ERA5 with LAM and global models are always very similar. In the African domain however, the LAM spends more time less correlated to ERA5 than its driving model. Overall, it appears the LAMs do inherit the predictability limitations of their driving models to

a greater extent than the CTC does. One–way boundaries in a small zonal extent of the tropics may also be detrimental for predictability in some contexts, to an extent that outweighs the benefits of higher resolution and better model physics.

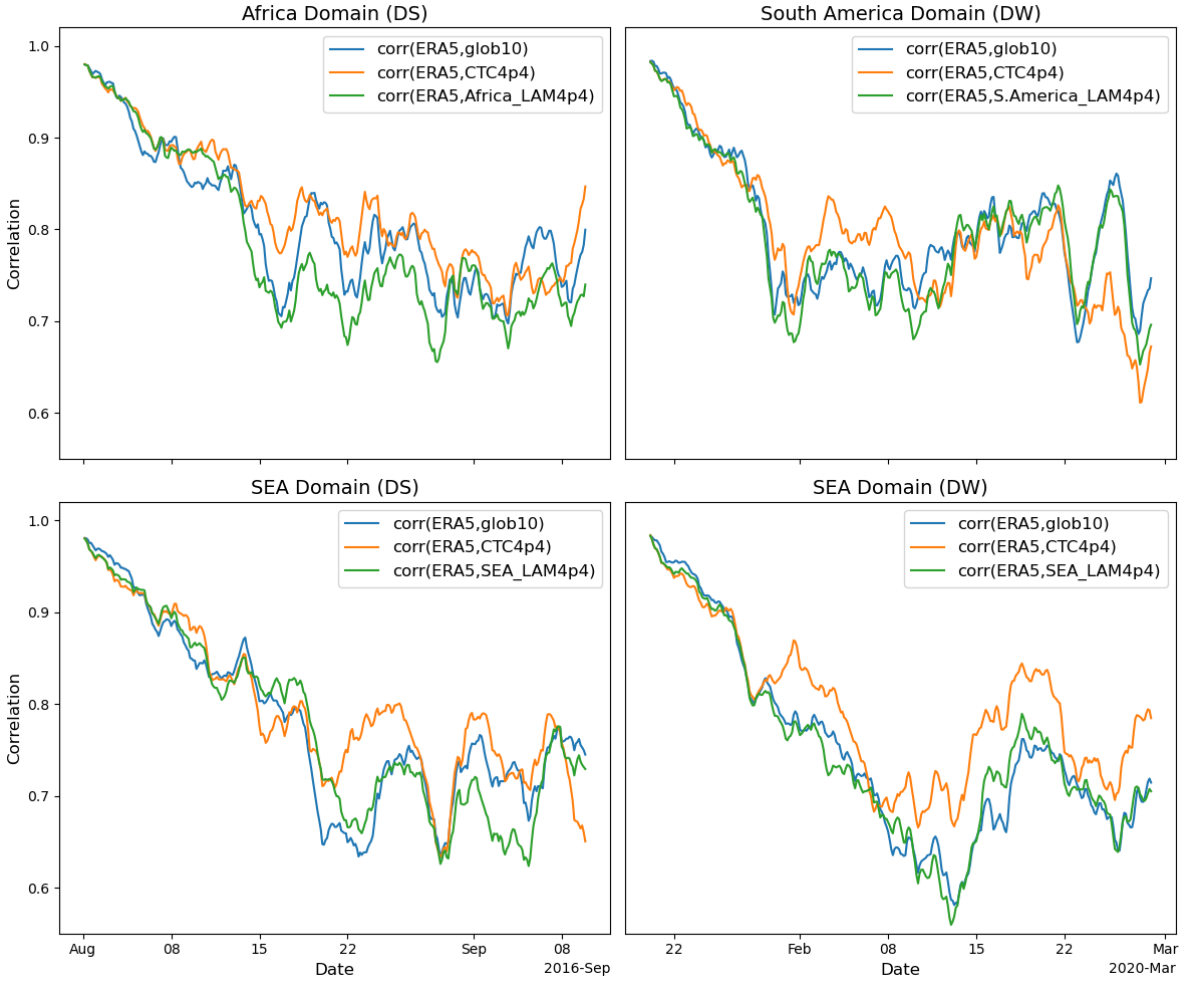


Figure 5.11: As for Figure 5.10, but now showing correlations between model and ERA5 reanalysis TCV for the same domain and period.

5.2.3 Summary of Part 2

In part 2 of this chapter, we have utilised the design of the K-Scale modelling hierarchy to explore the relative impacts of boundary conditions and model physics on simple diagnostics of rainfall variability and atmospheric moisture structure in limited area domains of the tropics. The chosen diagnostics, autocorrelation of rainfall and decorrelation of column vapour, are simple but have been used in previous work to achieve similar model evaluation aims.

The first comparison of rainfall autocorrelations was between the GAL9 global configuration with parametrized convection and the RAL3 CTC with explicit convection. We found that

explicit convection in the tropics brings autocorrelations closer to those observed in satellite retrieval data, in agreement with previous work by Spät et al. (2024). Also as in previous studies, Tropical Africa in the Boreal Summer is a hotspot for negative autocorrelation which represents a different type of daily variability from that found in the majority of the tropics. This negative autocorrelation indicates the high occurrence of alternating wet–dry days, and has been associated in the literature with propagating wave modes and potential land surface feedbacks. Focussing then on the mean autocorrelation over the Africa LAM domain, we find using RAL3 physics lowers mean autocorrelation compared to equivalent configurations with GAL9 physics. We also find that the global model with RAL3 physics, and the nested models driven by it, have mean autocorrelations closer to observations. Domain size and resolution affect autocorrelation much less than the model physics used in both nested or driving model. However, a dependence in particular on meridional boundary conditions indicates possible improvements to model rainfall variability when convection in extratropical interaction is resolved explicitly.

The decorrelation analysis of column moisture here shows that the structure of models' moisture fields diverge from each other and from reanalysis differently depending on multiple aspects of model configuration. Principally, we have confirmed the hypothesis that moisture structure in limited tropical domains remains measurably closer to the global driving model than in a pan–tropical domain. We find that the limited area approach bestows no clear benefit to predicting regional moisture evolution over the global model, as measured by decorrelation from reanalysis. In contrast, moisture in the pan–tropical domain with explicit convection stays more closely correlated with reanalysis for longer, especially in the Austral Summer in South–East Asia domain. Future analysis of this kind would benefit from including different initialisations throughout the year, targeted domain size changes to include/exclude certain geographic features, and potentially repeating the analysis with coupled runs to allow for independent ocean–atmosphere interactions to further decorrelate the models from each other.

5.3 Conclusions and Discussion

From part 1 of this chapter, the key insight for future model development is that cold–pools and their origin in convective storms need to be well–represented or there is a risk of errors at much larger scales. Switching off a model process, while holding all else constant, is a powerfully

simple demonstration of the upscale effects of the removed process.

However, the EVAPOFF experiment is a very unrealistic realisation of the atmosphere – rain does evaporate in reality, and cold–pools really do exist as a result. The experiment is representative of the most extreme case of poor process representation. The assumption made, in order for the key insight above to be meaningful, is that other models with various model physics choices necessarily sit somewhere on the spectrum from the experiment to the real world. Here we have learnt only about the upscale impact of the cold–pools in the particular model configuration used. We assume that this importance transfers to both other models and to the real world, but we haven't explicitly shown it to be so.

In addition, because we have only one realisation of the experiment, our attribution of the differences in the mean states to cold–pool mechanisms relies heavily on physical reasoning and interpretation. A much smaller change to model physics may lead to similar magnitude differences after 30-40 days of simulation, or the results may be contradictory from another identical experiment but with different initial conditions. A more robust experiment therefore, which should certainly be considered if extending to longer timescales, would be to use an ensemble of models with a full range of both initial conditions and perturbed rainfall evaporation parameters.

The analysis in Part 2 is distinct from Part 1 in its strategy for model process evaluation. Part 1 deliberately suppresses realism at one scale and measures the impact at another scale. Part 2, in contrast, compares the larger scale patterns in multiple configurations that all attempt to maximise realism but use different modelling approaches (e.g. one–way nesting). The limitation here is that different modelling approaches necessitate having multiple and complicated differences between model configurations that confound any simple interpretation of process–level changes.

Both parts of this chapter are extensions of the ideas in Chapter 4 to larger scales; part 1 aggregates cold–pool effects beyond the mesoscale to regional circulation, and part 2 includes regional scale perspectives on lagged rainfall–rainfall correlations. In positioning the two parts together in the thesis, the intention is to first highlight the interconnection of process understanding and model evaluation. In Part 2 we showed examples where model physics related to convection, amongst other modelling choices, has the most influence on the large–scale diagnostics under assessment. This statement is supported at the process–level by the results of Part 1, and in

previous studies documenting improvements in model processes.

Process understanding does not always directly translate to improvements in all possible real–world applications. There will always be limits due to the resource intensity of the desired level of process realism. Realism of a given process, and the associated expenditure of resources, may be unnecessary in some contexts and not others. What process–understanding does always provide however, is confidence that a model is realistic because of realistic mechanisms. Confidence at the process–level transfers in particular to confidence in projections at the longer timescales (Baumberger et al., 2017; Doblas-Reyes et al., 2021). In the next chapter, we will explore how an observed relationship between spatial patterns of convection and interannual variability arises differently in two models with different representations of convection.

Chapter 6

Convective Clustering and Radiation Budgets in Regional Climate Simulations for Africa

The moisture dynamics and radiative feedbacks associated with deep convection in the tropical atmosphere play an important role in the energy budget of the Earth. However, the relationship of convection's spatial patterns to radiation, and the implications for climate uncertainty, are not yet fully understood (Tobin et al., 2012; Mauritsen and Stevens, 2015; Bläckberg and Singh, 2022). Recent work by Bony et al. (2020) shows that the spatial clustering of tropical convection is strongly associated with changes to the radiation budget at the global scale. This finding agrees with idealized radiative-convective equilibrium (RCE) modelling studies of the present climate (Muller and Held, 2012; Emanuel et al., 2014; Wing et al., 2017, 2020). The impacts of convective clustering on model radiation budgets have also been documented in a warmer mean state (Posselt et al., 2012; Wing, 2019; Zhang and Fueglistaler, 2019; Hartmann et al., 2019).

The physical mechanisms connecting convective clustering to radiation are complex and many (Wing and Emanuel, 2014). One commonly discussed mechanism for clustering of convection is the growth of dry and moist patches in the atmosphere via radiative feedbacks and associated mesoscale circulations (Bretherton et al., 2005; Muller and Held, 2012). The feedback most associated with clustering in both RCE experiments and observations is the drying of the free–troposphere in the non–convecting part of the domain (Tobin et al., 2012; Wing et al., 2017).

The result is a correlation between clustering of convection and a drier mean state. A drier free–troposphere is more transparent to longwave radiation and makes cloud less likely, and so there is a positive correlation between clustering and longwave cooling to space.

A negative correlation between net–TOA and measured clustering was demonstrated by Bony et al. (2020), using satellite observations at interannual timescales. They also found the positive correlation between clustering and mean drying, and the associated clear–sky longwave cooling. Importantly, the relationship found between clustering and net-TOA was independent of cloud–fraction, highlighting again that emergent spatial structure is coupled to the large–scale state beyond simple summations of parts.

Previous studies of convective clustering have focused on the tropical oceans in either observations or idealized simulations. The observational study by Bony et al. (2020) considers the whole region between 30° S and 30° N, but again this is more than 70% ocean. To determine if the same results can be found over land in particular, here we choose to investigate the clustering–radiation relationship over a mostly continental domain. Specifically, the largest landmass in the tropics, the African continent. Organised convection is abundant in Africa and is the dominant source of precipitation. We measure the clustering of convection in regional climate models of tropical Africa and compare this to observations. Similarly to Bony et al. (2020), we fit relationships between anomalies in the clustering and anomalies in the radiation budget. We determine if the same relationship and mechanism is measurable over the modelled African domain, as for the mean of the whole observed tropics, the latter of which is mostly ocean where mechanisms may differ.

We can also compare model radiation budget responses to convective clustering in both present and future climates, and between runs with explicit and parametrized convection. This addresses uncertainties in climate projections due to the representation of convection (Stevens and Bony, 2013; Bony et al., 2015). A more accurate representation of the observed relationship between organisation and radiation anomalies would further support the case for explicit convection in climate change simulations going forward (Stevens et al., 2019; Takayabu et al., 2022), or support arguments for developing better representations of organisation in future parameterizations.

6.1 Data and Methods

In this chapter we use model data from the CP4A project, as in Chapter 4. As a reminder, this includes four 10–year model runs over the African continent, two in a present climate and two in a future scenario. In each climate, 4.4km (CP4) and 25km (P25) runs were performed, with explicit and parametrized convection respectively. See Chapter 3.1.1 for further details of the simulations. For observations of convective clustering, we use the GridSat B1 infrared brightness temperature product described in Chapter 3.1.2.

Here there are no model outputs directly equivalent to Gridsat brightness temperature, so we instead identify deep convection in the models using 3-hourly outgoing longwave radiation (OLR). For Gridsat, we use a threshold of $T_b < 240$K to be a deep convective event as in Bony et al. (2020). Based on empirical conversions in Ohring et al. (1984), this is approximately OLR < 160 Wm^{-2} for the model data.

For fair comparison, we also regrid the CP4 and GridSat data onto the same 25km grid used by P25. Adjacent cells below the threshold are not likely to be part of the same updraft on the 25km grid so local minima calculation has not been used here. At the 25km scale, each grid cell below the threshold can represent multiple individual convective clouds, which may in turn be part of a larger system such as mesoscale convective systems (MCS). We are therefore only able to measure the level of clustering at scales beyond 25km using the resulting map of points. Importantly, this includes not only MCS but also larger-scale structures such as equatorial waves or similar synoptic scale convergence features.

To measure the degree of clustering in the domain at each model timestep we use the L_{org} index described in Chapter 3.2.2. We calculate 3-hourly L_{org} values, then collate them into a monthly time–series where each datapoint is the mean of a month's worth of 3–hourly L_{org} values. It is important to remember that these monthly means are not quantifying monthly mean OLR patterns but instantaneous patterns, since L_{org} is first calculated from snapshots of the OLR field, and then the means are taken. There is no smoothing or mean–taking of the cloud structures themselves beyond the required regridding to 25km.

The L_{org} index is similar to the index I_{org} used by Bony et al. (2020), but importantly L_{org} responds to changes in multi-scale structures in a way I_{org} cannot (see chapter 3). As such, L_{org} will allow us to compare clustering scale information between models, including how those

scales vary with the diurnal cycle. We know that these models have different diurnal cycles of convection, with implications for radiation budgets via differences in the phasing of cloud and incoming solar radiation. Mean diurnal cycle differences in clustering would likely constitute a significant link in the chain of mechanisms connecting differences in sub–grid physics to differences in the models' mean clustering–radiation relationships.

For observations of the radiation budget, we use monthly CERES EBAF TOA data (see chapter 3.1.2). Note that model data are from the 9 years 1998-2006, but the observations are from 2001-2009, since full year records from CERES are available only from 2001 onwards.

6.2 Measuring organisation of convection in regional climate models

6.2.1 Means, variability, and scales in the clustering index

Figure 6.1 shows characteristics of the mean L_{org} indices for each of the four model runs and for observations. Firstly, the left panel shows the mean normalized Besag's L–functions from which the index is derived (see chapter 3). In addition to the L–functions estimated from data, notated $\hat{L} = \hat{L}(R)$, the grey dotted line shows the L–function for a homogeneous Poisson process, which we shall refer to henceforth as just L. Note that $L(R)$=R for all R, and represents the expected result from a random pattern of convection.

The shape of all the $\hat{L}$ here indicates that all four runs and observations have convection more closely clustered than expected from a random pattern up to scales of approximately $0.7R_{max}$, and more regularly distributed than randomness above this scale. The dimensions of the domain used at 25km resolution is 256 × 256 gridpoints, which means $R_{max} = 236 \times 25km = 5900km$, so the crossover scale is ∼4000km. Below the crossover scale, CP4 and GridSat $\hat{L}$ are indistinguishable. The values of both P25 $\hat{L}$ curves here are larger than for observations and CP4, indicating slightly more clustering at those scales.

The index L_{org} is calculated as the integrated difference between the estimated L-function curves and the $L = R$ line representing randomness. While the absolute value of the mean index for a given model run is somewhat uninformative on its own, relative values and analysis of anomalies allow for comparison of the clustering between models and climates. In the centre panel of Figure 6.1, we see that P25 has a higher value of L_{org} in both climates, and a larger

increase between present and future at 10% versus a 3.4% increase in CP4. Both present climates have mean L_{org} close to that calculated from observations.

The right panel of Figure 6.1 shows kernel density estimates (i.e. estimated PDFs) of the monthly anomalies in L_{org} for each model run and for observations. In the present climate, both the models have larger variances in monthly anomalies than in observations. In the future climate, the difference between models is amplified, and the anomalies in CP4 L_{org} become more tightly distributed around zero, closer to the observations in the present climate. The climate change in the distribution of P25 L_{org} anomalies shows no equivalently clear reduction in variability.

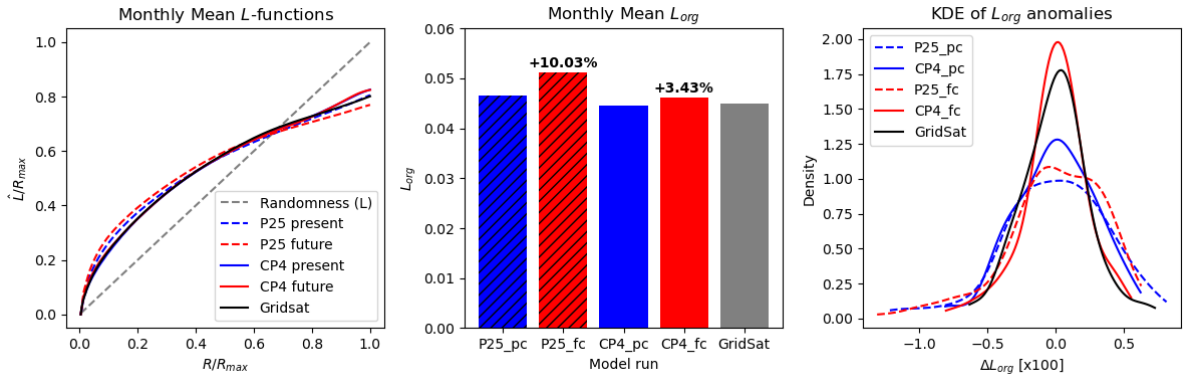


Figure 6.1: Estimated L–functions (left) used for calculating the mean L_{org} (centre). Estimated PDFs of monthly anomalies in L_{org} (right); anomalies are calculated after deseasonalizing each monthly time series and removing linear trends.

To better understand how the models differ, we need some physical interpretation of the scale information that the L_{org} calculation process confers. Firstly, the crossover scale from clustered to regular in Figure 6.1 makes sense in the context of the overall domain size, given that convection is broadly structured by the migrating rain bands and regional wet–seasons. At larger scales approaching the continental, the domain is simply split into a rainy part (entire regions in wet season) and a dry part (regions in dry season or subtropical zones). Hence, the L-function can only identify 'clusters' at or smaller than rainband/regional rains scale. We are, however, most interested in sub–structure of the parts of the domain with convection. These scales are where the complexities of mesoscale organisation or convective coupling in synoptic waves manifest. It is these smaller scales at which organisation is defined in Bony et al. (2020), and the relationship between clustering at these scales and the radiation budget is the primary concern of their paper and this chapter.

6.2.2 Diurnal cycles in the clustering index and clustering scales

It is well known from previous studies, including those using the same models as here, that explicit and parametrized convection lead to different diurnal cycles (Prein et al., 2015). Generally speaking, parametrized convection tends to initiate too much convection too early in the day. Parameterization has also been shown to affect the lifecycle of organised storms, including their nocturnal maintenance (Crook et al., 2019).

Studies such as Haerter et al. (2020) and Goswami et al. (2026) examine the impact of a diurnal cycle on measures of convective clustering, but only for idealized cycles and domains. Furthermore, while Bony et al. (2015) acknowledge that the diurnal cycle is a dominant mode of variability in clustering, they do not quantify its shape or amplitude. Here we compare the model's diurnal cycles in L_{org} and the L–function, to quantify if their spatial patterns of convection have distinct cycles from each other and from observations.

Figure 6.2 shows the mean diurnal cycle of the L_{org} index in all four runs and in observations. Comparing first the present climates, we see that both models have similar mean values of the index during the day and evening, from 12 to 21 UTC. Overnight, L_{org} stays approximately the same for P25 if not increasing slightly, while in CP4 the index drops by around 10%. This is consistent with the larger overall mean value of present climate L_{org} in P25 results from Figure 6.1. In the present climate therefore, it appears CP4 has a much clearer diurnal cycle in L_{org} that is absent in P25. However, compared to observations it is still not clear which model diurnal cycle is more realistic.

A more striking difference is how the two models' cycles change distinctly in the future climate. While the index increases evenly across the diurnal cycle in P25, only the overnight portion of the cycle appears affected in CP4. The mean daytime values of L_{org} in CP4 barely change between climates. This difference between a uniform increase and a diurnally dependant increase is also consistent with the larger overall mean L_{org} change in P25.

The representation of convection, via resolution and model physics choices, somehow affects the diurnal cycle in patterns of convection and changes to that cycle in a warmer future climate. Relating these L_{org} cycle differences to known model process differences is non–trivial however, due to the contributions of many scales to the index.

Bony et al. (2020) also do not quantify any temporal variability in the contributions of different

scales to their clustering index, including diurnal variability. Real mesoscale storm organisation is strongly diurnal especially over land (e.g. Crook et al. (2019)). We therefore move in the direction of a physical interpretation for the model differences in Figure 6.2 by examining diurnal cycles of clustering separately for each scale. We do this by comparing how much the L–function deviates from randomness at each scale and time of day.

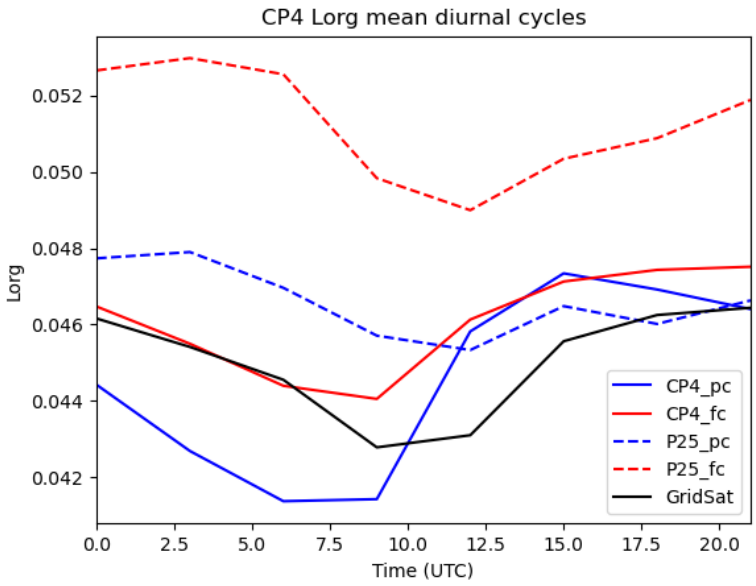


Figure 6.2: Mean diurnal cycles of L_{org}. Present climates model runs are in blue, future climates are in red. Solid lines are CP4 and dashed are P25. The black line is observations.

Figure 6.3 shows values of $(\hat{L} - L)/R_{max}$, plotted for scales R/R_{max} on the x-axis and for time of day on the y-axis. As in the one–dimensional L–functions, all runs have more clustered convection than random at scales below the crossover scale, indicated by blue shading. The sign of $(\hat{L} - L)$ appears to be dominantly a function of R and not of time of day. However, the two models show different behaviour in how the scales with largest $(\hat{L} - L)$ values change throughout the day.

In CP4, in both present and future climates, the scales of maximized $\hat{L} - L$ are between 0.1 and $0.2R_{max}$ from midnight to 9Z. Between 9Z and 12Z, the scales of largest $\hat{L} - L$ scales shift to between 0.2 and $0.3R_{max}$ where they remain for the rest of the day. A similar shifting of maximum clustering scales is also clear in the observations, but is entirely absent in P25 in both climates. In P25, the largest $\hat{L} - L$ values remain in the 0.1 to $0.2R_{max}$ range, with some variation in magnitude, throughout the diurnal cycle.

Relative to R_{max} of 5900km, the diurnal shift in $\hat{L} - L$ indicates that the most significant

clustering scales in CP4 and observations alternate from larger mesoscales (500-1000km) to synoptic scales (1200-1800km) during the diurnal cycle. The lack of shift in P25 indicates that scales of clustering are not so clearly a function of time of day. In addition, the model differences in future change to the mean diurnal L_{org} cycle are similar to the changes seen in the $(\hat{L} - L)$ magnitudes at the mesoscales. Where CP4 L_{org} increases overnight in the future climate, the mesoscale $(\hat{L} - L)$ also shows an increase between climates in Figure 6.3. Likewise in P25, the mesoscale (and some synoptic) clustering increases across the whole cycle, as does overall L_{org}.

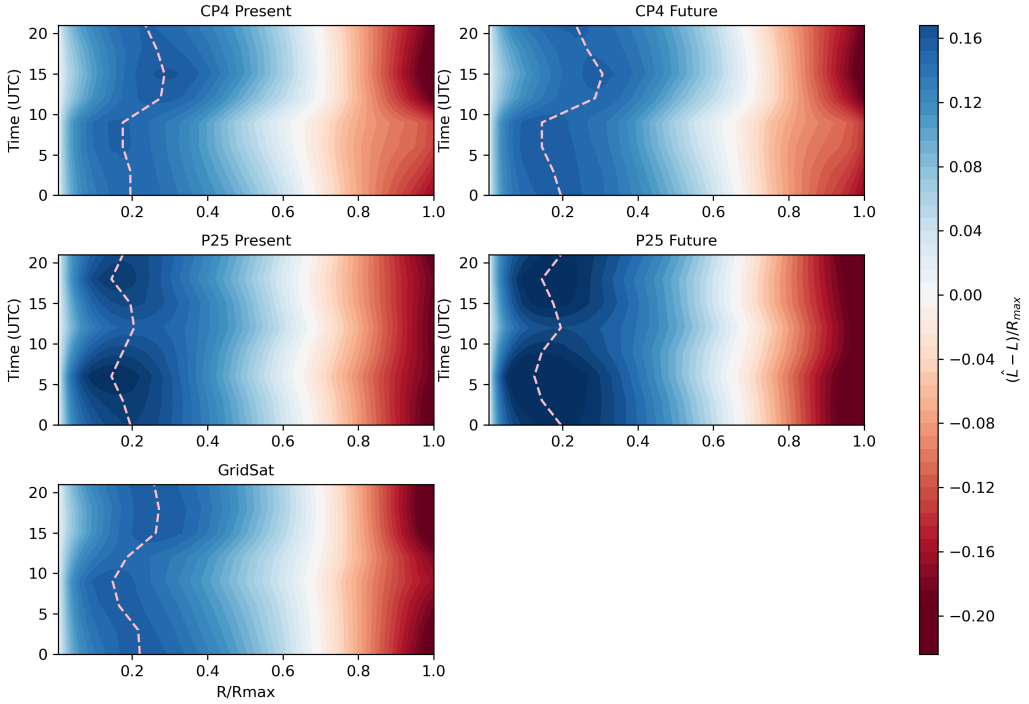


Figure 6.3: Mean diurnal cycles of $(\hat{L} - L)/R_{max}$ for each model run and for observations. Shaded contours shows values as a function of both normalized scale R/R_{max} and time of day. The white dotted line in each panel indicates the scale where $(\hat{L} - L)$ is maximised throughout the diurnal cycle.

6.2.3 Response of model clustering to warming as a function of scale

To compare the climate change in clustering at each set of scales more directly, Figure 6.4 shows the difference between the right and left columns of Figure 6.3 for each model. This is the climate change in $(\hat{L} - L)/R_{max}$, and so now blue (red) colours indicate which scales exhibit more (less) clustering in the future climate, and therefore which scales contribute more positively (negatively) to L_{org} and its future diurnal cycle. Change is now plotted against time of day and R rather than R/R_{max} to increase physical interpretability.

For scales larger than around 1000km, the sign of climate change in CP4 ($\hat{L}-L$) changes over the diurnal cycle. These sign changes must approximately cancel each other out for larger scales to give the overall mean L–function change seen at those scales in Figure 6.1. The only significant climate changes in the CP4 mean L–function are for scales smaller than 1000km, where the climate change is positive throughout the diurnal cycle with a clear overnight maxima in both magnitude and scale range. This is more clear when limiting the y–axis to only scales less than 1000km, as shown in the right column of Figure 6.4. With this zoomed in view of the mesoscales, we can see the $(\hat{L}-L)$ climate change is maximised at midnight at around 200-500km in scale, and minimized for this scale range at 15-18Z.

Climate change of $(\hat{L}-L)$ in P25, however, is very different, with no pattern of sign changes at any scale. Instead the scales that are on average more clustered in the present climate simply get more clustered and vice versa, as in the mean change in Figure 6.1. There is some diurnal variation in the magnitude of the change if not the sign, with overnight magnitudes being larger. As in CP4, increases in $(\hat{L}-L)$ are largest at the mesoscales. Zooming in on the P25 mesoscales shows that clustering increases are maximised at similar scales as in CP4, but twice rather than once in the diurnal cycle.

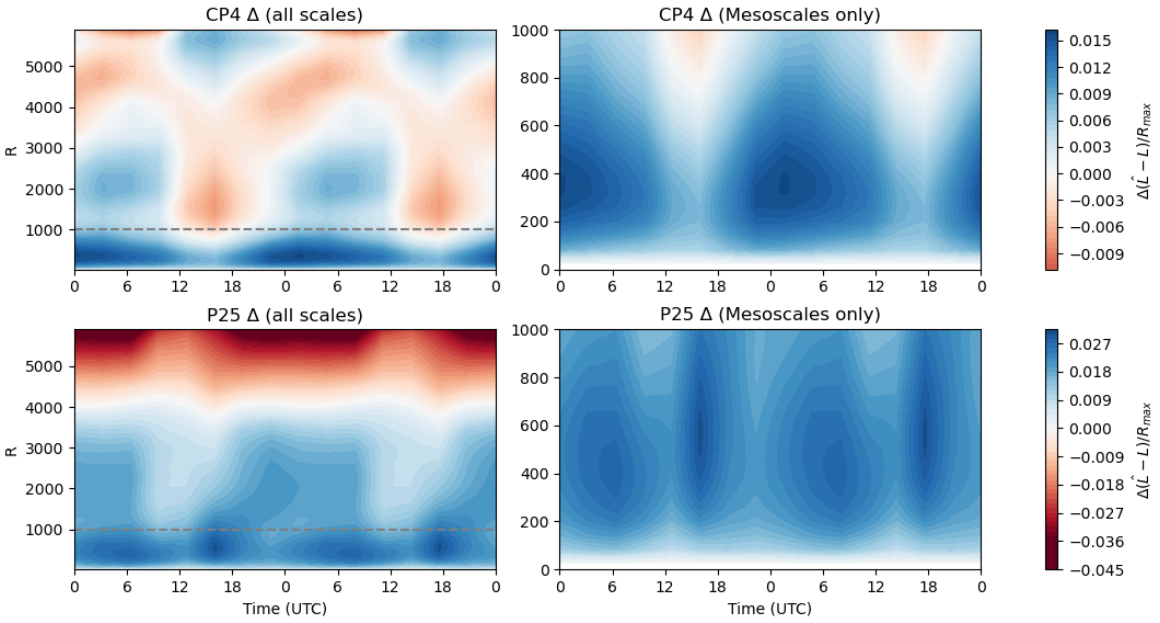


Figure 6.4: Climate change (future minus present) in mean diurnal cycles of $(\hat{L}-L)/R_{max}$. This is shown for all scales (left), and with the R-axis limited to mesoscales (right). Δ is shorthand for change. Note that here the time axis is repeated for clarity of interpreting values near 0UTC, and that different colour–scales are used for each model.

The measures of spatial structure calculated here do not on their own inform the importance of clustering for model climate. There is no reason to expect that a model will easily capture how spatial patterns relate to climate variability where this is observed in the real atmosphere. To know the importance of model differences in patterns of convection we must first know how related those patterns are to components of each model's energy budget, a major component of which is the radiation budget.

6.3 Clustering–radiation relationships

The primary result of Bony et al. (2020) is that clustering of deep convection in the tropics is negatively correlated with the net TOA radiation, independently of how much deep convection is present. Observed clustering is similarly negatively correlated with clear–sky net TOA radiation and with mid–level relative humidity. The proposed mechanism for the primary result is therefore the mean drying of the free–troposphere, as seen in idealized modelling (e.g. Wing (2019)). Free–tropospheric drying increases clear–sky longwave cooling of the atmosphere, therefore reducing net radiation.

In the context of climate modelling, it is important for models to reproduce these negative correlations between clustering and the radiation budget. A model without these relationships is missing some coupling between convection and radiation via intermediary spatial dynamics. Since TOA net radiation defines the net energy balance of the climate system, a lack of model coupling between radiation and other components of the system means that model can't represent any associated feedbacks on climate variability and change. Missing feedbacks are a source of error and uncertainty which reduce the quality of information needed for climate prediction and the associated decision making.

We have seen in Section 6.1 that the two models with different representations of convection have different characteristics in their spatial patterns of convection as measured by L_{org} and the underlying L–function. Those differences may be important for modelling radiation budget variability, depending on the extent to which the models reproduce the relationships in Bony et al. (2020). In this section we test the CP4-A models for negative correlation between net radiation and clustering of convection. We then highlight differences between the two models' results with respect to mechanisms in the literature, and known issues associated with parametrized convection such as weak moisture–convection coupling and incorrect diurnal cycles.

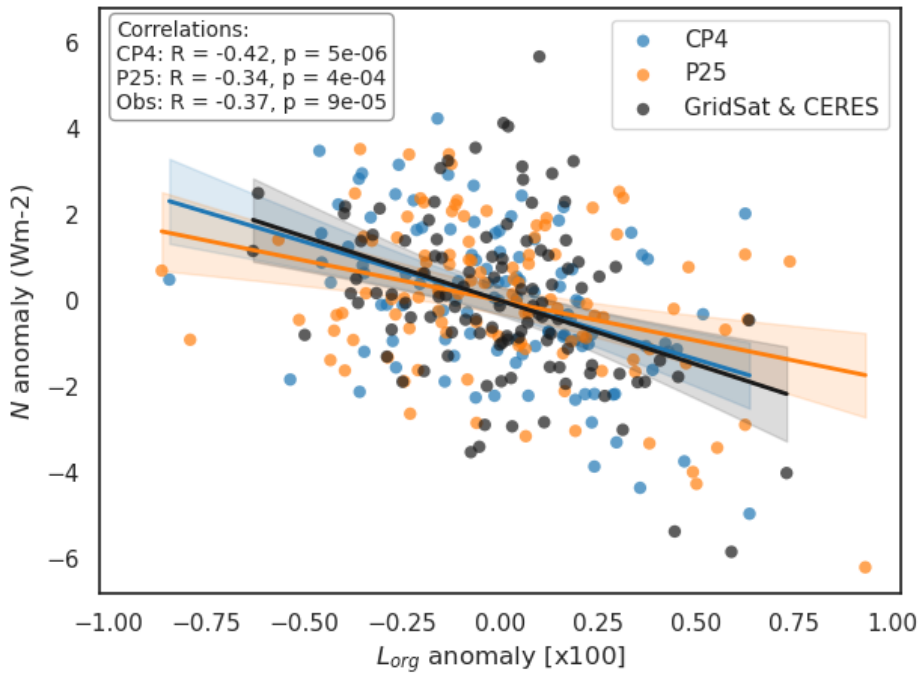


Figure 6.5: Relationships between detrended and deseasonalized monthly anomalies in African domain average net top–of–atmosphere radiation and clustering index L_{org}, for both CP4 and P25 models and for observations. Scatters are fitted with linear regressions with 95% confidence internals, and corresponding Pearson correlation R– and p–values are shown in the top left.

6.3.1 Net radiation and clustering over Africa

Figure 6.5 shows monthly anomalies in L_{org} against monthly anomalies in domain mean net TOA radiation (N) in the present climate. In both models and in observations, the two sets of anomalies are negatively correlated with high statistical significance ($p< 10^{-3}$). With the sample size of 108 months, the Pearson correlation coefficients are R = -0.42±0.088 and R = -0.34±0.091 for CP4 and P25 respectively, and R = -0.37±0.090 for observations. The model and observed relationships have large partial overlaps in their standard error ranges, and likewise in the 95% confidence intervals of respective linear fits. The relationship between model clustering and radiation is therefore not statistically distinct from that in observations in this sample, and neither model can be said to be more similar to observations. The above correlations imply that 7.8–21.1% of variance in N anomalies can be explained by L_{org} anomalies in observations, compared to 6.25–18.5% in P25 and 11–25.8% in CP4.

The most important budget term relating clustering to net cooling tropics–wide is clear–sky outgoing longwave. If this mechanism is present to some extent in the African domain, and in the models, then there should be a similar negative correlation between just clear–sky net

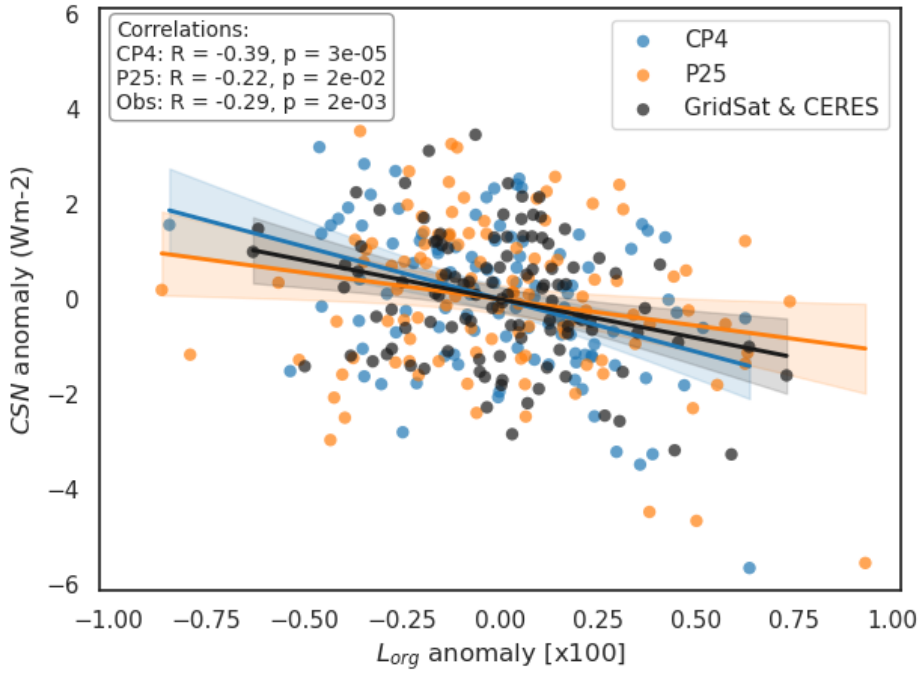


Figure 6.6: As in Figure 6.5, but for clear–sky net radiation and L_{org}.

(CSN) radiation and the L_{org} index. Replacing N with CSN produces Figure 6.6, where again both models and observations show negative correlations. Again the standard error ranges for corr(L_{org}, CSN) partially overlap for models and observations, and corr(L_{org}, CSN) error ranges partially overlap with those of corr(L_{org}, N).

6.3.2 Relationships with moisture and cloud

Figure 6.7 shows a grid of correlation coefficients for relationships between pairs of variables in the present climate in CP4. The variables include the clustering index L_{org} as well as the fraction of the grid defined as convective objects when calculating the index. Other variables in the correlation grid are domain means of N and CSN, as well as cloud–radiative effects ($CRE = N - CSN$), and 500hPa relative humidity ($RH500$). Because of sample size, we consider only larger differences in two given R–values as meaningful for interpretation, and only when both those correlations are very statistically significant.

In Figure 6.7, corr($L_{org}, RH500$) is negative and significant, similar to corr(L_{org}, N) and corr(L_{org}, CSN). There are also no correlations between convective fraction and L_{org} or any other variable. All these results are consistent with observations in Bony et al. (2020). Aside from relationships involving L_{org}, we see as expected that CSN anomalies are strongly positively correlated with

$RH500$. There is also a positive but weaker correlation between $RH500$ and N. Furthermore, CSN and CRE are also negatively correlated with high significance, as are CRE and $RH500$.

The same set of correlations for P25 are shown in Figure 6.8. Again, CSN and $RH500$ are strongly positively correlated as expected. However, similarly significant correlations as in CP4 between L_{org} and both CSN and $RH500$ are now absent. There is also no discrepancy between the strength of the correlations of N and CSN to $RH500$; net radiation anomalies are as strongly related to dryness as they would be if there were no clouds. The small but significant correlation of CRE with both CSN and $RH500$ seen in CP4 is also absent in P25.

6.3.3 Diurnal phasing in radiation budget relationships

Because of differences in the timing of convective cloud production, the two models have different diurnal cycles in their radiation budget terms. In addition, there are the diurnal differences in cloud spatial structures as diagnosed in Chapter 6.1. Knowing these two facts, we now consider whether similarities and differences between models in the above correlation grids might result from different processes occurring at different times of day.

In Figure 6.9, correlation R–values are plotted at 3-hourly intervals throughout the diurnal cycle. Statistical significance is now indicated symbolically and by opacity. Some similarities between models from the previous, non–diurnally separated correlations still hold. For example, the correlation between CSN and $RH500$ is significant and positive throughout the day in both models. In both models there are clear diurnal cycles in the correlations between N and both CSN and $RH500$; strong correlations in the evening and night, which weaken and lose significance during the day. Correlations between CRE and both CSN and $RH500$ also have strong cycles, which change sign between day and night.

The clear-sky drying and longwave cooling mechanism in Bony et al. (2020) relies on CSN being strongly correlated to N. However, in our domain it appears this is only true during the afternoon and overnight. Daytime variability in N is disconnected therefore from strong clear-sky humidity controls, and so the observed effect of clustering on N should be absent during the day. This is only true in CP4, where L_{org} and N are negatively correlated in diurnal phase with positive correlations between N and both RH and CSN. In P25, correlations of L_{org} and N are only during the day, out of phase with the conditions where the clear-sky drying mechanism could measurably influence N anomalies. Different diurnal phasing of the L_{org} –N relationship

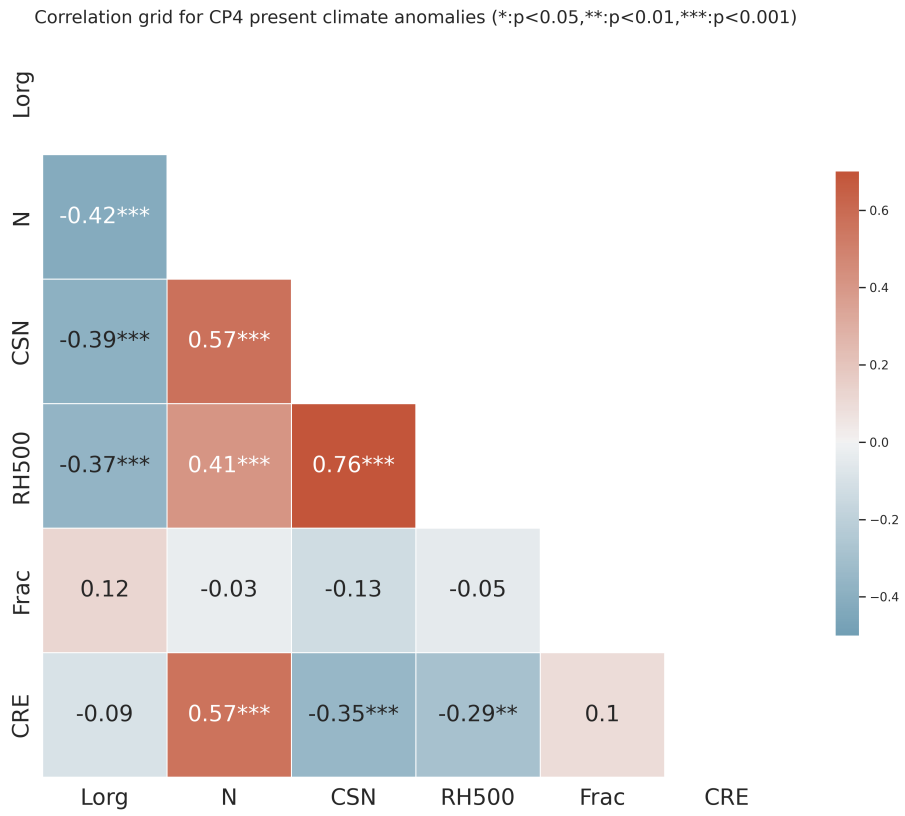


Figure 6.7: Grid of correlations between monthly anomalies (deseasonalized and detrended) in the CP4 present climate. Variables correlated are L_{org}, domain mean net (N) and clear–sky net (CSN) TOA radiation, domain mean mid–level relative humidity (RH500), deep convective fraction (frac), and domain mean cloud–radiative effects (CRE). Numbers and colours in each box indicate the Pearson R–value for the correlation, and the adjacent stars indicate statistical significance based on p–values. More stars means a more significant correlation.

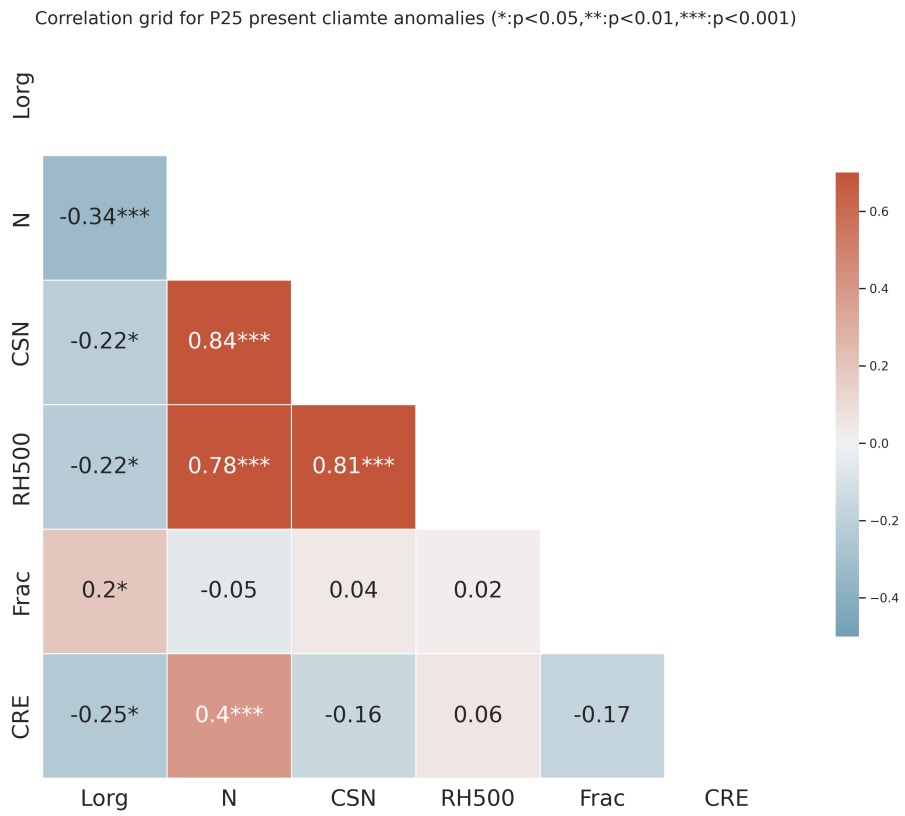


Figure 6.8: As for Figure 6.7, but for P25 in the present climate.

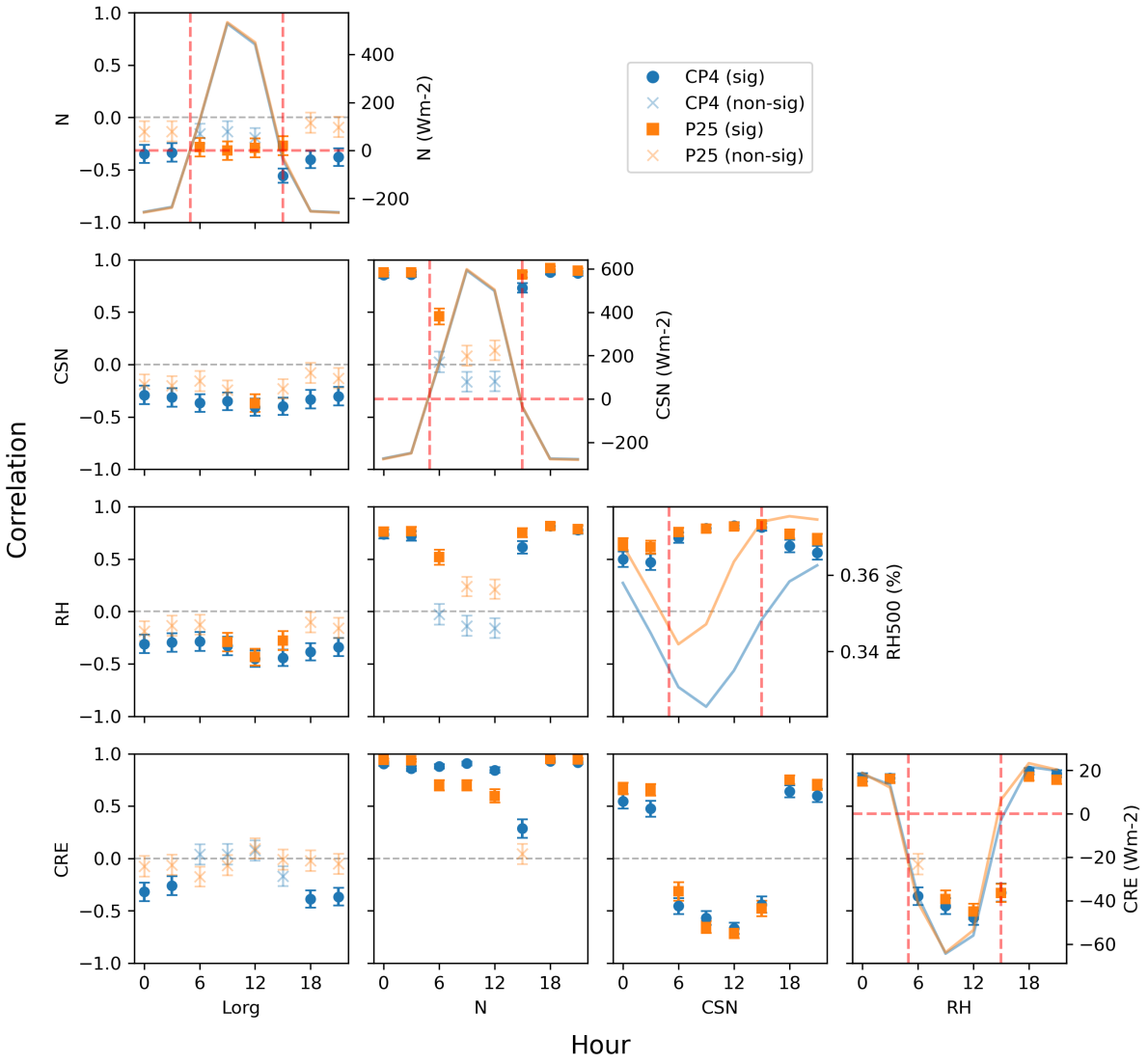


Figure 6.9: Grid of correlations between monthly anomalies (deseasonalized and detrended) in the model present climates, calculated separately for time of day at 3–hourly intervals. For each sub–figure, the hour is on the x–axis, and correlation R–value on the y–axis. The variables being correlated are labelled at the left of each row and the bottom of each column. Markers indicate the correlation for each hour, with standard error bars shown. Where correlations are statistically insignificant, they are plotted more faintly using a cross. On the rightmost plot in each row, the mean diurnal cycles of the row–variable are also plotted as solid lines (e.g. Mean N is plotted with the correlation of N and L_{org}). Lastly, vertical red dashed lines indicate where mean N changes sign in the diurnal cycle.

in the two models may therefore explain why there is better evidence for a clear–sky drying mechanism in CP4 in the non–diurnal result.

The lack of evidence for a clear–sky drying mechanism in P25 suggests that there is an alternative mechanism by which clustering influences net radiation in that model. That L_{org} only correlates to N during the day suggests that this alternative mechanism may involve predominantly shortwave effects which are absent at night. It has been shown that P25 produces mesoscale storms that initiate and dissipate too early, both during the daytime (Crook et al., 2019), and we have shown earlier that the mesoscales contribute most positively to L_{org} in P25 at all hours of the day. The daytime correlation of L_{org} to N could therefore be due to erroneous storm lifecycles and the strong shortwave cooling effect their anvils would have when produced in phase with peak insolation.

6.4 Conclusions and Discussion

In this chapter, we first measured structure in the spatial distribution of deep convection over an African domain in observations and in two regional climate models with different representations of convection. Both models are close to each other and to observations in time–mean measures of spatial structure. The diurnal cycle of the clustering, however, differs between the models. When we compared clustering as a function of both scale and time of day, we found that observed diurnal shifts in the principal scales of clustering are only reproduced by the model with explicit convection.

After quantifying the spatial patterns of convection in the models, we then showed that variability in those patterns is correlated to radiation budget anomalies, as has previously been observed over the global tropics. Both models are indistinguishable from observation in their correlation of inter–annual variabilities of clustering and net radiation. However, only with explicit convection is clustering similarly correlated to both clear–sky net radiation and to humidity. Therefore only the explicit model shows evidence for a mechanism similar to that proposed in observational and idealized modelling studies. We propose that this results from improvements to diurnal phasing of convection and storm lifecycles, relative to where in the cycle the clear-sky humidity mechanism can strongly impact net radiation. In our domain, clear-sky drying only actively correlates to net which in our domain is at night.

In conclusion, the explicit representation of convection, relative to the parameterized counterpart, is now associated with a better representation of scale–interaction processes with measurable impact on variability in the radiation budget. Because of the central role of net radiation in the Earth's energy budget, our findings support continued investment in the representation of tropical scale–interactions in climate models. Failure to properly represent convective scale–interactions can lead to unresolved inter–annual variability, or to variability driven by processes inconsistent with observations. Either of these outcomes increases uncertainty and reduces the quality of information derived from the model.

Future work should focus on a better process–based understanding of the role of diurnal phasing in correlating cloud clustering to net radiation. To do so would require reliable sub–daily observations of the TOA radiation budget over large areas, a much higher temporal resolution than the monthly CERES data used here. In our results, we have only shown that the models correlate clustering to radiation in parts of the diurnal cycle with opposite mean net radiative heating. That the explicit model is more realistic is supported by the further correlation of clustering to other fields, but it would be a more robust claim of realism if an equivalent diurnally dependant correlation exists in observations.

Beyond agreement with non–diurnal observational evidence, there are other process–based arguments for why CP4's diurnally dependant correlations in Figure 6.9 are more realistic. It is known from previous work that CP4 has better diurnal timing of convection (Stratton et al., 2018), and in Figure 6.3 we showed it better represents diurnal shifts in spatial patterns specifically. These improvements mean that the initiation and clustering of convection are more realistically phased with the radiation cycle. Previous work also shows that MCS dynamics and lifecycles are better represented with explicit convection (Crook et al., 2019). Bony et al. (2015) specifically propose that observed anomalies in clustering are due to changes in the ratio of MCS to isolated convection for a given cloud fraction. It follows that the signal of correlation between clustering and domain–mean longwave cooling in CP4 is strongest during hours when large MCSs are more frequent in that model, and when there is no attenuation from competing cloud or surface shortwave effects. The corresponding argument is that daytime mesoscale clustering in P25 represents ill–timed formation and dissipation of MCSs. A daytime correlation of clustering to net radiation in P25 then possibly results from shortwave cloud-radiative effects, but there is as yet no evidence that this is the case.

The representation of convection also affects moisture–convection coupling and the diurnal moisture cycle (Derbyshire et al., 2004; Birch et al., 2014). This is important because the diurnal phasing of moisture flux divergence patterns has implications for the clustering–radiation relationship, since humidity structures are the mediator of the longwave cooling mechanism. The formation of patterns of moisture convergence and divergence driven by diabatic heating in convective storms is conceptually similar to the moistening of moist regions and the growth of dry patches in arguments such as Muller and Held (2012), or the coarsening theory of Craig and Mack (2013). If moist convergence is maximised in the daytime hours when turbulent mixing is strong however, this may prevent maintenance of the distinct moist and dry patches of the free–troposphere and so limit the associated increase in mean radiative cooling. Likewise if convection is not adequately coupled to moisture locally, then positive moisture feedbacks are perhaps too weak compared to mixing and the moisture field remains too smooth. The impact of model physics on moisture feedbacks is a key theme of the next chapter.

Finally, while we measured increases in clustering in the modelled future climates, we found no correlations between future clustering and the future radiation budget. This is a surprising result that is not yet understood, but is important to untangle in any follow–up study. Climate change in clustering at the mesoscales is documented for other models, and is associated with more extreme rainfall in future storms (Bao et al., 2024). The intensification of rainfall in future storms has also been previously shown in CP4 (Fitzpatrick et al., 2020), with which the increased clustering measured here is therefore consistent. Increased clustering and rainfall intensity are both connected by thermodynamic arguments to increases in precipitation efficiency in a warmer climate with more atmospheric moisture, and this is associated with an iris–effect radiative–feedback that could be missing in GCMs (Clement and Soden, 2005; Mauritsen and Stevens, 2015).

Chapter 7

Moisture Budgets, Convective Processes, and the Bimodal Distribution of Water Vapour over the Tropical Oceans

This chapter is based on the following published article: Bassford et al. (2026). Tropical TCV as a process diagnostic: Connecting probability to processes in km–scale models via moisture budget statistics. Geophysical Research Letters, https://doi.org/10.1029/2025GL120807.

Water vapour is a fundamental component of the climate system, nowhere more so than in the tropics. The spatial distribution of total column vapour (TCV) is coupled to atmospheric dynamics via the production of rainfall and cloud, which are in turn major components of the energy budget. Water vapour directly interacts with radiation, as do the clouds it produces. Realistic vapour-circulation coupling is therefore essential for accurate modelling of the system on a range of timescales from hours to decades (Bony et al., 2015; Slingo et al., 2022).

Observations of TCV over the tropical oceans show a bimodal frequency distribution, with dry and moist peaks and a local minimum in between, around 48 mm in the annual mean distribution. Mapes et al. (2018) describes the narrow boundary between the moist and dry regions of the tropics as a 'moist margin', the location of which in physical space shifts significantly on synoptic timescales (Mapes et al., 2018; Robinson et al., 2024). Deep convection occurs almost

exclusively on the moist side of the margin; this and the narrowness of the margin are both the result of non-linear sensitivities of convection to column moisture (Neelin et al., 2009; Holloway and Neelin, 2010). The correct spatial representation of TCV at any given time is important for numerical weather prediction skill in both the tropics and extratropics, since circulation of air masses between the two can lead to impactful wet or dry anomalies (Roca et al., 2005; Knippertz et al., 2013; Aslam et al., 2024). Robinson et al. (2025) show that a large proportion of the spatial variability in the margin location is due to interaction with weather systems such as equatorial waves or extratropical potential vorticity anomalies. The perturbations to the margin coupled to these weather systems are associated with larger and longer precipitation events.

In a warmer future climate, there will be an increase in atmospheric moisture content and associated changes to precipitation distributions in both space and time (Schneider et al., 2010; Sherwood et al., 2010; Neelin et al., 2022). For current climate, there is also evidence for connections between the spatial patterns of convection, global radiation budgets (Bony et al., 2020), and tropical-subtropical moisture gradients (Hohenegger and Jakob, 2020). However, it remains uncertain how feedbacks between future convection and circulation contribute to climate sensitivity (Mauritsen and Stevens, 2015; Pendergrass et al., 2024). Inaccurate characterisation of current moisture distributions in global climate models (GCMs) creates uncertainty in projections of future precipitation patterns, given the dependence of the mechanisms on change in moisture.

A major source of uncertainty and error in global weather and climate models is in the parameterization of convection. The representation of convection affects both circulation and water cycles (Holloway et al., 2012; Birch et al., 2014; Jackson et al., 2020; Dauhut and Hohenegger, 2022). For example, parametrized models systematically underestimate the intensity of convective rainfall and produce light rainfall too frequently (Stephens et al., 2010; Chen et al., 2021; Ahn et al., 2024).

The bimodal nature of tropical TCV has been well characterized in observations and reanalysis (Mapes et al., 2018; Robinson et al., 2024), as has the failing of some climate models to reproduce this bimodality. In this chapter, we compare two km–scale models of the tropics with different treatments of convection and find that only one has a bimodal TCV distribution. We then show that dynamics of the moisture budget associated with maintaining the frequency minimum in

reanalysis are lacking in the model with parameterized convection. We then discuss bimodality in the context of coarser models, and their use in climate change projections.

7.1 Data

In this chapter we compare the two Cyclic Tropical Channel (CTC) runs from the Met Office K-Scale Hierarchy with both reanalysis (ERA5) and IMERG version 7 rainfall retrievals. The models are run on the N2560 grid (latitude $\times$ longitude = 5km $\times$ 8km at equator). Here we use the 40 day simulations initialised on 2016/08/01 (DYAMOND Summer). The differences between the two tropical channel runs are in their sub-grid physics parameterizations (see chapter 3 for details). The run referred to as the explicit model uses the RAL3.2 physics, including explicit convection. The run referred to as the parametrized model uses the GAL9 physics configuration, where parametrized refers to the convection scheme being active.

Restricting analysis of TCV bimodality to ocean domains only is consistent with previous work (Mapes et al., 2018; Robinson et al., 2024), and as in those works, is justified here by less reliable satellite retrievals of TCV over land due to higher surface emissivity. We therefore consider only data from columns over the tropical oceans between 25°N to 25°S, and uses 3-hourly instantaneous diagnostic outputs regridded to 1°.

Lastly, we acknowledge that comparing models to reanalysis has some limitations; reanalysis is not observation, and so diagnostics that co-locate retrieved rainfall with reanalysis moisture or other fields are less accurate than direct co-retrievals. However, since ERA5 assimilates satellite retrievals of water-vapour path (Hersbach et al., 2020; Trent et al., 2024) large-scale patterns are found to be consistent. A recent evaluation of TCV retrievals and reanalyses that assimilate them can be found in Trent et al. (2024).

7.2 TCV frequency distributions

The multi-year mean frequency distributions of reanalysis TCV and rainfall retrievals in Robinson et al. (2024) show that moist modal peak is located only around 1-2 mm drier than where the highest rainfall frequencies occur. In contrast, rainfall is minimal at TCV values below the moist margin threshold. Figure 7.1 shows 3-hourly $\times$ 1° grid frequency distributions of TCV over the oceans, filtered by rainfall rate and summed over the 40-day DYAMOND Summer pe-

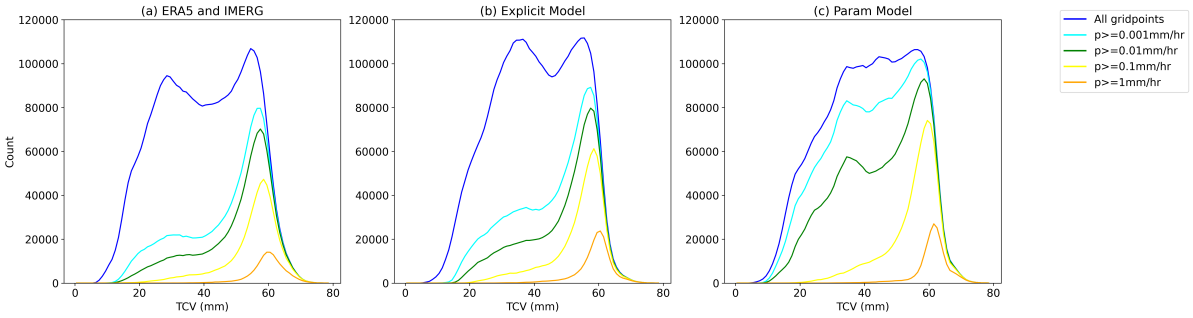


Figure 7.1: Frequency distributions of TCV for (a) ERA5 & IMERG (b) the explicit model, and (c) the parameterized model. Unconditional frequency distributions are shown in dark blue. Other distributions shown are when grid cells with rainfall below a threshold are excluded. Thresholds increase by factors of ten from $10^{-3}\,\mathrm{mm\,hr^{-1}}$ (cyan) to $1\,\mathrm{mm\,hr^{-1}}$ (orange).

riod for ERA5/IMERG and the two model runs. The observed distributions will look different to the multi-year annual means in the literature because of sample size and seasonality. Here we consider only the quality of bimodality and the associated presence and location of a moist margin in frequency space. We then consider how the presence or lack of bimodality and a margin relates to rainfall frequencies as a function of TCV.

In the unconditional TCV distribution (i.e. any rainfall rate), bimodality is present in ERA5 and the explicit model. For the parameterized model, the unconditional frequency distribution erroneously plateaus between approximately 30 and 60 mm. Where rainfall rates are relatively higher ($\geq 0.1\,\mathrm{mm\,hr^{-1}}$ on 1°), both models show the same behaviour as ERA5 and IMERG. Almost all locations with high rainfall rates are where TCV is high, around the moist peak of the unconditional distribution. This is also true for much lower rainfall thresholds ($\geq 0.001\,\mathrm{mm\,hr^{-1}}$ on 1°), but only in ERA5/IMERG and the explicit model. The parameterized model has high frequencies of weak rainfall across a wide range of TCVs, including at low values around 30 mm where the dry peak is seen in observations.

In Figure 7.1, the explicit model has TCV-precipitation co-location behaviour much closer to that of the observations/reanalysis. The parameterized model lacks bimodality in TCV, and rains lightly too often in drier columns. Producing too much light rain is a common issue with parameterized models (Ahn et al., 2024), so this alone is unsurprising. However, the relative error in the occurrence of light rain is far higher in columns with low to moderate TCV where the parameterized model lacks a dry frequency maximum or moist margin. Determining if rainfall biases are associated with TCV frequency biases requires an understanding of how TCV tendencies relate to the TCV distribution, and then an analysis of different contributions

to TCV tendencies using the moisture budget.

7.3 Relating the TCV distribution to the Moisture Budget

7.3.1 The moisture budget equation

The moisture budget equation describes contributions to the tendency of TCV and is written as

$$\frac{dQ}{dt} = E - P - \text{MFD}\,, \tag{7.1}$$

where Q is TCV, E is evaporation, P is precipitation, and MFD is vertically integrated moisture flux divergence.

7.3.2 Average and stochastic tendencies and their relationship to the frequency distribution

Previous studies have used a probabilistic representation of the relationship between Q and dQ/dt to connect idealized advection-condensation models with the observed moisture probability distribution function (PDF) in the mid-latitudes (O'Gorman and Schneider, 2006; Sukhatme and Young, 2011; Beucler, 2016). For example, Sukhatme and Young (2011) use Brownian parcel motion to model non-deterministic variability around the mean tendencies of parcels. They then calculated a steady-state moisture PDF, similar to that of a real atmospheric domain, using Fokker-Planck equations.

The following simplified stochastic model of TCV illustrates the utility of measuring the average relationship between Q and dQ/dt. 'Average tendency' is then used as a diagnostic tool in the next section comparing moisture budgets between models. This approach conceptually connects process-level behaviour in the models with their respective PDFs.

A simple idealized model is that the tendency has two contributions: tendency contribution from the mean relationship of dQ/dt to Q; plus some variability around that mean relationship from all other influences. Further idealizing that variability as random noise leads to the following stochastic equation for the change in moisture dQ over time dt,

$$dQ = \mu(Q)dt + \sigma(Q)dW_t, \tag{7.2}$$

where $\mu(Q)$ and $\sigma^2(Q)$ are the mean and variance in tendency over all columns with a given Q, and dW_t is a stochastic Wiener process.

The evolution of the PDF of Q in this simplified system $p(Q,t)$ is then given by the Fokker-Planck equation (Kwok, 2018),

$$\frac{\delta}{\delta t}p(Q,t) = -\frac{\delta}{\delta Q}[\mu(Q)p] + \frac{1}{2}\frac{\delta^2}{\delta Q^2}[\sigma^2(Q)p]\,. \tag{7.3}$$

The steady state solution p_{ss} of equation (7.3) is

$$p_{\text{ss}}(Q) = \frac{C}{\sigma^2(Q)}\exp\left(\int^Q \frac{2\mu(Q)}{\sigma^2(Q)}\,dQ\right), \tag{7.4}$$

where C is a constant. The presence and location of any local minima and maxima, and therefore the modality of the distribution, are determined by where $dp_{\text{ss}}/dQ = 0$, which is where $\mu = d\sigma^2/dQ$.

A bimodal PDF has three turning points: one at each of the two peaks of the distribution and one in between at the local minimum. The simple stochastic system will produce a steady bimodal PDF in Q if $dp_{\text{ss}}/dQ = 0$ has three solutions corresponding to those three turning points. A simple example of a bimodal system with a frequency minimum at $Q = Q_c$ is shown in Figure 7.2. The example system has a constant $\sigma^2 = k$, and a normal form bifurcation for $\mu(Q) = rQ_* - Q_*^3$, where $Q_* = Q - Q_c$ and $r > 0$. Since the variance in tendency σ^2 doesn't depend on Q, the turning points are where mean tendency $\mu(Q) = 0$. Figure 7.2 shows the example form of μ and the steady state PDF p_{ss} for this simplified system, which is bimodal. Shading and arrows illustrate the sign of the average tendency in four regions of the PDF.

The simple stochastic model and example system in Figure 7.2 illustrate the connection between statistics of the joint distribution of Q and dQ/dt, and the PDF of Q itself. Deriving a more complex and more realistic model is beyond the scope of this paper. However, any such model would include average tendency as represented by $\mu(Q)$ in Figure 7.2. The following section therefore focuses on connecting model processes to this average tendency via the moisture budget, leveraging the linear nature of means.

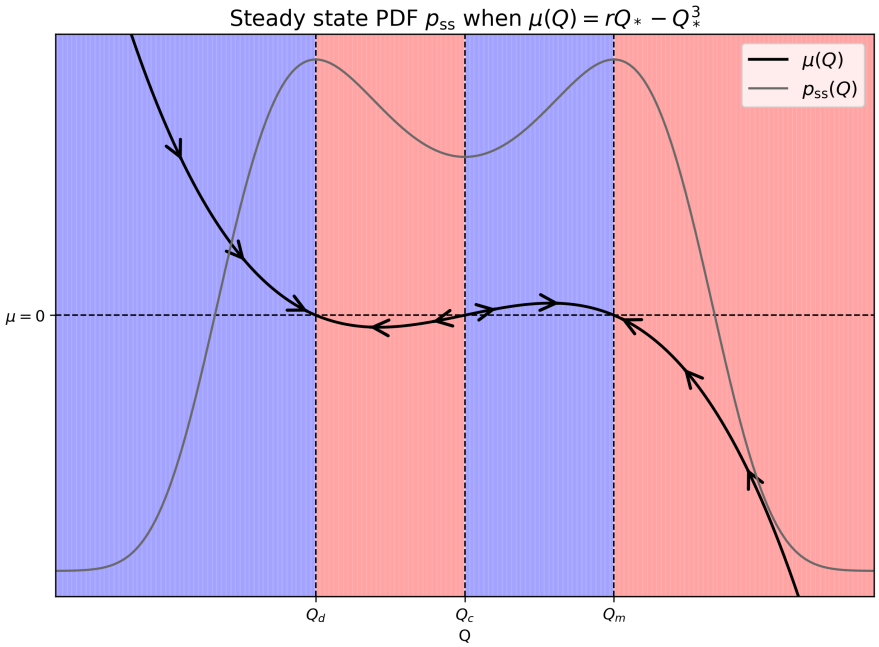


Figure 7.2: A conceptual example of how sign changes in $\mu(Q)$ can lead to a bimodal steady state PDF. The PDF shown is the steady state solution in equation (7.3) when $\mu(Q) = rQ_* - Q_*^3$ and constant $\sigma^2 = k > 0$. Blue regions are where μ is positive (moistening on average), and red where μ is negative (drying on average). Labelled on the x-axis are the three solutions to $\mu(Q) = 0$, which correspond to turning points in the PDF. Arrows on the $\mu(q)$ line indicate the direction of the mean flow in $(Q, dQ/dt)$ phase space.

7.3.3 Relating average tendency to physical processes using the moisture budget equation

A physical interpretation of Figure 7.2 describes a TCV phase-space with four distinct regions around three turning points of the TCV PDF, as in Figure 7.1(a) and (b). In the bimodal PDF, the two local maxima at Q_d and Q_m are the 'dry peak' and 'moist peak' respectively. The frequency minimum between the two peaks, at Q_c, is hereafter referred to as simply the 'minimum'. The average tendencies in these four regions are the following.

Region 1: Moistening in columns drier than the dry peak at Q_d.

Region 2: Drying in columns between the dry peak at Q_d and the minimum at Q_c.

Region 3: Moistening between the minimum at Q_c and the moist peak at Q_m.

Region 4: Drying in columns more moist than the moist peak at Q_m.

Writing the average tendency as $\mathbb{E}[\frac{dQ}{dt}|Q]$, the expected value of tendency for a given Q, then from equation (7.1)

$$\mathbb{E}\left[\frac{dQ}{dt}\middle|Q\right] \approx \overline{\frac{dQ}{dt}\middle|Q} \approx \overline{E|Q} - \overline{P|Q} + \overline{\mathrm{MFD}|Q}\,. \tag{7.5}$$

In equation (7.5) overbars represent means, and so $\overline{X|Q}$ is the 'mean X for a given Q' for each term X in the budget. Using equation (7.5), it is possible to relate the four regions of tendency to time means of each process.

The dry peaks of the TCV distributions in Figures 1(a) and 1(b) are between 25-35 mm, and so their Region 1 where $Q < Q_d$ is located predominantly in dry subtropical latitudes. Here precipitation is low, and MFD is small and positive from large scale subsidence. Evaporation increases with decreasing near surface relative humidity, which explains the shape of $\mathbb{E}[\frac{dQ}{dt}|Q]$ in Region 1 of Figure 7.2 for a given near-surface temperature, and assuming that the majority of this region's moisture is confined to the low levels near the surface.

Similarly in Region 4, TCV is bounded above by column saturation, and rapid increases in drying suggest that the well-documented non-linear increase in precipitation with TCV (e.g. Neelin et al. (2009)) exceeds any increases in moist convergence beyond the moist peak at Q_m.

Regions 2 and 3 contain the majority of the domain but the relative contribution of each budget term is less clear. These zones straddle the unstable fixed point at Q_c where $\mu = 0$ in Figure 7.2, where small changes in Q can lead to a sign change in $\mathbb{E}[\frac{dQ}{dt}|Q]$. This motivates a more thorough exploration of the relative contributions of each budget term to $\mathbb{E}[\frac{dQ}{dt}|Q]$ between the two peaks of the distributions in Figure 7.1.

7.3.4 Exploring expected tendencies in moisture budget analysis of low-rainfall environments

In Figure 7.1, differences between the TCV distributions in the models are primarily where precipitation is low. The impacts of the joint PDF of TCV and precipitation on the budget in equation (7.5) are direct via differences in $P|Q$, but also indirect via the coupling between $P|Q$ and $\mathrm{MFD}|Q$. This coupling is explored in Figures 7.3 which shows mean MFD for bins of Q and P. The common pattern in bin-mean MFD is convergence co-located with high rain and high moisture, and divergence where rain is lighter and columns are drier.

For a given rainfall rate, ERA5 moisture flux becomes on average more convergent with TCV. This is also true for the explicit model, but not for the parameterized model where $P < 0.1\,\mathrm{mm\,hr^{-1}}$,

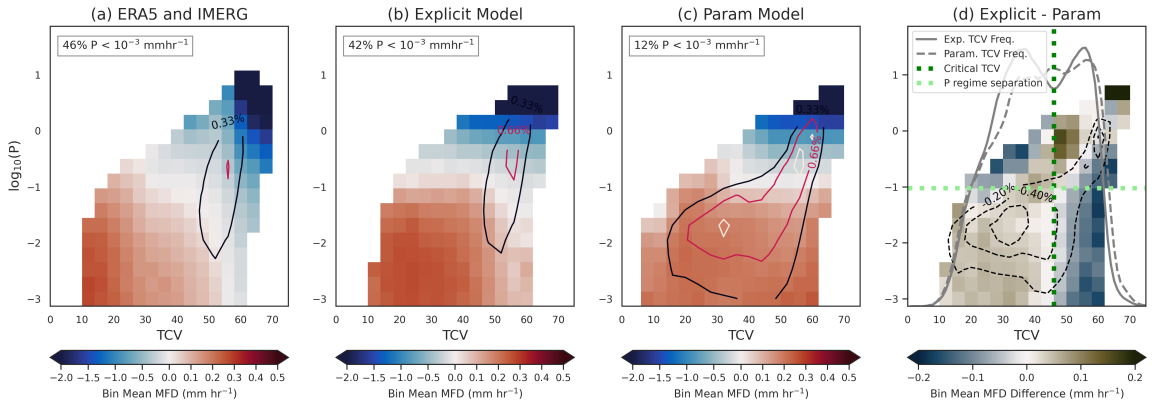


Figure 7.3: Distributions of MFD in TCV, $\log_{10}$(P) space. Shading shows bin-mean MFD for TCV, for (a)-(c) as in 7.1. Panel (d) shows the bin differences between explicit and parameterized models. Text on each subfigure indicates the proportion of the data where $P < 10^{-3}\,\mathrm{mm\,hr^{-1}}$. Contours show bin-density, other than (d) where they show the difference in bin-density between (b) and (c). Also overlaid in grey in (d) are TCV frequency distributions from Fig.7.1. The dark green line indicates the explicit model's frequency minimum, and the light green line highlights the change in the difference pattern above and below $P = 10^{-1}\,\mathrm{mm\,hr^{-1}}$.

where the model distributions differ most from each other in Figure 7.1. Figure 7.3(d) shows the difference between bin-means of the models. Below $\log P = -1$, there is a clear dipole in the difference along the TCV axis, centred at the frequency minimum in the TCV PDF for the explicit model. This shows that the explicit model has stronger moisture flux convergence on the moist side of the frequency minimum, and stronger divergence on the dry side. Contours in (c) and (d) show a second maxima in frequency in the parameterized model, and that light rain in drier columns collocates with less divergence in that region of (TCV, $\log P$) space than in the explicit model.

The differences in model MFD$|Q$ in Figure 7.3(d) motivate more specific analysis of the moisture budget where $P < 0.1\,\mathrm{mm\,hr^{-1}}$. For the time period simulated, and on a 1° grid, P is less than $0.1\,\mathrm{mm\,hr^{-1}}$ in similar proportions of the data (64% for IMERG, 63% for the explicit model, and 59% for the parameterized model).

Figure 7.4 shows $\overline{X|Q}' = \overline{X|Q} - \overline{X}$ for each term X in the budget, with $\overline{X|Q}'$ the difference between the mean where TCV$= Q$, and the overall mean across the range of TCV being considered. Using $\overline{X|Q}'$ quantifies the average relationship between each budget term and TCV, relative to any background moistening or drying which differs between models. For example, the y-axes of the third panel in Figure 7.4 should be interpreted as MFD at a given TCV being

more divergent than the mean where $y > 0$, and more convergent than the mean where $y < 0$.

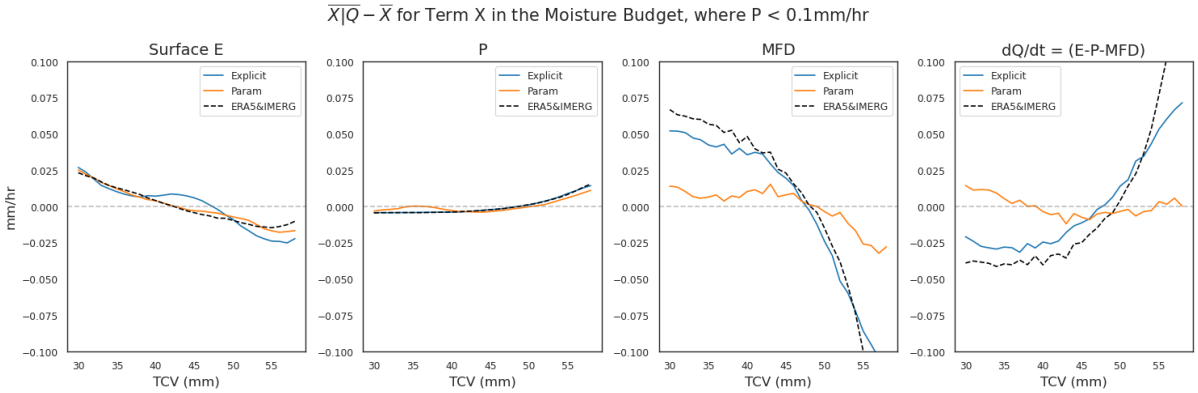


Figure 7.4: TCV bin-anomalies $\overline{X|Q}' = \overline{X|Q} - \overline{X}$ of mean moisture budget terms only where precipitation is less than 0.1 mm hr^{-1}. Bin-anomalies are defined for each term X as the mean of X where TCV $= Q$ in 1 mm bins minus the mean of X over the range of TCV from 30 to 60 mm.

For both models and ERA5, $\overline{E|Q}'$ decreases equally and approximately linearly with TCV, albeit with larger differences in the explicit model from the linearity found in reanalysis. $\overline{P|Q}'$ increases non-linearly with TCV even for these low rates, but the scale of this term is very small for all TCV bins considered.

$\overline{\text{MFD}|Q}'$ decreases non-linearly with TCV in the reanalysis and in the explicit model. Moreover, the sign changes in $\overline{\text{MFD}|Q}'$ co-locates with the 48 mm value defining the moist margin in Mapes et al. (2018). The scale of change in $\overline{\text{MFD}|Q}'$ across the range of TCV is also an order of magnitude larger than for $\overline{E|Q}'$ and $\overline{P|Q}'$. Consequently, an overall change in sign of $\overline{\frac{dQ}{dt}|Q}'$ occurs around 48 mm in ERA5, and ∼2mm drier in the explicit model due to the small differences in $\overline{E|Q}'$. This change of sign is from negative to positive, as expected at the frequency minimum that defines the boundary between Regions 2 and 3 of the PDF as described in section 7.3.3.

In the parameterized model the relationship between TCV and $\overline{\text{MFD}|Q}'$ is relatively flat, with only a small decrease starting above around 45 mm, and variation on the same order as the other terms. As a result, $\overline{\frac{dQ}{dt}|Q}'$ approximately follows $\overline{E|Q}'$ in drier columns, instead of $\overline{\text{MFD}|Q}'$, and is weakly positive. Above this, $\overline{\frac{dQ}{dt}|Q}'$ is relatively constant instead of increasing with Q. The weak moistening in columns with 30-40 mm of TCV, and the lack of a gradient in $\overline{\frac{dQ}{dt}|Q}'$ across the intermediate TCV range, is inconsistent with the conceptual description of Regions 2 and 3 and their shared boundary in section 7.3.3.

In the context of the Fokker-Planck framework in section 7.3.1, this approach using $\overline{X|Q}'$ ap-

proximates the steady-state condition for Regions 2 and 3 of the Q-space in Figure 7.2. This highlights differences between the models' moisture couplings that are distinct from differences in mean moistening or drying of these regions. The framework used here is simplified but effective for clear illustration of how leading order differences between model moist processes relate to differences in overall moisture distributions.

7.4 Conclusions and Discussion

The results of this chapter show that two km–scale models of the tropical atmosphere with different representations of convection have fundamentally different tropical column moisture distributions. The model with parameterized convection fails to represent the observed bimodal distribution, with two peaks at high and low column moisture, and a frequency minimum in–between referred to in previous work as the 'moist margin'. The lack of bimodality in the parameterized model is associated with the well-known issue of excessive probability of light rainfall. The excessive light rain is largely in dry to moderately moist columns where the moisture PDF lacks the dry frequency peak and a frequency minimum.

A simple stochastic model and Fokker-Planck equations illustrate how a bimodal moisture PDF can result from the statistical relationship between moisture and the tendency of moisture. This provides a connection between the TCV PDF and the moisture budget, via the TCV tendency term. Analyses of the mean relationships between TCV and the terms in the moisture budget in low-rain environments reveal that the model without bimodality lacks a strong relationship between TCV and moisture flux contributions to TCV tendency. This leads to the absence of a strong gradient in mean TCV tendency with respect to TCV; no strong increase in mean tendency across the moderate range of TCV values; and no sign change in mean tendency at the frequency minimum - all inconsistent with the maintenance of bimodality under the statistical framework.

The results in sections 7.2 and 7.3 show differences in moisture distributions and dynamics between explicit and parameterized convection when used at the same km–scale resolution. However some GCMs run at coarser resolution with parameterized convection do have bimodal TCV distributions (Mapes et al., 2018; He et al., 2022). The solution for correct moisture distributions is therefore more nuanced than simply going to higher resolution, suggesting assumptions in parameterization about moisture dynamics must be valid for the chosen resolution.

Diagnostics similar to those used in this chapter may help to understand model behaviour related to assumptions about moisture dynamics in parametrization.

An inherent challenge for coarser models is how they represent mesoscale phenomena without resolving them explicitly. For example, the spatial organisation of convection by mesoscale dynamics is well studied and known to be affected by parameterization (Hohenegger and Stevens, 2016; Colin et al., 2019; Wing et al., 2020). The moist margin is defined as a mesoscale feature in Mapes et al. (2018), so resolving it in the moisture PDF likely indicates some success in parameterizing the relevant scale interaction between convection and the mesoscale circulation of moisture. Mapes et al. (2018) also shows that composite precipitation and vertical motion both peak 200-400km equatorward of the moist margin. Using storm track data could uncover if these peaks are due to increased probability of Mesoscale Convective Systems (MCS) development near to the margin. Initial development of MCSs in this region is consistent with a description of Region 3 in Figure 7.2, where mesoscale convergence is moistening more than precipitation is drying, leading to further moistening and sustained rainfall.

Projections of future tropical precipitation under climate change are also affected by model representation of moisture-convection coupling. For example, Jackson et al. (2020) show that a future regional climate modelled with explicit convection has significant decreases in mean rainbelt vertical motion versus a parameterized counterpart. Underlying this result are differences in future changes to precipitation PDFs, which are coupled to changes in TCV PDFs via the moisture budget. Confidence in model representation of the future joint distribution of TCV and rainfall is contingent on the representation of the moisture distribution in the current climate.

We show that different model moisture distributions reflect systematic underlying differences in relationships between parts of the models' water budgets. This demonstrates the utility of the TCV distribution as a diagnostic for model physics-dynamics coupling across scales. Similar analysis is therefore a useful tool for evaluating existing or novel parameterization approaches in global models. Longer, global runs would allow for exploration of synoptic variability (Robinson et al., 2025), and by removing boundary condition constraints allow interactions with the extratropics (Jones et al., 2023). Complementary moisture budget analysis for columns with high rainfall rates would benefit from higher frequency model outputs, which improve budget closure when convective rainfall is intermittent over multi-hour periods. The results in this chapter support the view of TCV bimodality as a fundamental feature and measure of convection-

water coupling in the tropics. Determining whether models have the correct shape of the TCV distribution is then a valuable test of their moisture budget dynamics.

Chapter 8

Multi–Scale Structures in Tropical Convection: New Understanding and Future Directions

8.1 Overall Summary and Evaluation of Outcomes: Answering and Connecting the Research Questions

The questions asked at the beginning of the thesis were:

- Are there spatial correlations between precipitation locations on the same day, and what are the physical mechanisms responsible for these correlations?
- How can convection and its representation in models affect regional scale circulation and spatiotemporal distributions of moisture and precipitation?
- How does the spatial pattern of convection relate to the net top of atmosphere radiation budget in regional climate simulations of a tropical continent?
- How do the mean relationships between convective dynamics and moisture relate to the bimodal distribution of column moisture over the tropical oceans?

To answer each of these questions in turn was the specific aim of each results chapter. However, this does not make the results of one chapter unimportant in the context of other questions. Therefore in this section, we first summarise how each chapter met the intended aim, and then

we discuss the results in the context of other scales and of the other research questions.

Sub–daily patterns and mechanisms

In Chapter 4, we showed there are coherent correlations between convective rainfall locations in the morning with rainfall locations throughout the day. Spatial cross–correlations reveal a pattern of enhanced likelihood in later convection around locations with morning rainfall. The structure of this pattern at its largest, meso–synoptic scale, is ring–like when directional biases are removed. Furthermore, the structure of the probability patterns is similar to the aggregate effects of cold–pools and gravity wave propagation over the same period. It has been shown that strong convection is a source of both cold–pools and gravity waves, and both have been shown to enhance further convection away from their source. Our spatial statistics therefore likely reflect contributions from both mechanisms, as well as known land surface feedbacks. The main implication of Chapter 4 is the possibility of untapped predictability inherent in spatiotemporal statistical structure. The results are a good proof of concept to inform more sophisticated statistical or machine–learning based predictive tool development.

The structure of the cold pools contributions to rainfall probability patterns in Chapter 4 is also interesting with respect to rainfall autocorrelation in Chapter 5. A ring of enhancement is equivalent to a circle of enhancement plus a superimposed smaller circle of countering suppression with approximately the same centre. In Chapter 4, this smaller region of 'suppression' is a similar scale to the interior of the composite cold–pool, and also a similar scale at its largest to the 1° grid scale on which autocorrelation is calculated in Chapter 5. Mesoscale daily rainfall only every other day could therefore be linked to a recovery of the atmosphere from the previous nights cold–pool, something not considered in Spät et al. (2024). Observed cold–pool recovery times of 12 hours or more have been documented (Tompkins, 2001a; Provod et al., 2016). The atmosphere could therefore take the whole daytime to recover from a cold pool formed in the early hours, and by this time surface heating has ceased and so any new isolated convective initiation is unlikely until the following day. The recovery time may be longer than average from these overnight cold–pools, because there is less turbulent mixing of the boundary layer at night so the structure of the cold–pool can persist longer (Provod et al., 2016; Grant and van den Heever, 2016).

The concept of a cold–pool deformation radius, based on the initial depth of the cold–pool,

was also discussed in Chapter 4. The key point here is that rotational effects limit the scale of potential temperature perturbations in shallower layers more so than for the whole column. The deformation radius λ_R for a large cold–pool is therefore up to ∼1000km in Sahel latitudes, depending on the depth, intensity, and vertical mixing of the cold pool with layers above. This is as opposed to ∼10,000km for subsidence–generating deep gravity waves at these latitudes. Two strong cold–pools may therefore interact with each other if their centres are less than λ_R apart. Furthermore, interactions between cold–pools can lead to further convection (Torri and Kuang, 2019), and this would be more likely in the afternoon when initiation is most common. Interacting shallow circulations bridging existing mesoscale systems into synoptic envelopes of convection could help to explain the afternoon transition to larger scales of maximum clustering seen in Chapter 6 (Figure 6.3).

The suppression of later rain by earlier rain should also appear in the moisture budget dynamics of Chapter 7. In particular, the cold–pool–like suppression of later rain in Chapter 4 involves a dynamic drying contribution to column moisture tendency, through moist–divergence at low–levels. This could contribute to upper limits on the positive column moisture–rainfall feedback in high–moisture columns, where rainfall heating drives convergence that further moistens the column (Region 3 in Section 7.3.3). Higher rain rates generate stronger cold–pools, until the associated divergence could at some point balance or exceed moist convergence driven by latent heating above. Without net moisture convergence, precipitation cannot increase further without drying the column, and so the feedback stops (transition from Region 3 to 4 in 7.3.3).

Interactions of Convection with the Regional Scale

The results of Chapter 5 show first a direct example of how convection affects regional circulation, followed by a more general exploration of how different modelling approaches produce different regional properties of moisture and rainfall. For the direct example, it was shown that rainfall evaporation and the associated cold–pool gust fronts have a significant role in the large–scale thermodynamic, and therefore circulatory, structure of the West African Monsoon. These effects are both local and non–local to the region of significant evaporation in the Sahel boundary layer. Non–local effects are associated with eddy fluxes of temperature and momentum in gust fronts and tilted storms, both the result of strong cold–pools. These results explicitly confirm the results of previous studies and observations (Marsham et al., 2013; Garcia-Carreras et al., 2013; Trzeciak et al., 2017) by using bespoke model experiments with rainfall evaporation

deliberately turned off to suppress cold pools. Our results also agree with previous work on the implications; models need to represent cold–pools and their upscale effects in order to reduce large–scale circulation errors and uncertainties in forecasts and climate simulation.

The aim of Part 2 of Chapter 5 was to answer the rest of the associated research question, regarding spatio-temporality of rainfall and moisture. In these results, reproducing the regional pattern of observed autocorrelations of daily rainfall is affected by model representations of convection in pan-tropical domains, as in Spät et al. (2024). Building on this result, we find that for regional models the effect of domain size is insignificant for autocorrelation, compared to the effect of the sub–grid physics settings used both internally and in the model providing boundary conditions. In contrast, decorrelation of a convection–permitting regional models column moisture field from its parametrized global driver is strongly a function of that domain size, as is the similarity of column vapour evolution to reanalysis. Larger regional domains decorrelate from their driving model faster and more than smaller domains, and in some cases these larger domains with explicit convection provide signals of improved predictability at subseasonal timescales.

Total column vapour is used as a diagnostic in both Chapter 5 Part 2 and in Chapter 7. The decorrelation of LAM TCV from global drivers is a measure of the difference in spatial patterns over time, but one could also use TCV PDFs as in Chapter 7 to explore the impact of domain size. For largely oceanic regions such as the South–East Asia LAM domain, two models with similar synoptic variability of the Moist Margin (Robinson et al., 2024) would have more similar TCV PDFs and decorrelate more slowly. This is consistent with the decorrelation results of Chapter 5, and suggests synoptic weather systems associated with margin perturbations (Robinson et al., 2025) evolve similarly in global and regional LAM runs. This is also consistent with the lack of evidence that the LAM approach provides any benefit for predicting of the TCV field in the SEA domain, compared to running a pan–tropical channel.

Convective Clustering and Regional Energy Imbalance

In Chapter 6, we showed that the observed negative correlation between the spatial clustering of convection and net radiation holds for a regional Africa-only domain in the same observations, and in two models with different representations of convection. However, only the higher-resolution model with explicit convection showed evidence for the same mechanistic explanation

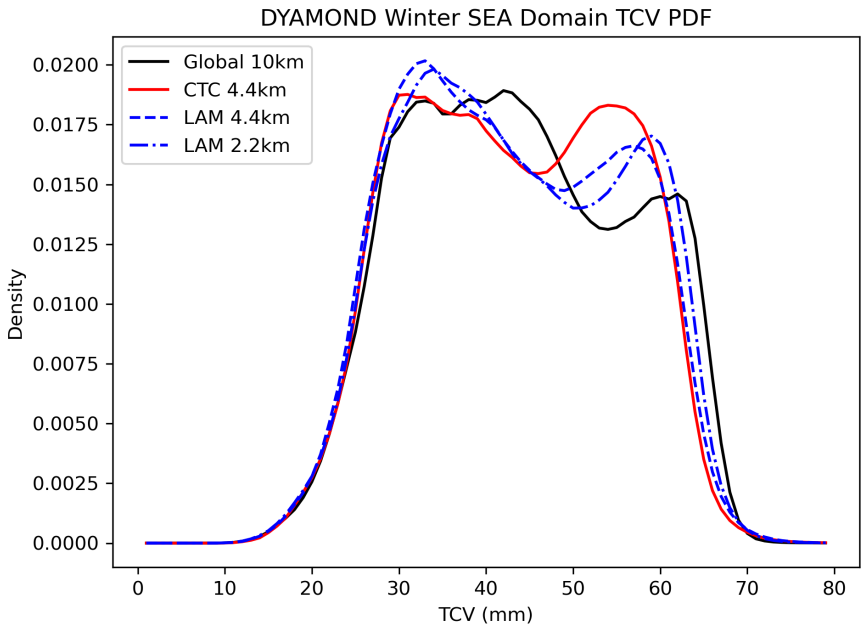


Figure 8.1: TCV PDFs over the South-East Asia LAM domain in DYAMOND Winter model runs Jan-Feb 2020. Dry mode values are independent of domain size, but moist modes in smaller domains are more shifted towards the global driver. Moist extremes appear consistent between the CTC and LAM with the same physics and resolution.

as in pan–tropical observations. We provide further evidence suggesting this mechanistic difference may be due to better diurnal phasing of convection, cloud and storm formation with the solar cycle.

Chapters 6 and 7 are related through moisture's role as the key mediator of the clustering–radiation relationship. As such, we might expect a detectable clustering signal in the TCV PDF diagnostics of Chapter 7. Figure 8.2 shows exactly this, using now reanalysis and the monthly I_{org} time–series (Semie and Bony) used in Bony et al. (2020) and Semie and Bony (2020). High and low clustering is associated with PDF variability only in the moist mode and not the dry mode. Conditioning the TCV PDF on CERES net radiation (N) terciles shows that high clustering and high N are associated with opposite anomalies to clustering in the moist mode of the TCV PDF, consistent with the negative correlation between I_{org} and N in Bony et al. (2020). High clustering and low N is associated with more extreme TCV values in the moist mode, and therefore with increased impacts of rainfall and humidity extremes (Neelin et al., 2022; Jackson et al., 2025). Lastly, there is an additional signal of increased dry mode frequency in months with high N, that is not explainable with low clustering alone. Another independent mechanism must be acting in the dry mode, alongside clustering in the moist mode,

in months with low N.

That clustering only interacts with N in the moist mode makes sense, because there isn't any deep organised convection elsewhere. The lack of any significant deep convection in the dry mode is the original motivation for understanding the modal split (Mapes et al., 2018; Robinson et al., 2024). The relationship of N to the dry–mode TCV distribution could instead be an expression of the other mechanism discussed in Bony et al. (2020), lower–tropospheric stability. A more stable lower troposphere is related to strong inversions and increases in low marine cloud cover. Estimated inversion strength is also negatively correlated to N, with the mechanism being increased cloud albedo from low clouds and free–tropospheric drying above. The increased frequency of dry-mode TCV columns in high N months could therefore be associated with strengthening large scale inversions in subsidence regions, and an increased fractional coverage or reflectivity of low clouds.

Tropical Moisture Distributions

Satellite estimates of TCV show a bimodal frequency distribution in total column vapor (TCV) over tropical oceans, with convective rainfall predominantly produced on the moist side of the frequency minimum between two modal peaks. In Chapter 7, we showed that a km–scale model of the tropics with explicit convection produces a bimodal TCV distribution, whereas the same model with parametrized convection does not. To answer the research question "what relates dynamics to bimodality?", we used concepts from statistical mechanics to relate TCV frequency to TCV tendency. We then isolated the moisture budget contributions to tendency in TCV phase-space to determine which process leads to the lack of bimodality in one of the models. The process–error was an incorrect relationship between moisture flux convergence and TCV in environments with little or no rainfall. The resulting lack of a strong gradient in TCV tendency with respect to TCV is inconsistent with that expected to maintain a TCV frequency minimum, and so bimodality is lost. Our results demonstrate significant value in the TCV distribution as a diagnostic for moisture budget dynamics.

To answer the research question, Chapter 7 focussed on how non–equilibrium processes in the moisture budget relate statistically to long–term persistence of characteristic bimodality. However, while bimodality may be a persistent in the tropical mean, other properties of the distribution are not necessarily stationary over time. In fact, recent trends in reanalysis (Figure 8.3)

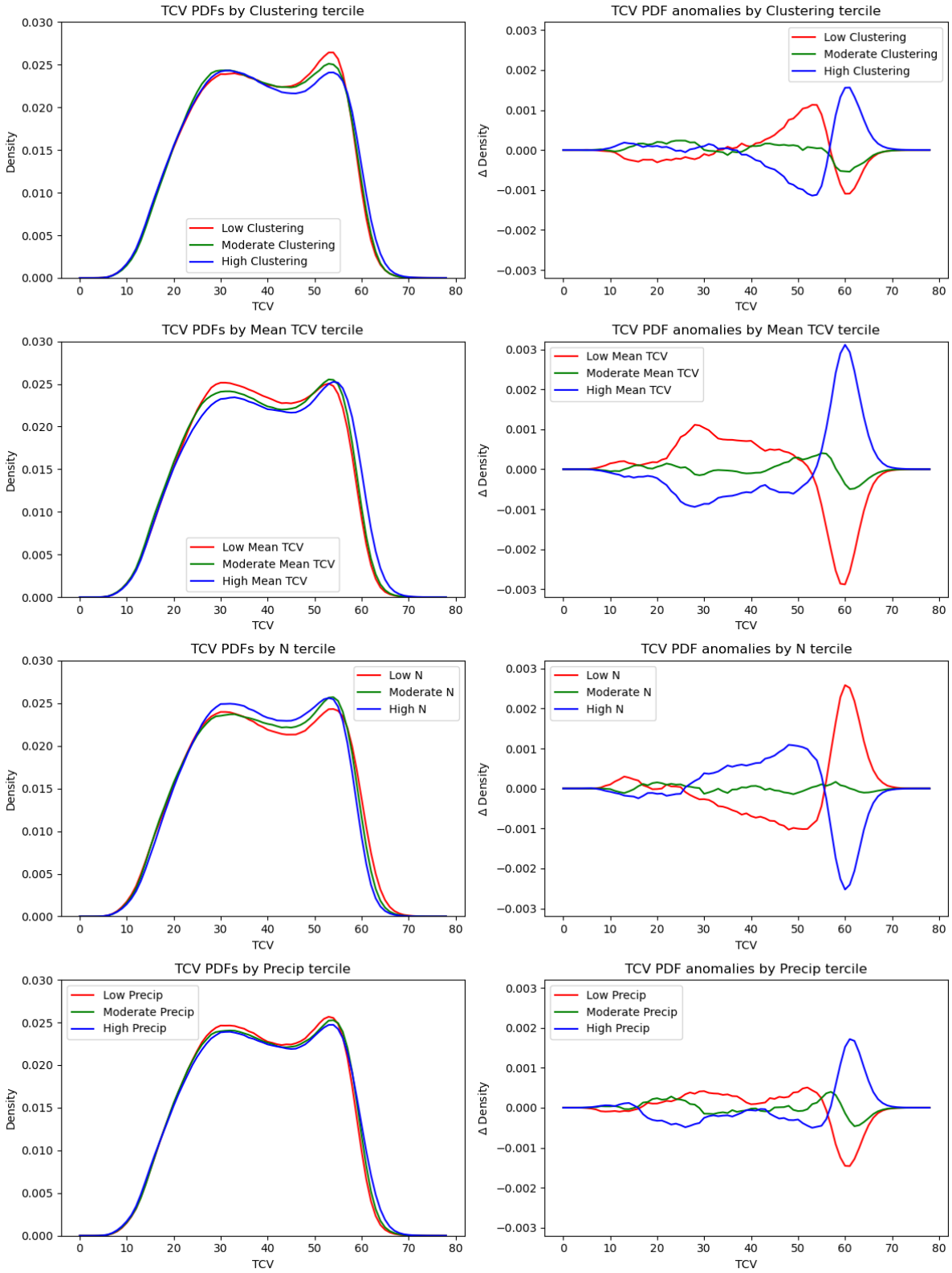


Figure 8.2: Monthly Mean ERA5 Tropical Ocean TCV PDFs from 2001-2017, grouped by terciles of convective clustering (I_{org}), mean TCV, net TOA radiation (N), and monthly mean precipitation (GPM IMERG). The first column shows the PDFs for each tercile, and the second column the anomalies associated with each tercile relative to the mean TCV PDF.

show multi–decadal climate change in the TCV PDF. Changes since 1990 include a reduction in the frequency of dry extremes and a large increase in frequency of moist extremes. Comparing the 1990s to the late 2010s and early 2020s, the margin and moist mode appear simply shifted to the right by 2-3kg^{-2}. This is consistent with documented Clausius–Clapeyron–like scaling of Tropical TCV (e.g. Allan et al. (2014)), under the observed 0.6-0.7K global warming trend since 1990 (∼0.2K/decade (Menne et al., 2018; Morice et al., 2021)). The dry mode change however is not in a simple shift to the right, but with the dry peak flattening slightly also.

The above changes do not imply any change in the moisture budget dynamics discussed in Chapter 7, just that the regions with statistical mean drying and moistening (see Figure 7.2) have shifted in TCV–space, potentially in response to global warming. Connecting TCV PDF trends to known but poorly modelled regional changes in atmospheric moisture and precipitation (Allan et al., 2014; Douville and Willett, 2023; Simpson et al., 2024), while leveraging the link to dynamics demonstrated in Chapter 7, could further extend the PDF's diagnostic utility to multi–decadal timescales.

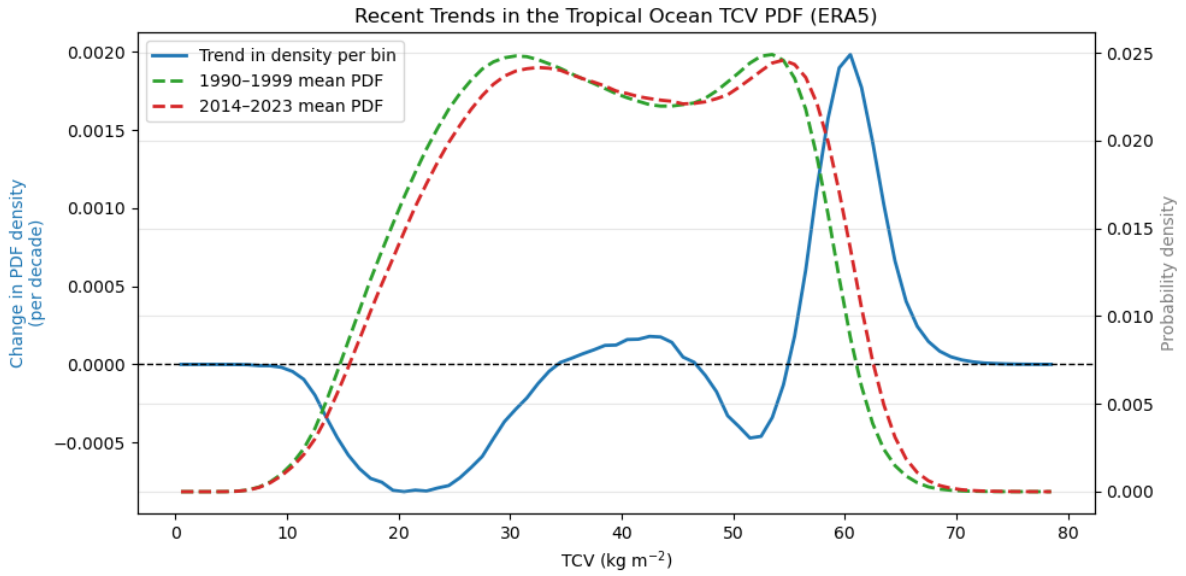


Figure 8.3: Decadal Mean ERA5 Total Column Vapour PDFs for 1990-1999 and 2014-2023, and the decadal trend in density for each 1kgm^{-2} wide bin. For example, the frequency of columns in just the 60-61kgm^{-2} bin has increased by around 0.2% per decade.

8.2 Current Limitations and Future Outlook

8.2.1 Limitations

Modelling limitations

Every chapter of this thesis has used simulation data from one modelling system, the Unified Model (UM). While this provides a seamless comparison of results across scales, quantifying systematic issues in multiple UM configurations is not a replacement for multi–model intercomparison. The simulations in this thesis are also all atmosphere–only, and so potentially important atmosphere–ocean feedbacks, such as surface temperatures responding to rainfall and cloud cover, are not represented. Exploration and comparison of the processes in our results in other modelling systems would therefore be valuable.

Within the modelling framework of the UM, we have used many different configurations. In particular, we have made significant use of limited domain, regional or pan–tropical domains with one–way nesting inside lower-resolution global runs. This approach has fundamental limitations for evaluating the benefits of higher–resolution or improved physics, because the coupling of those local benefits to global circulation is not possible with a one–way nested setup. The limitations of regional domains highlighted in Chapter 5 therefore apply to the results of all the other chapters.

An example from Chapter 5 is the systematic dependence of regional rainfall autocorrelation patterns on driving model physics. This result demonstrates the importance of cross–boundary circulation or wave propagation (e.g. (Spät et al., 2024)) for local variability of convection. For all Tropical–only simulations, equatorward flows from the mid–latitudes in the Hadley Circulation depend only on the chosen driving model, and likewise for zonal circulations into the limited African regional domain, such as Walker Circulations or the Tropical Easterly Jet (TEJ). The TEJ, for example, has a significant upstream component beyond the regional model boundaries, but interacts with the mid–level jet, Easterly Waves, and MCS processes in West Africa (Nicholson et al., 2007; Besson and Lemaître, 2014). In reality, tropical or regional variability is coupled to, and feeds back on, those meridional and zonal cross–boundary circulations. Use of a regional domain could therefore mask or inflate potential benefits of explicit convection in our results, such as in Chapter 6 where regional clustering does not feedback on the global circulation via the modulation of regional scale energy imbalances.

Finally, the length of the simulations used, and the fact all are single realizations, means that our results don't necessarily account for internal variability at every scale. The design of the K-Scale experiment is instead a set of models with the same initialisation but with different model configurations. While we have identified differences due to those modelling choices, we have not always been able to quantify whether those differences exceed the internal variability of each individual configuration, due to both short simulation length and a lack of an ensemble.

Methodology and data limitations

Methods in each chapter rely to some extent on thresholding variables to define binary maps or to explore a subset of the system dynamics. Thresholds are a limitation in the sense that they remove information, and can be somewhat arbitrary. However, in our work we have justified each threshold used either explicitly by demonstrating its value as a defining separation between distinct regimes, or with reference to the use of the same thresholds in previous published work.

Model output frequency affects some of our results, wherever instantaneous fields are needed, because the high–frequency variability of processes such as the rate of convective precipitation are not necessarily captured by 3–hourly outputs. Similarly, a lack of control over fields in model output is in this case limiting but not obstructive. For example, in Chapter 6, the lack of infrared brightness temperature emulation was mitigated using the empirical OLR conversion.

There are also limitations associated with performing the budget analysis in Chapter 7 using instantaneous rather than time–lagged methods (e.g. Wolding et al. (2020, 2022)). While we can compare directly the contributions of each process to instantaneous tendency, we can say less about causal relationships between processes than in the lagged case. Another limitation of Chapter 7 specifically is the use of column integrated measures, which prevents direct comparison to mechanistic arguments for the moist margin formation made by Masunaga and Mapes (2020), which include vertical circulation structures.

More generally, all the analyses in the thesis are designed to collapse the dimensionality of the data. This collapse is mostly either in the space or time dimensions to generate time–series or maps, or in both space and time for the case of PDFs. Interpretations are therefore made after removing information about one or more dimensions of variability. While a useful process for simplifying data for interpretation, this loss of information still represents a limitation to analyses of this kind. Some information loss is inherent in the analysis of scale–interactions,

because of how scales of variability need to be measured. For example, consider a variable $S(\mathbf{x}, t)$ in space and time, and the transform of that variable into wavenumber–frequency space $\hat{S}(\mathbf{k}, \omega)$. The field S itself gives exact information for each specific location and time, but all the scales of variability are mixed together. In contrast, $\hat{S}$ quantifies the scales of variability but provides no information about when and where that variability occurs. This problem relates to Fourier–uncertainty (Folland and Sitaram, 1997), in that it is not possible to quantify all information about scales and about spatiotemporal change without some uncertainty in either or both. An example of a useful compromise in climate science is wavelet analysis (Meyers et al., 1993; Torrence and Compo, 1998), the use of which could in future extent our analyses such that dimensions need not be collapsed as they have been here.

8.2.2 Future Tropical Scale–Interactions Research

Global climate simulation at km–scales

New opportunities in scale–interactions research largely follow continued advancement in modelling science and computational capacity. Global km–scale simulations have already started to become a priority at multiple modelling centres around the world (Segura et al., 2025; Gettelman et al., 2026). Eventually it may be feasible to run multi-model coupled km–scale ensembles for climate, which would mitigate the modelling limitations in this work regarding domains, timescales, and internal variability. However, these new simulations will require much evaluation before they can truly be considered better tools for improving physical understanding of the real atmosphere or for regional climate change. This evaluation of in–development global km–scale climate models is a direct application of the work in this thesis. For example, diagnosing correct clustering–radiation relationships and bimodal moisture distributions should form part of those evaluations.

An advantage of global climate simulations with km–scale resolutions is that they will be better tools than one–way nesting for understanding the covariance of large–scale circulations with their own substructure. Variability in large–scale features of the tropical atmosphere, such as the ITCZ or continental rainbands, needs to be continually examined from a perspective of non–independence between internal and external spatial structure. The frequency, size, intensity, efficiency, and spatial distribution of convection all likely contribute to the overall shape and strength of mean ascent within the ITCZ, and this internal structure also determines the actual

climate impacts. There are opportunities to connect existing theories for global ITCZ external structure and its change, such as Byrne and Schneider (2016a); Byrne et al. (2018), to rainband internal structure changes already quantified in regional km–scale studies like Jackson et al. (2020). This connection could also consider how convective clustering and joint moisture–precipitation distribution features, which are both unresolved in coarse GCMs, impact energy budget arguments for ITCZ external structure.

Conceptual models and idealization

Alongside the evaluation and utilisation of full complexity models, understanding scale–interaction relies on conceptual thinking. Understanding atmospheric structure as statistically emergent (Rizi, 2026) is one such conceptual aid. Convection and larger–scale circulation evolve on inherently separate timescales. As a consequence, smaller scale processes can impact larger scales statistically over time rather than deterministically at each timestep. The converse also occurs, such as how large–scale and time–mean structures do not determine exact instantaneous distributions of convection but instead affect probabilities. These are key themes in the results across all chapters in this thesis, where coherent behaviour emerges when aggregating over many events in space and time. The idea that coherence can emerge from processes that instantaneously appear chaotic and unpredictable is not in itself novel, but the scales at which the phenomenon occurs in our results are a potential frontier for such probabilistic thinking in atmospheric science. Results in Chapter 7 in particular, and to a lesser extent chapter 4, show that probabilistic thinking and stochasticity have significant utility for larger scales than usually considered by such approaches. Conceptual and statistical models of emergent atmospheric behaviour will inform evaluations of future km–scale GCMs, and of future parameterizations for where they are needed.

Our work therefore supports connecting statistical or stochastic representations of smaller scale processes to large–scale circulation or thermodynamic structure, using existing and new conceptual frameworks. An example would be connecting the bimodal column moisture distribution to conceptual models of bi–stability in moisture dynamics. In Craig and Mack (2013) and Windmiller and Craig (2019), moisture (Q) tendency is modelled as a reaction–diffusion process with a double–well potential $V(Q)$, such that $dQ/dt = -dV/dQ + D\nabla^2 Q$. This simple model distributes moisture in a similar way to our simple stochastic model in Chapter 7, because the expected tendency that produces a bimodal PDF has this same double–well structure,

and stochastic variance acts diffusively in Q–space. The coarsening behaviour of Craig and Mack (2013), together with a stochastic representation of the critical moisture–precipitation relationship (e.g. Neelin et al. (2009)) could explain a tropical atmosphere split into a near–homogeneously moist region where deep convection is possible but not deterministic, and a dry region with no deep convection (Mapes et al., 2018). Intermediate moisture states are unstable in the double–well structure of coarsening dynamics, and so boundaries between moist and dry regions remain narrow in near–equilibrium (Windmiller and Craig, 2019), just like the observed tropical moist margin. Development of these ideas could combine the efforts of idealized modellers and tropical meteorologists into more robust conceptual models for real tropical moisture dynamics.

Applications for impact assessment and mitigation

As stated at the beginning of the thesis, applications of atmospheric research aim to mitigate the impacts of weather and climate phenomena on human lives and systems. A key tool in impact reduction is early warnings at multiple lead times, which rely on forecasting and prediction tools. Chapter 4 discussed in detail the application of the patterns found there to same–day precipitation early warning systems. Additional early warning systems could be informed or improved using the results of other chapters, and each set of phenomena more directly tied to impacts through interdisciplinary studies connecting them with economic and health outcomes.

For example, tracking synoptic and seasonal shifts in the spatial position of the Tropical Moist Margin could inform agricultural planning for island nations and other coastal regions, and early warning of rainfall extremes over a range of timescales. Because the Margin delineates where significant convective rainfall is and isn't likely on a given day (Mapes et al., 2018; Robinson et al., 2024), the more time a region spends inside the Margin during a given season provides approximate upper bounds on days with significant precipitation. Statistics of synoptic and subseasonal variability in the Margin could be correlated to seasonal rainfall totals and variance, and soil moisture accumulation rates, all of which are valuable for agricultural planning (Nieuwolt, 1982; Bombardi et al., 2020; Feldman et al., 2024).

Robinson et al. (2024) also show that the vertical structure of synoptic perturbations to the Tropical Moist Margin includes coincident positive anomalies in boundary layer humidity and temperature. Similar anomalies are seen during humid heat extremes in the Indo–Pacific and

South–East Asian regions in Jackson et al. (2025). Margin perturbations near islands or coastal regions could therefore be associated with high wet–bulb temperatures that define those humid heatwaves. Furthermore, it has been shown that Equatorial Wave and MJO activity modulate both the Moist Margin (Robinson et al., 2025) and daily humid heat risks in South–East Asia (Hidayat et al., 2026). We have shown that some model configurations do not resolve the Moist Margin, but if this is rectified then rainfall and humidity impact warnings in the associated forecasting systems could be improved.

Concluding Remarks

Understanding scale–interactions in the tropics remains a key challenge of the atmospheric sciences. This thesis strongly supports the rationale that convection is the primary mediator of scale–interaction in the tropics. The work in this thesis has demonstrated the importance of convective scale–interaction across a full range of scales from daily to interannual, and from tens to tens of thousands of kilometres. These results contribute new process–understanding of how intermediary scale spatial structure can emerge from convective processes, and of the relationship of this emergent structure to regional and global scale variability.

Better process–understanding is key for improving the skill of weather and climate models, and for improving confidence in their physical realism. This thesis confirms that implementing process improvements in models at the convective scale leads to benefits across the full scale–spectrum. Future modelling efforts, whether physical or data–driven, should continue to be evaluated with respect to existing and developing process–understanding, if those models are to be used with confidence for important decision making.

Bibliography

S. Abramian, C. Muller, and C. Risi. Extreme Precipitation in Tropical Squall Lines. *Journal of Advances in Modeling Earth Systems*, 15(10):e2022MS003477, 2023. ISSN 1942-2466. doi: 10.1029/2022MS003477.

F. Adames. The Basic Equations under Weak Temperature Gradient Balance: Formulation, Scaling, and Types of Convectively Coupled Motions. *Journal of the Atmospheric Sciences*, 79(8):2087–2108, Aug. 2022. ISSN 0022-4928, 1520-0469. doi: 10.1175/JAS-D-21-0215.1.

S. Ageet, D. Parker, H. Msemo, W. Colenbrander, E. de Coning, M. Gijben, J. Gonçalves, D. Groves, F. Imbwae, K. Juhanko, G. Kieth, N. Kroese, J. Marsham, D. Mataya, N. Mbuli, G. Monjane, M. Monjane, M. Murambadoro, A. Perrels, A. Roberts, E. Sebego, J. Stander, T. Tawane, C. Taylor, K. Vincent, and C. Vosloo. Weather and Climate Information Services Early Warning for Southern Africa (WISER-EWSA) testbed 1. June 2024. doi: https://doi.org/10.48785/100/267.

F. Ahmed and C. Schumacher. Convective and stratiform components of the precipitation-moisture relationship. *Geophysical Research Letters*, 42(23):10,453–10,462, 2015. ISSN 1944-8007. doi: 10.1002/2015GL066957.

M.-S. Ahn, P. A. Ullrich, J. Lee, P. J. Gleckler, H.-Y. Ma, C. R. Terai, P. A. Bogenschutz, and A. C. Ordonez. Bimodality in simulated precipitation frequency distributions and its relationship with convective parameterizations. *npj Clim Atmos Sci*, 7(1):1–9, June 2024. ISSN 2397-3722. doi: 10.1038/s41612-024-00685-3.

D. A. Alfaro. Low-Tropospheric Shear in the Structure of Squall Lines: Impacts on Latent Heating under Layer-Lifting Ascent. *Journal of the Atmospheric Sciences*, 74(1):229–248, Jan. 2017. ISSN 0022-4928, 1520-0469. doi: 10.1175/JAS-D-16-0168.1.

R. P. Allan, C. Liu, M. Zahn, D. A. Lavers, E. Koukouvagias, and A. Bodas-Salcedo. Physically consistent responses of the global atmospheric hydrological cycle in models and observations. *Surveys in Geophysics*, 35:533–552, 2014. doi: 10.1007/s10712-012-9213-z.

S. R. Anderson, S. J. Cole, C. Klein, C. M. Taylor, C. A. Diop, and M. Kamara. Nowcasting convective activity for the Sahel: A simple probabilistic approach using real-time and historical satellite data on cloud-top temperature. *Quarterly Journal of the Royal Meteorological Society*. ISSN 1477-870X. doi: 10.1002/qj.4607.

S. R. Anderson, S. J. Cole, C. Klein, C. M. Taylor, C. A. Diop, and M. Kamara. Nowcasting convective activity for the Sahel: A simple probabilistic approach using real-time and historical satellite data on cloud-top temperature. *Quarterly Journal of the Royal Meteorological Society*, Nov. 2023. ISSN 1477-870X. doi: 10.1002/qj.4607.

T. Andrews and M. J. Webb. The Dependence of Global Cloud and Lapse Rate Feedbacks on the Spatial Structure of Tropical Pacific Warming. *Journal of Climate*, 31(2):641–654, Jan. 2018. ISSN 0894-8755, 1520-0442. doi: 10.1175/JCLI-D-17-0087.1.

M. Andrychowicz, L. Espeholt, D. Li, S. Merchant, A. Merose, F. Zyda, S. Agrawal, and N. Kalchbrenner. Deep Learning for Day Forecasts from Sparse Observations. July 2023. doi: 10.48550/arXiv.2306.06079.

A. Arakawa. The Cumulus Parameterization Problem: Past, Present, and Future. *Journal of Climate*, 17(13):2493–2525, July 2004. ISSN 0894-8755, 1520-0442. doi: 10.1175/1520-0442(2004)017⟨2493:RATCPP⟩2.0.CO;2.

A. Arakawa and W. H. Schubert. Interaction of a Cumulus Cloud Ensemble with the Large-Scale Environment, Part I. *Journal of the Atmospheric Sciences*, 31(3):674–701, Apr. 1974. ISSN 0022-4928, 1520-0469. doi: 10.1175/1520-0469(1974)031⟨0674:IOACCE⟩2.0.CO;2.

A. A. Aslam, J. Schwendike, S. C. Peatman, C. E. Birch, M. A. Bollasina, and P. Barrett. Mid-level dry air intrusions over the southern Maritime Continent. *Quarterly Journal of the Royal Meteorological Society*, 150(759):727–745, 2024. ISSN 1477-870X. doi: 10.1002/qj.4618.

Astropy Collaboration, A. M. Price-Whelan, P. L. Lim, N. Earl, N. Starkman, L. Bradley, D. L. Shupe, A. A. Patil, L. Corrales, C. E. Brasseur, M. N

"othe, A. Donath, E. Tollerud, B. M. Morris, A. Ginsburg, E. Vaher, B. A. Weaver, J. Tock-

nell, W. Jamieson, M. H. van Kerkwijk, T. P. Robitaille, B. Merry, M. Bachetti, H. M. G "unther, T. L. Aldcroft, J. A. Alvarado-Montes, A. M. Archibald, A. Bódi, S. Bapat, G. Barentsen, J. Bazán, M. Biswas, M. Boquien, D. J. Burke, D. Cara, M. Cara, K. E. Conroy, S. Conseil, M. W. Craig, R. M. Cross, K. L. Cruz, F. D'Eugenio, N. Dencheva, H. A. R. Devillepoix, J. P. Dietrich, A. D. Eigenbrot, T. Erben, L. Ferreira, D. Foreman-Mackey, R. Fox, N. Freij, S. Garg, R. Geda, L. Glattly, Y. Gondhalekar, K. D. Gordon, D. Grant, P. Greenfield, A. M. Groener, S. Guest, S. Gurovich, R. Handberg, A. Hart, Z. Hatfield-Dodds, D. Homeier, G. Hosseinzadeh, T. Jenness, C. K. Jones, P. Joseph, J. B. Kalmbach, E. Karamehmetoglu, M. Kałuszyński, M. S. P. Kelley, N. Kern, W. E. Kerzendorf, E. W. Koch, S. Kulumani, A. Lee, C. Ly, Z. Ma, C. MacBride, J. M. Maljaars, D. Muna, N. A. Murphy, H. Norman, R. O'Steen, K. A. Oman, C. Pacifici, S. Pascual, J. Pascual-Granado, R. R. Patil, G. I. Perren, T. E. Pickering, T. Rastogi, B. R. Roulston, D. F. Ryan, E. S. Rykoff, J. Sabater, P. Sakurikar, J. Salgado, A. Sanghi, N. Saunders, V. Savchenko, L. Schwardt, M. Seifert-Eckert, A. Y. Shih, A. S. Jain, G. Shukla, J. Sick, C. Simpson, S. Singanamalla, L. P. Singer, J. Singhal, M. Sinha, B. M. Sipőcz, L. R. Spitler, D. Stansby, O. Streicher, J. Šumak, J. D. Swinbank, D. S. Taranu, N. Tewary, G. R. Tremblay, M. d. Val-Borro, S. J. Van Kooten, Z. Vasović, S. Verma, J. V. de Miranda Cardoso, P. K. G. Williams, T. J. Wilson, B. Winkel, W. M. Wood-Vasey, R. Xue, P. Yoachim, C. Zhang, A. Zonca, and A. P. Contributors. The astropy project: Sustaining and growing a community-oriented open-source project and the latest major release (v5.0) of the core package. , 935(2):167, Aug. 2022. doi: 10.3847/1538-4357/ac7c74.

A. Badrinath, L. D. Monache, N. Hayatbini, W. Chapman, F. Cannon, and M. Ralph. Improving precipitation forecasts with convolutional neural networks. *Weather and Forecasting*, 38(2): 291 – 306, 2023. doi: 10.1175/WAF-D-22-0002.1.

A. J. Baker, B. Vannière, and P. L. Vidale. On the Realism of Tropical Cyclone Intensification in Global Storm-Resolving Climate Models. *Geophysical Research Letters*, 51(17): e2024GL109841, 2024. ISSN 1944-8007. doi: 10.1029/2024GL109841.

J. Bao, B. Stevens, L. Kluft, and C. Muller. Intensification of daily tropical precipitation extremes from more organized convection. *Science Advances*, 10(8):eadj6801, Feb. 2024. doi: 10.1126/sciadv.adj6801.

H. Bartana, C. I. Garfinkel, O. Shamir, and J. Rao. Projected future changes in equatorial wave

spectrum in CMIP6. *Climate Dynamics*, 60(11):3277–3289, June 2023. ISSN 1432-0894. doi: 10.1007/s00382-022-06510-y.

E. J. Barton, C. Klein, C. M. Taylor, J. Marsham, D. J. Parker, B. Maybee, Z. Feng, and L. R. Leung. Soil moisture gradients strengthen mesoscale convective systems by increasing wind shear. *Nature Geoscience*, 18(4):330–336, Apr. 2025. ISSN 1752-0908. doi: 10.1038/s41561-025-01666-8.

C. Baumberger, R. Knutti, and G. Hirsch Hadorn. Building confidence in climate model projections: an analysis of inferences from fit. *WIREs Climate Change*, 8(3):e454, 2017. doi: https://doi.org/10.1002/wcc.454.

P. Bechtold. Challenges in Tropical Numerical Weather Prediction at ECMWF. In D. A. Randall, J. Srinivasan, R. S. Nanjundiah, and P. Mukhopadhyay, editors, *Current Trends in the Representation of Physical Processes in Weather and Climate Models*, pages 29–50. Springer, Singapore, 2019. ISBN 9789811333965. doi: 10.1007/978-981-13-3396-5_2.

P. Bechtold, N. Semane, P. Lopez, J.-P. Chaboureau, A. Beljaars, and N. Bormann. Representing equilibrium and nonequilibrium convection in large-scale models. *Journal of the Atmospheric Sciences*, 71(2):734 – 753, 2014. doi: 10.1175/JAS-D-13-0163.1.

J. Berner, U. Achatz, L. Batté, L. Bengtsson, A. d. l. Cámara, H. M. Christensen, M. Colangeli, D. R. B. Coleman, D. Crommelin, S. I. Dolaptchiev, C. L. E. Franzke, P. Friederichs, P. Imkeller, H. Järvinen, S. Juricke, V. Kitsios, F. Lott, V. Lucarini, S. Mahajan, T. N. Palmer, C. Penland, M. Sakradzija, J.-S. v. Storch, A. Weisheimer, M. Weniger, P. D. Williams, and J.-I. Yano. Stochastic Parameterization: Toward a New View of Weather and Climate Models. *Bulletin of the American Meteorological Society*, 98(3):565–588, Mar. 2017. ISSN 0003-0007, 1520-0477. doi: 10.1175/BAMS-D-15-00268.1.

L. Besson and Y. Lemaître. Mesoscale Convective Systems in Relation to African and Tropical Easterly Jets. *Monthly Weather Review*, 142(9):3224–3242, Sept. 2014. ISSN 1520-0493, 0027-0644. doi: 10.1175/MWR-D-13-00247.1.

T. Beucler. A correlated stochastic model for the large-scale advection, condensation and diffusion of water vapour. *Quarterly Journal of the Royal Meteorological Society*, 142(697):1721–1731, 2016. ISSN 1477-870X. doi: 10.1002/qj.2768.

G. Biagioli and A. M. Tompkins. A Dimensionless Parameter for Predicting Convective Self-Aggregation Onset in a Stochastic Reaction-Diffusion Model of Tropical Radiative-Convective Equilibrium. *Journal of Advances in Modeling Earth Systems*, 15(5):e2022MS003231, 2023a. ISSN 1942-2466. doi: 10.1029/2022MS003231.

G. Biagioli and A. M. Tompkins. Measuring Convective Organization. *Journal of the Atmospheric Sciences*, 80(12):2769–2789, Nov. 2023b. ISSN 0022-4928, 1520-0469. doi: 10.1175/JAS-D-23-0103.1.

M. Biasutti. Rainfall trends in the African Sahel: Characteristics, processes, and causes. *Wiley Interdisciplinary Reviews. Climate Change*, 10(4):e591, 2019. ISSN 1757-7780. doi: 10.1002/wcc.591.

C. E. Birch, D. J. Parker, A. O'Leary, J. H. Marsham, C. M. Taylor, P. P. Harris, and G. M. S. Lister. Impact of soil moisture and convectively generated waves on the initiation of a West African mesoscale convective system. *Quarterly Journal of the Royal Meteorological Society*, 139(676):1712–1730, 2013. ISSN 1477-870X. doi: 10.1002/qj.2062.

C. E. Birch, D. J. Parker, J. H. Marsham, D. Copsey, and L. Garcia-Carreras. A seamless assessment of the role of convection in the water cycle of the West African Monsoon. *Journal of Geophysical Research: Atmospheres*, 119(6):2890–2912, 2014. ISSN 2169-8996. doi: 10.1002/2013JD020887.

J. Bjerknes. Atmospheric teleconnections from the equatorial pacific. *Monthly Weather Review*, 97(3):163–172, Mar. 1969. ISSN 1520-0493, 0027-0644. doi: 10.1175/1520-0493(1969)097⟨0163:ATFTEP⟩2.3.CO;2.

C. P. O. Bläckberg and M. S. Singh. Increased Large-Scale Convective Aggregation in CMIP5 Projections: Implications for Tropical Precipitation Extremes. *Geophysical Research Letters*, 49(9):e2021GL097295, 2022. ISSN 1944-8007. doi: 10.1029/2021GL097295.

R. J. Bombardi, V. Moron, and J. S. Goodnight. Detection, variability, and predictability of monsoon onset and withdrawal dates: A review. *International Journal of Climatology*, 40(2):641–667, 2020. doi: 10.1002/joc.6264.

M. Bonavita. On some limitations of current machine learning weather prediction models.

Geophysical Research Letters, 51(12):e2023GL107377, 2024. doi: https://doi.org/10.1029/2023GL107377. e2023GL107377 2023GL107377.

S. Bony, B. Stevens, D. M. W. Frierson, C. Jakob, M. Kageyama, R. Pincus, T. G. Shepherd, S. C. Sherwood, A. P. Siebesma, A. H. Sobel, M. Watanabe, and M. J. Webb. Clouds, circulation and climate sensitivity. *Nature Geosci*, 8(4):261–268, Apr. 2015. ISSN 1752-0908. doi: 10.1038/ngeo2398.

S. Bony, B. Stevens, D. Coppin, T. Becker, K. A. Reed, A. Voigt, and B. Medeiros. Thermodynamic control of anvil cloud amount. *Proceedings of the National Academy of Sciences*, 113 (32):8927–8932, Aug. 2016. doi: 10.1073/pnas.1601472113.

S. Bony, A. Semie, R. J. Kramer, B. Soden, A. M. Tompkins, and K. A. Emanuel. Observed Modulation of the Tropical Radiation Budget by Deep Convective Organization and Lower-Tropospheric Stability. *AGU Advances*, 1(3):e2019AV000155, 2020. ISSN 2576-604X. doi: 10.1029/2019AV000155.

S. Bordoni and T. Schneider. Monsoons as eddy-mediated regime transitions of the tropical overturning circulation. *Nature Geoscience*, 1(8):515–519, Aug. 2008. ISSN 1752-0908. doi: 10.1038/ngeo248.

Z. B. Bouallègue, M. C. A. Clare, L. Magnusson, E. Gascón, M. Maier-Gerber, M. Janoušek, M. Rodwell, F. Pinault, J. S. Dramsch, S. T. K. Lang, B. Raoult, F. Rabier, M. Chevallier, I. Sandu, P. Dueben, M. Chantry, and F. Pappenberger. The rise of data-driven weather forecasting: A first statistical assessment of machine learning–based weather forecasts in an operational-like context. *Bulletin of the American Meteorological Society*, 105(6):E864 – E883, 2024. doi: 10.1175/BAMS-D-23-0162.1.

C. S. Bretherton and A. H. Sobel. A Simple Model of a Convectively Coupled Walker Circulation Using the Weak Temperature Gradient Approximation. *Journal of Climate*, 15(20): 2907–2920, Oct. 2002. ISSN 0894-8755, 1520-0442. doi: 10.1175/1520-0442(2002)015⟨2907:ASMOAC⟩2.0.CO;2.

C. S. Bretherton, M. E. Peters, and L. E. Back. Relationships between water vapor path and precipitation over the tropical oceans. *Journal of Climate*, 17(7):1517 – 1528, 2004. doi: 10.1175/1520-0442(2004)017⟨1517:RBWVPA⟩2.0.CO;2.

C. S. Bretherton, P. N. Blossey, and M. Khairoutdinov. An Energy-Balance Analysis of Deep Convective Self-Aggregation above Uniform SST. *Journal of the Atmospheric Sciences*, 62 (12):4273–4292, Dec. 2005. ISSN 0022-4928, 1520-0469. doi: 10.1175/JAS3614.1.

J. R. Brown, M. Lengaigne, B. R. Lintner, M. J. Widlansky, K. van der Wiel, C. Dutheil, B. K. Linsley, A. J. Matthews, and J. Renwick. South Pacific Convergence Zone dynamics, variability and impacts in a changing climate. *Nature Reviews Earth & Environment*, 1(10): 530–543, Oct. 2020. ISSN 2662-138X. doi: 10.1038/s43017-020-0078-2.

R. W. Burpee. The Origin and Structure of Easterly Waves in the Lower Troposphere of North Africa. *Journal of the Atmospheric Sciences*, 29(1):77–90, Jan. 1972. ISSN 0022-4928, 1520-0469. doi: 10.1175/1520-0469(1972)029⟨0077:TOASOE⟩2.0.CO;2.

M. Bush, D. L. A. Flack, H. W. Lewis, S. I. Bohnenstengel, C. J. Short, C. Franklin, A. P. Lock, M. Best, P. Field, A. McCabe, K. Van Weverberg, S. Berthou, I. Boutle, J. K. Brooke, S. Cole, S. Cooper, G. Dow, J. Edwards, A. Finnenkoetter, K. Furtado, K. Halladay, K. Hanley, M. A. Hendry, A. Hill, A. Jayakumar, R. W. Jones, H. Lean, J. C. K. Lee, A. Malcolm, M. Mittermaier, S. Mohandas, S. Moore, C. Morcrette, R. North, A. Porson, S. Rennie, N. Roberts, B. Roux, C. Sanchez, C.-H. Su, S. Tucker, S. Vosper, D. Walters, J. Warner, S. Webster, M. Weeks, J. Wilkinson, M. Whitall, K. D. Williams, and H. Zhang. The third Met Office Unified Model-JULES Regional Atmosphere and Land Configuration, RAL3. *Geoscientific Model Development Discussions*, pages 1–58, November 2024. doi: 10.5194/gmd-2024-201.

M. P. Byrne and T. Schneider. Energetic Constraints on the Width of the Intertropical Convergence Zone. *Journal of Climate*, July 2016a. doi: 10.1175/JCLI-D-15-0767.1.

M. P. Byrne and T. Schneider. Narrowing of the ITCZ in a warming climate: Physical mechanisms. *Geophysical Research Letters*, 43(21):11,350–11,357, 2016b. ISSN 1944-8007. doi: 10.1002/2016GL070396.

M. P. Byrne, A. G. Pendergrass, A. D. Rapp, and K. R. Wodzicki. Response of the Intertropical Convergence Zone to Climate Change: Location, Width, and Strength. *Current Climate Change Reports*, 4(4):355–370, Dec. 2018. ISSN 2198-6061. doi: 10.1007/s40641-018-0110-5.

L. M. V. Carvalho, C. Jones, and B. Liebmann. The South Atlantic Convergence Zone: Intensity, Form, Persistence, and Relationships with Intraseasonal to Interannual Activity and

Extreme Rainfall. *Journal of Climate*, 17(1):88–108, Jan. 2004. ISSN 0894-8755, 1520-0442. doi: 10.1175/1520-0442(2004)017⟨0088:TSACZI⟩2.0.CO;2.

P. Ceppi, F. Brient, M. D. Zelinka, and D. L. Hartmann. Cloud feedback mechanisms and their representation in global climate models. *WIREs Climate Change*, 8(4):e465, 2017. ISSN 1757-7799. doi: 10.1002/wcc.465.

P. B. Cerlini, M. Saraceni, and L. Silvestri. Competing Effect of Radiative and Moisture Feedback in Convective Aggregation States in Two CRMs. *Journal of Advances in Modeling Earth Systems*, 15(2):e2022MS003323, 2023. ISSN 1942-2466. doi: 10.1029/2022MS003323.

J. G. Charney. A Note on Large-Scale Motions in the Tropics. *Journal of the Atmospheric Sciences*, 20(6):607–609, Nov. 1963. ISSN 0022-4928, 1520-0469. doi: 10.1175/1520-0469(1963)020⟨0607:ANOLSM⟩2.0.CO;2.

J. G. Charney and A. Eliassen. On the Growth of the Hurricane Depression. *Journal of the Atmospheric Sciences*, 21(1):68–75, Jan. 1964. ISSN 0022-4928, 1520-0469. doi: 10.1175/1520-0469(1964)021⟨0068:OTGOTH⟩2.0.CO;2.

D. Chen, A. Dai, and A. Hall. The Convective-To-Total Precipitation Ratio and the "Drizzling" Bias in Climate Models. *Journal of Geophysical Research: Atmospheres*, 126(16):e2020JD034198, 2021. ISSN 2169-8996. doi: 10.1029/2020JD034198.

A. C. Clement and B. Soden. The sensitivity of the tropical-mean radiation budget. *Journal of Climate*, 18(16):3189 – 3203, 2005. doi: 10.1175/JCLI3456.1.

S. J. Cole, S. Anderson, A. Diop, C. Taylor, C. Klein, S. Wells, G. Nash, and M. Diagne. Nowcasting Flood Impacts of Convective storms in the Sahel. Technical Report EGU22-13445, Copernicus Meetings, Mar. 2022. URL `https://meetingorganizer.copernicus.org/EGU22/EGU22-13445.html`.

M. Colin, S. Sherwood, O. Geoffroy, S. Bony, and D. Fuchs. Identifying the Sources of Convective Memory in Cloud-Resolving Simulations. *Journal of the Atmospheric Sciences*, Mar. 2019. doi: 10.1175/JAS-D-18-0036.1.

K. H. Cook. Generation of the african easterly jet and its role in determining west african precipitation. *Journal of Climate*, 12(5):1165 – 1184, 1999. doi: 10.1175/1520-0442(1999)012⟨1165:GOTAEJ⟩2.0.CO;2.

K. H. Cook. The South Indian Convergence Zone and Interannual Rainfall Variability over Southern Africa. *Journal of Climate*, 13(21):3789–3804, Nov. 2000. ISSN 0894-8755, 1520-0442. doi: 10.1175/1520-0442(2000)013⟨3789:TSICZA⟩2.0.CO;2.

R. Cornforth, Z. Mumba, D. J. Parker, G. Berry, N. Chapelon, K. Diakaria, M. Diop-Kane, V. Ermert, A. H. Fink, P. Knippertz, J. P. Lafore, A. Laing, S. Lepape, R. Maidment, J. Methven, B. Orji, D. Osika, E. Poan, R. Roca, S. Rowell, R. Smith, T. Spengler, C. M. Taylor, C. Thorncroft, J.-C. Vincendon, C. Yorke, and C. Thorncroft. *Synoptic Systems*, chapter 2, pages 40–89. John Wiley Sons, Ltd, 2017. ISBN 9781118391297. doi: https://doi.org/10.1002/9781118391297.ch2.

G. C. Craig and J. M. Mack. A coarsening model for self-organization of tropical convection. *Journal of Geophysical Research: Atmospheres*, 118(16):8761–8769, 2013. ISSN 2169-8996. doi: 10.1002/jgrd.50674.

G. C. Craig, A. H. Fink, C. Hoose, T. Janjić, P. Knippertz, A. Laurian, S. Lerch, B. Mayer, A. Miltenberger, R. Redl, M. Riemer, K. I. Tempest, and V. Wirth. Waves to Weather: Exploring the Limits of Predictability of Weather. *Bulletin of the American Meteorological Society*, 102(11):E2151–E2164, Nov. 2021. ISSN 0003-0007, 1520-0477. doi: 10.1175/BAMS-D-20-0035.1.

J. Crook, C. Klein, S. Folwell, C. M. Taylor, D. J. Parker, R. Stratton, and T. Stein. Assessment of the Representation of West African Storm Lifecycles in Convection-Permitting Simulations. *Earth and Space Science*, 6(5):818–835, 2019. ISSN 2333-5084. doi: 10.1029/2018EA000491.

P. Das, A. Posch, N. Barber, M. Hicks, K. Duffy, T. Vandal, D. Singh, K. v. Werkhoven, and A. R. Ganguly. Hybrid physics-AI outperforms numerical weather prediction for extreme precipitation nowcasting. *npj Clim Atmos Sci*, 7(1):1–15, Nov. 2024. ISSN 2397-3722. doi: 10.1038/s41612-024-00834-8.

T. Dauhut and C. Hohenegger. The contribution of convection to the stratospheric water vapor: The first budget using a global storm-resolving model. *Journal of Geophysical Research: Atmospheres*, 127(5):e2021JD036295, 2022. doi: https://doi.org/10.1029/2021JD036295.

M. Davison and P. Haynes. A simple model linking radiative–convective instability, convective aggregation and large-scale dynamics. *Weather and Climate Dynamics*, 5(3):1153–1185, Sept. 2024. doi: 10.5194/wcd-5-1153-2024.

S. H. Derbyshire, I. Beau, P. Bechtold, J.-Y. Grandpeix, J.-M. Piriou, J.-L. Redelsperger, and P. M. M. Soares. Sensitivity of moist convection to environmental humidity. *Quarterly Journal of the Royal Meteorological Society*, 130(604):3055–3079, 2004. doi: https://doi.org/10.1256/qj.03.130.

M. Diaz and A. Aiyyer. The Genesis of African Easterly Waves by Upstream Development. *Journal of the Atmospheric Sciences*, Nov. 2013. doi: 10.1175/JAS-D-12-0342.1.

F. J. Doblas-Reyes, A. A. Sörensson, M. Almazroui, A. Dosio, W. J. Gutowski, R. Haarsma, R. Hamdi, B. Hewitson, W.-T. Kwon, B. L. Lamptey, D. Maraun, T. S. Stephenson, I. Takayabu, L. Terray, A. Turner, and Z. Zuo. Linking global to regional climate change. In V. Masson-Delmotte, P. Zhai, A. Pirani, S. L. Connors, C. Péan, S. Berger, N. Caud, Y. Chen, L. Goldfarb, M. I. Gomis, M. Huang, K. Leitzell, E. Lonnoy, J. B. R. Matthews, T. K. Maycock, T. Waterfield, O. Yelekçi, R. Yu, and B. Zhou, editors, *Climate Change 2021: The Physical Science Basis. Contribution of Working Group I to the Sixth Assessment Report of the Intergovernmental Panel on Climate Change*, chapter 10, pages 1363–1512. Cambridge University Press, Cambridge, United Kingdom and New York, NY, USA, 2021. doi: 10.1017/9781009157896.012.

H. Douville and K. M. Willett. A drier than expected future, supported by near-surface relative humidity observations. *Science Advances*, 9:eade6253, 2023. doi: 10.1126/sciadv.ade6253.

A. J. Drager and S. C. van den Heever. Characterizing convective cold pools. *Journal of Advances in Modeling Earth Systems*, 9(2):1091–1115, June 2017. doi: 10.1002/2016MS000788.

J.-P. Duvel. On Vortices Initiated over West Africa and Their Impact on North Atlantic Tropical Cyclones. *Monthly Weather Review*, 149(2):585–601, Feb. 2021. ISSN 1520-0493, 0027-0644. doi: 10.1175/MWR-D-20-0252.1.

T. J. Elless and R. D. Torn. Investigating the factors that contribute to african easterly wave intensity forecast uncertainty in the ecmwf ensemble prediction system. *Monthly Weather Review*, 147(5):1679 – 1698, 2019. doi: 10.1175/MWR-D-18-0071.1.

K. Emanuel, A. A. Wing, and E. M. Vincent. Radiative-convective instability. *Journal of Advances in Modeling Earth Systems*, 6(1):75–90, 2014. ISSN 1942-2466. doi: 10.1002/2013MS000270.

K. A. Emanuel, J. David Neelin, and C. S. Bretherton. On large-scale circulations in convecting atmospheres. *Quarterly Journal of the Royal Meteorological Society*, 120(519):1111–1143, 1994. ISSN 1477-870X. doi: 10.1002/qj.49712051902.

A. F. Feldman, X. Feng, A. J. Felton, A. G. Konings, A. K. Knapp, J. A. Biederman, and B. Poulter. Plant responses to changing rainfall frequency and intensity. *Nature Reviews Earth & Environment*, 5:276–294, 2024. doi: 10.1038/s43017-024-00534-0.

X. Feng, G.-Y. Yang, K. I. Hodges, and J. Methven. Equatorial waves as useful precursors to tropical cyclone occurrence and intensification. *Nature Communications*, 14(1):511, Jan. 2023a. ISSN 2041-1723. doi: 10.1038/s41467-023-36055-5.

Z. Feng, L. R. Leung, N. Liu, J. Wang, R. A. Houze Jr, J. Li, J. C. Hardin, D. Chen, and J. Guo. A Global High-Resolution Mesoscale Convective System Database Using Satellite-Derived Cloud Tops, Surface Precipitation, and Tracking. *Journal of Geophysical Research: Atmospheres*, 126(8):e2020JD034202, 2021. ISSN 2169-8996. doi: 10.1029/2020JD034202.

Z. Feng, L. R. Leung, J. Hardin, C. R. Terai, F. Song, and P. Caldwell. Mesoscale Convective Systems in DYAMOND Global Convection-Permitting Simulations. *Geophysical Research Letters*, 50(4):e2022GL102603, 2023b. ISSN 1944-8007. doi: 10.1029/2022GL102603.

Z. Feng, A. F. Prein, J. Kukulies, T. Fiolleau, W. K. Jones, B. Maybee, Z. L. Moon, K. M. Núñez Ocasio, W. Dong, M. J. Molina, M. G. Albright, M. Rajagopal, V. Robledo, J. Song, F. Song, L. R. Leung, A. C. Varble, C. Klein, R. Roca, R. Feng, and J. F. Mejia. Mesoscale Convective Systems Tracking Method Intercomparison (MCSMIP): Application to DYAMOND Global km-Scale Simulations. *Journal of Geophysical Research: Atmospheres*, 130 (8):e2024JD042204, 2025. ISSN 2169-8996. doi: 10.1029/2024JD042204.

S. Ferrett, G.-Y. Yang, S. J. Woolnough, J. Methven, K. Hodges, and C. E. Holloway. Linking extreme precipitation in Southeast Asia to equatorial waves. *Quarterly Journal of the Royal Meteorological Society*, 146(727):665–684, 2020. ISSN 1477-870X. doi: 10.1002/qj.3699.

P. R. Field, A. Hill, B. Shipway, K. Furtado, J. Wilkinson, A. Miltenberger, H. Gordon, D. P. Grosvenor, R. Stevens, and K. Van Weverberg. Implementation of a double moment cloud microphysics scheme in the UK met office regional numerical weather prediction model. *Quarterly Journal of the Royal Meteorological Society*, 149(752):703–739, 2023. ISSN 1477-870X. doi: 10.1002/qj.4414.

A. H. Fink, T. Engel, V. Ermert, R. van der Linden, M. Schneidewind, R. Redl, E. Afiesimama, W. M. Thiaw, C. Yorke, M. Evans, and S. Janicot. *Mean Climate and Seasonal Cycle*, chapter 1, pages 1–39. John Wiley Sons, Ltd, 2017a. ISBN 9781118391297. doi: https://doi.org/10.1002/9781118391297.ch1.

A. H. Fink, T. Engel, V. Ermert, R. van der Linden, M. Schneidewind, R. Redl, E. Afiesimama, W. M. Thiaw, C. Yorke, M. Evans, and S. Janicot. *Mean Climate and Seasonal Cycle*, chapter 1, pages 1–39. John Wiley Sons, Ltd, 2017b. ISBN 9781118391297. doi: https://doi.org/10.1002/9781118391297.ch1.

D. L. Finney, J. H. Marsham, D. P. Walker, C. E. Birch, B. J. Woodhams, L. S. Jackson, and S. Hardy. The effect of westerlies on East African rainfall and the associated role of tropical cyclones and the Madden-Julian Oscillation. *Quarterly Journal of the Royal Meteorological Society*, 146(727):647–664, Jan. 2020. ISSN 0035-9009. doi: 10.1002/qj.3698.

R. G. J. Fitzpatrick, C. L. Bain, P. Knippertz, J. H. Marsham, and D. J. Parker. The West African Monsoon Onset: A Concise Comparison of Definitions. *Journal of Climate*, 28(22): 8673–8694, Nov. 2015. ISSN 0894-8755, 1520-0442. doi: 10.1175/JCLI-D-15-0265.1.

R. G. J. Fitzpatrick, C. L. Bain, P. Knippertz, J. H. Marsham, and D. J. Parker. On What Scale Can We Predict the Agronomic Onset of the West African Monsoon? *Monthly Weather Review*, 144(4):1571–1589, Apr. 2016a. ISSN 1520-0493, 0027-0644. doi: 10.1175/MWR-D-15-0274.1.

R. G. J. Fitzpatrick, D. J. Parker, and P. D. Willetts. Assessing the level of spatial homogeneity of the agronomic Indian monsoon onset. *Geophysical Research Letters*, 43(22):11,867–11,874, 2016b. ISSN 1944-8007. doi: 10.1002/2016GL070711.

R. G. J. Fitzpatrick, D. J. Parker, J. H. Marsham, D. P. Rowell, F. M. Guichard, C. M. Taylor, K. H. Cook, E. K. Vizy, L. S. Jackson, D. Finney, J. Crook, R. Stratton, and S. Tucker. What Drives the Intensification of Mesoscale Convective Systems over the West African Sahel under Climate Change? *Journal of Climate*, 33(8):3151–3172, Apr. 2020. ISSN 0894-8755, 1520-0442. doi: 10.1175/JCLI-D-19-0380.1.

E. Flaounas, S. Janicot, S. Bastin, R. Roca, and E. Mohino. The role of the Indian monsoon onset in the West African monsoon onset: observations and AGCM nudged simulations. *Climate Dynamics*, 38(5):965–983, Mar. 2012. ISSN 1432-0894. doi: 10.1007/s00382-011-1045-x.

G. B. Folland and A. Sitaram. The uncertainty principle: A mathematical survey. *Journal of Fourier Analysis and Applications*, 3:207–238, 1997. doi: 10.1007/BF02649110.

P. Forster, T. Storelvmo, K. Armour, W. Collins, J.-L. Dufresne, D. Frame, D. J. Lunt, T. Mauritsen, M. D. Palmer, M. Watanabe, M. Wild, and H. Zhang. The earth's energy budget, climate feedbacks, and climate sensitivity. In V. Masson-Delmotte, P. Zhai, A. Pirani, S. L. Connors, C. Péan, S. Berger, N. Caud, Y. Chen, L. Goldfarb, M. I. Gomis, M. Huang, K. Leitzell, E. Lonnoy, J. B. Matthews, T. Maycock, T. Waterfield, O. Yelekçi, R. Yu, and B. Zhou, editors, *Climate Change 2021: The Physical Science Basis. Contribution of Working Group I to the Sixth Assessment Report of the Intergovernmental Panel on Climate Change*, pages 923–1054. Cambridge University Press, Cambridge, United Kingdom and New York, NY, USA, 2021. doi: 10.1017/9781009157896.009.

S. Gadgil. The monsoon system: Land–sea breeze or the ITCZ? *Journal of Earth System Science*, 127(1):1, Jan. 2018. ISSN 0973-774X. doi: 10.1007/s12040-017-0916-x.

K. Gao, L. Harris, M. Bender, J.-H. Chen, L. Zhou, and T. Knutson. Regulating fine-scale resolved convection in high-resolution models for better hurricane track prediction. *Geophysical Research Letters*, 50(13):e2023GL103329, 2023. doi: https://doi.org/10.1029/2023GL103329. e2023GL103329 2023GL103329.

L. Garcia-Carreras, D. J. Parker, and J. H. Marsham. What is the Mechanism for the Modification of Convective Cloud Distributions by Land Surface–Induced Flows? *Journal of the Atmospheric Sciences*, Mar. 2011. doi: 10.1175/2010JAS3604.1.

L. Garcia-Carreras, J. H. Marsham, D. J. Parker, C. L. Bain, S. Milton, A. Saci, M. Salah-Ferroudj, B. Ouchene, and R. Washington. The impact of convective cold pool outflows on model biases in the Sahara. *Geophysical Research Letters*, 40(8):1647–1652, 2013. ISSN 1944-8007. doi: 10.1002/grl.50239.

R. Geen, S. Bordoni, D. S. Battisti, and K. Hui. Monsoons, ITCZs, and the Concept of the Global Monsoon. *Reviews of Geophysics*, 58(4):e2020RG000700, 2020. ISSN 1944-9208. doi: 10.1029/2020RG000700.

A. Gettelman, P. L. Vidale, B. Stevens, F. Ziemen, Z. Feng, H. Konow, T. Kölling, L. Kluft, W. Jones, S. Pasqualetto, Y. Wu, S. Brose, J. Clyne, L. Fita, S. Green, L. Harris, M. A. Hart, J. Kukulies, B. Medeiros, T. M. Merlis, M. Muetzelfeldt, R. Pincus, R. P. da Rocha,

M. Satoh, H. Su, D. Takasuka, C. Terai, P. Ullrich, and T. Zhou. Hacking km-scale models: A participative model for climate information. *Bulletin of the American Meteorological Society*, pages BAMS–D–25–0183.1, 2026. doi: 10.1175/BAMS-D-25-0183.1.

A. E. Gill. Studies of moisture effects in simple atmospheric models: The stable case. *Geophysical & Astrophysical Fluid Dynamics*, 19(1-2):119–152, Feb. 1982. ISSN 0309-1929. doi: 10.1080/03091928208208950.

A. O. Gonzalez, G. Mora Rojas, W. H. Schubert, and R. K. Taft. Transient aspects of the Hadley circulation forced by an idealized off-equatorial ITCZ. *Journal of Advances in Modeling Earth Systems*, 9(1):668–690, 2017. ISSN 1942-2466. doi: 10.1002/2016MS000837.

B. B. Goswami, Z. Lu, and C. Muller. Convective self-aggregation in diurnally oscillating sea surface temperature and solar forcing experiments. *Journal of Advances in Modeling Earth Systems*, 18(1):e2024MS004576, 2026. doi: https://doi.org/10.1029/2024MS004576. e2024MS004576 2024MS004576.

L. D. Grant and S. C. van den Heever. Cold pool dissipation. *Journal of Geophysical Research: Atmospheres*, 121(3):1138–1155, 2016. doi: https://doi.org/10.1002/2015JD023813.

J. O. Haerter. Convective Self-Aggregation As a Cold Pool-Driven Critical Phenomenon. *Geophysical Research Letters*, 46(7):4017–4028, 2019. ISSN 1944-8007. doi: 10.1029/2018GL081817.

J. O. Haerter and C. Muller. Mechanisms for the Self-Organization of Tropical Deep Convection. In *Clouds and their Climatic Impacts*, pages 179–193. American Geophysical Union (AGU), 2023. ISBN 978-1-119-70035-7. doi: 10.1002/9781119700357.ch8.

J. O. Haerter, B. Meyer, and S. B. Nissen. Diurnal self-aggregation. *npj Climate and Atmospheric Science*, 3(1):1–11, July 2020. ISSN 2397-3722. doi: 10.1038/s41612-020-00132-z.

L. J. Harrington, D. Frame, A. D. King, and F. E. L. Otto. How Uneven Are Changes to Impact-Relevant Climate Hazards in a 1.5 °C World and Beyond? *Geophysical Research Letters*, 45(13):6672–6680, 2018. ISSN 1944-8007. doi: 10.1029/2018GL078888.

N. C. G. Hart, C. J. C. Reason, and N. Fauchereau. Cloud bands over southern Africa: seasonality, contribution to rainfall variability and modulation by the MJO. *Climate Dynamics*, 41 (5):1199–1212, Sept. 2013. ISSN 1432-0894. doi: 10.1007/s00382-012-1589-4.

N. C. G. Hart, R. Washington, and R. A. Stratton. Stronger Local Overturning in Convective-Permitting Regional Climate Model Improves Simulation of the Subtropical Annual Cycle. *Geophysical Research Letters*, 45(20):11,334–11,342, 2018. ISSN 1944-8007. doi: 10.1029/2018GL079563. _eprint: https://onlinelibrary.wiley.com/doi/pdf/10.1029/2018GL079563.

D. L. Hartmann, P. N. Blossey, and B. D. Dygert. Convection and Climate: What Have We Learned from Simple Models and Simplified Settings? *Current Climate Change Reports*, 5 (3):196–206, Sept. 2019. ISSN 2198-6061. doi: 10.1007/s40641-019-00136-9.

J. He, H. Brogniez, and L. Picon. Evaluation of tropical water vapour from CMIP6 global climate models using the ESA CCI Water Vapour climate data records. *Atmospheric Chemistry and Physics*, 22(18):12591–12606, Sept. 2022. ISSN 1680-7316. doi: 10.5194/acp-22-12591-2022.

I. M. Held and A. Y. Hou. Nonlinear Axially Symmetric Circulations in a Nearly Inviscid Atmosphere. *Journal of the Atmospheric Sciences*, 37(3):515–533, Mar. 1980. ISSN 0022-4928, 1520-0469. doi: 10.1175/1520-0469(1980)037⟨0515:NASCIA⟩2.0.CO;2.

I. M. Held and B. J. Soden. Robust Responses of the Hydrological Cycle to Global Warming. *Journal of Climate*, Nov. 2006. doi: 10.1175/JCLI3990.1.

H. Hersbach, B. Bell, P. Berrisford, S. Hirahara, A. Horányi, J. Muñoz-Sabater, J. Nicolas, C. Peubey, R. Radu, D. Schepers, A. Simmons, C. Soci, S. Abdalla, X. Abellan, G. Balsamo, P. Bechtold, G. Biavati, J. Bidlot, M. Bonavita, G. De Chiara, P. Dahlgren, D. Dee, M. Diamantakis, R. Dragani, J. Flemming, R. Forbes, M. Fuentes, A. Geer, L. Haimberger, S. Healy, R. J. Hogan, E. Hólm, M. Janisková, S. Keeley, P. Laloyaux, P. Lopez, C. Lupu, G. Radnoti, P. de Rosnay, I. Rozum, F. Vamborg, S. Villaume, and J.-N. Thépaut. The era5 global reanalysis. *Quarterly Journal of the Royal Meteorological Society*, 146(730):1999–2049, 2020. doi: https://doi.org/10.1002/qj.3803.

H. Hersbach, B. Bell, P. Berrisford, G. Biavati, A. Horányi, J. Muñoz Sabater, J. Nicolas, C. Peubey, R. Radu, I. Rozum, D. Schepers, A. Simmons, C. Soci, D. Dee, and J.-N. Thépaut. Era5 hourly data on pressure levels from 1940 to present, 2023a. URL `https://doi.org/10.24381/cds.bd0915c6`.

H. Hersbach, B. Bell, P. Berrisford, G. Biavati, A. Horányi, J. Muñoz Sabater, J. Nicolas, C. Peubey, R. Radu, I. Rozum, D. Schepers, A. Simmons, C. Soci, D. Dee, and J.-N. Thépaut. Era5 hourly data on single levels from 1940 to present, 2023b. Accessed on 27-03-2025.

A. M. Hidayat, C. E. Birch, L. S. Jackson, J. Schwendike, C. Sanchez, and A. J. Matthews. Synoptic-to-interannual drivers of humid heat variability in equatorial southeast asia. *npj Climate and Atmospheric Science*, 2026. doi: 10.1038/s41612-026-01451-3.

J. Hoeller, J. O. Haerter, and N. A. Da Silva. Characteristics of Station-Derived Convective Cold Pools Over Equatorial Africa. *Geophysical Research Letters*, 51(6):e2023GL107308, 2024. ISSN 1944-8007. doi: 10.1029/2023GL107308.

C. Hohenegger and C. Jakob. A Relationship Between ITCZ Organization and Subtropical Humidity. *Geophysical Research Letters*, 47(16):e2020GL088515, 2020. ISSN 1944-8007. doi: 10.1029/2020GL088515.

C. Hohenegger and B. Stevens. Coupled radiative convective equilibrium simulations with explicit and parameterized convection. *Journal of Advances in Modeling Earth Systems*, 8 (3):1468–1482, 2016. ISSN 1942-2466. doi: 10.1002/2016MS000666.

C. E. Holloway and J. D. Neelin. Moisture Vertical Structure, Column Water Vapor, and Tropical Deep Convection. *Journal of the Atmospheric Sciences*, June 2009. doi: 10.1175/2008JAS2806.1.

C. E. Holloway and J. D. Neelin. Temporal Relations of Column Water Vapor and Tropical Precipitation. *Journal of the Atmospheric Sciences*, Apr. 2010. doi: 10.1175/2009JAS3284.1.

C. E. Holloway and S. J. Woolnough. The sensitivity of convective aggregation to diabatic processes in idealized radiative-convective equilibrium simulations. *Journal of Advances in Modeling Earth Systems*, 8(1):166–195, Mar. 2016. doi: 10.1002/2015MS000511.

C. E. Holloway, S. J. Woolnough, and G. M. S. Lister. Precipitation distributions for explicit versus parametrized convection in a large-domain high-resolution tropical case study. *Quarterly Journal of the Royal Meteorological Society*, 138(668):1692–1708, 2012. ISSN 1477-870X. doi: 10.1002/qj.1903.

C. E. Holloway, A. A. Wing, S. Bony, C. Muller, H. Masunaga, T. S. L'Ecuyer, D. D. Turner, and P. Zuidema. Observing Convective Aggregation. *Surv Geophys*, 38(6):1199–1236, Nov. 2017. ISSN 1573-0956. doi: 10.1007/s10712-017-9419-1.

L. A. Holt, M. J. Alexander, L. Coy, A. Molod, W. Putman, and S. Pawson. Tropical Waves and the Quasi-Biennial Oscillation in a 7-km Global Climate Simulation. *Journal of the*

Atmospheric Sciences, 73(9):3771–3783, Sept. 2016. ISSN 0022-4928, 1520-0469. doi: 10.1175/JAS-D-15-0350.1.

J. R. Holton. Tropical dynamics. In R. Dmowska, J. R. Holton, and H. Ross, editors, *An Introduction to Dynamic Meteorology*, pages 370–406. Academic Press, 2004. ISBN 9780123540157.

T. Horinouchi. Modulation of Seasonal Precipitation over the Tropical Western/Central Pacific by Convectively Coupled Mixed Rossby-Gravity Waves. *Journal of the Atmospheric Sciences*, 70(2):600–606, Feb. 2013. ISSN 0022-4928. doi: 10.1175/JAS-D-12-0283.1.

B. J. Hoskins and G.-Y. Yang. The Detailed Dynamics of the Hadley Cell. Part II: December–February. *Journal of Climate*, 34(2):805–823, Jan. 2021. ISSN 0894-8755, 1520-0442. doi: 10.1175/JCLI-D-20-0504.1.

B. J. Hoskins, G.-Y. Yang, and R. M. Fonseca. The detailed dynamics of the June–August Hadley Cell. *Quarterly Journal of the Royal Meteorological Society*, 146(727):557–575, 2020. ISSN 1477-870X. doi: 10.1002/qj.3702.

P. Hosseinzadehtalaei, R. Hamdi, H. Moradkhani, P. Termonia, and H. Tabari. Inequality in human exposure to future climate extremes. *Nat Commun*, 16(1):8058, Aug. 2025. ISSN 2041-1723. doi: 10.1038/s41467-025-63385-3.

A. Y. Hou, R. K. Kakar, S. Neeck, A. A. Azarbarzin, C. D. Kummerow, M. Kojima, R. Oki, K. Nakamura, and T. Iguchi. The Global Precipitation Measurement Mission. *Bulletin of the American Meteorological Society*, 95(5):701–722, May 2014. ISSN 0003-0007, 1520-0477. doi: 10.1175/BAMS-D-13-00164.1.

R. A. Houze. 100 Years of Research on Mesoscale Convective Systems. *Meteorological Monographs*, 59(1):17.1–17.54, Jan. 2018. doi: 10.1175/AMSMONOGRAPHS-D-18-0001.1.

R. A. Houze Jr. Mesoscale convective systems. *Reviews of Geophysics*, 42(4), 2004. ISSN 1944-9208. doi: 10.1029/2004RG000150.

J.-S. Hsieh and K. H. Cook. On the Instability of the African Easterly Jet and the Generation of African Waves: Reversals of the Potential Vorticity Gradient. *Journal of the Atmospheric Sciences*, 65(7):2130–2151, July 2008. ISSN 0022-4928, 1520-0469. doi: 10.1175/2007JAS2552.1.

G. J. Huffman, D. T. Bolvin, D. Braithwaite, K.-L. Hsu, R. J. Joyce, C. Kidd, E. J. Nelkin, S. Sorooshian, E. F. Stocker, J. Tan, D. B. Wolff, and P. Xie. Integrated Multi-satellite Re-

trievals for the Global Precipitation Measurement (GPM) Mission (IMERG). In V. Levizzani, C. Kidd, D. B. Kirschbaum, C. D. Kummerow, K. Nakamura, and F. J. Turk, editors, *Satellite Precipitation Measurement: Volume 1*, pages 343–353. Springer International Publishing, Cham, 2020. ISBN 978-3-030-24568-9. doi: 10.1007/978-3-030-24568-9_19.

G. J. Huffman, E. F. Stocker, D. T. Bolvin, E. J. Nelkin, and J. Tan. Gpm imerg final precipitation l3 half hourly 0.1 degree × 0.1 degree v07, 2023. Accessed on 09-01-2025.

L. S. Jackson, D. L. Finney, E. J. Kendon, J. H. Marsham, D. J. Parker, R. A. Stratton, L. Tomassini, and S. Tucker. The Effect of Explicit Convection on Couplings between Rainfall, Humidity, and Ascent over Africa under Climate Change. *Journal of Climate*, 33(19):8315–8337, Oct. 2020. ISSN 0894-8755, 1520-0442. doi: 10.1175/JCLI-D-19-0322.1.

L. S. Jackson, J. H. Marsham, D. J. Parker, D. L. Finney, R. G. J. Fitzpatrick, D. P. Rowell, R. A. Stratton, and S. Tucker. The Effect of Explicit Convection on Climate Change in the West African Monsoon and Central West African Sahel Rainfall. *Journal of Climate*, Mar. 2022. doi: 10.1175/JCLI-D-21-0258.1.

L. S. Jackson, C. E. Birch, G. Chagnaud, J. H. Marsham, and C. M. Taylor. Daily rainfall variability controls humid heatwaves in the global tropics and subtropics. *Nat Commun*, 16 (1):3461, Apr. 2025. ISSN 2041-1723. doi: 10.1038/s41467-025-58694-6.

C. Jakob, M. S. Singh, and L. Jungandreas. Radiative Convective Equilibrium and Organized Convection: An Observational Perspective. *Journal of Geophysical Research: Atmospheres*, 124(10):5418–5430, 2019. ISSN 2169-8996. doi: 10.1029/2018JD030092.

N. Jeevanjee and D. M. Romps. Convective self-aggregation, cold pools, and domain size. *Geophysical Research Letters*, 40(5):994–998, 2013. ISSN 1944-8007. doi: 10.1002/grl.50204.

N. Jeevanjee, I. Held, and V. Ramaswamy. Manabe's Radiative–Convective Equilibrium. *Bulletin of the American Meteorological Society*, 103(11):E2559–E2569, Nov. 2022. ISSN 0003-0007, 1520-0477. doi: 10.1175/BAMS-D-21-0351.1.

G. C. Johnson, J. M. Lyman, and N. G. Loeb. Improving estimates of Earth's energy imbalance. *Nature Climate Change*, 6(7):639–640, July 2016. ISSN 1758-6798. doi: 10.1038/nclimate3043.

C. D. Jones, J. K. Hughes, N. Bellouin, S. C. Hardiman, G. S. Jones, J. Knight, S. Liddicoat,

F. M. O'Connor, R. J. Andres, C. Bell, K.-O. Boo, A. Bozzo, N. Butchart, P. Cadule, K. D. Corbin, M. Doutriaux-Boucher, P. Friedlingstein, J. Gornall, L. Gray, P. R. Halloran, G. Hurtt, W. J. Ingram, J.-F. Lamarque, R. M. Law, M. Meinshausen, S. Osprey, E. J. Palin, L. Parsons Chini, T. Raddatz, M. G. Sanderson, A. A. Sellar, A. Schurer, P. Valdes, N. Wood, S. Woodward, M. Yoshioka, and M. Zerroukat. The hadgem2-es implementation of cmip5 centennial simulations. *Geoscientific Model Development*, 4(3):543–570, 2011. doi: 10.5194/gmd-4-543-2011.

R. W. Jones, C. Sanchez, H. Lewis, J. Warner, S. Webster, and J. Macholl. Impact of Domain Size on Tropical Precipitation Within Explicit Convection Simulations. *Geophysical Research Letters*, 50(17):e2023GL104672, 2023. ISSN 1944-8007. doi: 10.1029/2023GL104672.

F. Judt. Atmospheric Predictability of the Tropics, Middle Latitudes, and Polar Regions Explored through Global Storm-Resolving Simulations. *Journal of the Atmospheric Sciences*, Jan. 2020. doi: 10.1175/JAS-D-19-0116.1.

F. Judt and R. Rios-Berrios. Resolved Convection Improves the Representation of Equatorial Waves and Tropical Rainfall Variability in a Global Nonhydrostatic Model. *Geophysical Research Letters*, 48(14):e2021GL093265, 2021. ISSN 1944-8007. doi: 10.1029/2021GL093265.

K. Kashinath, M. Mustafa, A. Albert, J.-L. Wu, C. Jiang, S. Esmaeilzadeh, K. Azizzadenesheli, R. Wang, A. Chattopadhyay, A. Singh, A. Manepalli, D. Chirila, R. Yu, R. Walters, B. White, H. Xiao, H. A. Tchelepi, P. Marcus, A. Anandkumar, P. Hassanzadeh, and n. Prabhat. Physics-informed machine learning: case studies for weather and climate modelling. *Philosophical Transactions of the Royal Society A: Mathematical, Physical and Engineering Sciences*, 379(2194):20200093, Feb. 2021. doi: 10.1098/rsta.2020.0093.

R. J. Keane, K. D. Williams, A. J. Stirling, G. M. Martin, C. E. Birch, and D. J. Parker. Fast biases in monsoon rainfall over southern and central india in the met office unified model. *Journal of Climate*, 32(19):6385 – 6402, 2019. doi: 10.1175/JCLI-D-18-0650.1.

R. J. Keane, D. J. Parker, E. Dunn-Sigouin, E. W. Kolstad, and J. H. Marsham. Mid-latitude versus tropical scales of predictability and their implications for forecasting. *Meteorological Applications*, Apr. 2025. ISSN 1350-4827.

E. J. Kendon, R. A. Stratton, S. Tucker, J. H. Marsham, S. Berthou, D. P. Rowell, and C. A. Senior. Enhanced future changes in wet and dry extremes over Africa at convection-permitting

scale. *Nature Communications*, 10(1):1794, Apr. 2019. ISSN 2041-1723. doi: 10.1038/s41467-019-09776-9.

G. N. Kiladis, M. C. Wheeler, P. T. Haertel, K. H. Straub, and P. E. Roundy. Convectively coupled equatorial waves. *Reviews of Geophysics*, 47(2), 2009. ISSN 1944-9208. doi: 10.1029/2008RG000266.

B. Kirsch, C. Hohenegger, and F. Ament. Morphology and growth of convective cold pools observed by a dense station network in Germany. *Quarterly Journal of the Royal Meteorological Society*, 150(759):857–876, 2024. ISSN 1477-870X. doi: 10.1002/qj.4626.

C. Klein and C. M. Taylor. Dry soils can intensify mesoscale convective systems. *Proceedings of the National Academy of Sciences*, 117(35):21132–21137, Sept. 2020. doi: 10.1073/pnas.2007998117.

K. R. Knapp, S. Ansari, C. L. Bain, M. A. Bourassa, M. J. Dickinson, C. Funk, C. N. Helms, C. C. Hennon, C. D. Holmes, G. J. Huffman, J. P. Kossin, H.-T. Lee, A. Loew, and G. Magnusdottir. Globally gridded satellite observations for climate studies. *Bulletin of the American Meteorological Society*, 92(7):893 – 907, 2011. doi: 10.1175/2011BAMS3039.1.

P. Knippertz, H. Wernli, and G. Gläser. A Global Climatology of Tropical Moisture Exports. *Journal of Climate*, 26(10):3031–3045, May 2013. ISSN 0894-8755, 1520-0442. doi: 10.1175/JCLI-D-12-00401.1.

S. F. Kwok. *Langevin and Fokker–Planck Equations and their Generalizations*. World Scientific Publishing Company, 2018. ISBN 9789813228405.

J.-P. Lafore and M. W. Moncrieff. A numerical investigation of the organization and interaction of the convective and stratiform regions of tropical squall lines. *Journal of Atmospheric Sciences*, 46(4):521 – 544, 1989. doi: 10.1175/1520-0469(1989)046⟨0521:ANIOTO⟩2.0.CO;2.

J. P. Lafore, N. Chapelon, M. Diop, B. Gueye, Y. Largeron, S. Lepape, O. Ndiaye, D. J. Parker, E. Poan, R. Roca, R. Roehrig, C. Taylor, and M. Moncrieff. *Deep Convection*, chapter 3, pages 90–129. John Wiley Sons, Ltd, 2017a. ISBN 9781118391297. doi: https://doi.org/10.1002/9781118391297.ch3.

J. P. Lafore, N. Chapelon, M. Diop, B. Gueye, Y. Largeron, S. Lepape, O. Ndiaye, D. J. Parker, E. Poan, R. Roca, R. Roehrig, C. Taylor, and M. Moncrieff. Deep Convection. In

Meteorology of Tropical West Africa, pages 90–129. John Wiley & Sons, Ltd, 2017b. ISBN 978-1-118-39129-7. doi: 10.1002/9781118391297.ch3.

A. G. Laing, R. Carbone, V. Levizzani, and J. Tuttle. The propagation and diurnal cycles of deep convection in northern tropical Africa. *Quarterly Journal of the Royal Meteorological Society*, 134(630):93–109, 2008. ISSN 1477-870X. doi: 10.1002/qj.194.

A. G. Laing, R. E. Carbone, and V. Levizzani. Cycles and Propagation of Deep Convection over Equatorial Africa. *Monthly Weather Review*, 139(9):2832–2853, Sept. 2011. ISSN 1520-0493, 0027-0644. doi: 10.1175/2011MWR3500.1.

C. Lavaysse, C. Flamant, S. Janicot, D. J. Parker, J.-P. Lafore, B. Sultan, and J. Pelon. Seasonal evolution of the West African heat low: a climatological perspective. *Climate Dynamics*, 33 (2):313–330, Aug. 2009. ISSN 1432-0894. doi: 10.1007/s00382-009-0553-4.

F. Li, D. Rosa, W. D. Collins, and M. F. Wehner. "super-parameterization": A better way to simulate regional extreme precipitation? *Journal of Advances in Modeling Earth Systems*, 4 (2), 2012. doi: https://doi.org/10.1029/2011MS000106.

Y.-K. Lim, S. D. Schubert, O. Reale, M.-I. Lee, A. M. Molod, and M. J. Suarez. Sensitivity of Tropical Cyclones to Parameterized Convection in the NASA GEOS-5 Model. *Journal of Climate*, 28(2):551–573, Jan. 2015. ISSN 0894-8755, 1520-0442. doi: 10.1175/JCLI-D-14-00104.1.

Y.-L. Lin. *Mesoscale convective systems*, page 322–378. Cambridge University Press, 2007.

R. D. Lindzen. PLANETARY WAVES ON BETA-PLANES. *Monthly Weather Review*, 95 (7):441–451, July 1967. ISSN 1520-0493, 0027-0644. doi: 10.1175/1520-0493(1967)095⟨0441:PWOBP⟩2.3.CO;2.

R. S. Lindzen and A. V. Hou. Hadley Circulations for Zonally Averaged Heating Centered off the Equator. *Journal of the Atmospheric Sciences*, 45(17):2416–2427, Sept. 1988. ISSN 0022-4928, 1520-0469. doi: 10.1175/1520-0469(1988)045⟨2416:HCFZAH⟩2.0.CO;2.

E. N. Lorenz. The predictability of a flow which possesses many scales of motion. *Tellus A*, 21 (3):289, Jan. 1969. ISSN 1600-0870. doi: 10.3402/tellusa.v21i3.10086.

E. D. Maloney, F. Adames, and H. X. Bui. Madden–Julian oscillation changes under anthro-

pogenic warming. *Nature Climate Change*, 9(1):26–33, Jan. 2019. ISSN 1758-6798. doi: 10.1038/s41558-018-0331-6.

S. Manabe and R. T. Wetherald. Thermal Equilibrium of the Atmosphere with a Given Distribution of Relative Humidity. *Journal of the Atmospheric Sciences*, 24(3):241–259, May 1967. ISSN 0022-4928, 1520-0469. doi: 10.1175/1520-0469(1967)024⟨0241:TEOTAW⟩2.0.CO;2.

G. Mandorli and C. J. Stubenrauch. Assessment of object-based indices to identify convective organization. *Geoscientific Model Development*, 17(21):7795–7813, Nov. 2024. ISSN 1991-959X. doi: 10.5194/gmd-17-7795-2024.

B. Mapes. Evolutionary theory of convective organization. *Journal of the Atmospheric Sciences*, -1(aop), July 2025. ISSN 0022-4928, 1520-0469. doi: 10.1175/JAS-D-24-0066.1.

B. Mapes and R. Neale. Parameterizing Convective Organization to Escape the Entrainment Dilemma. *Journal of Advances in Modeling Earth Systems*, 3(2), 2011. ISSN 1942-2466. doi: 10.1029/2011MS000042.

B. E. Mapes. Gregarious Tropical Convection. *Journal of the Atmospheric Sciences*, 50(13): 2026–2037, July 1993. ISSN 0022-4928, 1520-0469. doi: 10.1175/1520-0469(1993)050⟨2026:GTC⟩2.0.CO;2.

B. E. Mapes. Evolutionary theory of convective organization. *arXiv preprint*, Apr. 2024. doi: 10.48550/arXiv.2404.03480.

B. E. Mapes, E. S. Chung, W. M. Hannah, H. Masunaga, A. J. Wimmers, and C. S. Velden. The Meandering Margin of the Meteorological Moist Tropics. *Geophysical Research Letters*, 45(2):1177–1184, Jan. 2018. ISSN 0094-8276. doi: 10.1002/2017GL076440.

J. H. Marsham, N. S. Dixon, L. Garcia-Carreras, G. M. S. Lister, D. J. Parker, P. Knippertz, and C. E. Birch. The role of moist convection in the West African monsoon system: Insights from continental-scale convection-permitting simulations. *Geophysical Research Letters*, 40 (9):1843–1849, 2013. ISSN 1944-8007. doi: 10.1002/grl.50347.

H. Masunaga and B. E. Mapes. A Mechanism for the Maintenance of Sharp Tropical Margins. *Journal of the Atmospheric Sciences*, Apr. 2020. doi: 10.1175/JAS-D-19-0154.1.

V. Mathon, H. Laurent, and T. Lebel. Mesoscale Convective System Rainfall in the Sahel.

Journal of Applied Meteorology and Climatology, 41(11):1081–1092, Nov. 2002. ISSN 1520-0450, 0894-8763. doi: 10.1175/1520-0450(2002)041⟨1081:MCSRIT⟩2.0.CO;2.

T. Matsuno. Quasi-Geostrophic Motions in the Equatorial Area. *Journal of the Meteorological Society of Japan. Ser. II*, 44(1):25–43, 1966. doi: 10.2151/jmsj1965.44.1_25.

T. Mauritsen and B. Stevens. Missing iris effect as a possible cause of muted hydrological change and high climate sensitivity in models. *Nature Geoscience*, 8(5):346–351, May 2015. ISSN 1752-0908. doi: 10.1038/ngeo2414.

B. Maybee, J. H. Marsham, C. M. Klein, D. J. Parker, E. J. Barton, C. M. Taylor, H. Lewis, C. Sanchez, R. W. Jones, and J. Warner. Wind Shear Effects in Convection–Permitting Models Influence MCS Rainfall and Forcing of Tropical Circulation. *Geophysical Research Letters*, 51(17):e2024GL110119, 2024. ISSN 1944-8007. doi: 10.1029/2024GL110119.

B. Maybee, J. Bassford, J. H. Marsham, H. Lewis, P. Field, C. Klein, and D. J. Parker. How sensitive are sahelian mesoscale convective systems to cold-pool suppression? *Quarterly Journal of the Royal Meteorological Society*, 151(772):e5032, 2025a. doi: https://doi.org/10.1002/qj.5032.

B. Maybee, C. Klein, C. M. Taylor, H. Burns, and J. H. Marsham. Homogeneous Soil Moisture Fields Suppress Sahelian MCS Frequency. *Geophysical Research Letters*, 52(22):e2025GL118583, 2025b. ISSN 1944-8007. doi: 10.1029/2025GL118583.

V. C. Mayta and F. A. Corraliza. The Stirring Tropics: The Ubiquity of Moisture Modes and Moisture–Vortex Instability. *Journal of Climate*, Feb. 2024. doi: 10.1175/JCLI-D-23-0145.1.

A. Mekonnen, C. D. Thorncroft, and A. R. Aiyyer. Analysis of convection and its association with african easterly waves. *Journal of Climate*, 19(20):5405 – 5421, 2006. doi: 10.1175/JCLI3920.1.

M. J. Menne, C. N. Williams, B. E. Gleason, J. J. Rennie, and J. H. Lawrimore. The global historical climatology network monthly temperature dataset, version 4. *Journal of Climate*, 31:9835–9854, 2018. doi: 10.1175/JCLI-D-18-0094.1.

B. Meyer and J. O. Haerter. Mechanical Forcing of Convection by Cold Pools: Collisions and Energy Scaling. *Journal of Advances in Modeling Earth Systems*, 12(11):e2020MS002281, 2020. ISSN 1942-2466. doi: 10.1029/2020MS002281.

S. D. Meyers, B. G. Kelly, and J. J. O'Brien. An introduction to wavelet analysis in oceanography and meteorology: With application to the dispersion of yanai waves. *Monthly Weather Review*, 121:2858–2866, 1993. doi: 10.1175/1520-0493(1993)121⟨2858:AITWAI⟩2.0.CO;2.

M. W. Moncrieff. Organized convective systems: Archetypal dynamical models, mass and momentum flux theory, and parametrization. *Quarterly Journal of the Royal Meteorological Society*, 118(507):819–850, 1992. doi: https://doi.org/10.1002/qj.49711850703.

M. W. Moncrieff. The Multiscale Organization of Moist Convection and the Intersection of Weather and Climate. In *Climate Dynamics: Why Does Climate Vary?*, pages 3–26. American Geophysical Union (AGU), 2010. ISBN 978-1-118-67039-2. doi: 10.1029/2008GM000838.

M. W. Moncrieff. Toward a Dynamical Foundation for Organized Convection Parameterization in GCMs. *Geophysical Research Letters*, 46(23):14103–14108, 2019. ISSN 1944-8007. doi: 10.1029/2019GL085316.

M. W. Moncrieff, C. Liu, and P. Bogenschutz. Simulation, Modeling, and Dynamically Based Parameterization of Organized Tropical Convection for Global Climate Models. *Journal of the Atmospheric Sciences*, 74(5):1363–1380, May 2017. ISSN 0022-4928, 1520-0469. doi: 10.1175/JAS-D-16-0166.1.

H. Moon, L. Gudmundsson, B. P. Guillod, V. Venugopal, and S. I. Seneviratne. Intercomparison of daily precipitation persistence in multiple global observations and climate models. *Environmental Research Letters*, 14(10):105009, Oct. 2019. ISSN 1748-9326. doi: 10.1088/1748-9326/ab4169.

C. P. Morice, J. J. Kennedy, N. A. Rayner, J. P. Winn, E. Hogan, R. E. Killick, R. J. H. Dunn, T. J. Osborn, P. D. Jones, and I. R. Simpson. An updated assessment of near-surface temperature change from 1850: The hadcrut5 data set. *Journal of Geophysical Research: Atmospheres*, 126(3):e2019JD032361, 2021. doi: https://doi.org/10.1029/2019JD032361. e2019JD032361 2019JD032361.

V. Moron and A. W. Robertson. Interannual variability of Indian summer monsoon rainfall onset date at local scale. *International Journal of Climatology*, 34(4):1050–1061, 2014. ISSN 1097-0088. doi: 10.1002/joc.3745.

F. Morris, J. Schwendike, D. J. Parker, and C. Bain. How Is Synoptic-Scale Circulation Influ-

enced by the Dynamics of Mesoscale Convection in Convection-Permitting Simulations over West Africa? *Journal of the Atmospheric Sciences*, 81(4):765–782, apr 2024. ISSN 0022-4928, 1520-0469. doi: 10.1175/JAS-D-22-0032.1.

J. P. Mulholland, J. M. Peters, and H. Morrison. How Does Vertical Wind Shear Influence Entrainment in Squall Lines? *Journal of the Atmospheric Sciences*, 78(6):1931–1946, June 2021. ISSN 0022-4928, 1520-0469. doi: 10.1175/JAS-D-20-0299.1.

C. Muller and S. Bony. What favors convective aggregation and why? *Geophysical Research Letters*, 42(13):5626–5634, 2015. ISSN 1944-8007. doi: 10.1002/2015GL064260.

C. Muller, D. Yang, G. Craig, T. Cronin, B. Fildier, J. O. Haerter, C. Hohenegger, B. Mapes, D. Randall, S. Shamekh, and S. C. Sherwood. Spontaneous Aggregation of Convective Storms. *Annual Review of Fluid Mechanics*, 54(1):133–157, 2022. doi: 10.1146/annurev-fluid-022421-011319.

C. J. Muller and I. M. Held. Detailed Investigation of the Self-Aggregation of Convection in Cloud-Resolving Simulations. *Journal of the Atmospheric Sciences*, 69(8):2551–2565, Aug. 2012. ISSN 0022-4928, 1520-0469. doi: 10.1175/JAS-D-11-0257.1.

C. J. Muller, L. E. Back, P. A. O'Gorman, and K. A. Emanuel. A model for the relationship between tropical precipitation and column water vapor. *Geophysical Research Letters*, 36(16), 2009. ISSN 1944-8007. doi: 10.1029/2009GL039667.

C. Munday, R. Washington, and N. Hart. African Low-Level Jets and Their Importance for Water Vapor Transport and Rainfall. *Geophysical Research Letters*, 48(1):e2020GL090999, 2021. ISSN 1944-8007. doi: 10.1029/2020GL090999.

J. D. Neelin, O. Peters, J. W.-B. Lin, K. Hales, and C. E. Holloway. Rethinking convective quasi-equilibrium: observational constraints for stochastic convective schemes in climate models. *Philosophical Transactions of the Royal Society A: Mathematical, Physical and Engineering Sciences*, 366(1875):2579–2602, 05 2008. ISSN 1364-503X. doi: 10.1098/rsta.2008.0056.

J. D. Neelin, O. Peters, and K. Hales. The Transition to Strong Convection. *Journal of the Atmospheric Sciences*, 66(8):2367–2384, Aug. 2009. ISSN 0022-4928, 1520-0469. doi: 10.1175/2009JAS2962.1.

J. D. Neelin, C. Martinez-Villalobos, S. N. Stechmann, F. Ahmed, G. Chen, J. M. Norris, Y.-H.

Kuo, and G. Lenderink. Precipitation Extremes and Water Vapor. *Curr Clim Change Rep*, 8(1):17–33, Mar. 2022. ISSN 2198-6061. doi: 10.1007/s40641-021-00177-z.

S. E. Nicholson. A revised picture of the structure of the "monsoon" and land ITCZ over West Africa. *Climate Dynamics*, 32(7):1155–1171, June 2009. ISSN 1432-0894. doi: 10.1007/s00382-008-0514-3.

S. E. Nicholson. Climate and climatic variability of rainfall over eastern Africa. *Reviews of Geophysics*, 55(3):590–635, 2017. ISSN 1944-9208. doi: 10.1002/2016RG000544.

S. E. Nicholson. The ITCZ and the Seasonal Cycle over Equatorial Africa. *Bulletin of the American Meteorological Society*, 99(2):337–348, Feb. 2018. ISSN 0003-0007, 1520-0477. doi: 10.1175/BAMS-D-16-0287.1.

S. E. Nicholson, A. I. Barcilon, M. Challa, and J. Baum. Wave Activity on the Tropical Easterly Jet. *Journal of the Atmoshperic Sciences*, July 2007. doi: 10.1175/JAS3946.1.

S. Nieuwolt. Tropical rainfall variability — the agroclimatic impact. *Agriculture and Environment*, 7(2):135–148, 1982. ISSN 0304-1131. doi: https://doi.org/10.1016/0304-1131(82)90003-0.

K. M. N. Ocasio, J. L. Evans, and G. S. Young. A Wave-Relative Framework Analysis of AEW–MCS Interactions Leading to Tropical Cyclogenesis. *Monthly Weather Review*, 148(11):4657–4671, Nov. 2020. ISSN 1520-0493, 0027-0644. doi: 10.1175/MWR-D-20-0152.1.

G. Ohring, A. Gruber, and R. Ellingson. Satellite determinations of the relationship between total longwave radiation flux and infrared window radiance. *Journal of Applied Meteorology and Climatology*, 23(3):416 – 425, 1984. doi: 10.1175/1520-0450(1984)023⟨0416:SDOTRB⟩2.0.CO;2.

P. A. O'Gorman and T. Schneider. Stochastic Models for the Kinematics of Moisture Transport and Condensation in Homogeneous Turbulent Flows. *Journal of the Atmospheric Sciences*, Nov. 2006. doi: 10.1175/JAS3794.1.

T. N. Palmer. A Nonlinear Dynamical Perspective on Climate Prediction. *Journal of Climate*, Feb. 1999. ISSN 1520-0442. doi: 10.1175/1520-0442(1999)012%3C0575:ANDPOC%3E2.0.CO;2.

R. E. Pandya and D. R. Durran. The influence of convectively generated thermal forcing on

the mesoscale circulation around squall lines. *Journal of Atmospheric Sciences*, 53(20):2924 – 2951, 1996. doi: 10.1175/1520-0469(1996)053⟨2924:TIOCGT⟩2.0.CO;2.

D. J. Parker. Cold pools in shear. *Quarterly Journal of the Royal Meteorological Society*, 122 (535):1655–1674, 1996. ISSN 1477-870X. doi: 10.1002/qj.49712253509.

D. J. Parker, R. R. Burton, A. Diongue-Niang, R. J. Ellis, M. Felton, C. M. Taylor, C. D. Thorncroft, P. Bessemoulin, and A. M. Tompkins. The diurnal cycle of the west african monsoon circulation. *Quarterly Journal of the Royal Meteorological Society*, 131(611):2839–2860, 2005a. doi: https://doi.org/10.1256/qj.04.52.

D. J. Parker, C. D. Thorncroft, R. R. Burton, and A. Diongue-Niang. Analysis of the african easterly jet, using aircraft observations from the jet2000 experiment. *Quarterly Journal of the Royal Meteorological Society*, 131(608):1461–1482, 2005b. doi: https://doi.org/10.1256/qj.03.189.

D. J. Parker, A. Fink, S. Janicot, J.-B. Ngamini, M. Douglas, E. Afiesimama, A. Agusti-Panareda, A. Beljaars, F. Dide, A. Diedhiou, T. Lebel, J. Polcher, J.-L. Redelsperger, C. Thorncroft, and G. A. Wilson. The Amma Radiosonde Program and its Implications for the Future of Atmospheric Monitoring Over Africa. *Bulletin of the American Meteorological Society*, 89(7):1015–1028, July 2008. ISSN 0003-0007, 1520-0477. doi: 10.1175/2008BAMS2436.1.

D. J. Parker, P. Willetts, C. Birch, A. G. Turner, J. H. Marsham, C. M. Taylor, S. Kolusu, and G. M. Martin. The interaction of moist convection and mid-level dry air in the advance of the onset of the Indian monsoon. *Quarterly Journal of the Royal Meteorological Society*, 142 (699):2256–2272, 2016. ISSN 1477-870X. doi: 10.1002/qj.2815.

D. J. Parker, A. M. Blyth, S. J. Woolnough, A. J. Dougill, C. L. Bain, E. d. Coning, M. Diop-Kane, A. K. Foamouhoue, B. Lamptey, O. Ndiaye, P. Ruti, E. A. Adefisan, L. K. Amekudzi, P. Antwi-Agyei, C. E. Birch, C. Cafaro, H. Carr, B. Chanzu, S. J. Clarke, H. Coskeran, S. K. Danuor, F. M. d. Andrade, K. Diakaria, C. Dione, C. A. Diop, J. K. Fletcher, A. T. Gaye, J. L. Groves, M. Gudoshava, A. J. Hartley, L. C. Hirons, I. Ibrahim, T. D. James, K. A. Lawal, J. H. Marsham, J. N. Mutemi, E. C. Okogbue, E. Olaniyan, J. B. Omotosho, J. Portuphy, A. J. Roberts, J. Schwendike, Z. T. Segele, T. H. M. Stein, A. L. Taylor, C. M. Taylor, T. A. Warnaars, S. Webster, B. J. Woodhams, and L. Youds. The African SWIFT Project: Growing Science Capability to Bring about a Revolution in Weather Prediction.

Bulletin of the American Meteorological Society, 103(2):E349–E369, Feb. 2022. ISSN 0003-0007, 1520-0477. doi: 10.1175/BAMS-D-20-0047.1.

A. G. Pendergrass, M. P. Byrne, O. Watt-Meyer, P. Maher, and M. J. Webb. Impact of ITCZ width on global climate: ITCZ-MIP. *Geoscientific Model Development*, 17(16):6365–6378, Aug. 2024. ISSN 1991-959X. doi: 10.5194/gmd-17-6365-2024.

O. Peters and J. D. Neelin. Critical phenomena in atmospheric precipitation. *Nature Physics*, 2(6):393–396, June 2006. ISSN 1745-2481. doi: 10.1038/nphys314.

D. Popke, B. Stevens, and A. Voigt. Climate and climate change in a radiative-convective equilibrium version of ECHAM6. *Journal of Advances in Modeling Earth Systems*, 5(1):1–14, 2013. ISSN 1942-2466. doi: 10.1029/2012MS000191.

B. Pospichal, D. Karam, S. Crewell, C. Flamant, A. Hünerbein, O. Bock, and F. Saïd. Diurnal cycle of the intertropical discontinuity over west africa analysed by remote sensing and mesoscale modelling. *Quarterly Journal of the Royal Meteorological Society*, 136(S1):92–106, 2010. doi: https://doi.org/10.1002/qj.435.

D. J. Posselt, S. v. d. Heever, G. Stephens, and M. R. Igel. Changes in the Interaction between Tropical Convection, Radiation, and the Large-Scale Circulation in a Warming Environment. *Journal of Climate*, 25(2):557–571, Jan. 2012. ISSN 0894-8755, 1520-0442. doi: 10.1175/2011JCLI4167.1.

A. F. Prein, W. Langhans, G. Fosser, A. Ferrone, N. Ban, K. Goergen, M. Keller, M. Tölle, O. Gutjahr, F. Feser, E. Brisson, S. Kollet, J. Schmidli, N. P. M. van Lipzig, and R. Leung. A review on regional convection-permitting climate modeling: Demonstrations, prospects, and challenges. *Reviews of Geophysics*, 53(2):323–361, 2015. ISSN 1944-9208. doi: 10.1002/2014RG000475.

M. Provod, J. H. Marsham, D. J. Parker, and C. E. Birch. A Characterization of Cold Pools in the West African Sahel. *Monthly Weather Review*, 144(5):1923–1934, May 2016. ISSN 1520-0493, 0027-0644. doi: 10.1175/MWR-D-15-0023.1.

A. Rasheeda Satheesh, P. Knippertz, A. H. Fink, E.-M. Walz, and T. Gneiting. Sources of predictability of synoptic-scale rainfall during the West African summer monsoon. *Quarterly*

Journal of the Royal Meteorological Society, 149(757):3721–3737, 2023. ISSN 1477-870X. doi: 10.1002/qj.4581.

R. W. Reynolds, T. M. Smith, C. Liu, D. B. Chelton, K. S. Casey, and M. G. Schlax. Daily high-resolution-blended analyses for sea surface temperature. *Journal of Climate*, 20(22):5473 – 5496, 2007. doi: 10.1175/2007JCLI1824.1.

R. Rios-Berrios, K. Emanuel, G. H. Bryan, B. Medeiros, and J. Done. Response of Tropical Climate and Extreme Precipitation to Ocean Temperature in Convection-Permitting Aquaplanet Simulations. *Journal of Advances in Modeling Earth Systems*, 17(10):e2025MS005119, 2025. ISSN 1942-2466. doi: 10.1029/2025MS005119.

A. K. Rizi. What is emergence, after all? *PNAS Nexus*, 5(2):pgag010, 02 2026. ISSN 2752-6542. doi: 10.1093/pnasnexus/pgag010.

A. J. Roberts, J. K. Fletcher, J. Groves, J. H. Marsham, D. J. Parker, A. M. Blyth, E. A. Adefisan, V. O. Ajayi, R. Barrette, E. de Coning, C. Dione, A. Diop, A. K. Foamouhoue, M. Gijben, P. G. Hill, K. A. Lawal, J. Mutemi, M. Padi, T. I. Popoola, P. Rípodas, T. H. Stein, and B. J. Woodhams. Nowcasting for Africa: advances, potential and value. *Weather*, 77(7):250–256, 2022. ISSN 1477-8696. doi: 10.1002/wea.3936.

C. Robinson, S. Narsey, and C. Jakob. Synoptic variability in the tropical oceanic moist margin. *Journal of Geophysical Research: Atmospheres*, 129(11):e2024JD040814, 2024. doi: https://doi.org/10.1029/2024JD040814.

C. Robinson, S. Narsey, C. Jakob, and H. Nguyen. Weather systems associated with synoptic variability in the moist margin. *Weather and Climate Dynamics*, 6(2):369–385, Apr. 2025. doi: 10.5194/wcd-6-369-2025.

R. Roca, J.-P. Lafore, C. Piriou, and J.-L. Redelsperger. Extratropical Dry-Air Intrusions into the West African Monsoon Midtroposphere: An Important Factor for the Convective Activity over the Sahel. *Journal of the Atmospheric Sciences*, Feb. 2005. doi: 10.1175/JAS-3366.1.

M. J. Rodwell and B. J. Hoskins. Monsoons and the dynamics of deserts. *Quarterly Journal of the Royal Meteorological Society*, 122(534):1385–1404, 1996. ISSN 1477-870X. doi: 10.1002/qj.49712253408.

R. Roehrig, D. Bouniol, F. Guichard, F. Hourdin, and J.-L. Redelsperger. The Present and

Future of the West African Monsoon: A Process-Oriented Assessment of CMIP5 Simulations along the AMMA Transect. *Journal of Climate*, 26(17):6471–6505, Sept. 2013. ISSN 0894-8755, 1520-0442. doi: 10.1175/JCLI-D-12-00505.1.

R. Rotunno, J. B. Klemp, and M. L. Weisman. A Theory for Strong, Long-Lived Squall Lines. *Journal of the Atmospheric Sciences*, 45(3):463–485, Feb. 1988. ISSN 0022-4928, 1520-0469. doi: 10.1175/1520-0469(1988)045⟨0463:ATFSLL⟩2.0.CO;2.

J. H. Ruppert and C. Hohenegger. Diurnal Circulation Adjustment and Organized Deep Convection. *Journal of Climate*, 31(12):4899–4916, June 2018. ISSN 0894-8755, 1520-0442. doi: 10.1175/JCLI-D-17-0693.1.

S. S. Rushley, D. Kim, C. S. Bretherton, and M.-S. Ahn. Reexamining the Nonlinear Moisture-Precipitation Relationship Over the Tropical Oceans. *Geophysical Research Letters*, 45(2): 1133–1140, 2018. ISSN 1944-8007. doi: 10.1002/2017GL076296.

J. O. Russell, A. Aiyyer, J. D. White, and W. Hannah. Revisiting the connection between African Easterly Waves and Atlantic tropical cyclogenesis. *Geophysical Research Letters*, 44 (1):587–595, 2017. ISSN 1944-8007. doi: 10.1002/2016GL071236.

J. O. H. Russell, A. Aiyyer, and J. Dylan White. African Easterly Wave Dynamics in Convection-Permitting Simulations: Rotational Stratiform Instability as a Conceptual Model. *Journal of Advances in Modeling Earth Systems*, 12(1):e2019MS001706, 2020. ISSN 1942-2466. doi: 10.1029/2019MS001706.

T. Schneider. The General Circulation of the Atmosphere. *Annual Review of Earth and Planetary Sciences*, 34(1):655–688, 2006. doi: 10.1146/annurev.earth.34.031405.125144.

T. Schneider and S. Bordoni. Eddy-Mediated Regime Transitions in the Seasonal Cycle of a Hadley Circulation and Implications for Monsoon Dynamics. *Journal of the Atmospheric Sciences*, 65(3):915–934, Mar. 2008. ISSN 0022-4928, 1520-0469. doi: 10.1175/2007JAS2415.1.

T. Schneider, P. A. O'Gorman, and X. J. Levine. Water Vapor and the Dynamics of Climate Changes. *Reviews of Geophysics*, 48(3), 2010. ISSN 1944-9208. doi: 10.1029/2009RG000302.

T. Schneider, T. Bischoff, and G. H. Haug. Migrations and dynamics of the intertropical

convergence zone. *Nature*, 513(7516):45–53, Sept. 2014. ISSN 1476-4687. doi: 10.1038/nature13636.

C. J. Schreck. Kelvin Waves and Tropical Cyclogenesis: A Global Survey. *Monthly Weather Review*, 143(10):3996–4011, Oct. 2015. ISSN 1520-0493, 0027-0644. doi: 10.1175/MWR-D-15-0111.1.

C. J. Schreck, J. Molinari, and A. Aiyyer. A Global View of Equatorial Waves and Tropical Cyclogenesis. *Monthly Weather Review*, 140(3):774–788, Mar. 2012. ISSN 1520-0493, 0027-0644. doi: 10.1175/MWR-D-11-00110.1.

C. Schumacher and R. A. Houze. Stratiform rain in the tropics as seen by the trmm precipitation radar. *Journal of Climate*, 16(11):1739 – 1756, 2003. doi: 10.1175/1520-0442(2003)016⟨1739:SRITTA⟩2.0.CO;2.

C. Schumacher and R. A. Houze JR. Stratiform precipitation production over sub-saharan africa and the tropical east atlantic as observed by trmm. *Quarterly Journal of the Royal Meteorological Society*, 132(620):2235–2255, 2006a. doi: https://doi.org/10.1256/qj.05.121.

C. Schumacher and R. A. Houze JR. Stratiform precipitation production over sub-Saharan Africa and the tropical East Atlantic as observed by TRMM. *Quarterly Journal of the Royal Meteorological Society*, 132(620):2235–2255, 2006b. ISSN 1477-870X. doi: 10.1256/qj.05.121.

C. Schumacher, R. A. Houze, and I. Kraucunas. The Tropical Dynamical Response to Latent Heating Estimates Derived from the TRMM Precipitation Radar. *Journal of the Atmospheric Sciences*, June 2004. ISSN 1520-0469.

R. S. Schumacher and K. L. Rasmussen. The formation, character and changing nature of mesoscale convective systems. *Nature Reviews Earth & Environment*, 1(6):300–314, June 2020. ISSN 2662-138X. doi: 10.1038/s43017-020-0057-7.

J. Schwendike, P. Govekar, M. J. Reeder, R. Wardle, G. J. Berry, and C. Jakob. Local partitioning of the overturning circulation in the tropics and the connection to the Hadley and Walker circulations. *Journal of Geophysical Research: Atmospheres*, 119(3):1322–1339, 2014. ISSN 2169-8996. doi: 10.1002/2013JD020742.

J. Schwendike, G. J. Berry, K. Fodor, and M. J. Reeder. On the Relationship Between the Madden-Julian Oscillation and the Hadley and Walker Circulations. *Journal of Geo-*

physical Research: Atmospheres, 126(4):e2019JD032117, 2021. ISSN 2169-8996. doi: 10.1029/2019JD032117.

H. Segura, X. Pedruzo-Bagazgoitia, P. Weiss, S. K. Müller, T. Rackow, J. Lee, E. Dolores-Tesillos, I. Benedict, M. Aengenheyster, R. Aguridan, G. Arduini, A. J. Baker, J. Bao, S. Bastin, E. Baulenas, T. Becker, S. Beyer, H. Bockelmann, N. Brüggemann, L. Brunner, S. K. Cheedela, S. Das, J. Denissen, I. Dragaud, P. Dziekan, M. Ekblom, J. F. Engels, M. Esch, R. Forbes, C. Frauen, L. Freischem, D. García-Maroto, P. Geier, P. Gierz, A. González-Cervera, K. Grayson, M. Griffith, O. Gutjahr, H. Haak, I. Hadade, K. Haslehner, S. ul Hasson, J. Hegewald, L. Kluft, A. Koldunov, N. Koldunov, T. Kölling, S. Koseki, S. Kosukhin, J. Kousal, P. Kuma, A. U. Kumar, R. Li, N. Maury, M. Meindl, S. Milinski, K. Mogensen, B. Niraula, J. Nowak, D. S. Praturi, U. Proske, D. Putrasahan, R. Redler, D. Santuy, D. Sármány, R. Schnur, P. Scholz, D. Sidorenko, D. Spät, B. Sützl, D. Takasuka, A. Tompkins, A. Uribe, M. Valentini, M. Veerman, A. Voigt, S. Warnau, F. Wachsmann, M. Wacławczyk, N. Wedi, K.-H. Wieners, J. Wille, M. Winkler, Y. Wu, F. Ziemen, J. Zimmermann, F. A.-M. Bender, D. Bojovic, S. Bony, S. Bordoni, P. Brehmer, M. Dengler, E. Dutra, S. Faye, E. Fischer, C. van Heerwaarden, C. Hohenegger, H. Järvinen, M. Jochum, T. Jung, J. H. Jungclaus, N. S. Keenlyside, D. Klocke, H. Konow, M. Klose, S. Malinowski, O. Martius, T. Mauritsen, J. P. Mellado, T. Mieslinger, E. Mohino, H. Pawłowska, K. Peters-von Gehlen, A. Sarré, P. Sobhani, P. Stier, L. Tuppi, P. L. Vidale, I. Sandu, and B. Stevens. nextgems: entering the era of kilometer-scale earth system modeling. *Geoscientific Model Development*, 18(20):7735–7761, 2025. doi: 10.5194/gmd-18-7735-2025.

A. Semie and S. Bony. Monthly iorg index of deep convective organization across the tropical belt (30s-30n).

A. G. Semie and S. Bony. Relationship Between Precipitation Extremes and Convective Organization Inferred From Satellite Observations. *Geophysical Research Letters*, 47(9): e2019GL086927, 2020. ISSN 1944-8007. doi: 10.1029/2019GL086927.

C. A. Senior, J. H. Marsham, S. Berthou, L. E. Burgin, S. S. Folwell, E. J. Kendon, C. M. Klein, R. G. Jones, N. Mittal, D. P. Rowell, L. Tomassini, T. Vischel, B. Becker, C. E. Birch, J. Crook, A. J. Dougill, D. L. Finney, R. J. Graham, N. C. G. Hart, C. D. Jack, L. S. Jackson, R. James, B. Koelle, H. Misiani, B. Mwalukanga, D. J. Parker, R. A. Stratton, C. M. Taylor, S. O. Tucker, C. M. Wainwright, R. Washington, and M. R. Willet. Convection-

Permitting Regional Climate Change Simulations for Understanding Future Climate and Informing Decision-Making in Africa. *Bulletin of the American Meteorological Society*, 102 (6):E1206–E1223, June 2021. ISSN 0003-0007, 1520-0477. doi: 10.1175/BAMS-D-20-0020.1.

Y. L. Serra, A. Rowe, D. K. Adams, and G. N. Kiladis. Kelvin Waves during GOAmazon and Their Relationship to Deep Convection. *Journal of the Atmospheric Sciences*, 77(10): 3533–3550, Oct. 2020. ISSN 0022-4928, 1520-0469. doi: 10.1175/JAS-D-20-0008.1.

S. C. Sherwood, R. Roca, T. M. Weckwerth, and N. G. Andronova. Tropospheric water vapor, convection, and climate. *Reviews of Geophysics*, 48(2), 2010. ISSN 1944-9208. doi: 10.1029/2009RG000301.

L. G. Silvers, B. Stevens, T. Mauritsen, and M. Giorgetta. Radiative convective equilibrium as a framework for studying the interaction between convection and its large-scale environment. *Journal of Advances in Modeling Earth Systems*, 8(3):1330–1344, 2016. ISSN 1942-2466. doi: 10.1002/2016MS000629.

I. R. Simpson, K. A. McKinnon, D. Kennedy, D. M. Lawrence, F. Lehner, and R. Seager. Observed humidity trends in dry regions contradict climate models. *Proceedings of the National Academy of Sciences*, 121:e2302480120, 2024. doi: 10.1073/pnas.2302480120.

J. Slawinska, O. Pauluis, A. J. Majda, and W. W. Grabowski. Multiscale Interactions in an Idealized Walker Cell: Analysis with Isentropic Streamfunctions. *Journal of the Atmospheric Sciences*, 73(3):1187–1203, Feb. 2016. ISSN 0022-4928, 1520-0469. doi: 10.1175/JAS-D-15-0070.1.

J. Slingo, P. Bates, P. Bauer, S. Belcher, T. Palmer, G. Stephens, B. Stevens, T. Stocker, and G. Teutsch. Ambitious partnership needed for reliable climate prediction. *Nature Climate Change*, 12(6):499–503, June 2022. ISSN 1758-6798. doi: 10.1038/s41558-022-01384-8. Publisher: Nature Publishing Group.

R. K. Smith. On the theory of cisk. *Quarterly Journal of the Royal Meteorological Society*, 123 (538):407–418, 1997. ISSN 1477-870X. doi: 10.1002/qj.49712353808.

A. H. Sobel, J. Nilsson, and L. M. Polvani. The Weak Temperature Gradient Approximation and Balanced Tropical Moisture Waves. *Journal of the Atmospheric Sciences*, 58(23):3650–3665,

Dec. 2001. ISSN 0022-4928, 1520-0469. doi: 10.1175/1520-0469(2001)058⟨3650:TWTGAA⟩2.0.CO;2.

A. H. Sobel, G. Bellon, and J. Bacmeister. Multiple equilibria in a single-column model of the tropical atmosphere. *Geophysical Research Letters*, 34(22), Nov. 2007. ISSN 1944-8007. doi: 10.1029/2007GL031320.

D. Spät, M. Biasutti, D. Schuhbauer, and A. Voigt. Autocorrelation—a simple diagnostic for tropical precipitation variability in global kilometer-scale climate models. *Geophysical Research Letters*, 51(17):e2024GL108856, 2024. doi: https://doi.org/10.1029/2024GL108856.

A. K. Steiner, B. C. Lackner, and M. A. Ringer. Tropical convection regimes in climate models: evaluation with satellite observations. *Atmospheric Chemistry and Physics*, 18(7):4657–4672, Apr. 2018. ISSN 1680-7316. doi: 10.5194/acp-18-4657-2018.

C. C. Stephan, N. Žagar, and T. G. Shepherd. Waves and coherent flows in the tropical atmosphere: New opportunities, old challenges. *Quarterly Journal of the Royal Meteorological Society*, 147(738):2597–2624, 2021. ISSN 1477-870X. doi: 10.1002/qj.4109.

B. A. Stephens and C. S. Jackson. Abrupt transitions in an atmospheric single-column model with weak temperature gradient approximation. *Weather and Climate Dynamics*, 1(2):389–404, Aug. 2020. doi: 10.5194/wcd-1-389-2020.

G. L. Stephens, T. L'Ecuyer, R. Forbes, A. Gettelmen, J.-C. Golaz, A. Bodas-Salcedo, K. Suzuki, P. Gabriel, and J. Haynes. Dreary state of precipitation in global models. *Journal of Geophysical Research: Atmospheres*, 115(D24), 2010. ISSN 2156-2202. doi: 10.1029/2010JD014532.

B. Stevens. Atmospheric Moist Convection. *Annual Review of Earth and Planetary Sciences*, 33(1):605–643, 2005. doi: 10.1146/annurev.earth.33.092203.122658.

B. Stevens and S. Bony. What Are Climate Models Missing? *Science*, 340(6136):1053–1054, May 2013. doi: 10.1126/science.1237554.

B. Stevens, M. Satoh, L. Auger, J. Biercamp, C. S. Bretherton, X. Chen, P. Düben, F. Judt, M. Khairoutdinov, D. Klocke, C. Kodama, L. Kornblueh, S.-J. Lin, P. Neumann, W. M. Putman, N. Röber, R. Shibuya, B. Vanniere, P. L. Vidale, N. Wedi, and L. Zhou. DYAMOND: the DYnamics of the Atmospheric general circulation Modeled On Non-hydrostatic Domains.

Progress in Earth and Planetary Science, 6(1):61, Sept. 2019. ISSN 2197-4284. doi: 10.1186/s40645-019-0304-z.

R. A. Stratton, C. A. Senior, S. B. Vosper, S. S. Folwell, I. A. Boutle, P. D. Earnshaw, E. Kendon, A. P. Lock, A. Malcolm, J. Manners, C. J. Morcrette, C. Short, A. J. Stirling, C. M. Taylor, S. Tucker, S. Webster, and J. M. Wilkinson. A Pan-African Convection-Permitting Regional Climate Simulation with the Met Office Unified Model: CP4-Africa. *Journal of Climate*, May 2018. doi: 10.1175/JCLI-D-17-0503.1.

F. M. Strnad, K. M. Hunt, N. Boers, and B. Goswami. Intraseasonal synchronization of extreme rainfall between North India and the Sahel. *Quarterly Journal of the Royal Meteorological Society*, 151(769):e4946, 2025. ISSN 1477-870X. doi: 10.1002/qj.4946.

J. Sukhatme and W. R. Young. The advection–condensation model and water-vapour probability density functions. *Quarterly Journal of the Royal Meteorological Society*, 137(659): 1561–1572, 2011. ISSN 1477-870X. doi: 10.1002/qj.869.

C. Sánchez, J. Methven, S. Gray, and M. Cullen. Linking rapid forecast error growth to diabatic processes. *Quarterly Journal of the Royal Meteorological Society*, 146(732):3548–3569, 2020. ISSN 1477-870X. doi: 10.1002/qj.3861.

I. Takayabu, R. Rasmussen, E. Nakakita, A. Prein, H. Kawase, S.-I. Watanabe, S. A. Adachi, T. Takemi, K. Yamaguchi, Y. Osakada, and Y.-H. Wu. Convection-Permitting Models for Climate Research. *Bulletin of the American Meteorological Society*, 103(1):E77–E82, Jan. 2022. ISSN 0003-0007, 1520-0477. doi: 10.1175/BAMS-D-21-0043.1.

S. Taraphdar, P. Mukhopadhyay, L. R. Leung, F. Zhang, S. Abhilash, and B. N. Goswami. The role of moist processes in the intrinsic predictability of Indian Ocean cyclones. *Journal of Geophysical Research: Atmospheres*, 119(13):8032–8048, 2014. ISSN 2169-8996. doi: 10.1002/2013JD021265.

C. M. Taylor, P. P. Harris, and D. J. Parker. Impact of soil moisture on the development of a Sahelian mesoscale convective system: a case-study from the AMMA Special Observing Period. *Quarterly Journal of the Royal Meteorological Society*, 136(S1):456–470, 2010. ISSN 1477-870X. doi: 10.1002/qj.465.

C. M. Taylor, A. Gounou, F. Guichard, P. P. Harris, R. J. Ellis, F. Couvreux, and M. De Kauwe.

Frequency of Sahelian storm initiation enhanced over mesoscale soil-moisture patterns. *Nature Geoscience*, 4(7):430–433, July 2011a. ISSN 1752-0908. doi: 10.1038/ngeo1173.

C. M. Taylor, D. J. Parker, N. Kalthoff, M. A. Gaertner, N. Philippon, S. Bastin, P. P. Harris, A. Boone, F. Guichard, A. Agusti-Panareda, M. Baldi, P. Cerlini, L. Descroix, H. Douville, C. Flamant, J.-Y. Grandpeix, and J. Polcher. New perspectives on land–atmosphere feedbacks from the African Monsoon Multidisciplinary Analysis. *Atmospheric Science Letters*, 12(1): 38–44, 2011b. ISSN 1530-261X. doi: 10.1002/asl.336.

C. M. Taylor, C. E. Birch, D. J. Parker, N. Dixon, F. Guichard, G. Nikulin, and G. M. S. Lister. Modeling soil moisture-precipitation feedback in the Sahel: Importance of spatial scale versus convective parameterization. *Geophysical Research Letters*, 40(23):6213–6218, 2013. ISSN 1944-8007. doi: 10.1002/2013GL058511.

C. M. Taylor, D. Belušić, F. Guichard, D. J. Parker, T. Vischel, O. Bock, P. P. Harris, S. Janicot, C. Klein, and G. Panthou. Frequency of extreme Sahelian storms tripled since 1982 in satellite observations. *Nature*, 544(7651):475–478, Apr. 2017. ISSN 1476-4687. doi: 10.1038/nature22069.

C. M. Taylor, C. Klein, C. Dione, D. J. Parker, J. Marsham, C. A. Diop, J. Fletcher, A. A. S. Chaibou, D. B. Nafissa, V. S. Semeena, S. J. Cole, and S. R. Anderson. Nowcasting tracks of severe convective storms in West Africa from observations of land surface state. *Environmental Research Letters*, 17(3):034016, Feb. 2022. ISSN 1748-9326. doi: 10.1088/1748-9326/ac536d.

C. D. Thorncroft and B. J. Hoskins. An idealized study of African easterly waves. I: A linear view. *Quarterly Journal of the Royal Meteorological Society*, 120(518):953–982, 1994. ISSN 1477-870X. doi: 10.1002/qj.49712051809.

C. D. Thorncroft, N. M. J. Hall, and G. N. Kiladis. Three-dimensional structure and dynamics of african easterly waves. part iii: Genesis. *Journal of the Atmospheric Sciences*, 65(11):3596 – 3607, 2008. doi: 10.1175/2008JAS2575.1.

I. Tobin, S. Bony, and R. Roca. Observational Evidence for Relationships between the Degree of Aggregation of Deep Convection, Water Vapor, Surface Fluxes, and Radiation. *Journal of Climate*, 25(20):6885–6904, Oct. 2012. ISSN 0894-8755, 1520-0442. doi: 10.1175/JCLI-D-11-00258.1.

M. Todd and R. Washington. Circulation anomalies associated with tropical-temperate troughs in southern Africa and the south west Indian Ocean. *Climate Dynamics*, 15(12):937–951, Dec. 1999. ISSN 1432-0894. doi: 10.1007/s003820050323.

L. Tomassini. Mesoscale Circulations and Organized Convection in African Easterly Waves. *Journal of the Atmospheric Sciences*, 75(12):4357–4381, Dec. 2018. ISSN 0022-4928, 1520-0469. doi: 10.1175/JAS-D-18-0183.1.

L. Tomassini. The Interaction between Moist Convection and the Atmospheric Circulation in the Tropics. *Bulletin of the American Meteorological Society*, 101(8):E1378–E1396, Aug. 2020. ISSN 0003-0007, 1520-0477. doi: 10.1175/BAMS-D-19-0180.1.

L. Tomassini and G.-Y. Yang. Tropical moist convection as an important driver of Atlantic Hadley circulation variability. *Quarterly Journal of the Royal Meteorological Society*, 148 (748):3287–3302, 2022. ISSN 1477-870X. doi: 10.1002/qj.4359.

L. Tomassini, D. J. Parker, A. Stirling, C. Bain, C. Senior, and S. Milton. The interaction between moist diabatic processes and the atmospheric circulation in African Easterly Wave propagation. *Quarterly Journal of the Royal Meteorological Society*, 143(709):3207–3227, 2017. ISSN 1477-870X. doi: 10.1002/qj.3173.

A. M. Tompkins. Organization of Tropical Convection in Low Vertical Wind Shears: The Role of Cold Pools. *Journal of the Atmospheric Sciences*, 58(13):1650–1672, July 2001a. ISSN 0022-4928, 1520-0469. doi: 10.1175/1520-0469(2001)058⟨1650:OOTCIL⟩2.0.CO;2.

A. M. Tompkins. Organization of Tropical Convection in Low Vertical Wind Shears: The Role of Water Vapor. *Journal of the Atmospheric Sciences*, mar 2001b. ISSN 1520-0469.

A. M. Tompkins and A. G. Semie. Organization of tropical convection in low vertical wind shears: Role of updraft entrainment. *Journal of Advances in Modeling Earth Systems*, 9(2): 1046–1068, 2017. ISSN 1942-2466. doi: 10.1002/2016MS000802.

C. Torrence and G. P. Compo. A practical guide to wavelet analysis. *Bulletin of the American Meteorological Society*, 79:61–78, 1998. doi: 10.1175/1520-0477(1998)079⟨0061:APGTWA⟩2.0.CO;2.

G. Torri and Z. Kuang. On Cold Pool Collisions in Tropical Boundary Layers. *Geophysical Research Letters*, 46(1):399–407, 2019. ISSN 1944-8007. doi: 10.1029/2018GL080501.

G. Torri, Z. Kuang, and Y. Tian. Mechanisms for convection triggering by cold pools. *Geophysical Research Letters*, 42(6):1943–1950, 2015. ISSN 1944-8007. doi: 10.1002/2015GL063227.

K. E. Trenberth. Conceptual Framework for Changes of Extremes of the Hydrological Cycle with Climate Change. *Climatic Change*, 42(1):327–339, May 1999. ISSN 1573-1480. doi: 10.1023/A:1005488920935.

K. E. Trenberth. Changes in precipitation with climate change. *Climate Research*, 47:123–138, Mar. 2011. ISSN 1616-1572, 0936-577X. doi: 10.3354/cr00953.

K. E. Trenberth, L. Cheng, Y. Pan, J. Fasullo, and M. Mayer. Distinctive Pattern of Global Warming in Ocean Heat Content. *Journal of Climate*, 38(9):2155–2168, Apr. 2025. ISSN 0894-8755, 1520-0442. doi: 10.1175/JCLI-D-24-0609.1.

T. Trent, M. Schröder, S.-P. Ho, S. Beirle, R. Bennartz, E. Borbas, C. Borger, H. Brogniez, X. Calbet, E. Castelli, G. P. Compo, W. Ebisuzaki, U. Falk, F. Fell, J. Forsythe, H. Hersbach, M. Kachi, S. Kobayashi, R. E. Kursinski, D. Loyola, Z. Luo, J. K. Nielsen, E. Papandrea, L. Picon, R. Preusker, A. Reale, L. Shi, L. Slivinski, J. Teixeira, T. Vonder Haar, and T. Wagner. Evaluation of total column water vapour products from satellite observations and reanalyses within the GEWEX Water Vapor Assessment. *Atmospheric Chemistry and Physics*, 24(16):9667–9695, August 2024. ISSN 1680-7316. doi: 10.5194/acp-24-9667-2024.

T. M. Trzeciak, L. Garcia-Carreras, and J. H. Marsham. Cross-Saharan transport of water vapor via recycled cold pool outflows from moist convection. *Geophysical Research Letters*, 44(3):1554–1563, 2017. ISSN 1944-8007. doi: 10.1002/2016GL072108.

S. N. Tulich and G. N. Kiladis. Squall Lines and Convectively Coupled Gravity Waves in the Tropics: Why Do Most Cloud Systems Propagate Westward? *Journal of the Atmospheric Sciences*, 69(10):2995–3012, Oct. 2012. ISSN 0022-4928, 1520-0469. doi: 10.1175/JAS-D-11-0297.1.

A. G. Turner, G. S. Bhat, G. M. Martin, D. J. Parker, C. M. Taylor, A. K. Mitra, S. N. Tripathi, S. Milton, E. N. Rajagopal, J. G. Evans, R. Morrison, S. Pattnaik, M. Sekhar, B. K. Bhattacharya, R. Madan, M. Govindankutty, J. K. Fletcher, P. D. Willetts, A. Menon, J. H. Marsham, , the INCOMPASS team, K. M. R. Hunt, T. Chakraborty, G. George, M. Krishnan, C. Sarangi, D. Belušić, L. Garcia-Carreras, M. Brooks, S. Webster, J. K. Brooke, C. Fox, R. C. Harlow, J. M. Langridge, A. Jayakumar, S. J. Böing, O. Halliday, J. Bowles, J. Kent,

D. O'Sullivan, A. Wilson, C. Woods, S. Rogers, R. Smout-Day, D. Tiddeman, D. Desai, R. Nigam, S. Paleri, A. Sattar, M. Smith, D. Anderson, S. Bauguitte, R. Carling, C. Chan, S. Devereau, G. Gratton, D. MacLeod, G. Nott, M. Pickering, H. Price, S. Rastall, C. Reed, J. Trembath, A. Woolley, A. Volonté, and B. New. Interaction of convective organization with monsoon precipitation, atmosphere, surface and sea: The 2016 incompass field campaign in india. *Quarterly Journal of the Royal Meteorological Society*, 146(731):2828–2852, 2020. doi: https://doi.org/10.1002/qj.3633.

K. van der Wiel, A. J. Matthews, D. P. Stevens, and M. M. Joshi. A dynamical framework for the origin of the diagonal south pacific and south atlantic convergence zones. *Quarterly Journal of the Royal Meteorological Society*, 141(691):1997–2010, 2015. doi: https://doi.org/10.1002/qj.2508.

D. P. van Vuuren, J. Edmonds, M. Kainuma, K. Riahi, A. Thomson, K. Hibbard, G. C. Hurtt, T. Kram, V. Krey, J.-F. Lamarque, T. Masui, M. Meinshausen, N. Nakicenovic, S. J. Smith, and S. K. Rose. The representative concentration pathways: an overview. *Climatic Change*, 109(1):5, Aug. 2011. doi: 10.1007/s10584-011-0148-z.

A. C. Varble, Z. Feng, J. N. Marquis, Z. Zhang, A. Geiss, J. C. Hardin, and E. Jo. Updraft Width Modulates Ambient Atmospheric Controls on Convective Cloud Depth. *Journal of Geophysical Research: Atmospheres*, 129(23):e2024JD041769, Dec. 2024. ISSN 2169-897X. doi: 10.1029/2024JD041769.

D. G. Vincent. The South Pacific Convergence Zone (SPCZ): A Review. *Monthly Weather Review*, 122(9):1949–1970, Sept. 1994. ISSN 1520-0493, 0027-0644. doi: 10.1175/1520-0493(1994)122⟨1949:TSPCZA⟩2.0.CO;2.

P. Vogel, P. Knippertz, T. Gneiting, A. H. Fink, M. Klar, and A. Schlueter. Statistical Forecasts for the Occurrence of Precipitation Outperform Global Models over Northern Tropical Africa. *Geophysical Research Letters*, 48(3):e2020GL091022, 2021. ISSN 1944-8007. doi: 10.1029/2020GL091022.

C. M. Wainwright, J. H. Marsham, D. P. Rowell, D. L. Finney, and E. Black. Future Changes in Seasonality in East Africa from Regional Simulations with Explicit and Parameterized Convection. *Journal of Climate*, 34(4):1367–1385, Feb. 2021. ISSN 0894-8755. doi: 10.1175/JCLI-D-20-0450.1.

D. Walters, A. J. Baran, I. Boutle, M. Brooks, P. Earnshaw, J. Edwards, K. Furtado, P. Hill, A. Lock, J. Manners, C. Morcrette, J. Mulcahy, C. Sanchez, C. Smith, R. Stratton, W. Tennant, L. Tomassini, K. Van Weverberg, S. Vosper, M. Willett, J. Browse, A. Bushell, K. Carslaw, M. Dalvi, R. Essery, N. Gedney, S. Hardiman, B. Johnson, C. Johnson, A. Jones, C. Jones, G. Mann, S. Milton, H. Rumbold, A. Sellar, M. Ujiie, M. Whitall, K. Williams, and M. Zerroukat. The Met Office Unified Model Global Atmosphere 7.0/7.1 and JULES Global Land 7.0 configurations. *Geoscientific Model Development*, 12(5):1909–1963, May 2019. ISSN 1991-959X. doi: 10.5194/gmd-12-1909-2019.

H. Wang and R. Fu. The Influence of Amazon Rainfall on the Atlantic ITCZ through Convectively Coupled Kelvin Waves. *Journal of Climate*, 20(7):1188–1201, Apr. 2007. ISSN 0894-8755, 1520-0442. doi: 10.1175/JCLI4061.1.

M. J. Webb, T. Andrews, A. Bodas-Salcedo, S. Bony, C. S. Bretherton, R. Chadwick, H. Chepfer, H. Douville, P. Good, J. E. Kay, S. A. Klein, R. Marchand, B. Medeiros, A. P. Siebesma, C. B. Skinner, B. Stevens, G. Tselioudis, Y. Tsushima, and M. Watanabe. The cloud feedback model intercomparison project (cfmip) contribution to cmip6. *Geoscientific Model Development*, 10(1):359–384, 2017. doi: 10.5194/gmd-10-359-2017.

P. Webster. *Climatology of the Tropical Atmosphere and Upper Ocean*, chapter 1, pages 1–35. John Wiley Sons, Ltd, 2020a. ISBN 9781118648469. doi: https://doi.org/10.1002/9781118648469.ch1.

P. Webster. *Dynamics of the Large-Scale Monsoon*, chapter 16, pages 361–405. John Wiley Sons, Ltd, 2020b. ISBN 9781118648469. doi: https://doi.org/10.1002/9781118648469.ch16.

K. V. Weverberg, C. J. Morcrette, and I. Boutle. A Bimodal Diagnostic Cloud Fraction Parameterization. Part II: Evaluation and Resolution Sensitivity. *Monthly Weather Review*, Mar. 2021. doi: 10.1175/MWR-D-20-0230.1.

M. Wheeler and G. N. Kiladis. Convectively Coupled Equatorial Waves: Analysis of Clouds and Temperature in the Wavenumber–Frequency Domain. *Journal of the Atmospheric Sciences*, 56(3):374–399, Feb. 1999. ISSN 0022-4928, 1520-0469. doi: 10.1175/1520-0469(1999)056⟨0374:CCEWAO⟩2.0.CO;2.

J. D. White, A. Aiyyer, and J. O. H. Russell. The impact of orography on the african easterly

wave stormtrack. *Journal of Geophysical Research: Atmospheres*, 126(9):e2020JD033749, 2021. doi: 10.1029/2020JD033749. e2020JD033749 2020JD033749.

B. A. Wielicki, B. R. Barkstrom, E. F. Harrison, R. B. Lee, G. L. Smith, and J. E. Cooper. Clouds and the earth's radiant energy system (ceres): An earth observing system experiment. *Bulletin of the American Meteorological Society*, 77(5):853 – 868, 1996. doi: 10.1175/1520-0477(1996)077⟨0853:CATERE⟩2.0.CO;2.

P. D. Willetts, J. H. Marsham, C. E. Birch, D. J. Parker, S. Webster, and J. Petch. Moist convection and its upscale effects in simulations of the Indian monsoon with explicit and parametrized convection. *Quarterly Journal of the Royal Meteorological Society*, 143(703): 1073–1085, 2017. ISSN 1477-870X. doi: 10.1002/qj.2991.

D. R. Wilson and S. P. Ballard. A microphysically based precipitation scheme for the UK meteorological office unified model. *Quarterly Journal of the Royal Meteorological Society*, 125(557):1607–1636, 1999. ISSN 1477-870X. doi: 10.1002/qj.49712555707.

D. R. Wilson, A. C. Bushell, A. M. Kerr-Munslow, J. D. Price, and C. J. Morcrette. PC2: A prognostic cloud fraction and condensation scheme. I: Scheme description. *Quarterly Journal of the Royal Meteorological Society*, 134(637):2093–2107, 2008. ISSN 1477-870X. doi: 10.1002/qj.333.

J. M. Windmiller and G. C. Craig. Universality in the Spatial Evolution of Self-Aggregation of Tropical Convection. *Journal of the Atmospheric Sciences*, 76(6):1677–1696, June 2019. ISSN 0022-4928, 1520-0469. doi: 10.1175/JAS-D-18-0129.1.

A. A. Wing. Self-Aggregation of Deep Convection and its Implications for Climate. *Curr Clim Change Rep*, 5(1):1–11, Mar. 2019. ISSN 2198-6061. doi: 10.1007/s40641-019-00120-3.

A. A. Wing and T. W. Cronin. Self-aggregation of convection in long channel geometry. *Quarterly Journal of the Royal Meteorological Society*, 142(694):1–15, 2016. ISSN 1477-870X. doi: 10.1002/qj.2628.

A. A. Wing and K. A. Emanuel. Physical mechanisms controlling self-aggregation of convection in idealized numerical modeling simulations. *Journal of Advances in Modeling Earth Systems*, 6(1):59–74, 2014. ISSN 1942-2466. doi: 10.1002/2013MS000269.

A. A. Wing, K. Emanuel, C. E. Holloway, and C. Muller. Convective Self-Aggregation in

Numerical Simulations: A Review. *Surv Geophys*, 38(6):1173–1197, Nov. 2017. ISSN 1573-0956. doi: 10.1007/s10712-017-9408-4.

A. A. Wing, C. L. Stauffer, T. Becker, K. A. Reed, M.-S. Ahn, N. P. Arnold, S. Bony, M. Branson, G. H. Bryan, J.-P. Chaboureau, S. R. De Roode, K. Gayatri, C. Hohenegger, I.-K. Hu, F. Jansson, T. R. Jones, M. Khairoutdinov, D. Kim, Z. K. Martin, S. Matsugishi, B. Medeiros, H. Miura, Y. Moon, S. K. Müller, T. Ohno, M. Popp, T. Prabhakaran, D. Randall, R. Rios-Berrios, N. Rochetin, R. Roehrig, D. M. Romps, J. H. Ruppert Jr., M. Satoh, L. G. Silvers, M. S. Singh, B. Stevens, L. Tomassini, C. C. van Heerwaarden, S. Wang, and M. Zhao. Clouds and Convective Self-Aggregation in a Multimodel Ensemble of Radiative-Convective Equilibrium Simulations. *Journal of Advances in Modeling Earth Systems*, 12(9):e2020MS002138, 2020. ISSN 1942-2466. doi: 10.1029/2020MS002138.

B. Wolding, J. Dias, G. Kiladis, F. Ahmed, S. W. Powell, E. Maloney, and M. Branson. Interactions between Moisture and Tropical Convection. Part I: The Coevolution of Moisture and Convection. *Journal of the Atmospheric Sciences*, 77(5):1783–1799, May 2020. ISSN 0022-4928, 1520-0469. doi: 10.1175/JAS-D-19-0225.1.

B. Wolding, S. W. Powell, F. Ahmed, J. Dias, M. Gehne, G. Kiladis, and J. D. Neelin. Tropical Thermodynamic–Convection Coupling in Observations and Reanalyses. *Journal of the Atmospheric Sciences*, 79(7):1781–1803, July 2022. ISSN 0022-4928, 1520-0469. doi: 10.1175/JAS-D-21-0256.1.

B. O. Wolding, E. D. Maloney, S. Henderson, and M. Branson. Climate change and the Madden-Julian Oscillation: A vertically resolved weak temperature gradient analysis. *Journal of Advances in Modeling Earth Systems*, 9(1):307–331, 2017. ISSN 1942-2466. doi: 10.1002/2016MS000843.

N. Z. Wong and Z. Kuang. The Effect of Different Implementations of the Weak Temperature Gradient Approximation in Cloud Resolving Models. *Geophysical Research Letters*, 50(24): e2023GL104350, 2023. ISSN 1944-8007. doi: 10.1029/2023GL104350.

S.-P. Xie, C. Deser, G. A. Vecchi, J. Ma, H. Teng, and A. T. Wittenberg. Global Warming Pattern Formation: Sea Surface Temperature and Rainfall. *Journal of Climate*, 23(4):966–986, Feb. 2010. ISSN 0894-8755, 1520-0442. doi: 10.1175/2009JCLI3329.1.

J.-I. Yano and R. S. Plant. Convective quasi-equilibrium. *Reviews of Geophysics*, 50(4), 2012. ISSN 1944-9208. doi: 10.1029/2011RG000378.

J.-I. Yano and R. S. Plant. Why does arakawa and schubert's convective quasi-equilibrium closure not work? mathematical analysis and implications. *Journal of the Atmospheric Sciences*, 77(4):1371 – 1385, 2020. doi: 10.1175/JAS-D-19-0165.1.

J.-I. Yano, M. Bister, Fuchs, L. Gerard, V. T. J. Phillips, S. Barkidija, and J.-M. Piriou. Phenomenology of convection-parameterization closure. *Atmospheric Chemistry and Physics*, 13(8):4111–4131, Apr. 2013. ISSN 1680-7316. doi: 10.5194/acp-13-4111-2013.

C. Zhang, B. E. Mapes, and B. J. Soden. Bimodality in tropical water vapour. *Quarterly Journal of the Royal Meteorological Society*, 129(594):2847–2866, 2003. ISSN 1477-870X. doi: 10.1256/qj.02.166.

G. J. Zhang. Convective quasi-equilibrium in the tropical western pacific: Comparison with midlatitude continental environment. *Journal of Geophysical Research: Atmospheres*, 108 (D19), 2003. doi: https://doi.org/10.1029/2003JD003520.

Y. Zhang and S. Fueglistaler. Mechanism for Increasing Tropical Rainfall Unevenness With Global Warming. *Geophysical Research Letters*, 46(24):14836–14843, 2019. ISSN 1944-8007. doi: 10.1029/2019GL086058.